

Institut für Angewandte Photophysik
Fachrichtung Physik
Fakultät Mathematik und Naturwissenschaften
Technische Universität Dresden

Optimizing Organic Solar Cells – Transparent Electron Transport Materials for Improving the Device Performance

Dissertation
zur Erlangung des
akademischen Grades
Doctor rerum naturalium,
(Dr. rer. nat.)

vorgelegt von
Christiane Falkenberg
geboren am 31.05.1984 in Zwickau

Dresden 2011



Eingereicht am 02.12.2011

1. Gutachter: Prof. Dr. Karl Leo

2. Gutachter: Prof. Dr. Klaus Müllen

Verteidigt am 06.03.2012

Contents

Publications	3
Introduction	5
1 Basics of Organic Semiconductors & Principle of Organic Solar Cells	9
1.1 Organic Semiconductors	9
1.1.1 Properties of Organic Molecules	9
1.1.2 From Molecules to Solids	12
1.1.3 Molecular Doping	16
1.2 Organic Solar Cells	19
1.2.1 Conventional Silicon Solar Cells	19
1.2.2 The Organic Donor-Acceptor Heterojunction	25
1.2.3 The p-i-n Concept	28
2 Experimental	31
2.1 Materials	31
2.1.1 Standard Materials	31
2.1.2 Electron Transport Materials	34
2.2 Sample Preparation	39
2.3 Experimental Methods & Setups	41
2.3.1 Characterization of Single Layers	41
2.3.2 Characterization of Devices	46
3 HATCN	53
3.1 Characterization	53
3.1.1 Basic Physical Properties	53
3.1.2 Estimation of the Electron Affinity	56
3.2 Solar Cells	58
3.2.1 Injection Barriers & S-Kinks	58
3.2.2 Tailoring the Injection Barrier by Doping	61
3.2.3 Impedance Spectra	63
3.3 Summary	68
4 Bis-FI-NTCDI Derivatives	69
4.1 Characterization	69
4.1.1 Optical and Electrical Properties	69
4.1.2 Thin Film Morphology	71
4.1.3 Conductivity	75
4.2 Solar Cells	78
4.3 Summary	81
5 HATNA-Cl₆	83
5.1 Characterization	83
5.2 Solar Cells - Proof of Principle	86
5.3 Summary	87

6	Comparison of Transparent ETM in p-i-n and n-i-p Type Solar Cells	89
6.1	Optical Simulations	89
6.1.1	p-i-n Type Devices	90
6.1.2	n-i-p Type Devices	91
6.2	Solar Cells	92
6.2.1	n-C ₆₀ as Reference ETM	92
6.2.2	Performance of p-i-n Type Solar Cells with Varying ETM	96
6.2.3	n-i-p Type Solar Cells – Proof of Principle	101
6.3	Summary	103
7	Stability Issues	105
7.1	Lifetime of p-i-n Type Solar Cells with Different ETM	105
7.2	Impedance Spectroscopy Measurements	107
7.3	Summary	109
8	Summary and Outlook	111
8.1	Summary	111
8.2	Outlook	114
	Appendix A - Characteristic Parameters of Devices Presented in Chapter 6	117
	Appendix B - Database Numbers of Solar Cells Shown in this Thesis	119
	Appendix C - Abbreviations	121
	Appendix D - Materials	123
	Appendix E - Symbols	125
	Bibliography	130
	Acknowledgements	143
	Erklärung	147

Abstract

This thesis deals with the characterization and implementation of transparent electron transport materials (ETM) in vacuum deposited p-i-n type organic solar cells (OSC) for substituting the parasitically absorbing standard ETM composed of n-doped C_{60} . In addition to transparency in the visible range of the sun spectrum, the desired material properties include high electron mobility and conductivity, thermal and morphological stability, as well as good energy level alignment relative to the adjacent acceptor layer which is commonly composed of intrinsic C_{60} . In this work, representatives of three different material classes are evaluated with regard to the above mentioned criteria.

HATCN (hexaazatriphenylene hexacarbonitrile) is a small discoid molecule with six electron withdrawing nitrile groups at its periphery. It forms smooth thin films with an optical energy gap E_g^{opt} of 3.3eV, thus being transparent in the visible range of the sun spectrum. Doping with either 5wt% of the cationic n-dopant AOB or 7wt% of the proprietary material NDN1 effectively increases the conductivity to $7.6 \cdot 10^{-6}$ S/cm or $2.2 \cdot 10^{-4}$ S/cm, respectively. However, the fabrication of efficient OSC is impeded by the exceptionally high electron affinity (EA) of ≈ 4.8 eV that causes the formation of an electron injection barrier between n-HATCN and intrinsic C_{60} ($EA = 4.0$ eV). This work presents a strategy to remove the barrier by introducing doped and undoped C_{60} intermediate layers, thus demonstrating the importance of energy level matching in a multi-layer structure and the advantages of Fermi level control by doping.

Next, a series of six **Bis-FI-NTCDI** (N,N-bis(flourene-2-yl)-naphthalenetetracarboxylic diimide) compounds, which only differ by the length of the alkyl chains attached to the C9 positions of the fluorene side groups, is examined. When increasing the chain length from 0 to 6 carbon atoms, the energy levels remain nearly unchanged: We find $EA \approx 3.5$ eV as estimated from cyclic voltammetry, an ionization potential (IP) in the range between 6.45eV and 6.63eV, and $E_g^{\text{opt}} \approx 3.1$ eV which means that all compounds form transparent thin films. Concerning thin film morphology, the addition of side chains results in the formation of amorphous layers with a surface roughness < 1 nm on room temperature glass substrates, and (1.5 ± 0.5) nm for deposition onto glass substrates heated to 100°C . In contrast, films composed of the side chain free compound Bis-HFI-NTCDI exhibit a larger surface roughness of (2.5 ± 0.5) nm and 9nm, respectively, and are nanocrystalline already at room temperature. Moreover, the conductivity achievable by n-doping is very sensitive to the side chain length: Whereas doping of Bis-HFI-NTCDI with 7wt% NDN1 results in a conductivity in the range of 10^{-4} S/cm, the attachment of alkyl chains causes a conductivity which is more than three orders of magnitude smaller despite equal or slightly higher doping concentrations. The insufficient transport properties of the alkylated derivatives lead to the formation of pronounced s-kinks in the jV -characteristics of p-i-n type OSC while the use of n-Bis-HFI-NTCDI results in well performing devices.

The last material, **HATNA-Cl₆** (2,3,8,9,14,15- hexachloro-5,6,11,12,17,18-hexaazatrinaphthylene), exhibits $E_g^{\text{opt}} = 2.7$ eV and is therefore not completely transparent in the visible range of the sun spectrum. However, its energy level positions of $EA = 4.1$ eV and $IP = 7.3$ eV are well suited for the application as ETM in combination with i- C_{60} as acceptor. The compound is dopable with all available n-dopants, resulting in maximum conductivities of $\sigma = 1.6 \cdot 10^{-6}$, $3.5 \cdot 10^{-3}$, and $7.5 \cdot 10^{-3}$ S/cm at 7.5wt% AOB, $\text{Cr}_2(\text{hpp})_4$, and NDN1, respectively. Applying n-HATNA-Cl₆ instead of the reference ETM n- C_{60} results in a comparable or improved photocurrent density at an ETM thickness $d_{\text{ETM}} = 40$ nm or 120nm, respectively. At $d_{\text{ETM}} = 120$ nm, η is more than doubled as it increases from $\eta_{\text{n-C}_{60}} = 0.4\%$ to $\eta_{\text{n-HATNA-Cl}_6} = 0.9\%$.

Optical simulations show that the replacement of n- C_{60} by n-Bis-HFI-NTCDI, n-HATNA-Cl₆, or the previously studied n-NTCDA (naphthalenetetracarboxylic dianhydride) in p-i-n or n-i-p type device architectures is expected to result in an increased photocurrent due to reduced parasitic absorption. For quantifying the gain, the performance of **p-i-n type OSC with varying ETM** type and thickness is evaluated. Special care has to be taken when analyzing devices comprising the reference ETM n- C_{60} as its conductivity is sufficiently large to extend the area of the aluminum cathode and thus the effective device area which may lead to distorted results. Overall, the experiment is able to confirm the trends predicted by the optical simulation. At large ETM thickness in the range between 60 and 120nm, the window layer effect of the ETM is most pronounced. For instance, at $d_{\text{ETM}} = 120$ nm, $\eta_{\text{C}_{60}}$ is more than doubled using n-HATNA-Cl₆ and even more than tripled using n-Bis-HFI-NTCDI or n-NTCDA. At optimized device geometry the photocurrent gain is slightly less than expected but nonetheless, the efficiency is improved from $\eta_{\text{max}} = 2.1\%$ for n- C_{60} and n-HATNA-Cl₆ solar cells to $\eta_{\text{max}} = 2.3$ and 2.4%

for n-Bis-HfI-NTCDI and n-NTCDA devices, respectively. This development is supported by generally higher V_{oc} and FF in solar cells with transparent ETM.

Finally, p-i-n type solar cells with varying ETM are aged at a temperature of 50°C and an illumination intensity of approximately 2 suns. Having extrapolated **lifetimes** t_{80} of 36 500 and 14 000h and nearly unchanged jV -characteristics after 2 000h, n-C₆₀ and n-Bis-HfI-NTCDI devices exhibit the best stability. In contrast, n-NTCDA devices suffer from a constant decrease in I_{sc} while n-HATNA-Cl₆ solar cells show a rapid degradation of both I_{sc} and FF associated with a decomposition of the material or a complete de-doping of the ETM. Here, lifetimes of only 4 500h and 445h are achieved.

Zusammenfassung

Diese Dissertation beschäftigt sich mit der Charakterisierung und Implementierung transparenter Elektronentransportmaterialien (ETM) für vakuumprozessierte organische p-i-n Solarzellen (OSZ), in denen das bisher verwendete, parasitär absorbierende Standard ETM bestehend aus n-dotiertem C₆₀ ersetzt werden soll. Die gewünschten Materialeigenschaften beinhalten neben der Transparenz im sichtbaren Bereich des Sonnenspektrums eine hohe Elektronenbeweglichkeit und Leitfähigkeit, thermische und morphologische Stabilität, sowie eine Energieniveaueinpassung zur angrenzenden Akzeptorschicht, die gemeinhin aus intrinsischem C₆₀ besteht. In der vorliegenden Arbeit werden Vertreter dreier verschiedener Materialklassen mit Bezug auf die genannten Kriterien bewertet.

HATCN (Hexacyano Hexaazatriphenyl) ist ein kleines scheibenförmiges Molekül, das sechs elektronenziehende Nitrilgruppen beinhaltet. Es bildet glatte Dünnschichten mit einer optischen Energielücke von $E_g^{\text{opt}} = 3.3\text{eV}$, die folglich im sichtbaren Bereich des Sonnenspektrums transparent sind. Eine Dotierung mit 5wt% des kationischen n-Dotanden AOB oder 7wt% des proprietären Materials NDN1 erhöht die Leitfähigkeit auf $7.6 \cdot 10^{-6}\text{S/cm}$ oder $2.2 \cdot 10^{-4}\text{S/cm}$. Die Herstellung effizienter OSZ wird jedoch durch die außergewöhnlich hohe Elektronenaffinität (EA) von $\approx 4.8\text{eV}$ erschwert, welche die Entstehung einer Elektroneninjektionsbarriere zwischen n-HATCN und intrinsischem C₆₀ ($EA = 4.0\text{eV}$) verursacht. Es wird eine Strategie vorgestellt, mit der die Barriere mittels dotierter und undotierter C₆₀ Zwischenschichten entfernt werden kann. Das vorliegende Beispiel demonstriert eindrucksvoll die Wichtigkeit angepasster Energieniveaus in Mehrschichtstrukturen sowie die Vorteile molekularer Dotierung, mit deren Hilfe die Position des Fermi-niveaus innerhalb der Bandlücke kontrolliert werden kann.

Im nächsten Schritt wird eine Serie von **Bis-FI-NTCDI** Verbindungen (N,N-Di(9H-fluoren-2-yl)-naphthalintetracarboxydiimid) untersucht, die sich lediglich durch die Länge der in der C9 Position der Fluoren Seitengruppen angebrachten Alkylketten unterscheiden. Eine Verlängerung der Ketten von 0 auf 6 Kohlenstoffatome lässt die Energieniveaus nahezu unverändert: Mit Zyklovoltammetrie wird die EA auf $\approx 3.5\text{eV}$ abgeschätzt, das UPS Ionisationspotential (IP) findet sich im Bereich zwischen 6.45eV und 6.63eV , und E_g^{opt} beträgt $\approx 3.1\text{eV}$, d.h. alle Verbindungen bilden transparente Dünnschichten. Bezüglich der Morphologie führt die Präsenz von Seitenketten zur Entstehung amorpher Filme mit einer Oberflächenrauigkeit von $< 1\text{nm}$ auf Raumtemperatur Glassubstraten und $(1.5 \pm 0.5)\text{nm}$ auf auf 100°C geheizten Glassubstraten. Dagegen sind Schichten des seitenkettenfreien Materials Bis-HFI-NTCDI durch eine höhere Oberflächenrauigkeit von $(2.5 \pm 0.5)\text{nm}$ oder 9nm gekennzeichnet und bereits bei Raumtemperatur nanokristallin. Weiterhin ist die durch n-Dotierung erreichbare Leitfähigkeit stark von der Seitenkettenlänge abhängig: Während die Beimischung von 7wt% NDN1 die Leitfähigkeit von Bis-HFI-NTCDI auf 10^{-4}S/cm erhöht, verursacht die Gegenwart von Alkylketten trotz gleicher oder sogar höherer Dotierungskonzentrationen eine um mehr als drei Größenordnungen kleinere Leitfähigkeit. Die ungenügenden Transporteigenschaften der alkylierten Derivate führen zu der Bildung ausgeprägter S-Knicke in den jV -Kennlinien entsprechender p-i-n Solarzellen, während die Verwendung von n-Bis-HFI-NTCDI leistungsfähige Bauelemente ergibt.

Das letzte Material, **HATNA-Cl₆** (2,3,8,9,14,15-Hexachlor-5,6,11,12,17,18-hexaazatrinaphthylen) ist durch $E_g^{\text{opt}} = 2.7\text{eV}$ gekennzeichnet und somit im sichtbaren Bereich des Sonnenspektrums nicht vollständig transparent. Die Energieniveaus von $EA = 4.1\text{eV}$ und $IP = 7.3\text{eV}$ sind jedoch sehr gut für eine Anwendung als ETM in Kombination mit i-C₆₀ als Akzeptor geeignet. Die Verbindung ist mit allen verfügbaren n-Dotanden dotierbar, wobei maximale Leitfähigkeiten von $\sigma = 1.6 \cdot 10^{-6}$, $3.5 \cdot 10^{-3}$ und $7.5 \cdot 10^{-3}\text{S/cm}$ mit je 7.5wt% AOB, Cr₂(hpp)₄ und NDN1 erreicht werden. Die Verwendung von HATNA-Cl₆ anstelle des Referenzmaterials n-C₆₀ führt zu einer vergleichbaren oder erhöhten Photostromdichte wenn eine ETM Dicke von $d_{\text{ETM}} = 40\text{nm}$ oder 120nm gewählt wird. Bei $d_{\text{ETM}} = 120\text{nm}$ erhöht sich η um mehr als das Doppelte von $\eta_{\text{n-C60}} = 0.4\%$ auf $\eta_{\text{n-HATNA-Cl6}} = 0.9\%$.

Optische Simulationen zeigen, dass der Austausch von n-C₆₀ durch n-Bis-HFI-NTCDI, n-HATNA-Cl₆ oder das in einer früheren Studie untersuchte n-NTCDA (Naphthalintetracarboxydianhydrid) in p-i-n oder n-i-p Strukturen aufgrund der reduzierten parasitären Absorption zu einer Erhöhung des Photostromes führt. Um die Verbesserung zu quantifizieren wird die Leistung von **p-i-n OSZ bewertet, die in ETM Typ und Dicke variieren**. Bei der Auswertung von Solarzellen, die das Referenzmaterial n-C₆₀ beinhalten ist besondere Sorgfalt nötig, da dessen Leitfähigkeit ausreichend hoch ist um die Fläche der Aluminiumkathode und damit die effektive Solarzellenfläche auszudehnen, was zu einer Verfälschung der Messergebnisse führen kann. Insgesamt bestätigt das Experiment die von der optischen Simulation vorausgesagten Trends. Bei hohen ETM Dicken, zwischen 60 und 120nm, ist der Effekt des transparenten

ETM am stärksten ausgeprägt. Beispielsweise kann η_{C60} bei $d_{ETM} = 120\text{nm}$ unter Verwendung von n-HATNA-Cl₆ mehr als verdoppelt und unter Verwendung von n-Bis-HFl-NTCDI oder n-NTCDA sogar mehr als verdreifacht werden. Bei optimierter Bauteilgeometrie fällt die Erhöhung des Photostromes etwas niedriger aus als erwartet; die Effizienz kann dennoch von $\eta_{\text{max}} = 2.1\%$ für n-C₆₀ und n-HATNA-Cl₆ Solarzellen auf $\eta_{\text{max}} = 2.3$ und 2.4% für n-Bis-HFl-NTCDI und n-NTCDA gesteigert werden. Diese Entwicklung wird von den für transparente ETM generell höheren V_{oc} und FF unterstützt.

Schließlich werden p-i-n Solarzellen mit unterschiedlichen ETM bei einer Temperatur von 50°C und einer Beleuchtungsintensität von ca. 2 Sonnen gealtert. Mit extrapolierten **Lebensdauern** t_{80} von 36 500 und 14 000h sowie nahezu unveränderten jV -Kennlinien nach 2 000h zeigen n-C₆₀ und n-Bis-HFl-NTCDI Bauelemente die beste Stabilität. Im Gegensatz dazu nimmt I_{sc} der n-NTCDA Zellen kontinuierlich ab während n-HATNA-Cl₆ Bauteile eine schnelle Degradation von I_{sc} und FF zeigen, die entweder von einer Zersetzung des Materials oder einer vollständigen Entdotierung des ETM verursacht wird. Es werden Solarzellen-Lebensdauern von nur 4 500h und 445h erreicht.

Publications

Articles

- A1** C. Falkenberg, C. Uhrich, S. Olthof, B. Maennig, M. Riede, and K. Leo, *Efficient p-i-n type organic solar cells incorporating 1,4,5,8-naphthalenetetracarboxylic dianhydride as transparent electron transport material*. Journal of Applied Physics **104**, 034506 (2008).
- A2** C. Falkenberg, C. Uhrich, B. Maennig, M. K. Riede, and K. Leo, *1,4,5,8-Naphthalenetetracarboxylic dianhydride as transparent electron transport material in organic p-i-n solar cells*. Proceedings of SPIE **6999**, 69990S (2008).
- A3** J. Meiss, N. Allinger, C. Falkenberg, K. Leo, and M. Riede, *Transparent conductive layers for organic solar cells: simulation and experiment*. Proceedings of SPIE **7416**, 741603 (2009).
- A4** C. Falkenberg, S. Olthof, R. Rieger, M. Baumgarten, K. Muellen, K. Leo, and M. Riede, *The role of energy level matching in organic solar cells - Hexaazatriphenylene hexacarbonitrile as transparent electron transport material*. Solar Energy Materials & Solar Cells **95**, 927 (2011).
- A5** C. Falkenberg, *Improved photocurrent by using n-doped 2,3,8,9,14,15-hexachloro-5,6,11,12,17,18-hexaazatrinaphthylene (HATNA-Cl₆) as optical spacer layer in p-i-n type organic solar cells*, Journal of Applied Physics, in press.

Conference Contributions

- C1** C. Falkenberg, C. Uhrich, S. Olthof, B. Männig, M. Riede, and K. Leo, *NTCDA as transparent electron transport material in organic p-i-n solar cells*. 72. Jahrestagung der DPG, February 25th-29th 2008, Berlin (Poster).
- C2** C. Falkenberg, C. Uhrich, S. Olthof, B. Männig, M. Riede, and K. Leo, *NTCDA as transparent electron transport material in organic p-i-n solar cells*. SPIE Photonics Europe, April 07th-10th 2008, Strassburg (Talk).
- C3** C. Falkenberg, M. Baumgarten, R. Rieger, K. Muellen, K. Leo, and M. Riede, *New wide-gap electron transport materials for the application in small molecule organic solar cells*. 10th European Conference on Molecular Electronics, September 09th-12th 2009, Copenhagen (Poster).
- C4** C. Falkenberg, S. Olthof, M. Baumgarten, R. Rieger, K. Muellen, K. Leo, and M. Riede, *Hexaazatriphenylene and hexaazatrinaphthylene derivatives as electron transport materials in organic solar cells*. Frühjahrstagung der DPG, March 21th-26th 2010, Regensburg (Talk).
- C5** C. Falkenberg, M. Baumgarten, R. Rieger, K. Muellen, K. Leo, and M. Riede, *Hexaazatriphenylene and hexaazatrinaphthylene derivatives as electron transport materials in organic solar cells*. 9th International Symposium on Functional π -Electron Systems, May 23th-28th 2010, Atlanta (Poster).
- C6** C. Falkenberg, M. Hummert, S. Olthof, C. Schünemann, K. Leo, and M. Riede, *Influence of the molecular structure of electron transport materials on the performance of organic solar cells*. 75. Jahrestagung der DPG, March 13th-18th 2011, Dresden (Poster).

Patents

M. Hummert, C. Falkenberg, S. Olthof, M. Hermeau, M. Riede, K. Leo, *Solarzelle mit transparentem Elektronentransportmaterial*, application number: 10 2011 013 897.8, date of filing: 11.3.2011.

Introduction

In recent years, there has been a controversial discussion about the realization of a sustainable power supply for the earth's growing population. Due to the inevitably limited resources of fossil fuels, all scenarios project a strongly increasing significance of renewable technologies in the energy mix. However, the specific role of each technology is not easily predictable as it depends on a number of factors like the environmental conditions at each particular location, the ongoing competition for the most reliable technique at the lowest price, the adaption of the electricity grid and last but not least the political situation. With the sun as our largest energy supply, it is foreseeable that solar power will play a key role concerning the generation of heat and electricity. By 2050, photovoltaics could provide up to 30% of the world's electricity while today it covers less than 1%^[1]. Currently, silicon solar cells are the most established technology. Using monocrystalline silicon (c-Si), module efficiencies of 14...20%^[2-4] are achieved in mass production and even 25%^[5] in laboratory cells, while polycrystalline devices (pc-Si) reach about 13...15%^[2] and 20%^[5], respectively.

Despite its predominance, conventional silicon photovoltaics suffers from several drawbacks, such as a large energy consumption for the extraction of pure silicon and the fabrication of devices, or the comparatively high losses when cutting solid silicon blocks into thin slices of only several 100 μ m thickness. Competing technologies focus on the production of thin film devices which are characterized by lower material consumption, light weight, and potential for flexibility. Also here, silicon based solar cells can be found: Depositing silicon onto carrier materials like glass results in the formation of thin, amorphous layers which allow the fabrication of devices thinner than 1 μ m (a-Si). Though considerably less energy and raw material is needed for processing, the low efficiency of either 8...9%^[2] in large scale production or 10...12%^[5] in laboratory cells currently prevents a widespread application. The opposite holds true for gallium arsenide (GaAs) solar cells which achieve laboratory efficiencies as high as 28% with a simple device architecture and even 43% in a concentrated photovoltaic cell with a multijunction stack^[5]. However, they are too expensive for being used elsewhere but in special fields like space exploration. Cadmium telluride (CdTe) devices are in-between the two extremes. Although the module efficiency is only about 13%^[5,7], 17%^[5] are achieved in the laboratory cells and thus, the performance is comparable to that of good pc-Si devices. Despite the limited availability of cadmium and tellurium, the technology is competitive and several companies are currently running a large-scale production including the operation in solar parks. Finally, CIS (copper indium selenide: CuInSe₂) or CIGS (copper indium gallium selenide: CuIn_{1-x}Ga_xSe₂) systems constitute promising alternatives whose specific device properties can be tuned by changing the composition of the elements. While laboratory efficiencies of 20%^[5] are reported for single cells, values of about 12...16%^[5,8,9] are reached in modules.

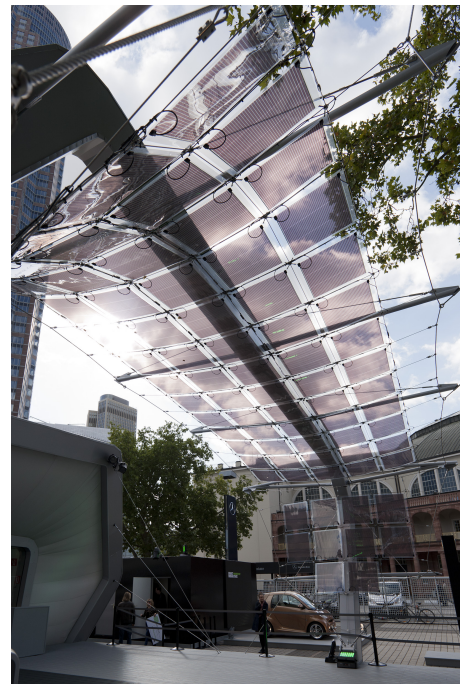


Figure 1: Solar gate presented by BASF and Konarka at the 64th International Motor Show in Frankfurt, Germany. It is made of 85 semitransparent polymer solar modules and contributes to a series of exhibitions called „the future of the city“. Power output, lifetime, and efficiency are undisclosed^[6].

The common disadvantage of all above described silicon-free technologies is the use of rare, limited and thus expensive elements like tellurium and indium or materials with potential health risks like arsenic, cadmium or tellurium.

Organic solar cells (OSC), which are the topic of this thesis, constitute an alternative thin film technology that shares the above given advantages of the inorganic technologies, but not necessarily their drawbacks. Due to the diversity of organic chemistry a huge amount of functionalized materials – most of them being relatively easy to synthesize and non-toxic – is available for application. Organic dyes are characterized by high absorption coefficients in the order of 10^5cm^{-1} which is why the thickness of complete devices is barely larger than 200nm. On the one hand, this allows the production of flexible devices and on the other hand even the realization of semitransparent solar cells which can be integrated into windows and glass facades. Figure 1 shows a futuristic example designed by BASF and Konarka for representing the technology at the 64th International Motor Show in Frankfurt, Germany. However, the so-called solar gate is rather a prestige object than a fully developed application as commonly, the efficiencies of organic solar modules is still in the range of 2...3%. Currently, OSC are entering the market as niche products and several start-up companies are working on commercializing the technology. Despite the low module efficiency, OSC show a very promising development since the first device with an efficiency of 1% was reported in 1986 by Ching Tang (Kodak)^[10]. Today, the record efficiency of laboratory scale devices of 1cm^2 size is at 8.3%^[5] and rapidly approaching 10%. Here, the two competing device types, polymeric and small molecule solar cells are on a par. While in the first case polymers are solution-cast onto the substrate, the latter devices are produced by a controlled evaporation of organic dyes in ultra-high vacuum. Either of the two approaches has its own benefits and drawbacks. However, in both cases the processing temperatures needed for device production are low compared to those required for any of the above described inorganic technologies. Overall, OSC are a promising and low-cost alternative to the established solar cell types. Current research efforts are mainly concentrated on improving device stability, implementing (semi-)transparent electrode materials, establishing the fabrication on flexible substrates, and tuning the absorption properties of the photoactive layers. The latter usually comprise a combination of donor and acceptor type compounds which form the charge generating region which is the heart of every solar cell.

Research conducted at the IAPP focuses on vacuum deposited small molecule organic solar cells. The device architecture is based on the so-called p-i-n concept^[11] which involves the principle of molecular doping that has been developed at this institute. Here, the photoactive heterojunction is sandwiched between a p-doped hole transport material (HTM) and an n-doped electron transport material (ETM) both of which are preferably transparent. The use of dedicated charge transport layers has several advantages: Due to their high conductivities they facilitate the extraction of photogenerated charge carriers towards the electrodes while at the same time they support the formation of ohmic contacts at the organic/metal interfaces. Furthermore, they serve as optical spacer materials separating the photoactive region from the electrodes, thus optimizing its position with respect to thin film optics. The design of suitable functional molecules for those transport layers is an important issue, because obtaining the desired optical and electrical properties like transparency, high charge carrier mobility, dopability, and energy level alignment relative to the adjacent active layer is essential for achieving good device performance. While on the side of hole transport several suitable materials are commercially available, the choice of ETM that are applicable in OSC is very limited. Therefore, it is a common practice to circumvent the use of ETM by inserting a thin organic buffer layer between the photoactive region and the metal cathode, thus protecting the absorber materials from the energy input during metal evaporation. Here, mostly the materials BCP (bathocuproine) or BPhen (bathophenanthroline) are used. Both are hardly n-dopable and as a consequence, their insufficient charge transport properties limit the buffer layer thickness to $< 15\text{nm}$ ^[12]. At the beginning of this thesis only two n-dopable ETM were available: On the one hand, C_{60} which is at the same time used as absorber material in the photoactive area. Although this leads to a perfect alignment of electron transport levels between acceptor and ETM, n- C_{60} parasitically absorbs light which is accordingly lost for the photogeneration of charge carriers. On the other hand, NTCDA (naphthalenetetracarboxylic dianhydride) had been identified as promising candidate in previous studies^[13-15]. Its transparency and favorable energy level positions are opposed by a disadvantageous layer morphology which limits the usability of NTCDA to certain device architectures.

This thesis aims at the identification of suitable organic compounds for the application as ETM in small molecule OSC. For this purpose, several materials are characterized with respect to the criteria of the p-i-n concept and subsequently employed in p-i-n type device structures. To evaluate the performance of the new ETM, the above mentioned, parasitically absorbing material n- C_{60} or the morphologically unfavorable n-

NTCDA are used as reference systems. Before focusing on the results, Chapter 1 will give a short overview of the basic physics of organic semiconductors followed by an introduction to the principles of organic solar cells. Chapter 2 presents the organic materials used in this work and subsequently describes the methods applied for sample preparation and characterization. The following investigation includes compounds from three different material classes. Chapters 3 - 4 give an overview of their physical properties including proof-of-principle applications solar cells, while Chapters 6 and 7 compare the performance of the most promising ETM candidates in p-i-n type OSC. First, the suitability of HATCN (hexaazatriphenylene hexacarbonitrile) – a material known for its strongly electron withdrawing nature – is examined in Chapter 3. The impact of its exceptionally large electron affinity on the energy level alignment within the device stack requires particular attention as it is responsible for the formation of electron injection barriers which are detrimental for the solar cell performance. It will be shown how the negative effects of misaligned electron affinities can be circumvented by means of doping. Chapter 4 presents a series of six Bis-FI-NTCDI (N,N-Bis(fluorene-2-yl)-naphthalenetetracarboxylic diimide) compounds that only differ by length of the alkyl side chains attached to the C9 positions of the fluorene groups. Starting with a side chain free compound (Bis-HFI-NTCDI), the number of carbon atoms in the chain is increased from 1 (methyl, Bis-MeFI-NTCDI) to 2 (ethyl, Bis-EtFI-NTCDI), 3 (propyl, Bis-PrFI-NTCDI), 4 (butyl, Bis-BuFI-NTCDI) and 6 (hexyl, Bis-HexFI-NTCDI). The influence of this variation on the materials physical properties like energy level positions, morphology and charge carrier transport are studied, and finally related to the compounds performance as ETM in p-i-n type solar cells. The last material that is characterized in the framework of this thesis is HATNA-Cl₆ which is introduced in Chapter 5. To quantify the anticipated benefits of transparent ETM, Chapter 6 presents a study of p-i-n type solar cells comprising either n-Bis-HFI-NTCDI or n-HATNA-Cl₆, which are the most promising ETM candidates identified in the previous Chapters, or the reference materials n-C₆₀ and n-NTCDA. The compounds performance as optical spacer layers is evaluated by varying the ETM thickness between 0 and 210nm and comparing the resulting short circuit current densities with values estimated from an optical simulation. Finally, the performance of representative n-i-p devices is presented for proving the applicability of n-Bis-HFI-NTCDI and n-HATNA-Cl₆ in inverted device structures. The last Chapter addresses device stability which is a crucial issue regarding the commercialization of organic solar cells. Here, the lifetimes t_{80} of p-i-n type devices comprising different ETM are compared.

1 Basics of Organic Semiconductors & Principle of Organic Solar Cells

This Chapter introduces the most relevant features of organic semiconductors concerning their application in organic electronic devices. First, the formation of molecular orbitals and their dependence on the molecular structure will be discussed. This is followed by a brief description of organic solids including their optical and charge transport properties, supplemented by a discussion of molecular doping. Subsequently, the principle of organic solar cells will be presented and compared to the principle of conventional inorganic pn-junctions.

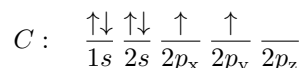
1.1 Organic Semiconductors

1.1.1 Properties of Organic Molecules

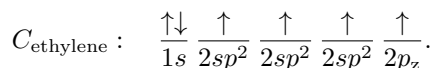
Conjugated π electron systems

Organic thin films which are commonly used for the application in organic electronic devices are usually composed of aromatic hydrocarbons. The semiconducting properties of such compounds arise from the existence of an extended π electron system that is composed of delocalized electrons. In contrast, molecules without any double bonds like for instance alkyl chains only contain much stronger σ bonds with localized electrons leading to a large band gap and insulating properties.

The pre-condition for the formation of π bonds is the so-called sp^2 -hybridization of atomic orbitals. A simple example for molecules exhibiting this type of bonding is ethylene (C_2H_4). Here, two carbon atoms with the ground state configuration



are combined. The energetically most favorable molecular state is achieved by a mixture of the atomic s orbital $\phi(s)$ with both p orbitals $\phi(p_x)$ and $\phi(p_y)$, resulting in the formation of three sp^2 hybrid orbitals and one remaining p_z orbital per carbon atom:



All three hybrid orbitals lie in a plane with the central carbon atom forming an isoscelene triangle with bond angles of 120° . The strong carbon-carbon σ bond in ethylene originates from the large overlap of two sp^2 orbitals which results in a strong energetic splitting between the binding σ orbital that is twice occupied, and the unoccupied σ^* antibonding orbital as sketched in Figure 1.1. The remaining p_z orbitals are perpendicular to the plane. Their comparably small overlap results in a much weaker splitting between the likewise twice occupied binding π and the empty antibonding π^* orbital. As a simple example for aromatic molecules, benzene (C_6H_6) is added to Figure 1.1. It is a planar ring-shaped molecule that consists of six carbon atoms which are connected by σ bonds. The electrons occupying the p_z orbitals are delocalized above and below the plane and form a conjugated system. As it is typical for organic semiconductors, in benzene and in ethylene the highest occupied molecular orbital (HOMO) is formed by π states whereas the lowest unoccupied molecular orbital (LUMO) is constituted by the antibonding π^* states. Typical π - π^* energy gaps are in the order of only a few electron volt. Therefore, photons from the infrared to the ultraviolet spectral range usually have sufficient energy to optically excite such molecules.

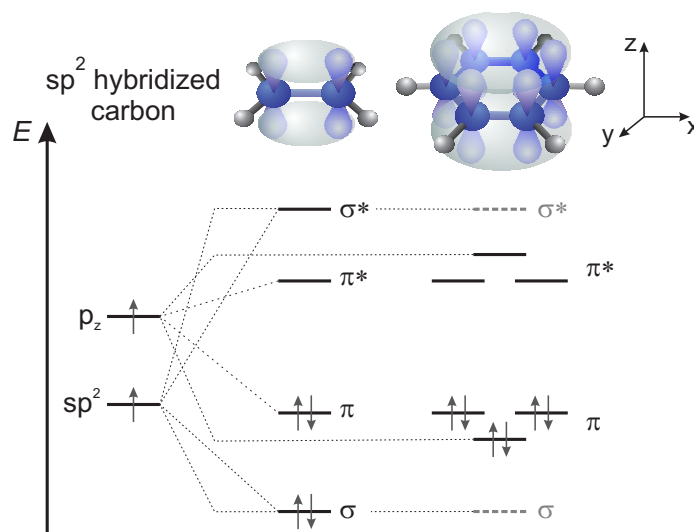


Figure 1.1: sp^2 -hybridization of valence electrons in ethylene and benzene. σ bonds are represented by thick blue or grey lines while π bonds which constitute of the remaining p_z orbitals are depicted as lobes which overlap in order to form a delocalized cloud of electrons. The energy diagram shows the energy level splitting. For a molecule with n carbon atoms, the p_z orbitals split into n π orbitals which are partly degenerate in case of benzene. The same applies for the σ orbitals (not shown here).

Molecular design

Considering the applicability of organic materials in electronic devices, the exact value of the energy gap (E_g) as well as the positions of the frontier orbitals relative to the vacuum level are important parameters. They depend on a number of factors which can not be treated independently and are thus not easy to predict without using quantum chemical calculations. However, there are some rules of thumb which are very helpful for categorizing molecules and which will be shortly discussed in the following paragraphs.

The **size of the conjugated system** is strongly influencing the energy gap between HOMO and LUMO. A very instructive example for this correlation is given by a study on a series of polyacenes published by Karl in 1974 which is reproduced in Figure 1.2^[16]. It is clearly seen that an increasing number of fused benzene rings shifts the energy levels closer towards each other, thus reducing the total band gap.

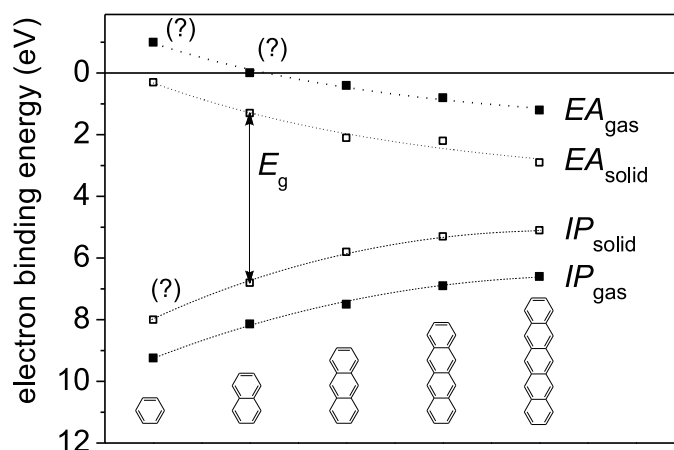


Figure 1.2: Ionization potentials (IP) of the highest occupied and electron affinities (EA) of the lowest unoccupied molecular levels for a series of polyacenes with increasing number of fused benzene rings. E_g is the resulting energy gap. Solid symbols represent gas phase values while the open symbols are derived from the crystalline state. For the question marked symbols no measurement values are available. (reproduced from Karl et al.^[16]).

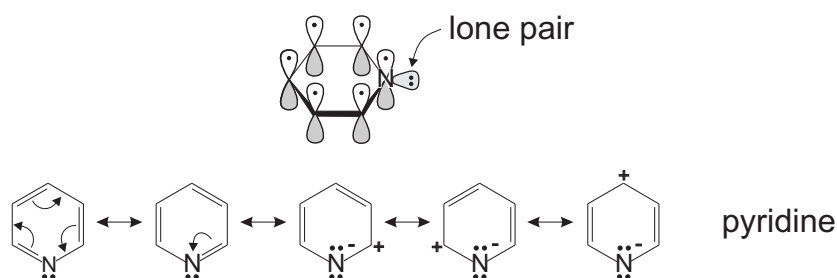


Figure 1.3: Electronic configuration of pyridine and M^- -effect introduced by the nitrogen heteroatom. The bonding and charge distribution can be represented by several contributing structures that collectively describe the actual molecular structure. This concept is called mesomerism or resonance.

Another important point is the influence of **heteroatoms and functional groups** which introduce so-called polar effects and thus affect the electronic properties of the molecules. In principle, there are two types of effects which often occur simultaneously: the mesomeric effect (M-effect) and the inductive effect (I-effect). The *M-effect* only involves electrons in π bonds and is relevant whenever a molecule can be represented by two or more structural formulas that differ only in the arrangement of the π electron system. Each of the representations stands for one way to describe the polarity within the conjugated system, i.e. a way to distribute the double bonds and partial charges. The quantum mechanically correct state is a superposition of all those so-called resonance structures. Compounds with a strong mesomeric effect have many potential structural representations and are more stable than compounds not showing this effect. As an example, Figure 1.3 shows the electronic configuration of pyridine, a benzene ring containing one nitrogen heteroatom. The nitrogen atom is sp^2 -hybridized and possesses one lone pair of electrons which is located in an sp^2 orbital parallel to the aromatic ring system and therefore does not increase the electron density in the π system. However, the high electronegativity of the nitrogen atom introduces an asymmetry to the system which is reflected by three possible resonance structures that contain positively charged carbon atoms.

The electronegativity of substituents does not only modify the π electron configuration, but does also affect the σ bonds. This influence is assigned to the inductive *I-effect*, which, in principle, causes the formation of a dipole that alters the charge distribution.

Both, the M- and the I-effect, can be either electron withdrawing („ M^- “ or „ I^- “) or electron releasing („ M^+ “ or „ I^+ “). Table 1.1 lists a number of examples for polar groups. Some of them can be both electron withdrawing or donating, depending on the respective molecular assembly. With regard to that, Figure 1.4 presents representatives for electron deficient or electron rich moieties which are frequently used as building blocks for functionalized molecules. Compounds (1) - (6) are characteristic parts of electron transport materials. Compared to carbon, nitrogen heteroatoms have a higher electronegativity and withdraw electrons from the π system, thus increasing the activation energy for chemical reactions and lowering the LUMO level. However, whether nitrogen is electron withdrawing or donating depends on the way it is bound. In case of triphenylamine (8), it donates its lone pair of electrons to the π system of the surrounding phenyl rings. Similarly, the sulfur heteroatom in thiophene (7) contributes two of its valence electrons to the π system while having the same electronegativity as carbon. Accordingly, in compounds (7) and (8) the heteroatoms increase the electron density of the conjugated system leading to a high HOMO level – a typical feature of hole transporting materials.

M^-	I^-	M^+	I^+
electron withdrawing		electron donating	
$-\text{NO}_2$ (nitro group)	$-\text{NO}_2$ (nitro group)	$-\text{O}^-$ (alcoholate)	$-\text{Alkyl}$
$-\text{COOR}$ (ester)	$-\text{COOH}$ (acid)	$-\text{OR}$ (ether)	
$-\text{CHO}$ (aldehyde)	$-\text{Aryl}$	$-\text{Aryl}$	
$-\text{CN}$ (cyano group)	$-\text{Cl}, \text{I}, \text{F}$	$-\text{Cl}, \text{I}, \text{F}$	
$-\text{CF}_3$ (trifluoromethyl)	$-\text{CR}=\text{O}$ (keto group)	$-\text{NR}_2$ (amine)	

Table 1.1: Functional groups and substituents with electron withdrawing (M^- and I^-) or electron donating (M^+ and I^+) character. Here, R stands for rest (e.g. an alkyl or aryl radical, or simply hydrogen).

Obviously, organic chemistry bears a great potential for fabricating functionalized molecules with a high level of variability. Often, small modifications in the molecular structure can lead to specific changes of the physical properties. The previous section could only touch the surface of this complex topic. Predicting the properties of a certain compound only by judging its molecular structure is a non-trivial, or even impossible venture that often involves sophisticated quantum chemical calculations.

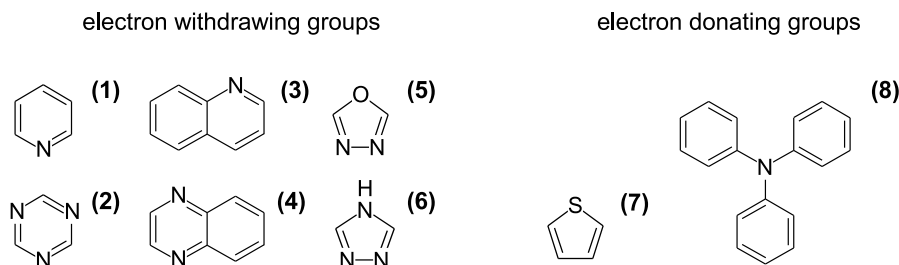


Figure 1.4: Some typical electron withdrawing moieties relevant for organic electronics (1) - (6) and electron donating groups (7) and (8): (1) pyridine, (2) triazine, (3) quinoline, (4) quinoxaline, (5) oxadiazole, (6) triazole, (7) thiophene, and (8) triphenylamine.

1.1.2 From Molecules to Solids

Considering the application of organic materials as semiconductors, the question arises to which extent the molecular properties described above can be transferred to the solid state. Molecular crystals are usually constituted of neutral molecules with fully occupied orbitals which condense in a non-covalently bound state. The intermolecular forces are dominated by short range van der Waals forces, i.e. dipole-dipole interactions, which are weak compared to the intramolecular forces. As a direct consequence, organic compounds commonly have a low melting, evaporation, or sublimation temperature, low dielectric constants in the range of $\epsilon = 1...6$ ^[17], and a small intrinsic conductivity. Furthermore, characteristic molecular properties as for instance intramolecular vibrational modes remain basically intact. The intermolecular forces finally become important regarding energy or charge transport.

Relaxation processes

As can be seen from the example displayed in Figure 1.2, the energy levels of molecules in the gas phase differ considerably from those observed in the solid state: Solids display a decreased ionization potential (*IP*) and an increased electron affinity (*EA*). Obviously, the intermolecular interactions influence the electronic structure in a systematic way. When talking about the solid state, i.e. the aggregation of many molecules, the terms HOMO and LUMO are not valid any more because they are only defined for isolated molecules. They are replaced by the more accurate expressions ionization potential and electron affinity which include effects introduced by the surrounding molecules and the presence of additional charges. Considering charge transport or energy level alignment in multi-layer systems, the energy levels of the neutral system become secondary – especially when interface dipoles are involved.

The ionization of a molecule causes several relaxation processes of the crystal lattice that occur on different time scales and energetically stabilize the charge carrier. The fastest process which happens within the first $10^{-16}...10^{-15}$ s is the electronic polarization of the surrounding neutral molecules. The displacement of π orbitals induces dipole moments and lowers the *IP* of the neutral state by the value of the polarization energy P_h while *EA* increases by the energy P_e . If, like in most cases, the ionized molecule does not have any permanent dipole moment, P_h equals P_e . Typical values for the polarization energy P of the crystal are between 1.5...2.0eV^[18]. As the localization time τ_h of a charge carrier on a molecule is usually $> 10^{-14}$ s, the charge carrier is usually always accompanied by its polarization cloud when moving from molecule to molecule. The quasi-static formation consisting of the charge carrier surrounded by a polarized lattice is called *electronic polaron* and commonly treated as quasi-particle. Considering the energetic position of the electronic conduction states, polarization is the most important factor.

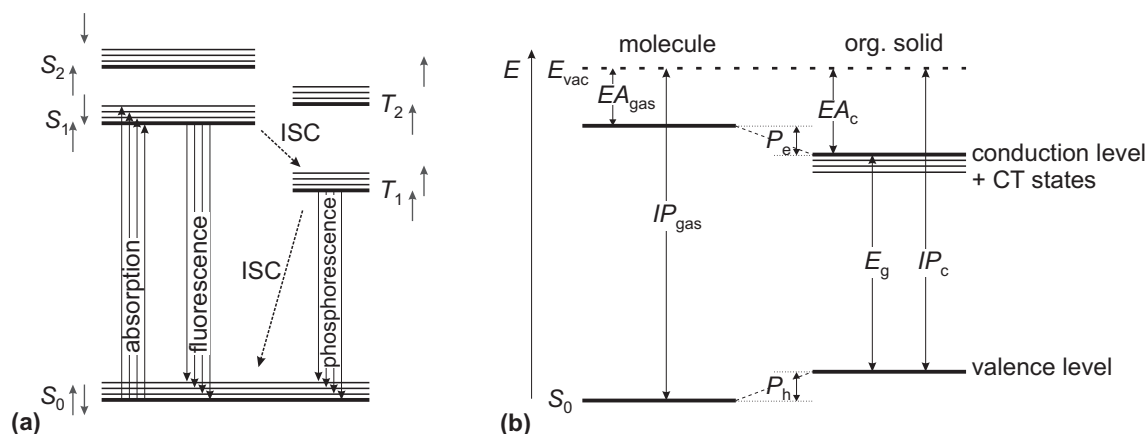


Figure 1.5: a) Radiative transitions absorption, fluorescence, and phosphorescence plotted in the energy level scheme of a free molecule. The intersystem crossing (ISC) between singlet states S and triplet states T is non-radiative. Further non-radiative transitions as the internal conversion from higher excited levels to S_1 or T_1 are omitted. b) Energy level scheme of a free organic molecule (left) and its corresponding solid state (right). The singlet ground state S_0 , the gas phase electron affinity EA_{gas} and the gas phase ionization potential IP_{gas} are given with respect to the vacuum energy E_{vac} . The transition from the gas phase to the crystalline phase shifts the energy levels by the above described polarization energies P_h and P_e for electrons and holes. EA_c , IP_c and E_g correspond to the electron affinity, the ionization potential and the electrical energy gap in the organic solid. Charge transfer (CT) states in which electron and hole are separated onto two neighboring molecules are plotted below the conduction level.

The electronic polarization is followed by the vibronic relaxation, an intramolecular process affecting the equilibrium configurations of the nuclei and accordingly the energy of the bonding and antibonding orbitals. It changes the binding forces between the atoms in the molecule by typically 10...100meV and occurs on a time scale of $\tau_v = 10^{-14} \dots 10^{-13} \text{s}$ ^[18]. This time scale is in the same order as the localization time τ_h , so the vibronic relaxation might not be complete when the charge carrier moves on. This is more likely to happen in disordered systems where the charge carriers move more slowly and a dynamic state called *vibronic polaron*, i.e. a vibronically relaxed polaron, may be formed.

The lattice relaxation, that means the mechanical deformation of the surrounding crystal lattice, is usually much slower than the localization time τ_h and is in the order of $\tau_l = 10^{-13} \dots 10^{-11} \text{s}$. The interaction energy of about 30meV is comparably low. Due to the large time scale, the formation of a *lattice polaron* is extremely unlikely and has no influence on charge transport.

Furthermore, the existence of trap states has to be taken into account. Shallow traps with a depth of $E_t \approx 30 \text{meV}$ have typical trapping times of $t_t > 10^{-10} \text{s}$ which is longer than the lattice relaxation time. Consequently, a local lattice polarization might occur and can deepen the existing trap by about 0.1eV.

Optical properties

Due to the weak van der Waals interactions, the optical properties of an organic solid are mainly determined by the properties of the single molecules which are only slightly changed by intermolecular forces. Figure 1.5a) displays the electronic states of an organic molecule including vibronic levels that are due to the movement of the nuclei at temperatures $> 0 \text{K}$. The absorption of a photon leads to the population of a vibrationally excited state, for instance the first excited singlet state S_1 , which decays non-radiatively to the excited ground state. The subsequent transition to S_0 is called *fluorescence* and is accompanied by the emission of a photon. Due to the existence of a weak spin-orbit coupling there is an alternative, but less probable pathway: The so-called intersystem crossing that involves a „forbidden“ spin transition, i.e. either a non-radiative transition from an excited singlet state S_n to an excited triplet state T_n or a direct excitation from S_0 to T_n . The $S_0 \rightarrow T_1$ absorption coefficient is roughly nine to ten orders of magnitude smaller than typical absorption coefficients of organic materials which are in the range of 10^5cm^{-1} . The intersystem crossing rate depends on the strength of the spin-orbit coupling and is therefore higher in systems which include heavy atoms. The radiative decay of a triplet state is called *phosphorescence* and is red-shifted compared to the fluorescence. Both concepts are exploited in organic light emitting diodes (OLEDs).

Figure 1.5b) compares the energy level schemes of a molecule (left) and the corresponding crystalline state (right). The molecular ground state S_0 is a singlet with a total spin $S = 0$ and corresponds to the HOMO which is usually occupied with an even number of electrons in aromatic systems. In addition to the gas phase ionization potential IP_{gas} , the gas phase electron affinity EA_{gas} is given with reference to the vacuum level E_{vac} . As described in the previous Section, the energy levels of a free molecule are shifted upon transition to the solid state. This shift, which is mainly due to polarization effects, is depicted schematically on the right side of Figure 1.5b) while exemplary measurement values for several polyacenes are shown in Figure 1.2. Valence and conduction level describe a situation in which HOMO and LUMO of two widely separated molecules are occupied. Furthermore, also excited states are affected by the energy shift. In organic solids, the first excited states S_1 and T_1 correspond to the excitation energy of so-called singlet and triplet excitons, i.e. excited states that are bound to one molecule. In case of a so-called *charge transfer state* (CT state), electron and hole are separated onto two neighboring molecules where they are still bound by the Coulomb force

$$F_C = \frac{1}{4\pi\epsilon\epsilon_0} \frac{e^2}{r^2} \quad (1.1)$$

with r being the distance between the two charges e , ϵ_0 being the vacuum permittivity and ϵ the permittivity of the organic medium. For most organic semiconductors ϵ is in the order of 1...6^[17] which is low compared to the permittivity of inorganic semiconductors as for instance silicon which exhibits $\epsilon = 12$. Accordingly, the electric field screening is higher in the latter case and reduces the Coulomb interaction between electrons and holes. Excitons in inorganic semiconductors are usually of *Wannier-Mott* type. Their radius is in most cases larger than the lattice spacing and the charges are quasi-free. In contrast, the attractive force between electrons and holes in organic solids, where the exciton is initially localized on one molecule, is much higher and the binding energy is comparably strong. Considering the typical dimensions of a molecule of $< 5\text{\AA}$ we find values between 0.3eV and 1.5eV^[19,20]. Thus, the optical energy gap is smaller than the electrical (or transport) gap by this value. Such strongly bound excitons are called *Frenkel excitons*.

Frenkel excitons can diffuse through the lattice in a particle-like fashion without involving a net charge transfer. There are generally two types of exciton transport mechanisms. The first is Dexter transfer^[21] which is based on the overlap between the wave functions of neighboring molecules. Thus, it is a short distance process that occurs on a length scale smaller than 2nm. It is the main transfer mechanism for triplet excitons. The alternative is a long range resonance transfer called Förster transfer^[22,23]. It is caused by a dipole-dipole coupling that mediates a non-radiative energy transfer involving the emission and absorption of a virtual photon. Förster transfer only applies for singlet excitons and is relevant on a length scale of up to 10nm.

Generally, the exciton diffusion length L_D , which is an important parameter for the operation of solar cells, can be described by

$$L_D = \sqrt{\tau_0 D} \quad (1.2)$$

with τ_0 as lifetime of the exciton and D as the diffusion coefficient. Commonly, the lifetime of triplet excitons and accordingly their diffusion length is longer due to the spin-forbidden intersystem transition. In literature, exciton diffusion lengths between 3 and 80nm are reported for common organic materials^[12].

Charge transport

At low temperatures pure organic solids with conjugated π -systems are commonly insulators. They display their semiconducting properties only in the presence of excess charge carriers that can be added to the system by, for instance, photo excitation or charge injection at high electric fields, but also by defects, impurities, or doping.

Generally, the current flow in an organic medium can be described by Ohm's law

$$\mathbf{j} = \hat{\sigma} \mathbf{F} \quad (1.3)$$

connecting the current density \mathbf{j} with the macroscopic electric field \mathbf{F} and the conductivity $\hat{\sigma}$ which is generally a tensor. Alternatively, especially when only one charge carrier type is present, a definition using the charge carrier density n , the charge q , and the drift velocity \mathbf{v}_D can be employed:

$$\mathbf{j} = qn\mathbf{v}_D. \quad (1.4)$$

The link between equations (1.3) and (1.4) is established by another, very important quantity, the charge carrier mobility $\hat{\mu}$ that is a tensor in the most general case of an anisotropic medium. It is defined by the equation

$$\mathbf{v}_D = \mu \mathbf{F}, \quad (1.5)$$

and related to the conductivity by

$$\hat{\sigma} = qn\hat{\mu}. \quad (1.6)$$

Typical values for the mobility in organic solids can range from $10^{-8}\text{cm}^2/\text{Vs}$ in up to $400\text{cm}^2/\text{Vs}$ ^[24] and depend very much on the specific semiconductor material, its purity, the temperature, as well as the electric field, and are furthermore related to the underlying conduction mechanism. The exact nature of the latter is still under debate. Nonetheless, it is generally accepted that classic band transport is rarely observed in organic semiconductors. It occurs usually only in ultrapure crystals at low temperatures^[24]. In case of band conduction, charge carriers have to be treated as coherent Bloch like wave functions in a periodic lattice. However, even in perfect organic crystals, the band width is commonly smaller than 700meV ^[18,25]. Generally, most organic solids lack a perfect crystallinity (that is only a necessary but not sufficient precondition for band conduction) and the above described polarization effects lead to a strong localization of the charge carriers on the lattice sites of the van der Waals bound solid. The localization is even enhanced in more disordered, i.e. polycrystalline or even amorphous systems that are usually more relevant considering actual applications. Here, the mean free path l_0 of the resulting polarons is hardly larger than the lattice constant $a_0 \approx 0.5\text{nm}$ and the time between scattering events is small compared to the charge carrier lifetime. In this situation, charge transport has to be described by means of a hopping model. Instead of the charge carrier lifetime one defines the hopping time τ_h that specifies the mean localization time of a charge carrier on a lattice site until it „jumps“ to the next lattice site. In contrast to band transport, polaron hopping is thermally activated. Overall, mobilities in disordered systems are usually several orders of magnitude smaller than those in crystals.

In literature, we find several theoretical approaches for hopping transport that are in good agreement with particular measurement results. In 1960 Miller and Abrahams presented a model that relates charge transport with phonon assisted tunneling of polarons between molecules in the presence of a weak electric field^[26]. The amorphous solid is represented by a network of random resistors each of which reflects the activation energy for a hopping step between two molecular sites. Hopping steps can either be between neighboring molecules (nearest-neighbor hopping, at elevated temperatures) or to more remote hopping sites which are favorable in energy (variable-range hopping, at low temperatures). The distribution of the temperature dependent resistors illustrates the structural disorder of the system.

Based on variable-range hopping and the resistor network by Miller and Abrahams, Vissenberg and Matters developed in 1998 a percolation model that describes the field effect mobility in amorphous organic layers^[27]. The model includes the filling of localized states by excess charge carriers as it is expected to occur, for instance, in the accumulation region of a field effect transistor. The remaining free charge carriers occupy states higher in energy and will thus need less activation energy for a hopping step. Vissenberg and Matters assume a Gaussian density of states (DOS), but only the tail states are taken into account for the conduction mechanism and are for this purpose approximated by an exponential DOS. The percolation model has been extended for the description of molecularly doped organic semiconductors by Männig et al. in 2001^[28].

The most widely used hopping model has been established by Bäessler et al.^[29]. It is a one particle model and uses a Gaussian DOS

$$G(E) = (2\pi\tilde{\sigma})^{-1/2} \exp\left(\frac{-E^2}{2\tilde{\sigma}^2}\right) \quad (1.7)$$

for describing the statistic distribution of site energies or the so-called *diagonal disorder* $G(E)$ having the width $\tilde{\sigma}$. The hopping rate ν_{ij} between two random hopping sites i and j is of Miller-Abrahams type. Here, two cases have to be distinguished: When hopping takes place to a state lower in energy, the hopping rate is constant while in case of hopping to a state higher in energy, the process has to be temperature assisted and a Boltzmann factor needs to be added

$$\nu_{ij} = \nu_0 \exp\left(-2\gamma a \frac{\Delta R_{ij}}{a}\right) \begin{cases} 1 & \varepsilon_j < \varepsilon_i \\ \exp\left(-\frac{\varepsilon_j - \varepsilon_i}{k_B T}\right) & \varepsilon_j > \varepsilon_i. \end{cases} \quad (1.8)$$

In that equation, k_B is the Boltzmann constant, T the temperature, ε_i and ε_j are the energies of the two hopping sites, ν_0 is a constant prefactor, ΔR_{ij} is the absolute value of the distance between i and j , a is

the average lattice distance and γ is the inverse Bohr radius when assigning the LUMO a hydrogen-like wave function. The factor $2\gamma\Delta R_{ij}$ is called overlap parameter and depends on the structural or so-called *off-diagonal disorder* of the molecules in the solid. It is described by a Gaussian distribution of the width Σ . Since the hopping transport problem cannot be solved entirely analytically, it has to be supplemented by Monte Carlo simulations of charge transport in a model system that finally lead to expressions for the temperature dependent mobility. At low electric fields the mobility can be expressed by

$$\mu = \mu_0 \exp \left[\left(-\frac{T_0}{T} \right)^2 \right] \quad (1.9)$$

with

$$T_0 = \frac{2\bar{\sigma}}{3k_B} \quad (1.10)$$

and with μ_0 being the mobility of the disorder free semiconductor at $T \rightarrow \infty$.

Additionally, in most disordered organic materials the mobility shows a characteristic dependence on the electric field which can generally be expressed by the phenomenological Poole-Frenkel formula

$$\mu(F, T) = \mu(F = 0, T) \exp \left(\beta(T) \sqrt{F} \right) \quad (1.11)$$

with β being a material dependent parameter that typically decreases with temperature – the so-called field amplification factor^[30]. More specific expressions for $\mu(F)$ and β depend on the applied model and are described elsewhere^[30-32].

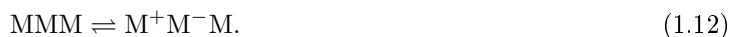
1.1.3 Molecular Doping

Doping is a powerful technique that can alter the intrinsic properties of pure semiconductors in a very specific way and consequently allows for a control of charge transport properties. It primarily affects the charge carrier density within a material which is, according to equation (1.6), directly proportional to the conductivity. While pure (intrinsic) organic materials display a very low conductivity of $\sigma \lesssim 10^{-10} \text{S/cm}$ ^[28], the conductivity of doped materials is in the range of $10^{-6} \dots 10^{-2} \text{S/cm}$ or even higher. Although, these values seem very small in comparison with those of crystalline inorganic semiconductors as for instance silicon, which already has an intrinsic conductivity of $\sigma \simeq 10^{-6} \text{S/cm}$ ^[33] and reaches doped conductivities of $\sigma \gtrsim 100 \text{S/cm}$ ^[34], they are absolutely sufficient concerning organic electronic devices. A more detailed explanation on this topic will be given along with the description of the typical p-i-n structures of solar cells which can be found in Section 1.2.3. In addition to the impact on the charge carrier density, doping shifts the Fermi level position within the energy gap and pins it close to the respective charge transport level^[35-38]. This effect considerably influences the energy level alignment to other organic materials as well as the charge injection properties at the interface to metallic electrodes which will also be described in further detail in Section 1.2.3.

Altogether, the application of doping allows for a higher level of freedom in device design, resulting in significant improvements of the electrical performance and the opportunity to implement new device concepts.

Principle of molecular doping

In intrinsic semiconductors, the Fermi level E_F is situated close to the middle of the energy gap and free charge carriers are generated by thermal or photoexcitation of the matrix molecules M:



Doping introduces impurity atoms or molecules which can either act as electron donors D or electron acceptors A



creating a charge transfer complex $\text{M}^- \text{D}^+$ or $\text{M}^+ \text{A}^-$. In order to generate free charges which can move through the matrix by means of hopping transport, the Coulomb attraction between the two ionized

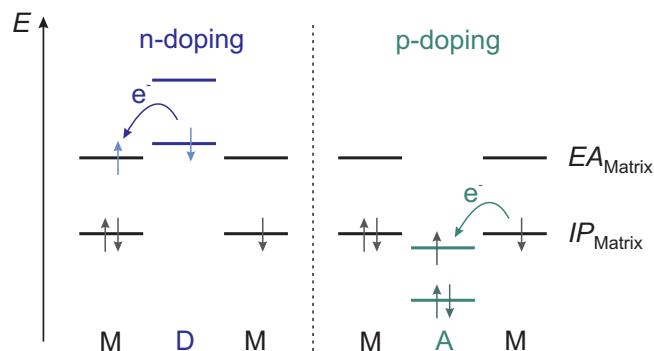


Figure 1.6: General doping mechanism for n-doping (left) and p-doping (right). The incorporation of dopant molecules leads to an electron transfer either from the HOMO of the n-dopant (donor, D) to the LUMO of the matrix (M) or from the HOMO of the matrix to the LUMO of the p-dopant (acceptor, A). This charge transfer is energetically favored and results in an increased electron or hole density in the matrix.

species has to be overcome, i.e. the complex needs to dissociate:



For this step, it is beneficial to have an energy offset between the ionization potential of the n-dopant and the electron affinity of the matrix or a respective offset between the ionization potential of the matrix and the electron affinity of the p-dopant. These two situations corresponding to n- and p-doping are depicted schematically in Figure 1.6. However, it has to be noted that the detailed mechanisms that lead to a permanent charge transfer are not yet fully understood.

In the following, several approaches for doping organic materials will be presented. As the focus of this work is on electron transport materials, n-type doping will be treated in more detail than p-type doping.

n-type doping

According to the above stated approach, a strong electron donor needs to be incorporated into the matrix in order to enhance the electron concentration. However, as strong donor materials are usually prone to reactions with oxygen, air-instability is an inherent problem of n-doping. There is a variety of distinct approaches to n-type doping that will be presented in the following.

1. **Doping with alkali metals:** Especially in the OLED community, the admixture of alkali atoms that easily donate their single valence electron to the organic matrix material is a widely used technique. Alternatively, an alkali metal interlayer can be inserted between the organic and the metal electrode in order to alter the electrode work function and to facilitate electron injection or extraction. Here, the most commonly applied materials are cesium, lithium or lithium fluoride^[39-44], but also doping with sodium or potassium has been reported^[41,45]. Alkali metals are able to dope even organic materials with a very small electron affinity like BPhen (4,7-diphenyl-1,10-phenanthroline, $EA \approx 2.9\text{eV}$ ^[46]) or BCP (2,9-dimethyl-4,7 diphenyl-1,10-phenanthroline, $EA = 1.6\text{eV}$ ^[35]). However, there are also some drawbacks: (1) Alkali metal doping requires very high doping ratios in the order of 1 atom per molecule for reaching sufficiently high conductivities^[42,47]. (2) The positively charged counter-ion that remains after the charge transfer may be ion-paired with the doped molecule and form a trap for the just donated electron. (3) The small alkali atoms exhibit a very high diffusivity – for instance Li has a diffusion length of $(70 \pm 10)\text{nm}$ in a BCP matrix^[48]. Thus, the formation of a sharp interface between n-doped regions and nominally intrinsic materials cannot be guaranteed and unintentional dopant diffusion might affect the device performance.
2. **Molecular donors with inherently low ionization potential:** If organic molecules are to be used as dopants, their energy level positions relative to those of the organic matrix need to fulfill certain requirements. As sketched in Figure 1.6 (left), the ionization potential of the n-dopant IP_{dopant} should be approximately equal to or even smaller than EA_{M} in order to achieve

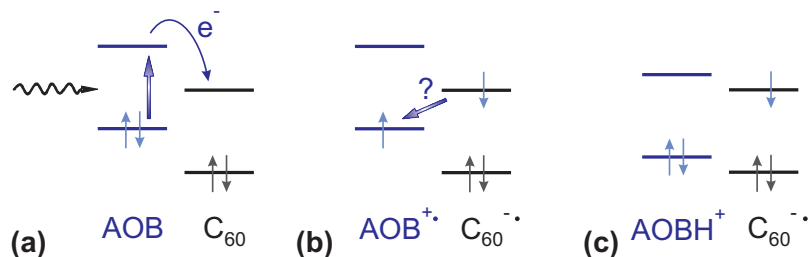


Figure 1.7: *n*-doping with cationic dyes illustrated for the example of the dopant AOB (acridine orange base) in C_{60} . a) Electrons are excited to the AOB LUMO either thermally or by illumination and are subsequently transferred to the energetically favorable LUMO of C_{60} . b) This leaves a positively charged radical $AOB^{+\bullet}$ cation and a negatively charged radical matrix ($C_{60}^{-\bullet}$) anion. A return of the radical electron to the LUMO of the matrix would contradict a permanent doping. c) A further reaction needs to take place that turns the unstable $AOB^{+\bullet}$ cation into the stable $AOBH^+$ having a fully occupied HOMO. This process impedes the back transfer of the excess electron from the matrix to the dopant and thus causes a permanent doping.

an energetically favorable and thus efficient charge transfer. However, it is difficult to find donor compounds with small enough ionization potentials to dope common electron transport materials like C_{60} ($EA = 4.0\text{eV}$ ^[49]) or Alq_3 (tris (8-hydroxy-quinolinato)-aluminum, $EA = 2.4\text{eV}$ ^[20]), because such materials are very reactive and unstable in air. Considering the oxidation potential of oxygen which is approximately 3.7eV ^[50,51], the problem becomes clear: molecular *n*-dopants with $IP \lesssim 3.7\text{eV}$ are readily oxidized and can only be stored and handled in an inert atmosphere. The dopant NDN1 (Novaled AG, Dresden), which has been used for fabricating solar cells in this thesis, is a prominent example for this kind of materials. Furthermore, $Cr_2(\text{hpp})_4$ ^[52], $Ru(\text{terpy})_2$, $Cr(\text{bpy})_3$ and $Cr(\text{TMB})_3$ ^[53,54] have been reported as air-unstable *n*-dopants.

Additional to these materials, there is a number of air-stable molecular *n*-dopants having larger ionization potentials but exhibiting less efficient charge transfer: For instance, BEDT-TTF (bis(ethylenedithio)-tetrathiafulvalene, $IP = 5.0\text{eV}$) is known to dope NTCDA (1,4,5,8-naphthalenetetracarboxylic dianhydride)^[55] and furthermore, TTN (tetrathianaphthacene, $IP = 4.4\text{eV}$)^[56,57] and BTQBT (bis(1,2,5-thiadiazolo)-*p*-quinobis(1,3-dithiole), $IP = 4.6\text{eV}$)^[58] are cited in literature.

Last but not least, there is a group of gas-phase dopants including the organometallic complexes $CoCp_2$ (cobaltocene, $IP = 4.0\text{eV}$)^[59,60] and DCM (decamethylcobaltocene, $IP \approx 3.2\text{eV}$)^[36]. Those materials display an extremely high vapor pressure and are commonly dispensed to the vacuum chamber in the gas phase rather than being evaporated from a crucible.

- Doping with cationic salts:** The application of cationic salts is a way to circumvent the use of air-unstable *n*-dopants with small ionization potentials. The method has been developed by A. Werner at the IAPP and is based on the activation of a stable precursor compound during the co-evaporation of dopant and organic matrix material^[61]. Figure 1.7 illustrates the underlying concept using the example of AOB (acridine orange base) that has an ionization potential of 5.0eV^* which is too large to allow for an electron transfer to the conduction level of C_{60} ^[62]. However, it is possible to excite an electron from the ground state to the first excited state of AOB which can subsequently be transferred to the energetically more favorable conduction level of a neighboring C_{60} molecule. This excitation is accomplished either by illumination or substrate heating during the doping process, but also post-treatment shows an effect. As sketched in Figure 1.7b), the charge transfer leaves two radical ions: $AOB^{+\bullet}$ and $C_{60}^{-\bullet}$. Now, the electron could return to the $AOB^{+\bullet}$ molecule which would contradict the experimentally observed permanent doping process. Instead, there has to be a second reaction channel impeding the electron back transfer. It is speculated that the unstable radical AOB cation undergoes a chemical reaction and is transformed into the stable product $AOBH^+$ that has a fully occupied valence level. As a result, doping becomes permanent. The validity of this hypothesis has been confirmed by FTIR (Fourier transform infrared spectroscopy) measurements of AOB, $AOBH^+$ and C_{60} :AOB mixed layers. The spectrum of the mixed film contains characteristic features of both, AOB and $AOBH^+$ which indicates that indeed a part of the AOB molecules is oxidized and forms $AOBH^+$. When doping with AOB, a fraction of the dopants undergoes a complete charge transfer while the rest stays neutral.

* Measured at IAPP by Selina Olthof.

Though doping with cationic dyes has the obvious advantage of using air-stable materials, the doping efficiency is in most cases smaller than achieved for air-unstable dopants with inherently low ionization potential. For instance, doping C_{60} with AOB leads to a conductivity that is about two orders of magnitude below the conductivity reached by n-doping with NDN1. Additional to AOB, the cationic salts PyB (pyronine B)^[59,63,64] and LCV (leuco crystal violet)^[65] have been applied as cationic n-dopants.

p-type doping

As sketched in Figure 1.6 (right), p-type doping involves a charge transfer from the valence level of the organic matrix material to the conduction level of the dopant. To achieve an efficient charge transfer to typical hole transport materials like ZnPc, MeO-TPD ($IP = 5.1\text{eV}^*$) or BPAPF ($IP = 5.6\text{eV}^*$), p-dopants have to be materials with particularly deep lying energy levels. Early doping experiments mainly involved the exposure of metalphthalocyanine crystals or thin films to residual gases like oxygen or halogenes which mostly resulted in an increase in conductivity and an improvement of the metal/organic contact properties^[66-71]. Ortho-chloranile was used as first molecular p-dopant already in 1960, however, it could not be incorporated during vacuum deposition of the phthalocyanine matrix material, but had to be applied by solution casting^[72].

Later on, other molecular dopants suitable for vacuum evaporation were introduced. These materials include TCNQ (tetracyanoquinodimethane) or DDQ (dichlorodicyanoquinone) which had to be used in concentrations as high as 30...50mol% in metalphthalocyanines to compensate for their low doping efficiency^[73]. Today, the most commonly applied p-dopant is F_4 -TCNQ that has an electron affinity of 5.24eV^[74,75]. Especially at elevated substrate temperatures, F_4 -TCNQ is very volatile which is detrimental for device stability^[76]. Thus, some effort has recently been spent on developing alternatives such as F_2 -HCNQ ($EA \approx 5.6\text{eV}$)^[77] or F_6 -TNAP ($EA \approx 5.4\text{eV}$)^[78]. Throughout this work a material with similar performance, denoted as NDP2 (purchased from Novald AG, Dresden), has been used as p-dopant.

Additional to the molecular dopants metal oxides like WO_3 ^[79], MoO_x ^[80-83] and ReO_3 ^[81], but also metal halides as CuI ^[81,84] and $FeCl_3$ ^[85] have been tested as p-dopants.

1.2 Organic Solar Cells

In general, a solar cell is a device that converts energy from the sunlight to electrical energy using the photovoltaic effect. In addition to the conventional mono- or polycrystalline silicon solar cells and high-performance gallium arsenide devices, thin film technologies become increasingly attractive for the market because of their light weight, low material consumption and potential flexibility. Again, most of them are based on inorganic semiconductors like a-Si (amorphous silicon) or inorganic compound semiconductors like CdTe (cadmium telluride) or CIGS systems (copper indium gallium selenide, $CuIn_{1-x}Ga_xSe_2$) and reach promising power conversion efficiencies of 12%, 17% and 20%, respectively^[5]. Except for polycrystalline silicon, these alternatives suffer from different drawbacks like for instance high production costs for monocrystalline silicon or GaAs devices, potentially limited material availability of compounds like tellurium, or indium and potential health risks considering tellurium, cadmium, or arsenic. However, it has to be noted that especially the latter two points are still under debate.

Considering those figures, the enormous variety of organic semiconductors that can be fabricated with high yield and at low cost is very promising. Lately, the research activity in the field of organic solar cells has increased tremendously and much effort is being put in a more detailed understanding of the underlying physical concepts, in developing new functionalized materials, and developing new design / device concepts that can help to improve the performance.

Before highlighting the peculiarities of organic solar cells, we will briefly discuss the physics of conventional silicon devices as it provides the basis for all further considerations.

1.2.1 Conventional Silicon Solar Cells

For converting solar energy into electrical energy, the absorption of light needs to be followed by the generation of free charge carriers and their subsequent extraction from the photoactive medium to electrical contacts. In inorganic solar cells the driving force for this process is commonly provided by building a

* Measured at IAPP by Selina Olthof.

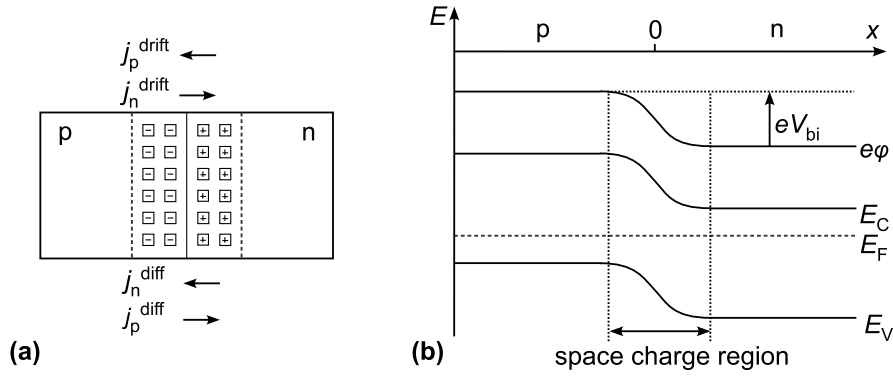


Figure 1.8: a) Schematic representation of the space charge region that forms at the contact between a p- and an n-doped semiconductor. The diffusion of majority charge carriers across the interface leads to an enhanced recombination of electrons and holes close to the contact and subsequently to the formation of a depletion zone. The remaining positively and negatively charged ions of the dopants produce an electric field that in turn drives a drift current of minority charge carriers. Drift and diffusion current compensate in case of electrochemical equilibrium. b) Resulting energy level diagram of a pn-junction. The electrical potential depends on the position relative to the interface and causes a bending of conduction and valence band (E_C and E_V) while the Fermi level (or electrochemical potential) is constant under equilibrium conditions.

so-called pn-junction between differently doped areas that are stacked on top of each other. In silicon, p-doping is realized by introducing trivalent impurity atoms like boron or aluminum while for n-doping pentavalent atoms like phosphorus or arsenic are used. The excess charge carriers generated by doping are normally only weakly bound and can be thermally activated. Thus, at room temperature, almost all dopant atoms are ionized and according to the Boltzmann approximation, the density of free majority charge carriers n_n , p_p is approximately equal to the density of dopants:

$$n_n \approx N_D \text{ und } p_p \approx N_A \quad (1.17)$$

with N_D , N_A being the density of donors or acceptors. As a consequence, the Fermi level E_F is shifted closer to the conduction band / valence band, thus increasing the effective density of electrons N_C / holes N_V . Taking $E_{F,n}$ and $E_{F,p}$ as resulting Fermi level positions the charge carrier densities can be written as

$$n_n = N_C \exp\left(\frac{E_{F,C} - E_C}{k_B T}\right) \quad (1.18)$$

and

$$p_p = N_V \exp\left(\frac{E_V - E_{F,V}}{k_B T}\right). \quad (1.19)$$

Figure 1.8a) visualizes what happens when the contact between p- and n-region is established: Due to the concentration gradient, the majority carriers will diffuse across the interface which leads to an enhanced recombination of electrons and holes in the contact area and leaves a region that is depleted of mobile charge carriers. Only the positively and negatively charged ions of the chemical impurities remain and generate an electric field at the junction. The resulting gradient in the electric potential φ drives a drift current of minority carriers which compensates the before mentioned diffusion current. This is of course a very simplified picture, because in fact each of the charge carriers feels both, the concentration gradient and the electrostatic force which even out in case of electrochemical equilibrium, i.e.

$$e \cdot \text{grad } \varphi = \text{grad } \xi \quad (1.20)$$

with e being the elementary charge and ξ the chemical potential. Hence, there is no net charge flow and the electrochemical potential η that is identified with the Fermi energy E_F is constant

$$\eta = (\xi - e\varphi) = E_F = \text{const.} \quad (1.21)$$

Figure 1.8b) shows the respective energy level diagram including the band bending of conduction and valence band E_C and E_V due to the potential difference which is also called built-in potential V_{bi} and can be derived from

$$V_{bi} = \varphi(x = +\infty) - \varphi(x = -\infty) \quad (1.22)$$

$$V_{bi} = \frac{1}{e}(E_{F,n} - E_{F,p}) \quad (1.23)$$

using $\xi(\pm\infty) = E_{F,n/p}$. Apparently, the built-in potential depends strongly on the level of doping. A more detailed expression involving the charge carrier densities (1.18) and (1.19) is given by

$$V_{bi} = \frac{k_B T}{e} \ln \left(\frac{n_n \cdot p_p}{n_i^2} \right) \quad (1.24)$$

where n_i is the charge carrier density in thermodynamic equilibrium

$$n_i = (N_C N_V)^{1/2} \exp \left(-\frac{1}{2} \frac{E_g}{k_B T} \right). \quad (1.25)$$

Taking into account the above made approximation (1.17), equation (1.24) becomes

$$V_{bi} = e E_g - \frac{k_B T}{e} \ln \left(\frac{N_C N_V}{N_D N_A} \right). \quad (1.26)$$

The current-voltage characteristics of such a pn-junction is given by the Shockley equation which describes the behavior of an ideal diode at an externally applied voltage V :

$$j(V) = j_s \left[\exp \left(\frac{eV}{k_B T} \right) - 1 \right]. \quad (1.27)$$

Here, j_s is the so-called saturation current density at high reverse voltages describing the case of an expanded depletion region. Under forward bias, the current increases exponentially with the applied voltage, while in reverse, the Boltzmann factor can be neglected and only the drift current of thermally generated charge carriers remains. The Shockley equation does not account for recombination processes taking place in the depletion region and accordingly it can only describe ideally rectifying diodes.

Quasi-Fermi levels

When disturbing the equilibrium, either by applying an external voltage that drives a current through the device and thus changes the charge concentrations, or by creating excess charge carriers upon photoexcitation, the distribution of electrons and holes cannot be described with one common Fermi level anymore. In case of an illuminated, inorganic pn-junction, the photogenerated Wannier-Mott excitons are readily converted into free excess charge carriers because they are only weakly bound. Those excess charge carriers can be extracted as photocurrent from the device. Due to the changed charge carrier concentrations, we find $np > n_i^2$. Because of the enhanced electron density, the Fermi level would have to approach the conduction band, but also the valence band as the hole density is increased as well. Hence, there is a splitting of E_F into two quasi-Fermi levels $E_{F,C}$ and $E_{F,V}$ describing the new population densities. We find

$$np = n_i^2 \exp \left(\frac{E_{F,C} - E_{F,V}}{k_B T} \right). \quad (1.28)$$

As the electrochemical potential of electrons and holes can be identified with their respective quasi-Fermi energies, the quasi-Fermi splitting determines the maximum electrochemical energy per electron-hole pair that can be extracted from the solar cell^[86]. A more detailed look on equation (1.28) reveals that the amount of obtainable energy increases logarithmically with the charge carrier density. Thus, a high charge carrier generation rate and low recombination are not only beneficial for achieving a high current, but also for maximizing the extractable energy in the form of the photovoltage.

Figure 1.9 displays the band diagram of an illuminated pn-junction under open circuit conditions, i.e. when the externally applied forward voltage counterbalances the photogenerated current, and conduction as well as valence band are ideally flat. In the given example, the quasi-Fermi level splitting that occurs in the space charge region $\frac{1}{e}(E_{F,C} - E_{F,V})$ is larger than the built-in potential given by the difference of Fermi levels in the doped regions. In this case the obtainable open circuit voltage V_{oc} of the device is limited by V_{bi} . The limitation could be overcome by increasing the doping concentrations which would shift the Fermi levels closer to the bands and thus increase V_{bi} .

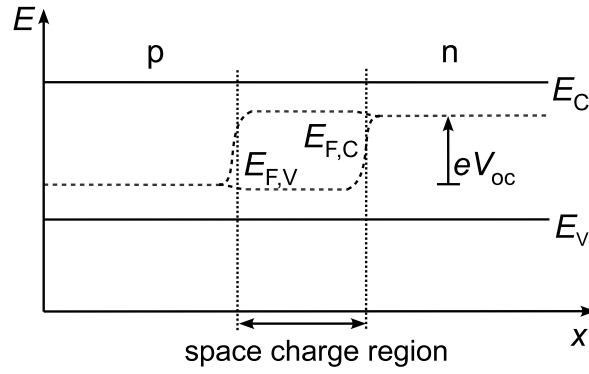


Figure 1.9: *pn-junction under illumination and open circuit conditions (externally applied voltage such that net current flow is zero). In this example the quasi-Fermi splitting in the depletion region exceeds the built-in potential that is given by the difference between the Fermi levels in the n-doped and p-doped region. This limits the obtainable open circuit voltage V_{oc} to a value smaller than the potential given by $(E_{F,C} - E_{F,V})/e$.*

Ideal solar cell: The Würfel picture

As mentioned above, the charge carriers are driven by the sum of an electrostatic force and a concentration difference, i.e. by gradients in the electric potential φ and the chemical potential ξ . The net current can accordingly be expressed by

$$j = \frac{\sigma_n}{e} \cdot \text{grad}(\xi_n - e\varphi) + \frac{\sigma_p}{e} \cdot \text{grad}(\xi_p - e\varphi) \quad (1.29)$$

$$j = \frac{\sigma_n}{e} \cdot \text{grad}(E_{F,C}) + \frac{\sigma_p}{e} \text{grad}(E_{F,V}) \quad (1.30)$$

where σ_i is the conductivity. In total, it is the gradient of the electrochemical potential, i.e. the gradient in quasi-Fermi levels, that is responsible for the current flow. According to this very general notation, the presence of an electric field is not the only driving force for separating electrons and holes, but also a concentration gradient can contribute to the charge carrier separation and extraction. Hence, Würfel suggests the design of an ideal device which is reproduced in Figure 1.10^[86]. The concept is realized by introducing selective contacts between the absorbing region B and the adjacent n-type and p-type regions A and C. Minority carriers are blocked at the respective interfaces due to a step in ionization potentials

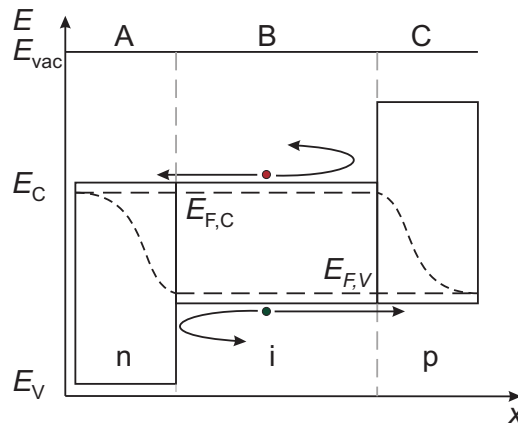


Figure 1.10: *Structure of an ideal solar cell as suggested by Würfel^[86]. Free charge carriers are exclusively generated in region B which is sandwiched between an n-type semiconductor A and a p-type semiconductor C with large band gaps. The quasi-Fermi levels in B match the Fermi levels for the majority carriers in A and C. The extraction of minority carriers on the „wrong“ side is prevented by the step in ionization potentials between A and B and in electron affinities between B and C, respectively. Thus, the interfaces act as semipermeable membranes causing a concentration gradient of electrons and holes which in turn drives the current.*

(for holes traveling from B to A) or a step in electron affinities (for electrons traveling from B towards C) whereas the transport levels for the majority carriers are aligned. More precisely, the Fermi energy in the transport layer needs to match the respective quasi-Fermi energy of electrons and holes in B under illumination in order to avoid an energy loss. Now, only a small gradient in the quasi-Fermi energies can drive the charge carriers towards the contacts.

Practically, the alignment of quasi-Fermi energies to the transport layers can be achieved by p- and n-type doping which, however, generates a built-in potential and introduces again an additional electrostatic driving force. In principle, the Würfel picture resembles organic solar cells fabricated according to the p-i-n concept in many aspects. Before discussing this subject in more detail in Section 1.2.3, the typical current-voltage characteristics of a solar cell will be presented.

Current-voltage characteristics

In order to obtain the current-voltage characteristics of a solar cell, the Shockley equation (1.27) that describes a pn-junction in the dark is supplemented by a photocurrent j_{photo} that is in a first approximation voltage independent

$$j(V) = j_s \left[\exp \left(\frac{Ve}{k_B T} \right) - 1 \right] - j_{\text{photo}}. \quad (1.31)$$

Figure 1.11 shows the respective jV -curve labeled with the most important characteristic parameters. Without applying any external voltage, the short circuit current density j_{sc} , which is the current normalized to the area of the solar cell, is flowing. In conformity with equation (1.31), i.e. in the ideal loss-free case, it is equal to the photocurrent j_{photo} . In case of open circuit, i.e. a net current flow of zero, the solar cell produces the open circuit voltage V_{oc} which is linked to the splitting of quasi-Fermi levels, or in the non-ideal case limited by the built-in voltage (compare Figure 1.9). The maximum power point MPP is the optimum operation point of the solar cell, because here it produces the highest power output $j_{\text{MPP}} \cdot V_{\text{MPP}} \cdot A$, where A is the area of the solar cell. Relating this maximum extractable power to the product of j_{sc} and V_{oc} gives the fill factor FF

$$FF = \frac{j_{\text{MPP}} \cdot V_{\text{MPP}}}{j_{\text{sc}} \cdot V_{\text{oc}}} \quad (1.32)$$

which is a measure for the quality of the device. The fill factor is one of the key parameters for describing the energy yield of solar cells. For inorganic silicon solar cells, it is usually larger than 70% or even 80% while for typical organic solar cells it is around 50 or 60%.

Finally, the most important parameter evaluating the quality of a solar cell is the power conversion efficiency η

$$\eta = \frac{j_{\text{sc}} V_{\text{oc}} FF}{I_{\text{light}}} \quad (1.33)$$

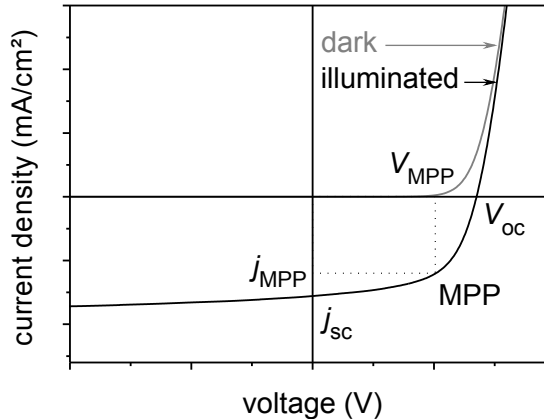


Figure 1.11: jV -characteristics of a solar cell under illumination and in dark along with the characteristic parameters: open circuit voltage V_{oc} , short circuit current density j_{sc} , as well as current j_{MPP} and voltage V_{MPP} at the maximum power point MPP.

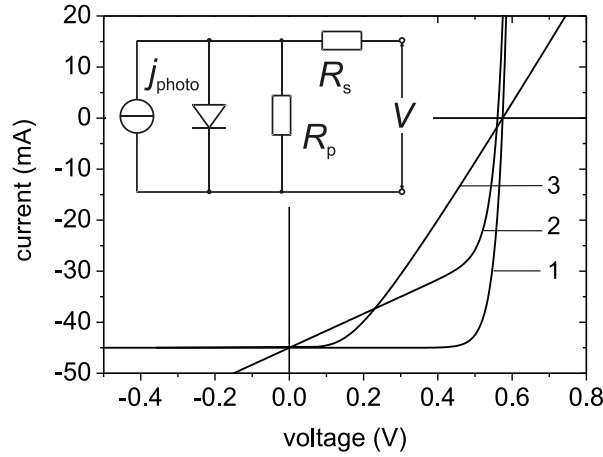


Figure 1.12: jV -curves of non-ideal solar cells according to equation (1.34). For all curves, $j_{\text{photo}} = 45 \text{ mA}$ and $j_s = 1 \cdot 10^{-8} \text{ mA}$, as typical for a silicon solar cell, are used. Solar cell (1) is the ideal case with $R_s = 0 \Omega$ and $R_p = \infty$ while device (2) has a higher parallel resistance $R_p = 40 \Omega$ at $R_s = 0 \Omega$, and device (3) has a higher series resistance $R_s = 8 \Omega$ at $R_p = \infty$.

with I_{light} being the illumination intensity of the light source. For ensuring comparability, the power conversion efficiency should be determined under certain standard reporting conditions (SRC), including the use of a standardized sun spectrum and measuring at a device temperature of 25°C ^[87,88]. jV -curves measured with a sun simulator usually have to be corrected for spectral mismatch. The procedure, necessary for correcting organic solar cells is further discussed in Section 2.3.2.

Deviations from the ideal current-voltage characteristics

As stated above, the Shockley equation (1.31) can only be used for describing ideal solar cells. In real devices, additional series and parallel resistances R_s and R_p have to be taken into account which means that they have to be included into the equivalent circuit of the ideal device that consisted only of a current source and a diode up to now. The inset in Figure 1.12 shows the resulting configuration which can be described using the equation

$$j(V) = j_s \left[\exp \left(\frac{e(V - R_s j(V))}{k_B T} \right) - 1 \right] + \frac{V - R_s j(V)}{R_p} - j_{\text{photo}}. \quad (1.34)$$

The impact of R_s and R_p on the resulting jV -curve is also depicted in Figure 1.12. While a series resistance $R_s > 0 \Omega$ mainly results from a voltage drop over the charge transport layers and the contacts and diminishes the slope of the jV -curve in forward direction, a parallel resistance $R_p < \infty$ causes an increase of the slope in reverse. Determining the origin of the parallel resistance is not trivial. In case of solar cells made of crystalline inorganic semiconductors, it is mainly due to short circuits emerging at grain boundaries or on surfaces. In organic solar cells, short-circuited paths between anode and cathode can, for instance, be caused by spikes in the ITO (indium tin oxide) ground electrode. However, the voltage dependence of the current density in reverse is not necessarily linked to real short circuits, but can also be due to a voltage assisted separation of excitons which would directly influence the charge carrier generation rate^[89]. Furthermore, also the recombination rate of free charge carriers is voltage dependent: At higher reverse bias the charge extraction is accelerated and hence the probability for recombination on the way to the electrodes is reduced. In silicon, such processes are negligible due to the much smaller exciton binding energy and superior charge transport properties.

The quality of the photocurrent collection at negative bias voltage is evaluated by the saturation factor Sat which is defined as the quotient of the current density at a reverse bias of -1 V and the short circuit current density

$$Sat = \frac{j(-1 \text{ V})}{j_{sc}}. \quad (1.35)$$

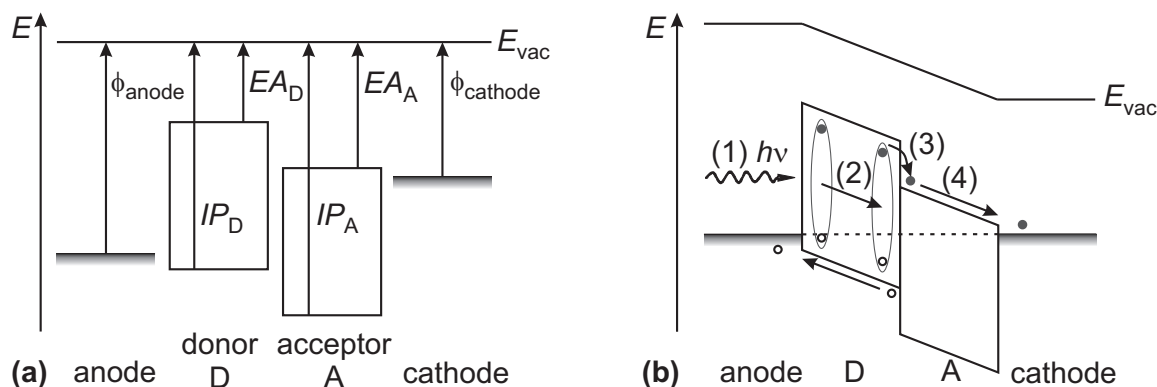


Figure 1.13: Energy level alignment at a flat donor/acceptor heterojunction. a) Energy levels of the involved materials before the contact and subsequent Fermi level alignment are established. b) Schematic energy level diagram of the device under short circuit conditions. For reasons of clarity, interface dipoles are omitted. Four steps are involved in the photocurrent generation: (1) the absorption of photons which leads to the generation of coulombically bound excitons, (2) the diffusion of the excitons to the donor-acceptor interface, (3) the separation of excitons into free electrons on the acceptor and free holes on the donor taking place at this interface, and finally (4) transport of the free charge carriers through the organic materials and extraction at the electrodes.

1.2.2 The Organic Donor-Acceptor Heterojunction

Due to the peculiarities of organic semiconductors, it is not possible to simply copy the principle of the pn-homojunction for building an organic solar cell. In contrast to the situation in inorganic materials, free charge carriers are not readily generated upon light absorption. Instead, the excitation produces tightly bound Frenkel excitons which have typical diffusion lengths of $\ll 100\text{nm}$ and are prone to rapid recombination. The transport of free charge carriers is characterized by comparably small conductivities and charge carrier mobilities. These factors basically limit the lifetime of excitons as well as free charge carriers and accordingly the total thickness of the device. However, when considering the high absorption coefficients of organic dyes which are in the range of 10^5cm^{-1} or even more, this is not necessarily a disadvantage. Considering the actual design of organic photovoltaic devices, there is another substantial argument against using a doped homojunction: The high level of impurities in organic materials demands a high level of doping. In practical terms this means that the dopant concentration has to be in the range of percent while in silicon it is typically only in the range of parts per million. A homojunction between doped organic materials would thus be characterized by a very thin space charge region and would rather provide a tunneling contact than a separating interface.

Hence, a modification of the conventional assembly is necessary in order to dissociate the excitons into free charge carriers. Instead of a doped pn-junction, a heterointerface between an undoped donor and an undoped acceptor material is used in organic devices. Since this concept was first introduced by Tang in 1986 it has become indispensable^[10]. Figure 1.13 shows a schematic energy level diagram of a very simple flat donor-acceptor heterojunction device under short circuit conditions in which the two organic materials are sandwiched between anode and cathode. In a very simplified picture, bringing the materials into contact causes an energy level alignment accompanied by a potential drop over the organic layers due to the difference of anode and cathode work function. In this picture, the occurrence of interface dipoles or level bending is neglected. The generation of a photocurrent in this configuration basically involves four steps:

- 1. Light absorption and exciton generation.** The absorption of a photon with sufficiently high energy $E_{\text{photon}} > E_{\text{gap}}$ leads to the generation of singlet excitons. Due to the high exciton binding energy, a thermally assisted ionization is highly unlikely. For a field assisted separation, very high electric fields in the order of 10^6V/cm are needed^[90]. The above described potential drop over the organic bilayer having a typical thickness in the order of 100nm cannot provide a sufficiently high field gradient for exciton dissociation. Hence, autoionization can be ruled out as channel for free charge carrier generation in organic solar cells based on molecular materials.
- 2. Exciton diffusion to the D/A heterojunction.** Once an exciton is generated, it needs to

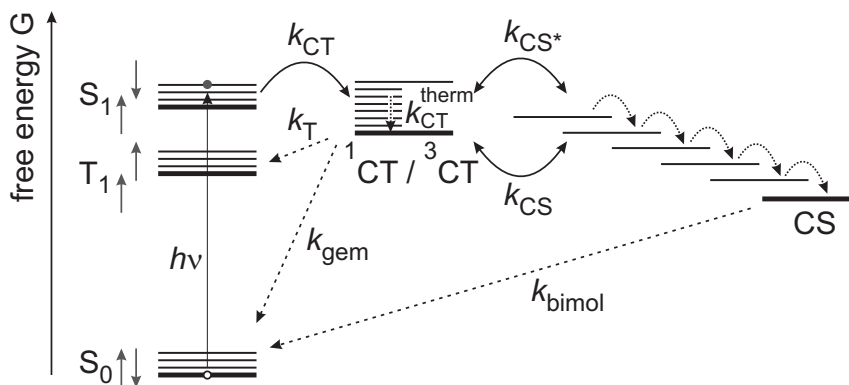


Figure 1.14: Schematic energy level diagram of the charge separation process at the donor/acceptor heterojunction. The absorption of a photon with energy $h\nu$ creates a singlet exciton which is converted to a geminate pair, the so-called charge transfer state (CT), with a rate constant k_{CT} . If the exciton initially carried some excess energy, a hot CT-state might be formed which can either relax to the CT ground state (which is either a singlet 1CT or triplet 3CT ; intermixing rate k_{ISC}) with a rate constant k_{CT}^{therm} , or immediately dissociate to a charge separated state CS with the rate constant k_{CS^*} . The thermalized CT-state can either dissociate (k_{CS}), recombine geminately to the ground state (k_{gem}), or be transferred to the triplet state T_1 (k_T). When the distance of the free (dissociated) charge carriers to the interface increases, the Coulomb attraction is reduced and the free energy of the charge carrier pair is reduced. Nevertheless, a bimolecular recombination to the ground state with k_{bimol} is always possible.

diffuse to the separating D/A interface. Diffusion happens via the transport mechanisms described in Section 1.1.2 (Förster and Dexter transfer) and is purely driven by diffusion as the exciton is an electrically neutral entity. The distance which an exciton can cover during its lifetime, the exciton diffusion length L_D , is commonly very small in organic materials ($\approx (3...80)\text{nm}$ ^[12]). Only excitons which are created within a distance of L_D from the D/A heterojunction can potentially contribute to the generation of free charge carriers. This fact limits the thickness of the photoactive bilayer and accordingly the obtainable photocurrent.

3. **Exciton separation at the D/A heterojunction.** In order to realize an exciton separation at the D/A interface, a suitable energy offset between the EA and IP of donor and acceptor is needed. When the total offset exceeds the Coulomb binding energy of the exciton E_B^{exc} – or in other words when the effective gap $IP_D - EA_A$ is in the range of or smaller than the exciton energy – a separation of the charges is energetically more favorable than the initial excitonic state and the electron will be transferred to the acceptor while the hole remains on the donor molecule. In this so-called charge transfer (CT-) state, electron and hole are still located on neighboring molecules, i.e. their spacial separation is in the order of (0.5...1)nm. As there is still a significant Coulomb attraction between the two, they are not truly separated. Further activation is necessary for creating free charges and for escaping the competing process of geminate recombination. The probability for the charge carriers to overcome the mutual Coulomb attraction is described by the Onsager-Braun model^[91–93], a modified Onsager theory which accounts for the finite lifetime of the CT-state. The model assigns a so-called thermalization radius a_{th} to the hot excitons which is then compared to the Coulomb capture radius r_C – the distance in which the Coulomb energy equals the thermal energy $k_B T$. r_C is estimated to be approximately 4nm in common organic materials^[94]. Depending on where the exciton is generated, either in the bulk or close to the heterojunction, it might reach the D/A interface thermally relaxed or still carrying some vibronic excess energy which could support the separation (due to a larger radius a_{th}). In addition to this thermally assisted separation, the presence of any applied electric field lowering the Coulomb potential has a large influence: At low electric fields the escape probability $P(E)$ is directly proportional to the field strength F . Either way, as schematically depicted in Figure 1.14, the separation into free charge carriers is a multi-step process which is likely to involve a loss in free energy. Moreover, the process is reversible and the CT-state can always be re-established from a partially dissociated state in which electron and hole are still closer than the Coulomb capture radius.

Depending on the energetics of the involved materials, a third process can occur. If the energy of

the triplet excitonic state T_1 in the donor is smaller than the energy of the CT-state, an electron back transfer can lead to the formation of a triplet exciton. Intersystem crossing can readily happen since the electronic coupling of the CT-state is relatively weak.

The complexity of the dissociation process suggests that particular care has to be taken when choosing appropriate donor and acceptor materials. To maximize the obtainable free energy and accordingly the open circuit voltage, the offset of donor and acceptor energy levels needs to be as small as possible. In literature a value of 0.3eV is assumed to be sufficient^[95], however, it has to be noted that this number is an estimate and might differ considerably for varying material systems.

4. **Charge transport and extraction.** As a last step the free charge carriers need to be transported through the organic medium and subsequently collected at the contacts. Here, a high charge carrier mobility and conductivity are beneficial for minimizing the probability of bimolecular recombination. Additionally, the metal/organic interface plays a crucial role: In order to achieve an ohmic contact, the respective transport level for electrons or holes needs to be aligned to the metal Fermi level. However, predicting the energetics of such an interface is often not straightforward because in most cases the common assumption of vacuum level alignment does not hold. Instead, various effects like charge transfer, chemical interactions, the presence of interface states or surface rearrangement due to adsorption of molecules etc. might lead to the formation of interface dipoles^[96,97]. For metal on organic interfaces the situation is even more complex, because here the interface is not even necessarily abrupt^[98,99].

Molecular doping can be utilized to avoid some of the above mentioned problems and to achieve an ohmic metal/organic contact.

Each of these four steps happens with a certain probability or efficiency η . Multiplying these efficiencies gives the external quantum efficiency $EQE(\lambda, V)$

$$EQE(\lambda, V) = \eta_A(\lambda) \cdot \eta_{ED}(\lambda) \cdot \eta_{CT}(\lambda, V) \cdot \eta_{CC}(V) \quad (1.36)$$

$$EQE(\lambda, V) = \eta_A(\lambda) \cdot IQE(\lambda, V), \quad (1.37)$$

i.e. the ratio of actually extracted charge carriers to the number of incident photons at a certain wavelength λ and at a certain externally applied voltage V . Here, $\eta_A(\lambda)$ is the probability for exciton generation upon absorption (1), $\eta_{ED}(\lambda)$ is the probability for the exciton to reach the D/A interface (2), $\eta_{CT}(\lambda, V)$ is the probability for charge transfer and dissociation (3), and $\eta_{CC}(V)$ is the charge collection efficiency which summarizes charge transport to and charge extraction at the electrodes (4). The product of the latter three, $\eta_{ED}(\lambda) \cdot \eta_{CT}(\lambda, V) \cdot \eta_{CC}(V)$, yields the internal quantum efficiency IQE which is the efficiency with which the actually absorbed photons are converted into collectable charge carriers. Due to the short exciton diffusion length which is generally much smaller than the optical absorption length, in most cases $\eta_{ED}(\lambda)$ (step (2)) is efficiency limiting while $\eta_{CT}(\lambda)$ and $\eta_{CC}(V)$ are assumed to be approximately 100%. For layers thinner than the optical absorption length, the absorption efficiency $\eta_A(\lambda)$ depends on the thickness of the organic material^[12].

When using flat heterojunction structures, the conflict between absorption depth and diffusion length inevitably limits the obtainable photocurrent. However, there are ways to circumvent this problem by changing the device architecture.

Bulk heterojunction

In the 1990s the so-called bulk heterojunction was introduced as novel concept capable to overcome the deficiencies of Tangs bilayer approach^[100-102]. As indicated in Figure 1.15, donor and acceptor are mixed in a way that the heterojunction is not flat anymore, but extends three-dimensionally throughout the bulk. In the ideal case it forms an interpenetrating network with both materials building closed percolation pathways which are connected to the respective electrode. Using such an architecture the device thickness is not limited by the exciton diffusion length any longer, because all excitons can in principle be generated within the reach of a separating interface. Instead, charge transport is now the limiting factor for the layer thickness. However, the ideal interpenetrating network as schematically depicted in Figure 1.15a) is difficult to achieve. Realistic mixed layers will rather resemble the sketch given in Figure 1.15b) and involve certain drawbacks. For instance, the percolation will not be perfect and „dead ends“ or isolated clusters with trapped charges will enhance the recombination of already separated charge carriers. Also the separation of the excitons themselves into a completely charge separated state will be more difficult because of an increase in disorder.

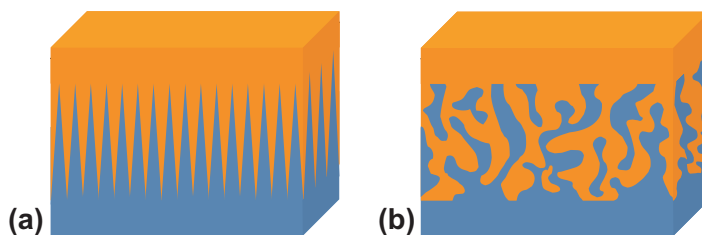


Figure 1.15: a) Morphology of a perfectly interpenetrating network of two compounds and b) sketch of a more realistic representation of a bulk heterojunction between two organic materials.

These examples show clearly that controlling the morphology is the key to efficient heterojunction devices. The optimum degree of intermixing is a tradeoff between optimized charge transport which requires a strong phase separation and maximized $\eta_{ED}(\lambda)$ which limits the phase separation to the exciton diffusion length. Since the 1990s this problem has been studied extensively. Besides the mixing ratio of donor and acceptor, the processing parameters play a crucial role. In case of solution processed polymer devices, these are mainly the polarity of the solvent, the content of additives as well as the annealing temperature for drying the mixed layer^[103,104]. For devices composed of vacuum deposited small molecules, the substrate temperature during deposition is the key factor^[105,106]. However, other approaches like organic vapor phase deposition instead of ordinary vacuum thermal evaporation^[107], the implementation of concentration gradients within the bulk layer^[108] or alternative preparation techniques^[109] have been tried.

1.2.3 The p-i-n Concept

Just sandwiching such a bulk or flat heterojunction between two electrodes is in principle sufficient to create a working solar cell. However, the performance that can be achieved this way is rather low. Especially for solar cells composed of small molecules, it proved to be necessary to insert a further buffer layer between the acceptor and the metal top contact. This additional layer protects the organic material against damage due to the metal deposition and can furthermore function as an exciton blocking layer that prevents the diffusion of excitons towards the electrode where quenching is likely to happen^[12]. Typical buffer materials are BCP (2,9-dimethyl-4,7-diphenyl-1,10-phenanthroline) and BPhen (bathophenanthroline; 4,7-diphenyl-1,10-phenanthroline), but also other organic compounds can be applied^[110,111]. Interestingly, the energy level positions of the buffer materials seem not to be relevant for achieving an ohmic contact. Peumans et al. suggested that it is not the molecular electron transport levels, but cathode induced defect states with energies higher than EA which are responsible for the electron conduction in those materials. The density of these defect states is assumed to decrease exponentially with the distance from the organic/metal interface. Hence, there is a critical layer thickness beyond which the intrinsic properties of the buffer material (low conductivity and mobility) become dominant again and reduce the charge carrier collection efficiency. For BCP this critical thickness was determined to be 15nm^[12] while in case of BPhen up to 30nm can be used without deteriorating device performance.

This inherent constraint regarding layer thickness can be circumvented by using molecularly doped layers as it is done in p-i-n configurations. The associated layer stack as well as the energy level diagram of an ideal p-i-n type solar cell are displayed in Figure 1.16. The photoactive donor/acceptor heterojunction is sandwiched between a p-doped hole transport material (HTM) and an n-doped electron transport material (ETM). Light enters the device through the ITO bottom contact and is reflected at the metal top contact. Due to thin film interference effects this results in the formation of an interference pattern having its intensity minimum at the metal back contact and the maximum within the photoactive layers. To use the full potential of the p-i-n concept, the transport materials need to fulfill the following basic requirements.

1. **Energy level alignment.** To avoid energy losses during charge carrier collection, an energy level alignment between the electron (hole) transport level of the n-doped (p-doped) ETM (HTM) and the adjacent acceptor (donor) material is necessary. In case of a bad alignment, either electron injection or extraction barriers might occur at the interface. Such barriers induce an accumulation of mobile charge carriers which in turn leads to a tremendous decrease in fill factor^[112-114].

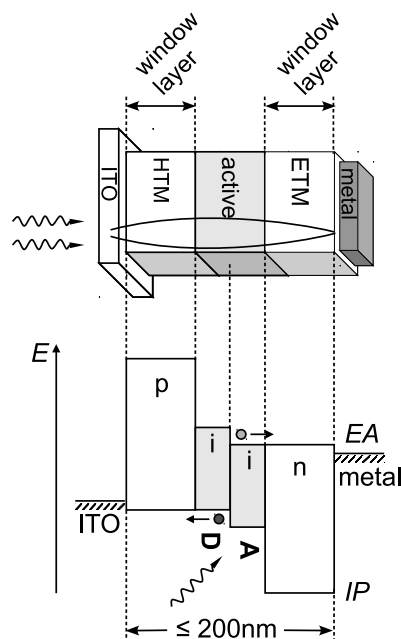


Figure 1.16: Simplified stack and energy level scheme of a solar cell with a planar heterojunction according to the *p-i-n* concept. The photoactive intrinsic donor (D) and acceptor (A) layers are sandwiched between doped transparent hole conducting (p) and electron conducting (n) window layers. Light enters the device through the ITO bottom contact and is reflected at the metal top contact, thereby creating an interference pattern within the stack. The maximum of the optical field profile can be adjusted to the donor and acceptor layers by varying the thickness of the transport layers. The energy level scheme shows the electron affinities (EA) and ionization potentials (IP) for an ideal device.

As will be seen in Chapter 3, doping plays a key role when it comes to the adjustment of energy levels.

2. **Transparency.** The additional charge transport materials should be transparent in the visible range of the sun spectrum, i.e. the optical bandgap should ideally be above 3eV. This way, the light intensity reaching the photoactive area is not weakened by parasitic absorption of photons in the transport layers. Absorption taking place in either ETM or HTM is called parasitic, because excitons which are generated here cannot contribute to the photocurrent as (i) they are too far away from the separating D/A interface for being converted into free charge carriers and (ii) there is a high probability for quenching at the dopant molecules or the metal electrode. Transparent charge transport materials are also denoted as *optical spacer* or *window materials*.
3. **Exciton blocking.** The interface between ETM and acceptor as well as the interface between HTM and donor should be exciton blocking. In principle, this feature is actually a direct consequence of transport level alignment in combination with the wide band gap of the transport materials that comes with transparency. As sketched in Figure 1.16 this creates a step in ionization potentials at the n-side and a step in electron affinities at the p-side. This energy barrier prevents the excitons from diffusing into the transport materials and rather promotes their propagation towards the D/A-heterojunction. Furthermore, it blocks the transport of minority carriers towards the „wrong“ contact.
4. **High conductivity.** An increase in conductivity can usually be achieved by doping which shifts the Fermi level towards the respective transport level. Assuming a transport layer thickness of 100nm and typical photocurrents of approximately 10mA/cm², a conductivity as high as 10⁻⁵S/cm results in a voltage drop in the order of only 0.01V over the doped layer. This estimation illustrates that even such a comparatively small value is more than enough to ensure an efficient charge transport towards the electrodes. In most cases, the enhanced charge carrier density that is introduced by doping can overcompensate low charge carrier mobilities.

Not only the charge transport process benefits from doping, but also charge extraction at the electrodes. As the contact between doped organic materials and metal is ohmic in most cases, doping makes the complicated search for compatible metal/organic combinations obsolete. For example it avoids the use of low work function metals as for example calcium or magnesium for electron injection. Instead of these highly reactive and air unstable materials, it is possible to simply use aluminum electrodes. Currently, there are two alternative approaches that explain the improved charge injection: The first assumes that a chemisorption of dopant molecules at the metal contact changes the metal work function and thereby reduces the electron or hole injection barrier^[115,116]. The second model is adapted from inorganic semiconductor physics and involves level bending at the metal/organic interface – an equivalent to band bending in inorganic semiconductors. As doping pins the Fermi level close to the charge transport level, Fermi level alignment will enforce a charge transfer at the interface which results in the formation of a narrow depletion layer at the contact. It is generally assumed that electrons (or holes) can easily tunnel through this space charge layer^[37,38].

5. **Smooth layers.** The formation of uniform films with low surface roughness is important if device geometries are to be used in which further layers are deposited on top of the respective transport layer. Rough underlayers influence the growth of all following layers and increase the risk of short circuits. However, when applying a very rough charge transport material as the topmost layer just below the metal top contact, no problems are to be expected^[14]. With regard to device lifetime, morphological stability upon heating or illumination is important.
6. **Thermal stability.** Last but not least, all materials applied in a solar cell stack should be thermally stable which means the decomposition temperature should be much higher than the evaporation temperature. Furthermore, a solar cell will be exposed to elevated temperatures during its operation. Thus, the organic materials, including doped layers, should also withstand post-annealing without changing performance. For the last point, high glass transition temperatures are beneficial.

A charge transport material fulfilling all these requirements is not only a powerful tool for circumventing charge extraction and contact problems, but also serves the optimization of the thin film optics. The high conductivity achieved by doping allows to adjust the transport layer thickness freely up to > 100nm without introducing ohmic losses. As will be shown in Chapter 6, shifting the photoactive materials into the maximum of the optical interference pattern can be easily achieved by tuning the thickness of the spacer layers. Here, especially the dimension of the spacer layer adjacent to the reflecting metal top contact plays a decisive role. In p-i-n geometries as displayed in Figure 1.16, this task is fulfilled by the electron transport material. However, as doping allows for a large degree of freedom in device design, other configurations like n-i-p, but also p-i-i, m-i-p, m-i-n, or tandem structures with doped optical spacers between the subcells are feasible^[106,112,117,118].

While a sufficiently large selection of hole transport materials fulfilling the above mentioned criteria is known and commercially available, the choice of suitable wide-gap electron transport materials is very limited. In state-of-the art p-i-n devices it is still common practice to use either thin exciton blocking layers composed of BPhen or BCP ($\leq 15\text{nm}$) or n-doped C₆₀^[119]. The latter is not transparent and does not provide any exciton blocking behavior when being combined with a photoactive system using i-C₆₀ as acceptor material. Another alternative is n-doped NTCDA which has a wide band gap and suitable energy level positions, but forms very rough and crystalline layers^[14,15].

It is the task of this thesis to find and study organic compounds which have the potential to be used as electron transport materials according to the above given catalog of criteria in order to finally exploit p-i-n concept in its whole extent.

2 Experimental

The following Chapter presents the materials used in this thesis as well as sample preparation techniques and experimental setups utilized for material and solar cell characterization.

2.1 Materials

The focus of this work is on improving the performance of standard p-i-n type solar cells^[11,14] by replacing n-doped C₆₀ – the reference ETM – with transparent ETM. As described in Section 1.2.3, an ETM needs to meet a number of criteria for allowing the fabrication of efficiently working devices. In addition to several general requirements concerning optical and transport properties as well as stability issues, it is of particular importance that the energy levels match the neighboring acceptor material that is commonly composed of intrinsic C₆₀. For testing and comparing the performance of the new ETM in solar cells, a certain standard device architecture is used. All materials except for the new ETM are standard materials with well known physical properties and will be described in the order in which they are arranged in a p-i-n type device: HTM & p-dopants/ donor/ acceptor/ ETM & n-dopants.

2.1.1 Standard Materials

MeO-TPD - hole transport material

The MeO-TPD (N,N,N',N'-tetrakis(4-methoxyphenyl)-benzidine) molecule displayed in Figure 2.1, comprises two triphenylamine units which are typical constituents of hole transporting materials. Thin films are fabricated by thermal evaporation in vacuum at a temperature of approximately 180°C using a density of 1.43g/cm^{3*}. MeO-TPD forms smooth layers on glass and organic materials which are transparent in the visible range of the sun spectrum. The thin films yield an optical energy gap of $E_g^{\text{opt}} = 2.9\text{eV}^\dagger$ and an ionization potential of 5.1eV determined by ultraviolet photoelectron spectroscopy (UPS)^[38]. Hence, the electron affinity can be estimated to be 2.2eV minus the exciton binding energy which is expected to be in the range of $> 0.3\text{eV}$. MeO-TPD is well p-dopable with either the commercially available dopant F₄-TCNQ or the proprietary material NDP2 which has been used as standard dopant throughout this work. In both cases conductivities as high as 10⁻³S/cm are reached by using molar ratios of 20:1^[38] or 10:1[‡], respectively.

MeO-TPD has been purchased from Sensient (Wolfen, Germany) and was cleaned twice by vacuum gradient sublimation before being used in our vacuum tool.

Alternative hole transport materials

Additional to MeO-TPD which is used as standard HTM in p-i-n type layer stacks, **BF-DPB** (N,N'-((diphenyl-N,N'-bis)9,9-dimethyl-fluoren-2-yl)-benzidine) or **BPAPF** (9,9-bis[4-(N,N-bis-biphenyl-4-yl-amino)phenyl]-9H-fluorene), both shown in Figure 2.1, are applied as HTM. The materials are deposited at temperatures of 180°C and 260°C, using thin film densities of 1.21 and 1.20g/cm^{3§}. Compared to MeO-TPD both compounds are found to have a better thermal stability[¶] while having similar optical energy gaps of $E_{g,\text{BF-DPB}}^{\text{opt}} = 3.0\text{eV}$ and $E_{g,\text{BPAPF}}^{\text{opt}} = 2.9\text{eV}$. BF-DPB, having an *IP* of 5.2eV[‡] basically replaces MeO-TPD in standard geometries, whereas BPAPF is used due to its high *IP* of 5.6eV[‡] which matches the *IP* of DCV6T. Either NDP2 or NDP9 are used for p-doping.

BF-DPB has been purchased from Sensient (Wolfen, Germany) and purified once by vacuum gradient sublimation. BPAPF is supplied by Lumtec (Hsin-Chu, Taiwan) and purified twice by vacuum gradient sublimation before being used in our vacuum tools.

* Profilometer measurement. † Measured at IAPP by René Michel. ‡ Measured at IAPP by Selina Olthof. § BF-DPB density determined at IAPP with a profilometer measurement; BPAPF density estimated. ¶ Measured at IAPP by Martin Hermenau.

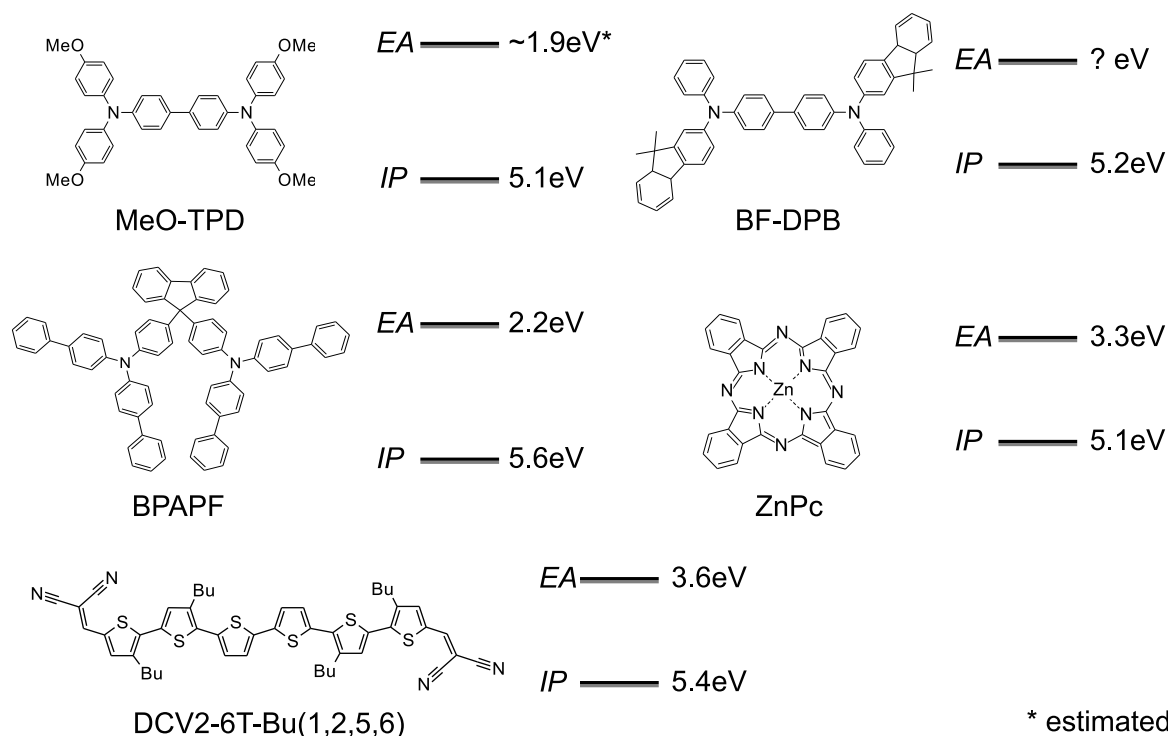


Figure 2.1: Organic materials MeO-TPD (*N,N,N',N'*-tetrakis(4-methoxyphenyl)-benzidine, HTM), BF-DPB (*N,N'*-((diphenyl-*N,N'*-bis)9,9,-dimethyl-fluoren-2-yl)-benzidine, HTM), BPAPF (9,9-bis[4-(*N,N*-bis-biphenyl-4-yl-amino)phenyl]-9*H*-fluorene, HTM), ZnPc (zinc phthalocyanine, donor), and DCV2-6T-Bu(1,2,5,6) (α - ω -bis-(dicyanovinylene) with butyl side chains, donor).

NDP2 and NDP9 - p-dopants

NDP2 and NDP9 are p-dopants developed by Novald AG (Dresden, Germany). Although their molecular structures are proprietary, both materials are preferred over the freely available material F₄-TCNQ (2,3,5,6-tetrafluoro-7,7,8,8-tetracyanoquinodimethane). Due to their higher evaporation temperatures of 136°C and 180°C the risk of contaminating the vacuum tool is markedly reduced in comparison with the use of the more volatile free dopant. As has been pointed out by Reineke et al.^[120], NDP2 works similarly well as F₄-TCNQ. It is used for p-doping MeO-TPD and BF-DPB. Compared to NDP2, NDP9 is even more effective and is therefore applied as p-dopant in materials with high ionization potentials like BPAPF.

NDP2 and NDP9 have been used as received from the Novald AG.

ZnPc - donor

ZnPc (zinc phthalocyanine), shown in Figure 2.1, belongs to the phthalocyanines, a group of macrocyclic compounds which are widely used as blue dyes. Its evaporation temperature is in the range of 300°C. Throughout this work a density of 1.34g/cm³ is used for thin film fabrication. This value was determined by a profilometer measurement whereas x-ray reflectometry (XRR) results indicate that the true density might be in the order of 1.55g/cm³ and thus slightly larger^[121]. ZnPc forms polycrystalline films in a triclinic (α -) or monoclinic (γ -) phase having a surface roughness $\leq 4\text{nm}$ ^[121]. The material is mainly absorbing in the spectral region from 550nm to 800nm and therefore shows an absorption complementary to C₆₀. An exciton diffusion length of (30 \pm 10)nm is reported in literature^[122]. The preferably hole conducting material exhibits a field effect hole mobility of $6.5 \cdot 10^{-4}\text{cm}^2/\text{Vs}$ ^[123]. Its ionization potential has been determined to be 5.1eV by UPS and is thus identical to the IP of MeO-TPD. The electron affinity, measured by inverse photoelectron spectroscopy (IPES), is 3.3eV^[75]. Considering these energy level positions, a barrier-free hole transfer from ZnPc to MeO-TPD as well as blocking of excitons generated in ZnPc can be expected at this particular organic/organic interface. When using ZnPc as donor

in combination with C_{60} as acceptor in a photoactive heterojunction of an organic solar cell results in an efficient exciton separation.

ZnPc has been purchased from TCI Europe (Antwerp, Belgium) and purified three to four times by vacuum gradient sublimation in order to improve the material quality.

DCV2-6T-Bu(1,2,5,6) - alternative donor

DCV2-6T-Bu(1,2,5,6) (butyl substituted α - ω -bis-(dicyanovinylene)) is a green absorber consisting of six thiophene units which are substituted by four butyl side chains at the thiophene backbone and two dicyanovinylene endgroups (compare Figure 2.1). Its evaporation temperature is in the range of 280°C. Based on a comparison with DCV2-6T-Et(2,2,4,4)^[124], the thin film density is estimated to be 1.3g/cm³. Compared to ZnPc, DCV2-6T-Bu(1,2,5,6) has a higher *IP* of 5.4eV. Therefore, when combining the material in a heterojunction with the acceptor C_{60} , a higher effective energy gap and consequently, a higher photovoltage is achieved. Detailed information about physical properties and the performance of DCV2-6T-Bu(1,2,5,6) in organic solar cells can be found in reference 125. In the following, the short name DCV6T will be used.

The material was purchased from Heliatek GmbH (Dresden, Germany) and outgased in vacuum prior to the deposition.

C_{60} - acceptor and reference electron transport material

The molecular structure of the buckminster fullerene C_{60} is displayed in Figure 2.2. It is a spherical molecule consisting of 60 carbon atoms which are arranged in the form of 12 pentagons and 20 hexagons resulting in a molecular diameter of only 7Å. C_{60} evaporates at 330...430°C and forms crystalline films at room temperature which are dominated by the face centered cubic (fcc) structure, but also contain small amounts of hexagonal close packed (hcp) and other phases^[126]. Despite the crystallinity, thin films are smooth having a surface roughness less than 2nm as determined by means of XRR. The thin film density used within the scope of this work has been measured with a profilometer and yields 1.54g/cm^{3*}. Other methods result in slightly higher values of (1.6 ± 0.1)g/cm³ †. The high electron mobility of 6.2·10⁻³cm²/Vs^[123], a high exciton diffusion length of 40nm^[121] as well as the ionization potential of 6.4eV ‡ and the electron affinity of 4.0eV^[49] make C_{60} an interesting acceptor material for organic solar cells. It can be combined with several donor materials like ZnPc, as it is done in the present work, DCV5T (α , α' -bis-(2,2-dicyanovinylene)-quinquethiophene)^[117], DCV6T (α , ω -bis-(dicyanovinylene)-sexithiophene)^[106], F₄-ZnPc^[127], DIP (diindenoperylene)^[128] or DIP derivatives^[129]. All of these donor compounds are absorbing in a higher wavelength range than C_{60} which mainly absorbs in the blue below 550nm and in the ultraviolet region. Currently, C_{60} is widely used as standard acceptor compound and only few alternatives like C₇₀^[130] or K12^[131] are known.

However, C_{60} does not only serve as acceptor material, but can also be employed as ETM. It is dopable with commercial dopants like for instance AOB or Cr₂(hpp)₄, and the non-commercial material NDN1 purchased from Novald AG. While with AOB a conductivity in the order of 10⁻²S/cm is reached^[62], NDN1-doping can even push the conductivity to values > 1S/cm. Although AOB would provide sufficient

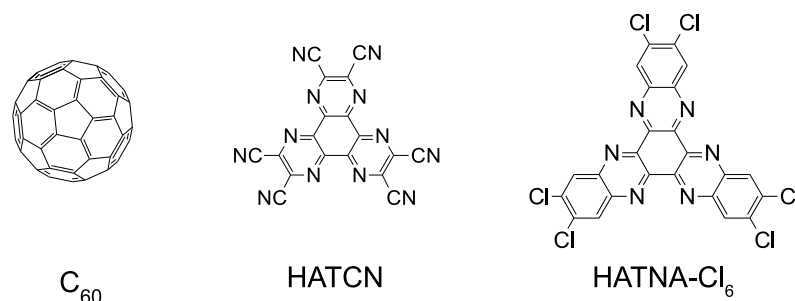


Figure 2.2: Various electron transport materials used in this thesis: C_{60} (reference ETM and acceptor), HATCN (hexaazatriphenylene-hexacarbonitril), and HATNA-Cl₆ (2,3,8,9,14,15-hexachloro-5,6,11,12,17,18-hexaazatrinaphthylene).

* Measured by Steffen Pfützner, IAPP. † X-ray reflectometry, measured at IAPP by Chris Elschner. ‡ Measured at IAPP by Selina Olthof.

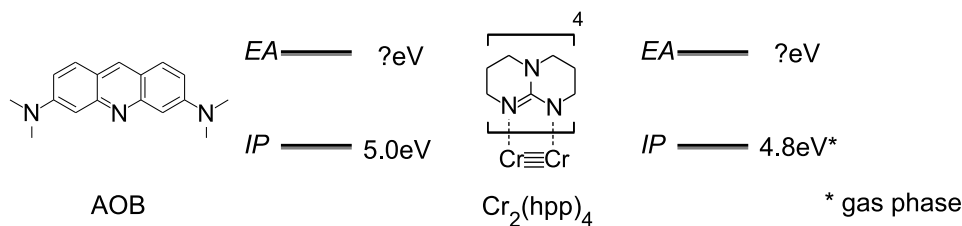


Figure 2.3: Molecular structures of the n-dopants AOB (acridine orange base) and $\text{Cr}_2(\text{hpp})_4$ (tetrakis(1,3,4,6,7,8-hexahydro-2H-pyrimido[1,2-a]pyrimidinato)dichromium (II)).

conductivity, we again prefer to apply the proprietary material NDN1 as dopant. Despite its outstanding transport properties, using n- C_{60} as ETM is only a temporary solution as it is neither a transparent material nor applicable as exciton blocking material when being combined with a photoactive system containing intrinsic C_{60} as acceptor. Therefore devices comprising n- C_{60} are expected to be less efficient than solar cells with completely transparent ETM. Throughout this thesis n- C_{60} will nevertheless be employed as reference ETM to evaluate the performance of the new test materials.

Several material batches purchased from BuckyUSA (Houston, USA), IPMS (Dresden, Germany) and CreaPhys (Dresden, Germany) have been used for single layer and device fabrication. All of them have been purified three to four times in order to compensate for potential differences.

NDN1, AOB and $\text{Cr}_2(\text{hpp})_4$ - n-dopants

NDN1 is used as standard n-dopant for our ETM. Like NDP2, it is a material developed by Novaled AG (Dresden, Germany) and its molecular structure is proprietary. It displays only a slightly higher doping efficiency than $\text{Cr}_2(\text{hpp})_4$ (tetrakis(1,3,4,6,7,8-hexahydro-2H-pyrimido[1,2-a]pyrimidinato)dichromium (II)) but is much stronger than the n-dopant AOB. In practice, this means that higher charge carrier densities and thus higher conductivities can be achieved when using the same doping concentrations. Concerning device fabrication the use of NDN1 is preferred for another reason: Due to its high evaporation temperature of 200°C the material is not as volatile as AOB, which already evaporates at 60°C. Thus, the risk of contaminating the evaporation tool is reduced. The evaporation temperature of $\text{Cr}_2(\text{hpp})_4$ is in the same range as the evaporation temperature of NDN1. However, there is only a limited amount of material available which is why $\text{Cr}_2(\text{hpp})_4$ can only be used for performing conductivity tests, but not for fabricating devices.

NDN1 and $\text{Cr}_2(\text{hpp})_4$ have been used as received from Novaled AG. Both materials are air-unstable and have to be handled in an inert atmosphere. AOB has been purchased from Sigma Aldrich (USA) and subsequently purified twice by vacuum gradient sublimation.

2.1.2 Electron Transport Materials

As already stated above, the ETM needs to match the acceptor used in the photoactive layer. This means, in principle, both donor and HTM can be replaced by other materials or material combinations without directly affecting the n-side. The p-i-n concept formulated in Section 1.2.3 provides the guidelines for developing suitable ETM. In this work HATCN, HATNA- Cl_6 , and several Bis-F1-NTCDI derivatives, i.e. representatives of three different material classes, were tested in addition to n- C_{60} and will be described in the following. In addition, NTCDA, a compound which has been examined for suitability as ETM in p-i-n type solar cells in previous work^[13-15] has been re-evaluated.

HATCN

HATCN (hexaazatriphenylene hexacarbonitrile), depicted in Figure 2.2, is a small discoid molecule with six highly electron withdrawing nitrile groups at its periphery. This configuration results in an electron deficient core typical for electron acceptors as it indicates a large electron affinity. However, there is no data about the electron affinity of HATCN thin films in literature. Estimations range from 5.2eV to 5.7eV^[132,133] and are for instance obtained by subtracting the optical energy gap from the ionization potential, thereby not accounting for the unknown exciton binding energy. The optical gap has been measured in solution and is between 3.1eV^[134] and 3.5eV^[135]; the ionization potential determined by

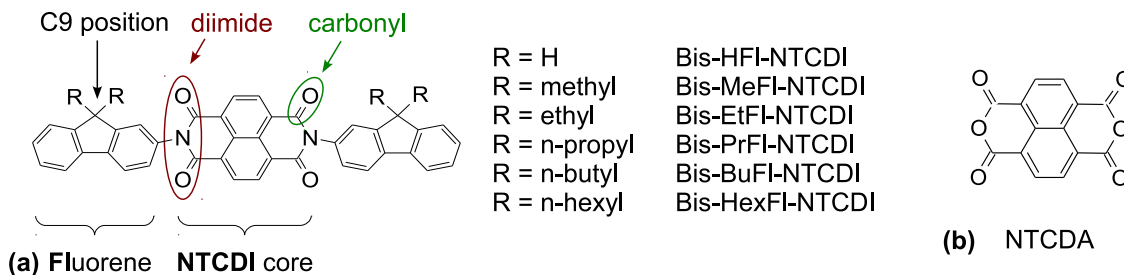


Figure 2.4: a) Molecular structures of Bis-FI-NTCDI derivatives including the nomenclature of the functional groups and substituents. Six different compounds with varying alkyl chain length in the R position are examined in this work: Bis-HFI-NTCDI (no side chain, *N,N*-Bis(fluorene-2-yl)-naphthalenetetracarboxylic diimide), Bis-MeFI-NTCDI (methyl side chain, *N,N*-Bis(9,9-dimethylfluorene-2-yl)-naphthalenetetracarboxylic diimide), Bis-EtFI-NTCDI (ethyl side chain, *N,N*-Bis(9,9-diethylfluorene-2-yl)-naphthalenetetracarboxylic diimide), Bis-PrFI-NTCDI (propyl side chain, *N,N*-Bis(9,9-dipropylfluorene-2-yl)-naphthalenetetracarboxylic diimide), Bis-BuFI-NTCDI (butyl side chain, *N,N*-Bis(9,9-dibutylfluorene-2-yl)-naphthalenetetracarboxylic diimide), and Bis-HexFI-NTCDI (hexyl side chain, *N,N*-Bis(9,9-dihexylfluorene-2-yl)-naphthalenetetracarboxylic diimide). b) Structural formula of NTCDA (1,4,5,8-naphthalenetetracarboxylic dianhydride).

UPS is in the range of 9.5eV to 9.9eV^[136]. The values for E_g^{opt} and IP are in good agreement with our own measurements which are discussed in Chapter 3.

Up to now HATCN has been used in a variety of applications: (1) The chemisorption of a HATCN monolayer on a metal substrate changes the metal work function. By this, an adjustment of electrical and structural properties of the interface between the metallic electrode and subsequently deposited organic materials was achieved^[137,138]. (2) Because of its large electron affinity which is in the range of the hole transporting level of NPB (4,4'-bis(N-phenyl-1-naphthylamino)biphenyl), HATCN can serve as hole injection layer at the anode of hole only devices^[139] or OLEDs^[132], i.e. it mediates the charge transport from either aluminum or ITO to NPB. (3) Similarly, it was used as charge generation layer (CGL) in tandem OLED structures, connecting two electroluminescent subunits^[134,135,140]. Again, this configuration benefits from the alignment of the HATCN electron transport level with the hole transport level of NPB on the one side and with the electron transport level of n-doped Alq₃ or BPhen on the other side. (4) Last but not least, the large electron affinity and the successful implementation of HATCN as CGL suggests that the material might be applicable as p-dopant, as well. Indeed, Yook et al. showed an improved OLED performance upon doping the hole transport layer composed of either NPB^[133] or CuPc^[141] with HATCN. However, the observed doping effect is very small.

Based on these findings, HATCN is identified as potential electron transport material for organic p-i-n type solar cells: It is transparent in the visible range of the sun spectrum and strongly electron accepting. However, its electron affinity is potentially larger than the electron affinity of the photoactive acceptor material C₆₀ ($EA = 4.0\text{eV}$) which can cause misaligned energy levels at the acceptor/ETM interface and, as a consequence, can diminish the device performance. Together with an extensive material characterization this effect will be addressed in more detail in Chapter 3. Furthermore, ways to circumvent this problem will be presented.

The material used in this work was synthesized at the Max Planck Institute for Polymer Research (MPIP, Mainz, Germany) and subsequently purified twice by vacuum gradient sublimation at the IAPP.

Bis-FI-NTCDI

Though a large variety of NTCDI (naphthalenetetracarboxylic diimide) derivatives is known and this material class is generally well established, NTCDI with fluorene side groups has so far not been reported. For this work, a series of six Bis-FI-NTCDI (*N,N*-Bis(fluorene-2-yl)-naphthalenetetracarboxylic diimide) compounds, shown in Figure 2.4a), has been synthesized, characterized and tested as ETM in organic p-i-n type solar cells. The compounds only differ from each other by the substituents attached to the C9

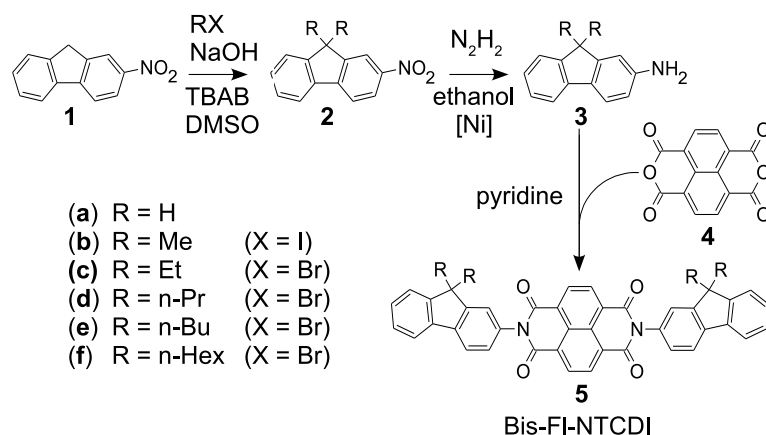


Figure 2.5: Synthesis route for obtaining Bis-FI-NTCDI compounds.

positions of the fluorene groups, marked with *R* in the structural formula. Starting with Bis-HFI-NTCDI with *R* = H, alkyl side chains of increasing length were attached. The number of carbon atoms in the chain is increased from 1 (methyl, Bis-MeFI-NTCDI) to 2 (ethyl, Bis-EtFI-NTCDI), 3 (propyl, Bis-PrFI-NTCDI), 4 (butyl, Bis-BuFI-NTCDI) and 6 (hexyl, Bis-HexFI-NTCDI) in order to study the influence of simple structural variations on the materials physical properties like energy level positions, morphology, and charge carrier transport.

NTCDI itself is known to be a transparent material which is preferably electron transporting^[142,143]. Compared to unsubstituted naphthalene, the frontier orbitals are shifted to higher binding energies due to the highly polar and electron withdrawing diimide moieties^[144]. As a result, the material becomes preferentially electron accepting. So far, NTCDI derivatives have mostly been applied as n-channel materials in organic field effect transistors (OFETs)^[143,144]. However, a similar material, NTCDA (1,4,5,8-naphthalenetetracarboxylic dianhydride), in which the nitrogen heteroatoms are replaced by oxygen, has already been tested as ETM in organic p-i-n type solar cells in previous work^[13]. Despite its promising electronic properties, a widespread application as ETM is inhibited by the presumably low glass transition temperature which leads to an island growth and surface roughnesses of $> 20\text{nm}$ ^[14,15] (for more information, see below). An increase of the glass transition temperature can be achieved by different approaches. For instance, increasing the molecular size and weight, incorporating bulky substituents into otherwise rigid molecules or enhancing the intermolecular interactions, e.g. by hydrogen bonding or by introducing bipolar forces, can prevent crystallization^[145,146].

To modify the molecular structure in a way that leads to the formation of an amorphous growth while at the same time preserves the favorable electronic properties of the NTCDI core, we chose to attach fluorene units as imide side groups. Fluorene-based oligomers and polymers are well studied regarding their application in organic electronic devices such as OFETs, OLEDs, OSCs and even organic solid state lasers. Plain fluorene without any substituents forms transparent thin films^[147] whereas the addition of chromophoric groups can shift the absorption as well as emission considerably, thus increasing the number of possible fields of application^[148]. An alkylation of the fluorene groups at the C9 position is expected not to reduce the transparency, but instead change the packing of the molecules and prevent crystallization.

The synthesis of all Bis-FI-NTCDI compounds was performed by Dr. Markus Hummert at the IAPP and follows the route displayed in Figure 2.5. As educts nitrofluorene (1) and NTCDA (4) are used. In a two-step synthesis, nitrofluorene is first alkylated at the C9 position by adding the corresponding alkylhalogenide in the presence of sodium hydroxide (NaOH) using dimethyl sulfoxid (DMSO) as solvent and tetrabutyl ammoniumbromide (TBAB) as phase transfer catalyst. A subsequent hydrogenation of the nitro group in the presence of nickel leads to the formation of fluorene-2-yl-amine (3). Both precursor compounds, fluorene-2-yl-amine and NTCDA are condensed in the low boiling solvent pyridine for achieving a higher purity. A more detailed description of the synthesis is provided in reference 149. In order to confirm the formation of Bis-FI-NTCDI as reaction product, several techniques like elementary analysis, infrared spectroscopy, electrospray ionization mass spectrometry (ESI-MS), ^1H (proton) as well as ^{13}C nuclear magnetic resonance (NMR) analysis are employed. Thermogravimetric analysis (TGA) as well as differential scanning calorimetry (DSC) are used for determining melting point and decomposition

temperature.

By the above described synthesis route, Bis-FI-NTCDI compounds can be obtained with an overall yield of 60...70%. Before being used in the vacuum system, the purity of the materials was further enhanced by vacuum gradient sublimation.

HATNA-Cl₆

Similar to the class of the hexaazatriphenylenes, hexaazatrinaphthylene (HATNA) owes its electron deficient character to the electronegative nitrogen heteroatoms which induce a charge redistribution along the σ bonds (I⁻-effect, see Section 1.1.1). Furthermore, they give rise to the existence of several resonance structures that describe the distribution of π electrons in the aromatic system^[150]. As nitrogen has the tendency to withdraw electrons from the conjugated π system, the resonance effect in HATNA is an M⁻-effect (see Section 1.1.1). Plain HATNA without any additional substituents at the periphery has an electron affinity of 2.8eV and an ionization potential of 6.6eV^[151,152]. By adding suitable substituents like functionalized alkyl chains, esters, or strongly electron withdrawing halogenes (e.g. chlorine or fluorine), the positions of the frontier orbitals can be shifted^[150,153]. Furthermore, the morphology of HATNA thin films depends on the side groups: By tuning the substituents, amorphous, crystalline, and columnar discotic liquid crystalline phases can be achieved^[150,151,154,155]. Especially structures with long flexible side chains attached to the rigid core form highly ordered columnar phases that stack with a strong overlap of their aromatic π systems^[154]. This way, charge carrier mobilities $> 0.01\text{cm}^2/\text{Vs}$ are obtained, which are likely to be electron mobilities^[151,155]. However, the application of HATNA derivatives as ETM has not yet been reported in literature.

For HATNA-Cl₆ (2,3,8,9,14,15-hexachloro-5,6,11,12,17,18-hexaazatrinaphthylene), displayed in Figure 2.2, an electron affinity of 4.1eV and an ionization potential of 7.5eV have been reported in literature^[150]. These energy levels are very promising concerning the requirements posed by the p-i-n device architecture: They indicate both, an alignment of electron transport levels, and an exciton blocking behavior at the interface to the acceptor material C₆₀. However, no further information about thin film growth, charge carrier mobility, or conductivity was available at the time this work started. Details on material characterization and the application of HATNA-Cl₆ as ETM are presented in Chapters 5 and 6.

The material used for device fabrication was synthesized and purified twice by Novald AG (Dresden, Germany).

NTCDA

NTCDA (1,4,5,8-naphthalenetetracarboxylic dianhydride) shown in Figure 2.4b) is not only a precursor material for the synthesis of Bis-FI-NTCDI compounds, but can also be applied as ETM itself. It evaporates at a temperature of approximately 130°C and forms very rough, polycrystalline layers on glass substrates and organic underlayers^[13,15]. Due to its pronounced island growth, it is difficult to specify the thin film density. In this thesis, a value of $\rho_{\text{NTCDA}} = 1.77\text{g}/\text{cm}^3$, determined by Born et al. for NTCDA single crystals, is used^[156]. However, it is likely that the effective density is smaller. Having an optical energy gap of 3.1eV, NTCDA is transparent in the visible range of the sun spectrum. The energy level positions, determined by photoelectron spectroscopy, meet the requirements of the p-i-n concept: In comparison to the acceptor C₆₀, the ionization potential is increased by 1.4eV reaching a value of 8.0eV^[14,35] while the electron affinity is 4.0eV^[35] – the same as in C₆₀. Furthermore, NTCDA is n-dopable with AOB as well as NDN1 leading to conductivities in the order of $1 \cdot 10^{-4}\text{S}/\text{cm}$ ^[13]. The field effect electron mobility of undoped thin films grown on silicon is in the order of $1 \cdot 10^{-3}\text{cm}^2/\text{Vs}$ ^[142]. It has been demonstrated that the application of n-doped NTCDA as transparent ETM in organic p-i-n type solar cells results in an improved photocurrent compared to conventional n-C₆₀ reference devices. However, its unfavorable morphology inhibits a widespread application^[13].

The material used in this work has been purchased from Sigma Aldrich (St. Louis, USA) and purified at least twice by vacuum gradient sublimation before being loaded to the vacuum system.

Other potential ETM

Several other fluorene derivatives that are depicted in Figure 2.6 have been characterized and evaluated with respect to their applicability as ETM in organic p-i-n type solar cells. Except for Bu-FI-ZnCl-ACN, which exhibits an optical energy gap of 2.0eV, all compounds are transparent in the visible range of the sun spectrum having an $E_{\text{g}}^{\text{opt}}$ larger than or equal to 2.8eV. Though most test materials fulfill the optical

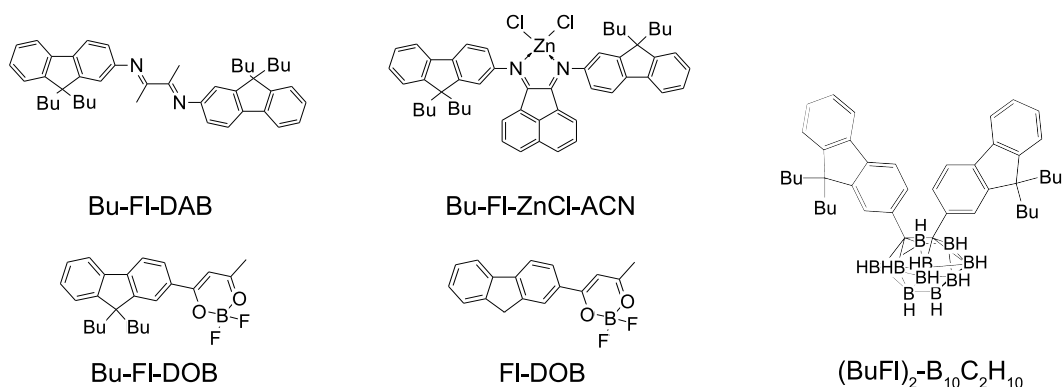


Figure 2.6: Further test materials which were found not to be applicable as ETM as doping could not increase the electron conductivity to sufficiently high values: *Bu-FI-DAB* (*N,N*-Bis(9,9-dibutylfluorene-2-yl)-1,4-diaza-2,3-dimethyl-1,3-butadiene), *Bu-FI-ZnCl-ACN* (Bis[(9,9-dibutylfluorene-2-yl)imino]acenaphthene zinc dichloride), $(\text{BuFI})_2\text{-B}_{10}\text{C}_2\text{H}_{10}$ (1,2-bis(9,9-dibutyl-fluorene-2-yl)carborane), *Bu-FI-DOB* (2-(difluoro-1,3,2-H-dioxaborinyl)-1,1'-(9,9-dibutyl-9H-fluorene)), and *FI-DOB* (2-(difluoro-1,3,2-H-dioxaborinyl)-1,1'-(9H-fluorene)).

material	type	supplier	density g/cm ³	$E_g^{\text{opt[e]}}$ eV	$IP^{\text{[f]}}$ eV	EA eV
MeO-TPD	HTM	Sensient	1.43 ^[a]	2.9	5.1	-
BF-DPB	HTM	Sensient	1.21 ^[a]	3.0	5.2	2.3 ^[g]
BPAPF	HTM	Lumtec	1.20 ^[b]	2.9	5.6	2.2 ^[m]
ZnPc	HTM / donor	TCI Europe	1.34 ^[a]	1.5	5.1	3.3 ^[h]
DCV2-6T-Bu(1,2,5,6)	donor	Heliatek GmbH	1.30 ^[b]	1.7	5.4	3.6 ^[g]
C ₆₀	ETM / acceptor	BuckyUSA	1.54 ^[a]	1.7	6.4	4.0 ^[i]
HATCN	ETM	MPIP Mainz	1.67 ^[a]	3.3	9.6	4.8 ^[b]
HATNA-Cl ₆	ETM	Novald AG	1.55 ^[a]	2.8	7.3	4.1 ^[j]
Bis-HfI-NTCDI	ETM	IAPP	1.25 ^[c]	3.0	6.6	3.8 ^[g]
Bis-MeFl-NTCDI	ETM	IAPP	1.12 ^[c]	3.1	6.5	3.8 ^[g]
Bis-EtFl-NTCDI	ETM	IAPP	1.10 ^[c]	3.1	6.5	3.7 ^[g]
Bis-PrFl-NTCDI	ETM	IAPP	1.05 ^[c]	3.1	6.5	3.7 ^[g]
Bis-BuFl-NTCDI	ETM	IAPP	1.10 ^[c]	3.1	6.6	3.7 ^[g]
Bis-HexFl-NTCDI	ETM	IAPP	1.10 ^[b]	3.1	6.6	3.7 ^[g]
NTCDA	ETM	Sigma Aldrich	1.77 ^[d]	3.1	8.0	4.0 ^[k]
NDP2	p-dopant	Novald AG	-	-	-	-
NDP9	p-dopant	Novald AG	-	-	-	-
NDN1	n-dopant	Novald AG	-	-	-	-
Cr ₂ (hpp) ₄	n-dopant	Novald AG	-	-	4.8 ^l	-
AOB	n-dopant	Sigma Aldrich	-	-	5.0	-

Table 2.1: Overview of materials used in this work and important properties thereof. Unless indicated otherwise, the physical values have been measured at IAPP. [a] profilometer measurement, [b] estimated, [c] XRR measurement, [d] Born et al.^[156], [e] from onset of absorption spectrum, [f] UPS measurement, [g] cyclic voltammetry measurement, [h] Gao et al.^[75], [i] Zhao et al.^[49], [j] Barlow et al.^[150], [k] Chan et al.^[35], [l] Cotton et al.^[52], [m] Tung et al.^[157].

requirements for charge transport materials according to the p-i-n concept, their electrical properties are insufficient. As doping with either AOB or NDN1 did not result in an increased conductivity, the materials would only introduce a large ohmic resistance to the device rather than to assist electron injection or extraction. Two of the materials, Bu-Fl-DAB and $(\text{BuFl})_2\text{-B}_{10}\text{C}_2\text{H}_{10}$, even degraded when they were exposed to ultraviolet radiation during the UPS measurement.

2.2 Sample Preparation

All samples are prepared by thermal evaporation of the organic substances under high or ultra-high vacuum. For this, different evaporation systems are used: the „UFO 1“, a multi-chamber evaporation tool (Bestec, Germany), and two „Lesker“ systems (K. J. Lesker, UK), each composed of one large vacuum chamber. Before discussing the peculiarities of both tools, common features will be described. The base pressure of the vacuum systems is always kept below 10^{-8} mbar. During evaporation of organic materials or metal this value can increase to a maximum of 10^{-6} mbar. The evaporation sources consist of a ceramic crucible which is surrounded by a heating wire made of tungsten and an additional copper shielding. The temperature can be measured and controlled by means of a Ni/CrNi thermocouple which is in contact with the bottom of the ceramic crucible and connected to a Eurotherm temperature control unit (models 2416, 2416e and 2408 in UFO 1 and Mini8 in Lesker). Metals are evaporated from ceramic (aluminum) or tungsten crucibles (gold, silver). The layer thickness as well as the evaporation rate are controlled by quartz crystal microbalances (Deposition Monitor XTM/2, Leybold Inficon Inc. or Thickness/Rate Monitor STM-100/MF, Syncon Instrument) which are located between source and sample position. By applying this method, it is possible to accomplish a controlled co-evaporation of two materials as sketched in Figure 2.7. For organic materials, typical evaporation temperatures and rates are in the range of 60...450°C and 0.1...0.6 Å/s. All materials have been purified by vacuum gradient sublimation prior to being loaded into the vacuum tool. This step does not only avoid an unintentional contamination of other materials kept in the same vacuum chamber, but also reduces the amount of impurities potentially introduced into the organic layers.

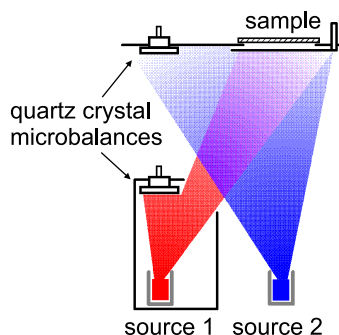


Figure 2.7: Co-evaporation of two organic compounds from separate evaporation sources. For both materials, the evaporation rate is determined individually by a quartz crystal monitor. Hence, a defined mixing ratio can be achieved.

Evaporation tool „UFO 1“

UFO 1 is a multi-chamber evaporation tool that is used to produce samples for an initial material analysis involving the characterization methods listed in Section 2.3.1. Additionally, first test solar cells are fabricated, here. The substrates are either made of plain glass or glass that is pre-coated with semitransparent ITO stripes and have a size of $(2.54 \times 2.54) \text{mm}^2$. Before being loaded to the evaporation tool, all substrates are cleaned using the cleaning procedure listed in Table 2.2a) and subsequently mounted into a Teflon sample holder. Pre-coated substrates, such as shown in Figure 2.8a), are used for solar cell fabrication. Usually, conducting silver paint is applied for establishing a good electric contact between the contacts at the sample holder and the ITO fingers. To dry the silver paint, the complete sample holder is heated up to 105°C for one hour in an oven. Although the major part of the sample preparation happens in the dust-free environment of a laminar flow box, in some cases it proves to be

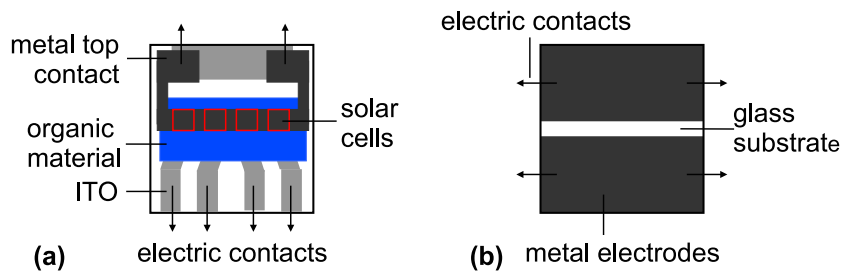


Figure 2.8: a) Configuration of a standard solar cell sample: organic layers (blue) and metal top contact (dark gray) are deposited onto a glass substrate that is pre-structured with semitransparent ITO contacts (light gray). The areas highlighted in red correspond to the intersection of ITO ground contact and metal top electrode. Here, we find the actual solar cell stacks. b) Substrate used for lateral conductivity measurements consisting of two metal electrodes, composed of either aluminum or gold deposited onto a clean glass substrate.

beneficial to treat the central part of the substrates surface additionally with the polymer First Contact (Optoprim, Germany), so as to remove residual dust particles.

Subsequently, the samples are transferred into the nitrogen atmosphere of a glovebox from where they can be loaded to the vacuum system. The tool consists of a central main chamber (Handler) from which the sample holders can be moved to several small vacuum chambers where the deposition of organic material or metal takes place. Furthermore, a storage chamber which can hold a total of 12 sample holders and a UPS / XPS analysis tool are accessible from the Handler chamber. Depending on the type of material that is to be deposited, i.e. photoactive material, ETM, HTM, or metal, different chambers are used for avoiding cross-contamination of donors or acceptors by dopants. All organic layers and the metal top contact are deposited through shadow masks. As there are four ITO fingers, using this substrate design results in four identical solar cells which are called *pixels* throughout this work.

Evaporation tool „Lesker“

Currently, there are two large custom-made single chamber vacuum systems in which all organic and metal sources are arranged in a circle below one large so-called *Lesker wafer* comprising 6x6 of the above described ITO-patterned substrates (see Figure 2.9a)). The cleaning procedure for these wafers is similar to the one used for the small UFO substrates and is listed in Table 2.2b). Inside the vacuum chamber, the wafer and respective shadow masks used for the controlled deposition of organic materials and metal contacts are rotating with a constant speed above the evaporation sources in order to achieve a homogeneous coverage. Additional shadow masks, called *wedges*, can be moved across the wafer from the sides and allow a selective deposition onto only one row or column. This way, it is possible to fabricate 6x6 different solar cell stacks in one run, i.e. under exactly the same conditions. In the Lesker A machine only the central part of the 6x6 wafer can be wedged which means that there is an output of 4x4 samples (these are still 64 solar cells) whereas in the Lesker B machine the full potential can be utilized. Furthermore, Lesker B allows heating the wafer during deposition up to 180°C. After the completion of the evaporation process, the substrate is being transferred to a nitrogen glovebox where the samples are encapsulated with a cover glass and a moisture getter by Dynic (Hong Kong, China) using UV-curing adhesive. Afterward, the wafer can be handled and measured in air.

The operation of the Lesker machines, cleaning of Lesker wafers and encapsulation of completed samples are performed by technicians from IAPP and Heliatek GmbH.

Doping

As already stated above, doping is performed by co-evaporation of the organic matrix material and the molecular dopant from two different crucibles (see Figure 2.7). All doping ratios referred to in this work are given in weight percent (wt%):

$$wt\% = \frac{m_D}{m_D + m_M} = \frac{\rho_D d_D}{\rho_D d_D + \rho_M d_M} \quad (2.1)$$

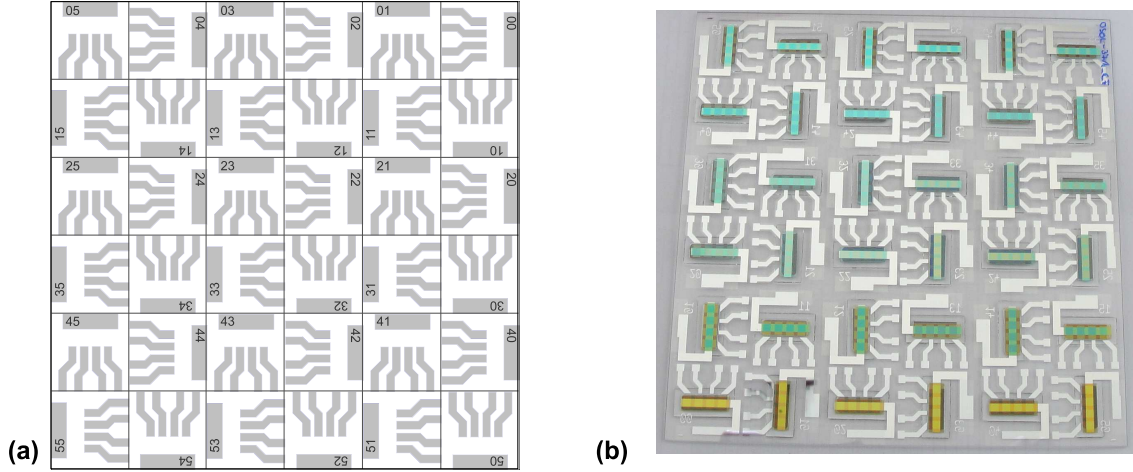


Figure 2.9: a) Design of a so-called Lesker wafer, a large glass substrate pre-coated with ITO which can be cut into 6x6 single substrates after production. By applying suitable shadow masks („wedging“) 6x6 different solar cell stacks can be produced in one Lesker run. b) Photograph of a complete Lesker wafer made in Lesker B.

cleaning step	time	cleaning step	time
ultrasonic bath: in NMP (methylpyrrolidone)	8min	ultrasonic bath: in NMP	20min
ultrasonic bath: in acetone	8min	rinsing in de-ionized water	5min
ultrasonic bath: in ethanol	8min	ultrasonic bath: de-ionized water	10min
ultrasonic bath: isopropanol	8min	ultrasonic bath: ethanol	10min
dry blowing with N ₂		spinrinser	15min
plasma cleaning in O ₂ plasma	10min	plasma cleaning in O ₂ plasma	10min

(a) UFO samples

(b) Lesker wafers

Table 2.2: Cleaning procedures used for glass and ITO substrates.

with $m_{D/M}$ being the mass per area, $\rho_{D/M}$ the respective density, and $d_{D/M}$ the correct thickness of dopant and matrix material. However, the densities of the dopants are usually not known which is why ρ_D is set equal to ρ_M , resulting in

$$wt\% = \frac{d_D^*}{d_D^* + d_M}. \quad (2.2)$$

This equation for the doping ratio contains only the exact thickness of the matrix material d_M and an effective dopant thickness d_D^* displayed by the quartz monitors. As $\rho_D \cdot d_D = \rho_M \cdot d_D^*$, equations (2.1) and (2.2) are equivalent and both give the exact doping ratio in weight percent.

2.3 Experimental Methods & Setups

2.3.1 Characterization of Single Layers

Optical properties

For evaluating the absorbance, single layers are deposited onto pre-cleaned quartz glass substrates. Reflection and transmission spectra are recorded either using a UV 3100 spectrometer (Shimadzu) that is able to cover a wavelength range from 200 to 900nm or a Lambda 900 transmission spectrometer (Perkin-Elmer) operating between 190 and a maximum of 3300nm. The optical density (absorbance) is then calculated by

$$OD(\lambda) = \log_{10} \frac{1}{T(\lambda)} \quad (2.3)$$

where T is the transmission of the thin film that is corrected for the transmission of the substrate. In doing so, we neglect any light scattering which might occur in the organic material or at the glass/organic interface.

For determining the optical constants $n(\lambda)$ (refraction index) and $k(\lambda)$ (extinction coefficient), reflection and transmission spectra of at least three single layers of different thickness are measured under normal incidence. The resulting curves are modeled with the program Multifit RT developed by R. Nitsche^[158] based on the work of T. Fritz^[159]. It works with a simple point-to-point method that does not involve any physical model and makes use of the Levenberg-Marquandt optimization algorithm.

Thin film density

The density of organic thin films is either determined by using a Dektak 150 surface profilometer (Veeco Instruments Inc.) or by x-ray reflectometry (XRR). The **profilometer** samples consist of a plain glass substrate that is only partially coated with the test material: Using a shadow mask, a sharp-edged step from the glass to the organic layer is created. As the diamond-tipped stylus can easily scratch the surface of the soft organic material when measuring the step height, the whole sample is additionally covered by a 70...100nm thick aluminum layer. By relating the step height d_{step} to the nominal thickness d_{nom} that is deposited using an assumed density ρ_{nom} , the real density ρ can be deduced by

$$\rho = \frac{\rho_{\text{nom}} d_{\text{nom}}}{d_{\text{step}}}. \quad (2.4)$$

Based on our experience with this method, the error for the film thickness larger than 10%.

For **XRR** measurements, approximately 50nm of the test material is deposited onto a plain glass substrate and subsequently measured under an angle of 0...5° (step width 0.01°, 30s per angle) using a HZG-4 (Seifert FPM) Bragg–Brentano x-ray reflectometer. The resulting reflectogram is evaluated with the program REFSIM* which is based on a recursive approach by Parrat^[160] and which considers the influence of the interface roughness following a model of Sinha et al.^[161]. This way, it is possible to determine film thickness, film roughness, and mass density of the organic material. Further details on the setup and the fitting routine are outlined by Schünemann et al.^[121]. The average error for the thin film density is 0.1g/cm³.

XRR measurements and data evaluation have been carried out by Christoph Schünemann.

Morphology

AFM. The topography of organic thin films is evaluated using an AFM Nanoscope IIIa (Digital Instrument, now Veeco Instruments Inc.) in tapping mode. For this purpose, NSC15 silicon tips (MikroMasch) with a stiffness in the range of 30...50N/m are used. All samples are prepared in UFO 1 and consist of a small $\sim (1 \times 1) \text{cm}^2$ glass substrate glued to a metallic sample holder using silver paint. The software WSxM is used for data analysis^[162].

XRD. For x-ray diffraction measurements, 100nm thick films of the test material are deposited onto a glass substrate covered with 10nm C₆₀. XRD patterns are recorded with an x-ray powder diffractometer URD-6 (Seifert FPM) in Bragg–Brentano geometry using Cu-K_α radiation that is monochromatized with a secondary graphite monochromator. The sample is rotated during the measurement in order to minimize the influence of the preferred orientation (texture) effect. The reflected radiation is recorded by a scintillation detector. Further details on the setup and the peak fitting routine are outlined by Schünemann et al.^[121].

GIXRD. Alternatively, some of the thin films are analyzed by grazing incidence x-ray diffraction. By using small incident angles that are fixed at $\omega < 1^\circ$ and scanning the scattered x-rays over a wide angular range, the penetration depth of the x-rays can be adjusted to be in the order of only a few nanometer. Due to the surface sensitivity of the method, the scattering volume and therefore the signal of the organic layer is increased whereas the background signal of the substrate is reduced. The interplane distance d is calculated by applying Bragg's law

$$n\lambda = 2d \sin \frac{2\theta}{2} \quad (2.5)$$

where n is an integer number, λ the wavelength of the incident wave, and 2θ is the scattering angle. The crystal size is determined using the program SizeCr which is based on the Scherrer formula and

* REFSIM, version 2.0, Bruker AXS GmbH (1999).

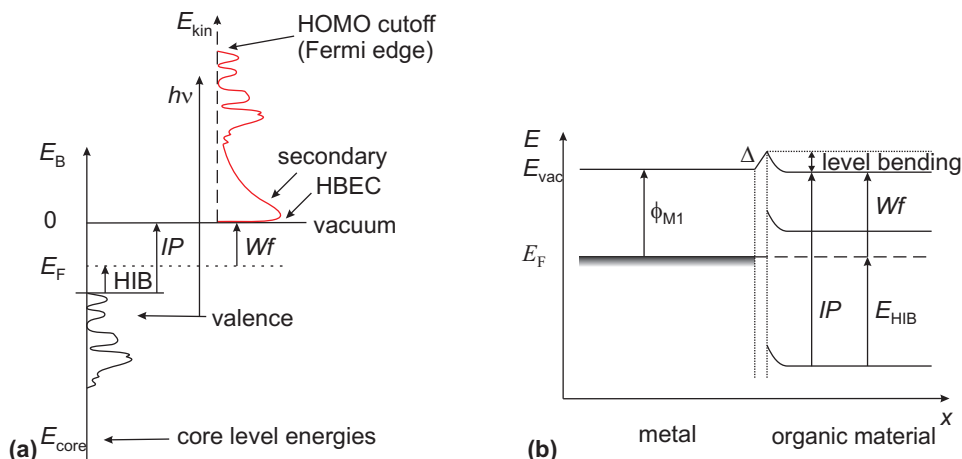


Figure 2.10: a) Principle of UPS (ultraviolet photoelectron spectroscopy): Exposing the surface of the organic sample to photons having the energy $h\nu$ leads to the photoemission of electrons. Electrons with a low binding energy E_B have a higher kinetic energy E_{kin} when they reach the detector. The distribution of kinetic energies detected in the analyzer resembles the density of valence states. Electrons coming directly from the Fermi edge have the highest kinetic energy and are assigned to the HOMO cutoff. The other end of the spectrum is characterized by a large background signal stemming from secondary electrons which lose a part of their kinetic energy due to scattering processes before leaving the sample surface. The point of zero kinetic energy is called high binding energy cutoff (HBEC). Furthermore, UPS gives access to measuring the hole injection barrier (HIB), the ionization potential (IP), and the work function (Wf) of the sample. b) Energy level scheme of an organic material on a metal substrate as it can be deduced from UPS spectra (scheme based on the behavior of an n-doped ETM on metal).

evaluates the full width half maximum of the Bragg peaks^[163]. Finally, the attenuation depth t of the x-rays into the organic material is determined using Henke code^[164]. The analysis of Bis-HF1-NTCDI thin films is carried out at PANalytical in Almelo (Netherlands) using an Empyrean thin film diffractometer that works with Cu- K_α radiation. The scattering signal is recorded with a PIXcel-3D area detector. HATNA-Cl₆ thin films are measured at Fraunhofer CNT (Dresden, Germany) utilizing a Bruker D8 Discover diffractometer in GIXRD scan mode. It operates with a Göbel mirror and Cu- K_α radiation in combination with a scintillation detector^[126].

AFM, XRD and GIXRD are performed in ambient conditions. The influence of oxygen and water on topography and crystallinity is unknown, and hence an impact on the results cannot be excluded. XRD measurements at IAPP have been carried out by Christoph Schünemann (IAPP) while the GIXRD measurements were either performed by Alexandr Levin (IAPP) at PANalytical or by Lutz Wilde (Fraunhofer CNT).

Photoelectron spectroscopy

Photoelectron spectroscopy (PES) is a surface sensitive technique that is used for obtaining information about the electronic structure of a sample and its chemical composition. It is based on the external photoeffect which describes the emission of electrons from the sample surface upon photoexcitation and was explained by Einstein in 1905. Depending on the energy of the photons, either the density of occupied valence states or the core levels of the atoms which form the organic solid is probed.

UPS (ultraviolet photoelectron spectroscopy) uses the He I excitation line (21.22eV) of a helium discharge lamp (UVS10/35, Specs) for creating photoelectrons in the sample surface. At this particular excitation energy, electrons residing in the upper 2...3 monolayers^[165] are able to escape from the solid with a certain kinetic energy E_{kin} that depends on the initial binding energy E_B . In order to collect all photoelectrons, an additional bias voltage of $-8V$ is applied between sample and analyzer (Phoibos HSA 100, Specs). As depicted in Figure 2.10a), the distribution of kinetic energies detected in the analyzer resembles the density of occupied valence states. Electrons coming directly from the Fermi edge have the highest kinetic energy and are assigned to the *HOMO cutoff* position in case of organic semiconductors. In case of metallic samples, the cutoff position directly corresponds to the metal work function. Electrons with very low kinetic energy have either been very tightly bound or lost a part of their initial energy due

to multiple inelastic scattering processes. Such electrons cause a large background signal that starts at $E_{\text{kin}} = 0\text{eV}$, the so-called *high binding energy cutoff* (HBEC), and decays towards higher E_{kin} . In order to evaluate the cutoff positions as accurately as possible, HBEC and HOMO cutoff region are additionally scanned using a smaller step width and a lens setting that allows for a better resolution. The error that is made when determining the cutoff positions is estimated to be $\pm 50\text{meV}$ for our setup.

Other than in Figure 2.10a), the UPS spectra are commonly not given on a kinetic energy scale, but the abscissa is converted to binding energies E_{B} . The test materials are evaporated onto a metallic substrate. As there will be Fermi level alignment between the metal and the organic layer, it is common practice to take the Fermi edge E_{F} of this substrate as zero point of the energy. The following parameters can be determined by UPS: The work function Wf of the sample is given by

$$Wf = h\nu - E_{\text{HBEC}} \quad (2.6)$$

where h is Planck's constant and ν the frequency of the UV light. The difference between the Fermi energy and the HOMO cutoff E_{HOMO} is identified with the hole injection barrier (HIB):

$$E_{\text{HIB}} = E_{\text{F}} - E_{\text{HOMO}}. \quad (2.7)$$

Finally, the ionization potential IP is determined by subtracting the width of the spectrum from the incident photon energy

$$IP = h\nu - (E_{\text{HBEC}} - E_{\text{HOMO}}). \quad (2.8)$$

For metals, the ionization potential is equal to the work function. While the absolute IP is calculated with an accuracy of 0.1eV , relative values obtained for a series of similar measurements can be given reliably with two significant digits.

The assumption of vacuum level alignment at metal/semiconductor or semiconductor/semiconductor interfaces that is often made for inorganic systems does not necessarily hold true in case of interfaces involving organic semiconductors^[96,97,166,167]. Here, the occurrence of interface dipoles needs to be taken into account. At metal organic interfaces, such an interface dipole Δ is seen as an abrupt shift in the HBEC position and is calculated by

$$\Delta = E_{\text{HBEC}}^{\text{metal}} - E_{\text{HBEC}}^{\text{organic}}. \quad (2.9)$$

Energy level schemes such as depicted in Figure 2.10b) can be deduced from the evaluation of UPS data. The scheme resembles the behavior of an n-doped material on top of a metal substrate. For determining the level bending, i.e. for obtaining a depth profile, many thin layers have to be deposited in a stepwise manner.

Similar to UPS, XPS (x-ray photoelectron spectroscopy) can also give information about level bending. However, its main purpose is to determine the chemical composition of a material. Instead of UV photons, it uses the $K_{\alpha 1/2}$ radiation of an aluminum cathode (soft x-ray source XR50, Specs) which has a much larger energy of 1486.6eV and therefore allows probing the localized core levels of the atoms. Due to the higher radiation energy, the probing depth is in the order of $8\text{...}10$ monolayers which is slightly larger than that of UPS. As core level electrons have well defined and characteristic binding energies, the XPS spectrum will consist of several distinct peaks that can be assigned to the elements which make up the organic molecules. Chemical shifts can occur when there are bonds between non-equivalent atoms, for instance a carbon-carbon bond can be distinguished from a carbon-nitrogen bond. In such a case, multiple peaks are observed which usually overlap. By relating the total peak areas for certain elements to each other, it is possible to draw conclusions on the stoichiometric ratio of molecules that make up the organic compound under investigation. Peak shifts upon multilayer deposition can be correlated to level bending processes. The evaluation of XPS results is done by fitting the characteristic peaks by a line shape that can be described as a convolution of a Gaussian and a Lorentzian function using the program XPSPEAK4.1*.

The PES chamber is directly connected to the UFO 1 system which allows the analysis of a large variety of materials or even layer stacks without breaking the vacuum. That way, the base pressure of the UPS/XPS chamber can be constantly held below 10^{-9}mbar . All UPS and XPS measurements were assisted either by Selina Olthof or Max Tietze.

* XPSPEAK4.1, written by Raymond Kwok, University of Hong Kong (2000).

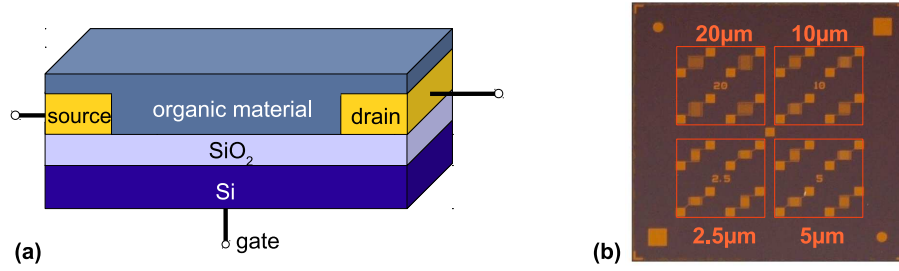


Figure 2.11: a) Typical bottom gate OFET sample using a silicon / silicon dioxide substrate as gate electrode and pre-deposited gold contacts as source and drain electrodes. b) Design of an OFET chip as delivered from Fraunhofer IPMS. The chip contains four bottom gate OFET structures for each of the four channel widths 2.5, 5, 10, and 20 μm .

Cyclic voltammetry

Cyclic voltammetry (CV) is used to examine the electrochemical properties of a substance in solution. For this, the organic material is dissolved in a suitable solvent like dichloromethane or acetonitrile in the presence of a conducting salt. The cyclic voltammogram is recorded with an m-Autolab potentiostat (Metrohm) in a single-component cell having a typical three electrode configuration. An inlaid platinum disk serves as working electrode, a platinum wire as counter electrode and a silver rod coated electrochemically with AgCl constitutes the reference electrode. All potentials are referenced to ferrocene/ferrocinium (Fc/Fc⁺) as internal redox standard^[168]. For correlating the measured reduction and oxidation potentials to solid state electron affinities and ionization potentials, the compounds half cell potentials $E_{1/2}^0$ versus ferrocene are often simply subtracted from the solid state ionization energy of ferrocene that is commonly referenced as 4.8eV^[169]. However, it was shown that a plain one-to-one correspondence between shifts in the redox potentials and the solid state energy levels is not valid. Instead, the empirical relationships

$$IP = (1.4 \pm 0.1) \cdot eE_{1/2}^0 + (4.6 \pm 0.1)\text{eV} \text{ and} \quad (2.10)$$

$$EA = (1.19 \pm 0.08) \cdot eE_{1/2}^0 + (4.78 \pm 0.17)\text{eV} \quad (2.11)$$

were found by D'Andrade et al.^[169] and Djurovich et al.^[19]. That way, it is possible to estimate the thin film energy levels of our test compounds which is particularly important concerning the electron affinity as we have no access to a direct measuring method for determining the thin film value. However, it has to be noted here that all CV results have to be handled with care as thin film effects are not taken into account.

The cyclic voltammetry measurements have been carried out by Dr. Markus Hummert.

Lateral conductivity

For testing the effect of doping on the lateral conductivity of our ETM matrix materials, we prepare a substrate according to the design depicted in Figure 2.8b): Prior to the deposition of the organic layer, a plain glass substrate is pre-coated with two metal electrodes either made of gold or aluminum. It comprises a metal-free channel of $(1.3 \pm 0.1)\text{mm}$ width that is created by using a homemade shadow mask during metal evaporation. By applying an external bias voltage of 10V between these electrodes, the lateral current can be measured in situ while co-depositing dopant and ETM. The corresponding lateral conductivity σ is evaluated by

$$\sigma(\text{S/cm}) = \frac{b \cdot I}{d \cdot l \cdot V} = \frac{1.3\text{mm}}{25\text{mm} \cdot 10\text{V}} \cdot \frac{I(\text{A})}{d(\text{nm})} \cdot 10^7 \quad (2.12)$$

with b being the width of the channel, I the lateral current, d the layer thickness, l the length of the channel, and V the external voltage. This way, it is possible to monitor the conductivity depending on layer thickness and doping ratio during layer fabrication in vacuum.

Mobility

All mobilities given in this thesis are field effect mobilities determined with bottom gate organic field effect transistors (OFET) having an n-Si/SiO₂ substrate working as gate and insulating layer with a

capacitance of 14.6nF/cm^2 . Gold source and drain contacts having a thickness of 30nm are deposited onto this kind of substrate. They form an interdigitating electrode structure with a channel width of 10nm and a channel length varying between $2.5, 5, 10, \text{ and } 20\mu\text{m}$. The OFET substrates are provided by Fraunhofer IPMS, pre-cleaned according to the procedure given in Table 2.2a), and subsequently transferred to the UFO 1 vacuum system where a single organic layer of $30\text{--}50\text{nm}$ thickness is deposited. Figure 2.11a) shows a schematic cross section of such a sample while in Figure 2.11b) the complete OFET chip is displayed in top view. In total, there are four OFET structures for each of the channel lengths.

The OFET characterization is performed at room temperature in nitrogen atmosphere using two Keithley source measurement units (SMU), one Keithley 2611A for the source/drain contacts and one Keithley 2400 for the gate contact. By changing the gate voltage V_G , the charge carrier density at the interface to the insulating layer is varied. When a certain threshold voltage V_{th} is exceeded, the accumulated free charge carriers create a conducting channel between source and drain electrode. The current $I_{\text{SD}}(V_{\text{SD}}, V_G)$ flowing through this channel is limited by the mobility and the transistor geometry. At small source-drain voltages $V_{\text{SD}} \ll V_G$, the current is directly proportional to V_{SD} – this regime is called linear regime. The source-drain current is given by

$$I_{\text{SD}} = \frac{W}{L} C \mu \left((V_G - V_{\text{th}}) V_{\text{SD}} - \frac{1}{2} V_{\text{SD}}^2 \right) \quad (2.13)$$

with W and L being channel width and length, C the capacitance per area, and μ the charge carrier mobility. When V_{SD} approaches $(V_G - V_{\text{th}})$, the conducting channel is narrowed close to the drain electrode as a result of the increased potential gradient. Finally, the channel is „pinched off“ and further enhancements of V_{SD} do not increase the source-drain current any more – the OFET is in saturation regime. Here, I_{SD} is given by

$$I_{\text{SD}} = \frac{W}{2L} C \mu (V_G - V_{\text{th}})^2. \quad (2.14)$$

For determining the mobility, we evaluate the saturation regime and measure the source-drain current $I_{\text{SD}}(V_{\text{SD}})$ for different gate voltages and using different OFET channel lengths.

OFET measurements and data evaluation have been carried out by Moritz Hein and Jens Jankowski.

2.3.2 Characterization of Devices

All solar cells shown in this work have been encapsulated immediately after production under nitrogen atmosphere and are characterized under ambient conditions.

Current-voltage characteristics

For determining the jV -characteristics of whole Lesker wafers, an automated setup (LIV robot) is used. The samples are either measured under dark conditions or illuminated under simulated sunlight (simulator 16S-003-300-AM1.5, Solarlight Company Inc.) that is incoupled by an optical fiber. The overall illumination intensity is determined with a calibrated silicon reference diode (Hamamatsu 1337-33BQ) prior to each measurement run. jV -curves are recorded with a step width of 0.05V in the range between -1.0V to 1.5V using a Keithley SMU 2400. The effective device area, which is necessary for calculating the current density, is determined by measuring the short circuit current I_{sc} by means of a shadow mask and relating it to I_{sc} of the unmasked device. Having an area of 5.1mm^2 , the size of the aperture is close to the actual overlap area between ITO anode and aluminum cathode of 6.44mm^2 . As the shaded regions act as large parallel resistance affecting the device performance, all jV -characteristics and accordingly V_{oc} , FF , and saturation are measured without aperture.

The characteristic curves of all 4 devices located on one sample are very similar, yielding relative errors (standard deviation relative to the mean value) smaller than 5% for all of the solar cell parameters. Considering a 6×6 Lesker wafer with identical solar cell stacks on each substrate, the relative errors for the characteristic parameters are 1% for V_{oc} , 5% for j_{sc} , 3% for the fill factor, 1% for the saturation, and 4% for the power conversion efficiency η – i.e. again the errors for most of the parameters are equal to or below 5%. These errors only describe the comparability of solar cells on one Lesker wafer and do not account for systematic errors of the measurement.

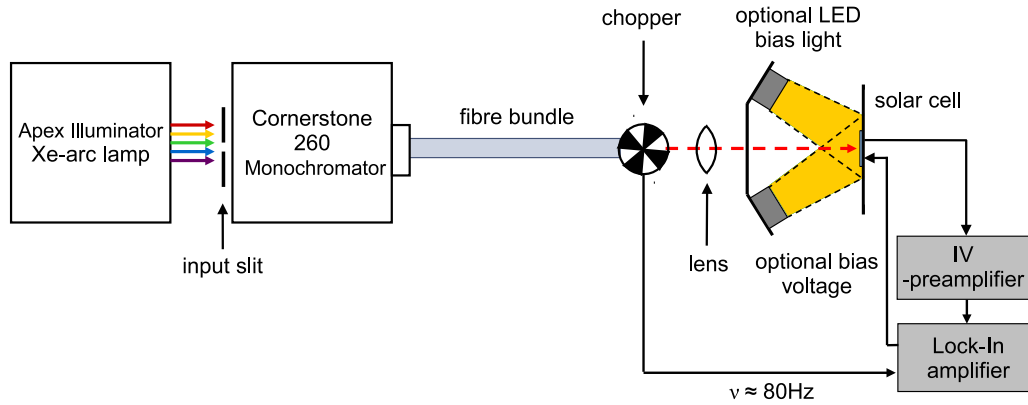


Figure 2.12: Setup for measuring the external quantum efficiency ($EQE(\lambda)$). Light coming from a xenon arc lamp is first monochromatized and subsequently chopped at a frequency of 80Hz before being focused either onto the solar cell or a silicon reference diode. The sample's response, i.e. the resulting photocurrent is detected by a lock-in amplifier. There is the option to apply an additional bias illumination with white or colored LEDs or to apply a bias voltage. Illustration following reference [170].

Spectral response and external quantum efficiency

The external quantum efficiency (compare Section 1.2.2) is determined using a home built setup schematically displayed in Figure 2.12. Light emitted by a xenon arc lamp is monochromatized and chopped with a frequency of 80Hz before being focused onto the sample position where either a silicon reference diode or the test solar cell is mounted. A lock-in amplifier is used for detecting the spectral response of the sample in the wavelength region between 300 and 900nm which is scanned with a step width of 5nm and applying a shadow mask with an aperture of 2.96mm². The spectral response $SR(\lambda)$ is defined as the current generated per incident illumination intensity at a certain wavelength λ and is given in A/W. It can be converted to the external quantum efficiency $EQE(\lambda)$ by

$$EQE(\lambda) = \frac{hc}{e\lambda} \cdot SR(\lambda) \quad (2.15)$$

with h being the Planck constant, c the speed of light, and e the elementary charge. Assuming that the EQE is absolute, it is possible to recalculate the short circuit current density of the test cell by multiplying the spectral response with the incident illumination spectrum and subsequently integrating over the accessible spectral range

$$j_{TC}^{sim} = \int_{\lambda_1}^{\lambda_2} SR(\lambda) \cdot E_{sim} d\lambda. \quad (2.16)$$

Here, E_{sim} is the spectral irradiance of the sun simulator. Likewise, the current density of the test cell under a hypothetical AM1.5 illumination can be calculated by

$$j_{TC}^{AM1.5} = \int_{\lambda_1}^{\lambda_2} SR(\lambda) \cdot E_{AM1.5} d\lambda. \quad (2.17)$$

As those calculations are limited to the measuring range of the EQE setup and as absolute EQE values are in most cases only an assumption, there will be deviations to the values which would be obtained by direct measurements of the jV -curves.

Mismatch factor

For ensuring the comparability of device performances, it is important to follow standardized measurement conditions as closely as possible^[171,172]. The so-called standard testing conditions (STC) or standard reporting conditions (SRC)^[88], which are used by authorized institutions for certifying solar cells, give a set of specifications including

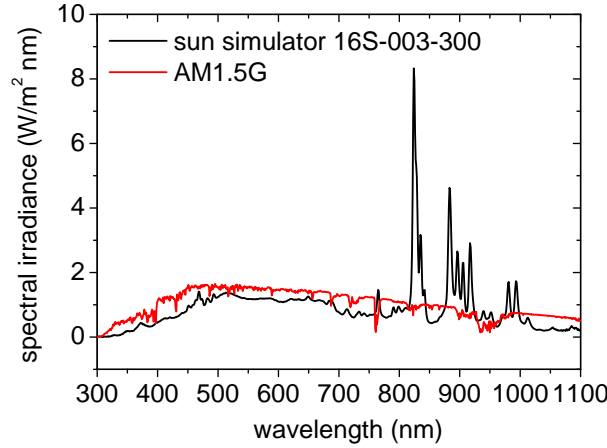


Figure 2.13: Illumination spectrum of the sun simulator 16S-003-300 normalized to an intensity of $100\text{mW}/\text{cm}^2$ in the given wavelength range of 300 to 1100nm in comparison with the standardized AM1.5G spectrum.

- a sample temperature of 25°C ,
- an illumination intensity of $100\text{mW}/\text{cm}^2$,
- and the use of a defined reference illumination spectrum. Here, the AM1.5G spectrum which is the ideal solar spectrum after traveling through 1.5 times the atmospheres thickness (corresponding to a solar zenith angle of 48.2°) is chosen. It is shown in Figure 2.13 together with the spectrum of the light emitted by our sun simulator.

The spectral mismatch between those two illumination sources has to be accounted for when calculating the efficiency of solar cells. Furthermore, the spectral responses of the test cell, i.e. the organic solar cell comprising narrow band organic absorbers and the silicon reference diode are different. The error can be expressed by the so-called *mismatch factor* M which is defined by

$$M = \frac{j_{\text{ref}}^{\text{AM1.5}}}{j_{\text{ref}}^{\text{sim}}} \cdot \frac{j_{\text{TC}}^{\text{sim}}}{j_{\text{TC}}^{\text{AM1.5}}}, \quad (2.18)$$

i.e. by relating the short circuit current densities of test cell and reference diode obtained when using either the simulated or the standardized AM1.5G illumination source. These currents can be calculated by convoluting the spectral response $SR(\lambda)$ of each device and the respective illumination spectrum. For instance we find the current of our reference diode under AM1.5G to be

$$j_{\text{ref}}^{\text{AM1.5}} = \int SR_{\text{ref}}(\lambda) \cdot E_{\text{AM1.5}} d\lambda \quad (2.19)$$

$$= 0.785\text{mA}. \quad (2.20)$$

Having determined the spectral response of the test cell $SR_{\text{TC}}(\lambda)$ with the EQE setup and knowing $SR_{\text{ref}}(\lambda)$ from a datasheet, M can easily be calculated by

$$M = \frac{\int SR_{\text{ref}}(\lambda) \cdot E_{\text{AM1.5}} d\lambda}{\int SR_{\text{ref}}(\lambda) \cdot E_{\text{sim}} d\lambda} \cdot \frac{\int SR_{\text{TC}}(\lambda) \cdot E_{\text{sim}} d\lambda}{\int SR_{\text{TC}}(\lambda) \cdot E_{\text{AM1.5}} d\lambda}. \quad (2.21)$$

In the ideal case, the mismatch factor is determined prior to the jV -measurement and can then be used to adjust the intensity of the solar simulator to a value for which the photocurrent produced by the organic test cell corresponds to the current it would generate under an AM1.5G illumination, i.e. $j_{\text{ref}}^{\text{sim}} = j_{\text{TC}}^{\text{AM1.5}}$. As can be seen from equation (2.18), this condition is fulfilled as soon as the reference diode produces a current of

$$j_{\text{ref, corr}}^{\text{sim}} = \frac{j_{\text{ref}}^{\text{AM1.5}}}{M}. \quad (2.22)$$

The corresponding, nominally measured intensity I_{corr} is determined by multiplying this current with the calibration factor c of the solar simulator and yields

$$I_{\text{corr}} = c \cdot j_{\text{ref, corr}}^{\text{sim}} = c \cdot \frac{j_{\text{ref}}^{\text{AM1.5}}}{M}. \quad (2.23)$$

Under such conditions the simulated intensity mimics the AM1.5G specifications and the whole jV -curve is measured mismatch corrected. As the mismatch factor strongly depends on the composition of the sample and is thus sensitive not only to the choice of materials, but also to layer thicknesses, the reference current has to be adjusted individually for each sample on a 6x6 or 4x4 Lesker wafer. However, for reasons of practicability, all solar cells presented in this work are measured using only one reference intensity $I_{\text{ref}}^{\text{sim}}$ for all devices. Depending on the mismatch factor M , this intensity corresponds to an effective intensity

$$I_{\text{eff}} = I_{\text{ref}}^{\text{sim}} \cdot M \quad (2.24)$$

$$= c \cdot j_{\text{ref}}^{\text{sim}} \cdot M \quad (2.25)$$

which is close to the mismatch corrected intensity for most devices. When discussing the results, I_{eff} will be listed along with the characteristic parameters. It is used to calculate the mismatch corrected efficiency

$$\eta = \frac{j_{\text{sc}} \cdot V_{\text{oc}} \cdot FF}{I_{\text{eff}}}. \quad (2.26)$$

All efficiencies and all intensities given in this work are mismatch corrected according to the procedure presented above. Due to technical reasons measuring at 25°C is not always possible, however, the deviation from this standard is kept as small as possible.

Optical simulations

Optical simulations are performed using a numerical algorithm^[173] based on the transfer matrix approach and Poynting vector computation^[174]. The input parameters of the model are the complex refractive indices of the materials constituting the organic solar cell^[159], as well as the layer thickness. The model is purely optical and can be used for calculating the distribution of the optical field within the layer stack, the photon absorption in each layer, and thus the maximum achievable photocurrent by assuming an IQE of 100%^[118,175]. As input for the simulation we use the sun spectrum of our solar simulator at the intensity that was used for the measurements. The optical simulation can not be performed in the whole spectral range of the illumination source because the optical constants of many materials are only available in a wavelength range from 350 to 800nm. Furthermore, the influence of dopants is mostly omitted, because the n & k values of many doped layers are currently unknown.

The simulation program OSOLemio, utilized in this work, was developed at the IAPP by Mauro Furno^[173].

Impedance spectroscopy

Impedance spectroscopy (IS) measures the dielectric properties of materials by applying an AC signal to the sample and detecting its response. By this, it can give access to dynamic properties of the electrical processes of complete OSC. Depending on the frequency f of the alternating input voltage

$$V(t) = V_{\text{bias}} + V_s \sin(2\pi f \cdot t), \quad (2.27)$$

the resulting current is phase shifted and a complex impedance

$$Z = \hat{R} + i\hat{X}, \quad (2.28)$$

with \hat{R} being the ohmic resistance and \hat{X} the reactance, arises. There are basically two measurement modes for evaluating the behavior of \hat{R} and \hat{X} : Either the frequency is varied while keeping a constant bias voltage V_{bias} (C - f -characteristics) or the bias voltage is changed while maintaining a constant frequency (C - V -characteristics). Here, C denotes the capacitance function which accounts for the fact that the data can be described by one single RC parallel circuit in most of the investigated frequency range. Figure 2.14 displays the equivalent circuit which is chosen to represent a typical organic solar cell and the related $C(f)$ and $R(f)$ curves. The circuit consists of one RC -element that describes the intrinsic

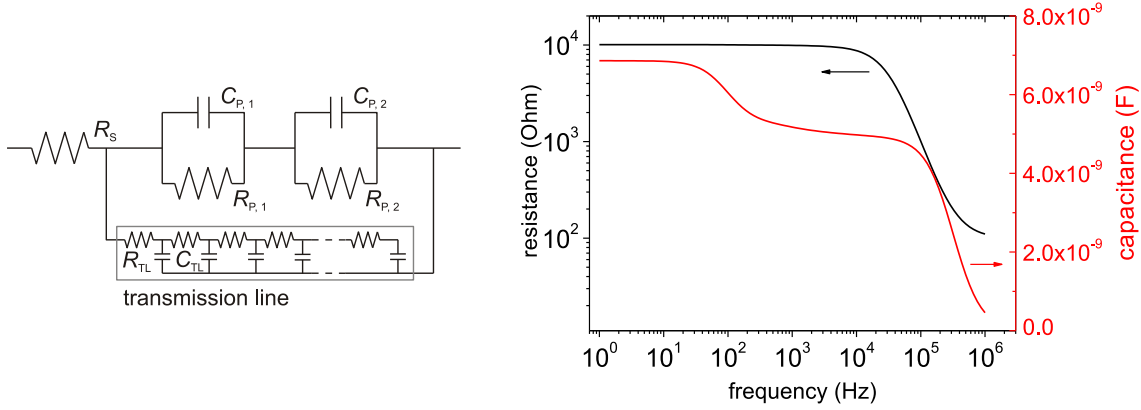


Figure 2.14: Example of a $C(f)$ and an $R(f)$ impedance spectrum for a typical equivalent circuit representing an organic solar cell using $R_S = 100\Omega$, $R_P = 10k\Omega$, $C_P = 5nF$, $R_{TL} = 2M\Omega$, and $C_{TL} = 2nF$.

photoactive layer, a series resistance R_S which mainly accounts for the resistance of the contacts, and a so-called transmission line which represents traps within the organic medium having a certain energy distribution^[176]. Within the given frequency range of 1MHz to 1Hz, only the intrinsic or nearly intrinsic layers dominate the device response. Thus, the main RC -element gives the geometric capacitance of the photoactive layers. The following general equations can be applied for calculating capacitance and resistance functions:

$$C(f) = - \frac{\hat{X}}{2\pi f(\hat{X}^2 + \hat{R}^2)} \quad (2.29)$$

$$R(f) = \frac{\hat{X}^2 + \hat{R}^2}{\hat{R}}. \quad (2.30)$$

In a frequency range which is dominated by one RC -element, $C(f)$ and $R(f)$ plots show a plateau. The capacitance of the plateau can be used to estimate the thickness of the layer which is represented by this RC -element by

$$d = \varepsilon\varepsilon_0 \frac{A}{C} \quad (2.31)$$

where A is the device area, ε is the relative permittivity of the respective material, and ε_0 is the dielectric constant. For describing the intrinsic layers composed of ZnPc and C_{60} we use a relative permittivity of $\varepsilon = 5^*$. For very high frequencies (in our example $> 10^5\text{Hz}$), the series resistance of the device becomes dominant while at low frequencies (in our example $< 10^2\text{Hz}$) an additional contribution of trap states might be observed.

By analyzing the bias voltage dependence of the geometric capacitance plateaus in a so-called Mott-Schottky diagram, which plots $1/C^2$ over V_{bias} , it is possible to evaluate the density of ionized molecules N_{ion} within the layer that is assigned to this specific plateau by^[34]

$$N_{\text{ion}} = \frac{2}{e\varepsilon\varepsilon_0} \left[-\frac{d(1/C^2)}{dV} \right]^{-1}. \quad (2.32)$$

Here, e is the elementary charge.

The IS measurements are performed in dark at room temperature using either a HP4284A LCR meter (for HATCN devices, see Chapter 3) or an Autolab PGSTAT302N (for Bis-F1-NTCDI devices, see Chapter 4, and for devices produced for ageing experiments, see Chapter 7). Depending on the measurement setup, the input AC signal V_s has an amplitude of 25mV or 15mV (rms) and the frequency can be varied between 1MHz and 100Hz or between 1MHz and 0.1Hz, respectively. The bias voltage is chosen within the range of -2.5V to 1.5V .

The impedance measurements at the Autolab system and data evaluation have been carried out by Lorenzo Burtone.

* Determined at IAPP by Lorenzo Burtone.

Lifetime

The devices are aged in a home built setup which has been developed in cooperation with Heliatek GmbH (Dresden, Germany). Here, the solar cells are kept at a constant temperature while being illuminated with LEDs emitting a broad white spectrum (LUXEON LXX2-PWC4-0220, 400...700nm, Philips). For ageing solar cells with different ETM, we choose a temperature of $(50 \pm 5)^\circ\text{C}$. The light intensities at the pixel positions are adjusted in a way that the initial short circuit current of pixel 1 is twice the value determined under one sun $I_{sc,0}^{P1} = 2 \cdot I_{sc}^{1\text{sun}}$ while for pixel 4 an intensity of 5 suns is chosen $I_{sc,0}^{P4} = 5 \cdot I_{sc}^{1\text{sun}}$. Each solar cell is connected to a load resistor of $2\text{k}\Omega$ and is thus operated close to the maximum power point. Changes in device performance are monitored by recording a jV -curve every two hours and extracting the development of all characteristic parameters as a function of time.

The lifetime of an organic solar cell is defined as the time it takes for the efficiency to decay to 80% of its initial value^[177]. This time t_{80} is evaluated by fitting the decay curve by a stretched exponential function of the general expression

$$\eta_{80} = A \cdot \exp \left[- \left(\frac{t}{\tau} \right)^\beta \right] \quad (2.33)$$

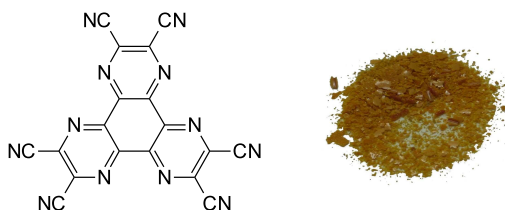
and extracting

$$t_{80} = -\tau \left(\ln \frac{0.8}{A} \right)^{1/\beta}. \quad (2.34)$$

with A , τ and β being fit parameters^[76].

The lifetime measurements were performed by Martin Hermenau.

3 HATCN - The Effect of Electron Injection Barriers and their Suppression by Doping



This Chapter introduces the material hexaazatriphenylene hexacarbonitrile (HATCN) as potential electron transport material for organic p-i-n type solar cells. The first focus will be on the characterization of its basic physical properties like thin film density, absorption, morphology, and energy level positions. Special attention will be paid to methods for estimating the electron affinity as this value is particularly important concerning the n-doping efficiency and their electron injection and extraction at the acceptor / ETM interface. It will be shown that HATCN has an exceptionally large EA. The second part deals with the impact of this finding on the solar cell performance and presents a strategy to remove the resulting transport barrier by means of doping.

3.1 Characterization

As described in Chapter 2, HATCN is strongly electron accepting which makes the material a promising candidate for an application as ETM. The figure above shows once again the molecular structure along with a picture of the substance right after purification by vacuum gradient sublimation. The sublimation is performed at a temperature of $T_s = 290^\circ\text{C}$ and results in the formation of a yellowish powder. The following Sections describe the characterization of the materials thin film properties regarding its applicability in p-i-n type organic solar cells.

3.1.1 Basic Physical Properties

Thin film density

Knowing the thin film density of a material is a key issue for depositing organic layers with a well defined thickness. The density of HATCN is determined by means of a profilometer measurement* and yields $1.67\text{g}/\text{cm}^3$ which is a large value compared to the other organic compounds used in this work (see Table 2.1). As the profilometer setup has not yet been available at the beginning of this thesis, most layers were produced using an estimated density of $1.3\text{g}/\text{cm}^3$ and afterward corrected for the right value.

Optical density

Figure 3.1 shows the optical densities of HATCN and C_{60} thin films, both deposited onto quartz glass substrates, in comparison with the illumination intensity of the standardized AM1.5 sun spectrum. Contrary to C_{60} , HATCN is transparent in the visible range of the sun spectrum, i.e. in the wavelength range between 380 and 780nm. The optical energy gap can be calculated from the onset of absorption at 377nm corresponding to $E_g^{\text{opt}} = 3.3\text{eV}$. The absorption of the photoactive material C_{60} already starts

* Measurement performed by Felix Holzmüller, IAPP.

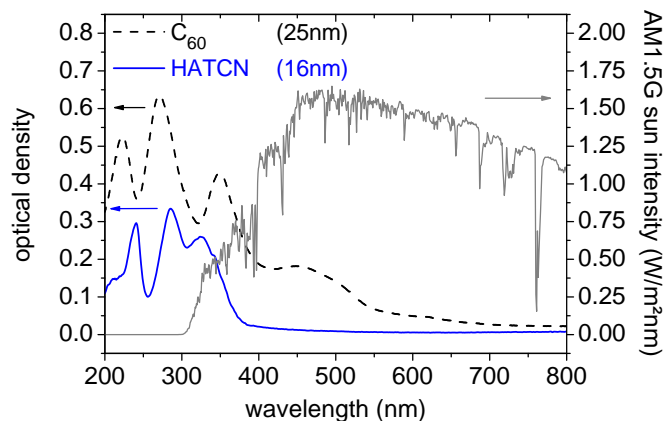


Figure 3.1: Optical density of HATCN in comparison with the optical density of C_{60} and the AM1.5G sun spectrum.

between 650 and 550nm while its main contribution to the photocurrent of a solar cell stems from the broad absorption band between 400 and 550nm. As HATCN does not show any parasitic absorption in this spectral region it is well suited as window layer in terms of the optical requirements of the p-i-n concept.

Morphology

Charge transport materials need to form smooth layers which do not necessarily have to be amorphous. Microcrystallinity can enhance the charge carrier mobility and thus improve charge transport if the current flow is in the same direction as the π - π stacking^[178–180] However, materials forming large crystallites or growing island-like cannot be easily incorporated into thin film stacks as their large surface roughness will influence the growth of all following layers. As demonstrated previously for the electron transport material NTCDA (1,4,5,8-naphthalenetetracarboxylic dianhydride)^[13,15], this problem can be circumvented by implementing the rough film as topmost layer below the metal electrode. NTCDA exhibits a prominent island growth resulting in films with a surface roughness in the range of 16nm. Hence, its application is limited to p-i-n type stacks while other layer sequences result in short circuits. Furthermore, predicting the thin film optics of layer stacks containing rough films is not trivial as there is neither a defined layer thickness, nor a smooth interface to the adjacent materials both of which is assumed in many optical models.

Figure 3.2 shows two AFM micrographs of the surface of a 12nm thin HATCN layer deposited onto a glass substrate. Additional to the standard cleaning procedure, the substrate is pretreated with the polymer „First Contact“ in order to remove residual dust particles. An influence of this treatment on the layer growth is excluded by examining an identical sample on a non-treated glass substrate (data not shown here). In each case, the surface exhibits a granular structure resulting in an average root mean

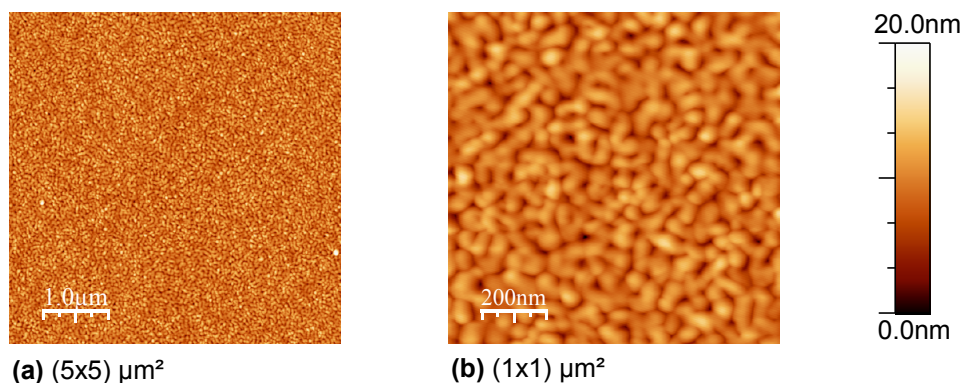


Figure 3.2: AFM images of the surface of a 12nm thin HATCN layer deposited onto a glass substrate.

square roughness of $(2.4 \pm 0.4)\text{nm}$. Though HATCN thin films are not absolutely smooth, the grains are small enough not to impede device fabrication. In Figure 3.2b), on a scale of $(1 \times 1)\mu\text{m}^2$, the formation of closed percolation pathways becomes apparent suggesting that a 12nm thin film is able to ensure a current flow in lateral direction. However, as there are some residual pinholes, it is advisable to use slightly thicker layers when applying HATCN as ETM in organic solar cells.

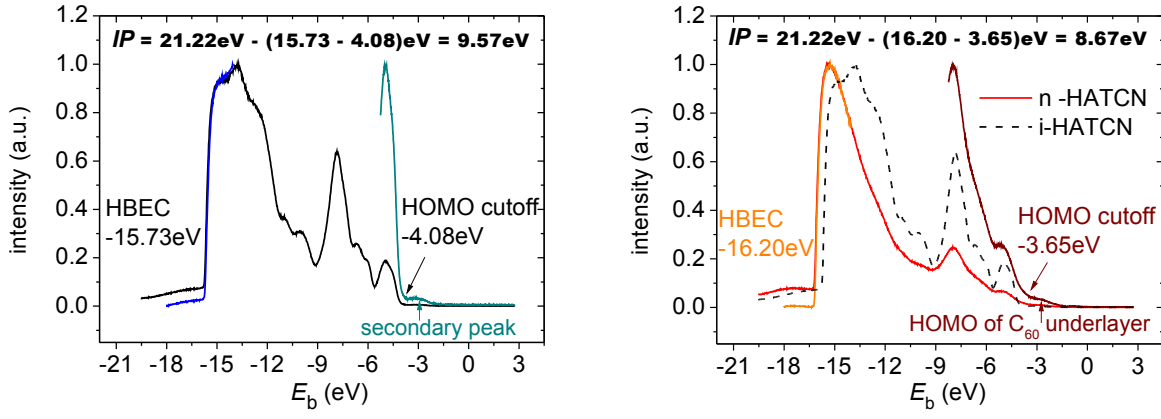
Conductivity

A sufficiently large conductivity is another important prerequisite for an ETM to work in a p-i-n configuration as presented in Chapter 2. According to equation (1.6) given in Section 1.1.2, the conductivity σ is proportional to the product of electron mobility μ_e and electron density n , both of which depend on the doping concentration. Concerning the mobility, there are different studies either showing a decrease^[181] or an increase^[28,64] of μ with increasing doping concentration. The latter effect is more commonly observed and generally explained by a gradual filling of low-mobility states or trap states in the tail of the Gaussian distribution of charge transport states^[28]. For a more detailed description, Arkhipov et al. suggest a model which additionally includes the counteracting effect of an increased energetic disorder and a broadening of the deep tail states of the DOS by the presence of dopants^[182]. The authors conclude that doping causes an increase of the mobility in strongly disordered systems with a comparably broad Gaussian DOS while it suppresses the mobility in weakly disordered systems which have an inherently narrow DOS. However, μ is not expected to decrease more quickly than with the inverse of the dopant concentration $(N_D)^{-1}$. Accordingly, the conductivity should increase upon doping even for materials with small DOS width. Indeed, it is shown, that the density of free charge carriers is strongly increased by the charge transfer taking place between dopant and matrix^[28,62,63,74]. As described in Section 1.1.3, the efficiency of this process is related to the electron affinity of the matrix material. For examining the doping effect in HATCN, the material is co-deposited with either 5wt% AOB or 7wt% NDN1 onto a standard conductivity substrate. To activate the cationic dopant AOB, the vacuum chamber is additionally illuminated with a 12V halogen lamp during evaporation^[62]. The conductivity is then evaluated from the lateral current according to equation (2.12) when applying an external bias voltage of 10V between the two predeposited gold electrodes. Doping with AOB or NDN1 results in maximum conductivities of $7.6 \cdot 10^{-6}\text{S/cm}$ or $2.2 \cdot 10^{-4}\text{S/cm}$, respectively. Compared to typical conductivities of intrinsic materials that are in the range of $10^{-10} \dots 10^{-8}\text{S/cm}$, both values correspond to an increase by several orders of magnitude. The former value of 10^{-6}S/cm is the lower limit considering the fabrication of efficient solar cells comprising thick doped layers ($> 100\text{nm}$). Thus, both dopants are sufficient to fulfill the demands of our solar cell structures. However, the use of NDN1 is preferred due to its better performance and its lower volatility. By evaluating the onset of the current flow in the in-situ measurements, the formation of closed percolation pathways at a layer thickness $> 10\text{nm}$ and the completion of closed layers at $> 17\text{nm}$ is confirmed. It has to be noted that the current flow in actual devices does not take place in the lateral direction studied by the conductivity measurements, but rather in the direction perpendicular to the substrate. Thus, the values given above can only be related to devices when the doped ETM is an isotropic medium.

Ionization Potential

As already pointed out in Chapter 2, the positions of the energy levels and particularly the adjustment of energy levels between neighboring layers is of particular importance for the device performance. The *IP* is determined directly by ultraviolet photoelectron spectroscopy which scans the valence states of a material*. Figure 3.3a) depicts the UPS spectrum of 9nm HATCN deposited onto a clean gold substrate. As neither the Au Fermi edge nor any of the characteristic gold valence features is visible, the formation of a closed layer can be assumed. The high resolution scan of the HOMO cutoff region reveals an additional peak at -2.1eV . By evaluating its energetic position with respect to the first HOMO peak, it is identified as secondary feature stemming from a satellite line of the helium discharge lamp having an excitation energy of 23.09eV , but only 2% of the illumination intensity of the original HeI excitation at 21.22eV . Hence, the small peak is only a representation of the original spectrum, shifted by 1.87eV towards lower binding energies. The *IP* is calculated by subtracting the width of the spectrum, determined by the difference between the actual HOMO cutoff $E_{\text{HOMO}} = -4.08\text{eV}$ and the high binding energy cutoff

* Measurement performed by Selina Olthof, IAPP.



(a) 9nm i-HATCN on a gold substrate.

(b) 10nm n-HATCN deposited onto a gold substrate covered with 12nm MeO-TPD (2wt%) and 8nm C₆₀.

Figure 3.3: UPS measurements of i-HATCN and n-HATCN. In each case, high binding energy cutoff and HOMO cutoff region have been scanned additionally with a smaller step width and a lens setting that allows for a better resolution.

HBEC = -15.73eV, from the HeI excitation energy

$$IP = 21.22\text{eV} - (15.73 - 4.08)\text{eV} \simeq 9.6\text{eV}. \quad (3.1)$$

Compared to other common organic materials this is an exceptionally high value^[19]. Consequently, the step in ionization energies at the C₆₀(IP = 6.4eV*)/n-HATCN interface is expected to be sufficiently large to allow for exciton blocking.

3.1.2 Estimation of the Electron Affinity

For ETM, the electron affinity EA is an even more important parameter than the ionization potential as it is not only related to the n-doping efficiency, but is also essential for achieving a barrier free electron extraction and injection from and into the device. More precisely, the electron transport levels at the interface between photoactive acceptor and ETM need to match which is in the simplest case achieved by equal electron affinities of acceptor and ETM. For HATCN, the EA values given in literature range from 3.5eV determined by DFT calculations^[183] to 5.7eV estimated by subtracting the optical energy gap from the UPS IP position^[133]. None of these numbers has been verified by a direct measurement method like inverse photoelectron spectroscopy (IPES). In the following, five approaches will be presented to further narrow down the given range to finally arrive at a reasonable estimation.

(1) **Optical gap.** When subtracting the optical gap of 3.3eV from the IP determined by UPS we need to consider the exciton binding energy E_B^{excit} which is the difference between the optical and the electrical energy gap of an organic semiconductor:

$$EA = IP - E_g^{\text{opt}} - E_B^{\text{excit}}. \quad (3.2)$$

According to Djurovich *et al.*^[19] who evaluated a large quantity of experimentally determined energy level values for many different organic materials, the electrical gap, also known as transport gap E_g^t , increases linearly with the optical energy gap E_g^{opt}

$$E_g^t = (1.39 \pm 0.15) E_g^{\text{opt}} - (0.46 \pm 0.38)\text{eV}. \quad (3.3)$$

Thus, the transport gap of HATCN is expected in the range of $(4.1 \pm 0.9)\text{eV}$ resulting in an electron affinity of $(5.5 \pm 0.9)\text{eV}$. However, as can be seen from the large errors in equation (3.3) this estimation is rather imprecise.

(2) **Photoactive donor-acceptor heterojunction.** Another possibility to estimate EA is the incorporation of HATCN into the photoactive donor-acceptor heterojunction of a p-i-n type solar cell

* Measured at IAPP by Selina Olthof.

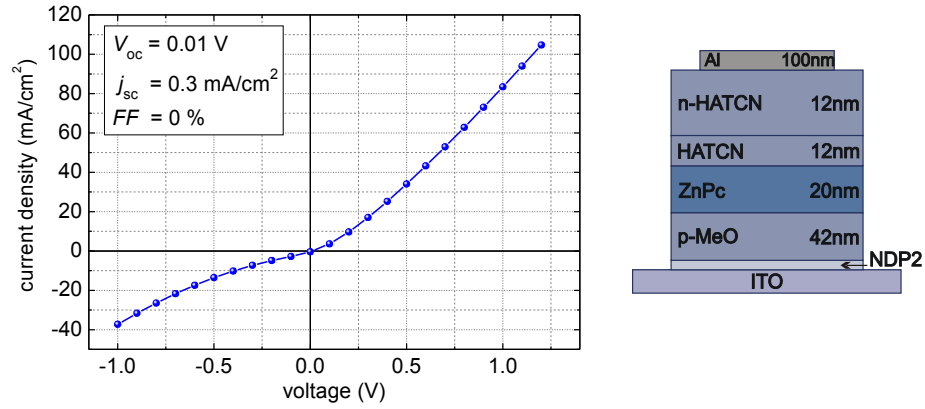


Figure 3.4: jV -curve and layer stack of a solar cell with a flat heterojunction between the donor ZnPc and a 15nm thin intrinsic HATCN layer as acceptor.

with the structure ITO/NDP2 (1nm)/MeO-TPD:NDP2 (40nm, 2wt%)/ZnPc (20nm)/HATCN (15nm)/HATCN:NDN1 (15nm, 7wt%)/Al (100nm). The open circuit voltage V_{oc} of the device scales with the effective energy gap between the IP of the donor ZnPc and the EA of the acceptor HATCN^[95,184–187]. As revealed by the resulting jV -curve depicted in Figure 3.4, the device shows a very bad performance with a short circuit current density of only 0.3 mA/cm^2 and negligible open circuit voltage. This means that EA_{HATCN} is indeed close to $IP_{\text{ZnPc}} = 5.1 \text{ eV}$ or even larger. A value smaller than $EA_{\text{HATCN}} = 4.8 \text{ eV}$ seems unlikely.

(3) HATCN as p-dopant. Materials with a large electron affinity can accept electrons from the valence level of materials with a sufficiently low ionization potential. This means they can act as p-dopants if the conditions depicted in Figure 3.5a) are fulfilled. The results obtained from the flat heterojunction solar cell indicate that HATCN might be applicable as p-dopant in either ZnPc or MeO-TPD, both having an ionization potential of 5.1 eV ^[38]. Therefore, lateral conductivity measurements are performed on thin films of ZnPc and MeO-TPD co-deposited with HATCN. However, up to a doping concentration of 10wt% an enhancement of the lateral current can not be observed. Such concentrations correspond to a high molar ratio of approx. 1:6 in ZnPc or 1:6.6 in MeO-TPD, i.e. further increasing the doping concentration is not useful as it would result in mixed layers. Due to the fact that HATCN does not act as p-dopant in the given host materials, it can be concluded that $EA_{\text{HATCN}} < 5.1 \text{ eV}$. Moreover, knowing that $F_4\text{-TCNQ}$, another common p-dopant, dopes NPB ($IP_{\text{NPB}} = 5.5 \text{ eV}$) even though its electron affinity of $EA_{F_4\text{-TCNQ}} = 5.24 \text{ eV}$ is by 0.26 eV smaller than the NPB ionization potential^[188], suggests that the electron affinity of HATCN might be even as small as 4.8 eV or less.

The finding that HATCN does not act as p-dopant in ZnPc or MeO-TPD is in contrast to the findings of Yook *et al.*^[133,141] who observed a slight increase in the current density of hole only devices upon co-

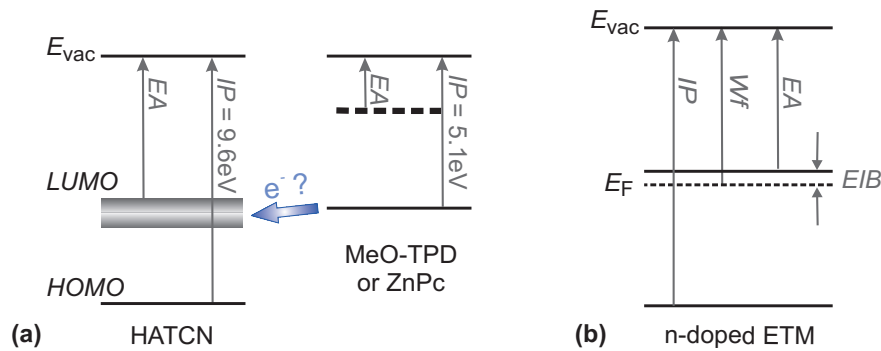


Figure 3.5: a) Suggested p-doping mechanism of HATCN in ZnPc or MeO-TPD in case of a sufficiently high HATCN electron affinity. b) Energy level scheme of an n-doped organic material: The Fermi level E_F is pinned close to the conduction level which decreases the electron injection barrier EIB with reference to the undoped material.

depositing HATCN with either CuPc ($IP_{\text{CuPc}} = 5.2\text{eV}$) or NPB ($IP_{\text{NPB}} = 5.5\text{eV}$). The authors cite an electron affinity of $EA_{\text{HATCN}} = 5.7\text{eV}$ which cannot be confirmed by our results.

(4) UPS work function of n-doped HATCN. It is possible to roughly estimate energy level positions by determining the work function of doped materials. As shown in Figure 3.5b), n-doping pins the Fermi level position close to the conduction level. If n-doping is subject to the same rules as p-doping, the distance between both levels, defined as the electron injection barrier (EIB), is dependent on the doping concentration and will saturate at a certain doping concentration^[38,82,189]. As was found for several p-doped systems, the saturated value of the HIB is not dependent on the choice of p-dopant, but on the tailing of the matrix materials DOS into the energy gap. For instance, a minimum HIB of 0.2eV was reported for ZnPc:F₄-TCNQ^[38]. It is assumed that similar results can be expected for n-doped systems, i.e. $EIB \geq 0.2\text{eV}$.

For measuring the work function of n-HATCN, the UPS spectrum of a 10nm thin film doped with 7wt% NDN1 is evaluated*. The layer is deposited onto a gold substrate covered with 12nm MeO-TPD (2wt%) and 8nm C₆₀. The reasons for choosing this specific sequence of underlayers, which is not expected to have a particular influence on the energy level positions of the bulk n-HATCN layer, are outlined in Section 3.2.2. Figure 3.3b) shows the resulting UPS spectrum: For low binding energies, the first HOMO peak of the underlying i-C₆₀ is still recognizable. It might be superimposed by a secondary peak stemming from a weak parasitic He radiation line, however, the two contributions are not clearly distinguishable. In comparison to the spectrum of 10nm intrinsic HATCN all valence band features are broadened due to n-doping. Additionally, the HOMO cutoff is shifted towards lower binding energies while the HBEC moves to higher binding energies. Altogether, this results in an IP of only 8.7eV which is by 0.9eV smaller than the IP of pristine HATCN. Such doping induced shifts of energy levels have been observed before for other material systems^[14,35]. According to equation (2.6), we calculate the work function by subtracting the HBEC from the excitation energy

$$Wf = 21.22\text{eV} - 16.20\text{eV} \simeq 5.0\text{eV}. \quad (3.4)$$

The electron affinity of n-HATCN cannot be larger than this value and is therefore expected in the range of $EA_{\text{n-HATCN}} \leq 4.8\text{eV}$ when assuming a minimum electron injection barrier of 0.2eV. However, this result should be treated with caution since not only the IP , but also the EA of doped HATCN might differ from the intrinsic value.

(5) DFT calculation. Last, the experimentally determined results are compared to a DFT calculation. Using the b3lyp method with the basis set 6-311+g{*}{*}, a LUMO energy of -4.94eV is found for the HATCN molecule[†]. This value is quite close to the thin film EA deduced above by various methods.

Considering all these estimates, the electron affinity of HATCN is expected to be in the range of (4.6...5.1)eV. As method (2) and (3) are believed to be of particular relevance, a value of $EA_{\text{HATCN}} = 4.8\text{eV}$ is assumed for further experiments.

3.2 Solar Cells

As revealed by the characterization, HATCN is well suited as ETM in terms of optical properties, morphology, and conductivity upon doping with common n-dopants. However, the exceptionally large electron affinity might constitute a problem concerning charge transport level alignment between the acceptor C₆₀ and n-HATCN in a typical p-i-n or n-i-p device structure. The next two sections give a detailed analysis of this problem and show ways to re-establish the energy level alignment.

3.2.1 Injection Barriers & S-Kinks

State-of-the-art small molecule organic solar cells use C₆₀ as photoactive acceptor material. Hence, the energy levels of a potential ETM need to match the C₆₀ levels in a way that guarantees a barrier-free electron extraction and injection. In a first approximation, the energetic position of the electron transport level can be identified with the value of a materials electron affinity. In the ideal case, which assumes vacuum level alignment between ETM and acceptor, both materials should have the same EA . This happens, for instance, when simply using n-doped C₆₀ as ETM. Figure 3.6a) gives a simplified energy level scheme of a standard p-i-n type solar cell using p-doped MeO-TPD as HTM, ZnPc and C₆₀ as

* Measurement performed by Selina Olthof, IAPP. † DFT calculation performed by Roland Gresser, IAPP.

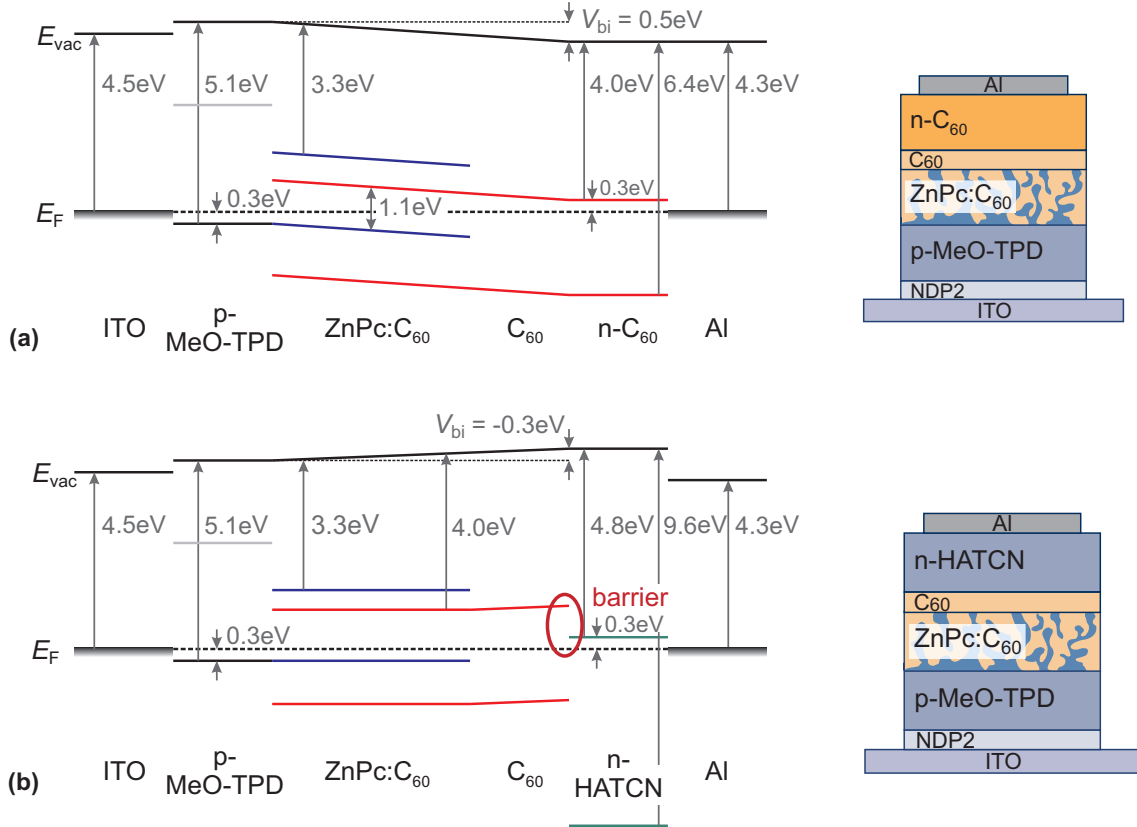


Figure 3.6: Suggested energy level schemes of (a) a reference p-i-n type solar cell using n-C₆₀ as ETM and (b) a corresponding device comprising n-HATCN. The following assumptions are made: (1) Fermi level alignment throughout the device; (2) Fermi level pinning close to the charge transport level in doped materials; (3) vacuum level alignment between doped and undoped organic materials; and (4) the absence of level bending at interfaces.

photoactive materials, n-C₆₀ as ETM and aluminum as cathode material. Several assumptions are made for creating this graph: (1) Fermi level alignment throughout the device; (2) Fermi level pinning close to the charge transport level in doped materials; (3) vacuum level alignment between doped and undoped organic materials; and (4) the absence of level bending at interfaces. However, in practice, deviations especially from the latter two points are expected^[139,190–194]. Considering the scheme in Figure 3.6a), we presume a value of 0.3eV for both the hole injection barrier in MeO-TPD and the electron injection barrier in n-C₆₀. As there are no steps in charge transport levels, this configuration results in a built-in voltage of about 0.5eV and an effective energy gap of 1.1eV at the photoactive heterojunction between ZnPc and i-C₆₀. Though the achievable open circuit voltage will be limited by the small built-in field^[112,113], a good device performance is expected. It has to be emphasized once again, that a more reliable picture of the electronic structure of a specific layer stack can only be obtained experimentally^[194]. In the present case, photoelectron spectroscopy is used for determining the energy level alignment at the n-C₆₀/i-C₆₀ interface which plays a central part for electron injection and extraction*. For this, a clean silver substrate is first covered with 15nm n-C₆₀ (3wt% NDN1) and, subsequent to a UPS measurement, with another 5nm i-C₆₀. The resulting energy level diagram, given in Figure 3.7a), shows that both the ionization potential and the work function of the doped material are only slightly increased compared to the undoped material by either 200meV or 100meV. If the electrical energy gap of C₆₀ remains unaffected by doping, this leads to a negligibly small step in electron affinities of only 100meV. Thus, the assumptions made in the energy level diagram presented in Figure 3.6a) are confirmed.

Regarding the case of an n-HATCN/C₆₀ interface, the situation is different. The suggested energy level scheme of a corresponding p-i-n device using n-HATCN instead of n-C₆₀ is given in Figure 3.6b). Assuming vacuum level alignment at the n-HATCN/C₆₀ interface results in an offset in electron affinities which can be associated with an energy barrier for electron transport. Furthermore, the built-in electric field of such

* Measurement performed by Selina Olthof, IAPP.

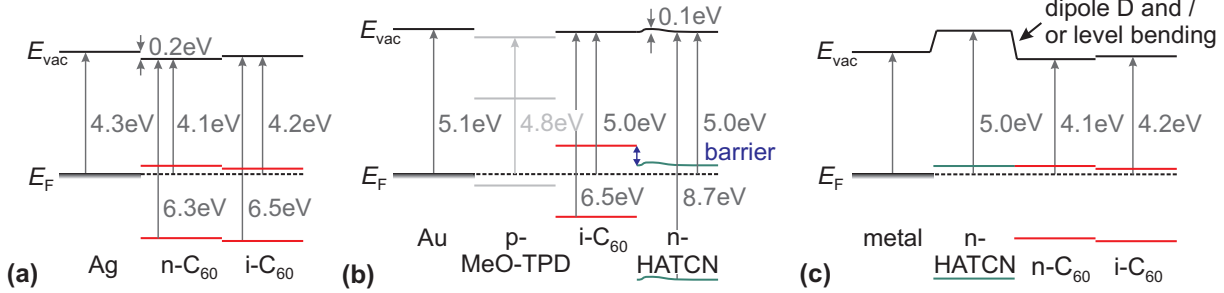


Figure 3.7: Schematic energy level diagrams of organic/organic interfaces: a) $i\text{-C}_{60}/n\text{-C}_{60}$, b) $i\text{-C}_{60}/n\text{-HATCN}$, and c) $i\text{-C}_{60}/n\text{-C}_{60}/n\text{-HATCN}$. The work functions and ionization potentials depicted in a) and b) have been determined by UPS while picture c) is a compilation of the situations observed in a) and b).

a device does not support charge carrier extraction, but can even be negative. Both facts are detrimental for device performance and should considerably affect the shape of the jV -characteristics. Again, the graph is only valid using the above given assumptions and hence the details are not quantitative, but only serve the visualization of the problem.

UPS measurements are used to confirm the assumed energy barrier between $i\text{-C}_{60}$ and $n\text{-HATCN}$. For that, an organic underlayer of 12nm p-doped MeO-TPD (2wt% NDP2) is deposited onto a clean gold substrate, followed by 8nm intrinsic C_{60} . After taking the UPS spectrum of pure C_{60} , $n\text{-HATCN}$ (7wt% NDN1) is deposited in a stepwise manner and further measurements are done at 0.2, 0.5, 1.0, 2.0, 5.0, 10.0 and 20.0nm $n\text{-HATCN}$ thickness. The resulting energy level scheme is depicted in Figure 3.7b). The $i\text{-C}_{60}$ work function on a p-MeO-TPD underlayer is 5.0eV and thus higher than the work function on an $n\text{-C}_{60}$ underlayer. This shows that the energy level positions of intrinsic materials are strongly dependent on the underlying material^[166,167]. The energetic conditions at the $i\text{-C}_{60}/n\text{-ETM}$ interface can be examined regardless of this fact. At the interface, we see a small dipole of only 0.2eV giving rise to an energy level shift towards lower binding energies which is reversed as the $n\text{-HATCN}$ layer grows thicker. However, the overall work function shift is negligible and therefore vacuum level alignment is nearly fulfilled. Another interesting effect is the reduction of HATCN's ionization potential upon n-doping. Compared to the intrinsic value of 9.6eV, the admixture of 7wt% NDN1 leads to an IP of 8.7eV. While for $n\text{-C}_{60}$ only a small IP decrease has been observed compared to $i\text{-C}_{60}$, a similarly high shift was measured for NDN1 doped NTCDA^[14]. As, however, this effect is irrelevant for our devices, it will not be further considered.

Several solar cell geometries are examined in order to analyze the effect of the mismatch in electron affinities between the acceptor $i\text{-C}_{60}$ and the ETM $n\text{-HATCN}$. All devices consist of the same sequence of HTM and active layers with ITO/NDP2 (1nm)/MeO-TPD:NDP2 (40nm, 2wt%)/ZnPc (5nm)/ZnPc: C_{60} (40nm, 1:2) and are completed by different combinations of electron transport materials followed by 100nm aluminum: In device A 31nm of $n\text{-HATCN}$ (7wt% NDN1) is deposited directly on top of the mixed ZnPc: C_{60} layer, in device B and C we insert 5nm or 10nm $i\text{-C}_{60}$ in between the mixed layer and $n\text{-HATCN}$. Figure 3.8 shows an overview of the layer structures as well as the jV -curves of all devices. The corresponding characteristic parameters including a mismatch corrected efficiency are listed in Table 3.1.

Device A, having a direct contact of $n\text{-HATCN}$ with the ZnPc: C_{60} bulk heterojunction, shows a symmetric jV -characteristics resembling a short circuit rather than a solar cell. Photocurrent and photovoltage are negligible. Considering the high EA of $n\text{-HATCN}$ which is very close to the hole transport level in ZnPc this result is to be expected: The energy level scheme of such a device resembles the picture given in Figure 3.6b) when simply leaving out the intrinsic C_{60} layer. $n\text{-HATCN}$ is in direct contact with the ZnPc: C_{60} blend which is expected to contain closed ZnPc percolation pathways and hence to establish a direct connection to the p-side. Due to the small energy distance between electron transport level of $n\text{-HATCN}$ and the hole transport level of ZnPc, the interface between both materials acts as recombination contact. It has been demonstrated recently that this effect, which is detrimental for our p-i-n type solar cells, can be exploited for building intermediate connecting layers in tandem OLED structures^[134].

To avoid the direct electron-to-hole conversion, an either 5 or 10nm thick intermediate layer composed of intrinsic C_{60} is inserted between the ZnPc: C_{60} mixed layer and $n\text{-HATCN}$ in **devices B and C**. As

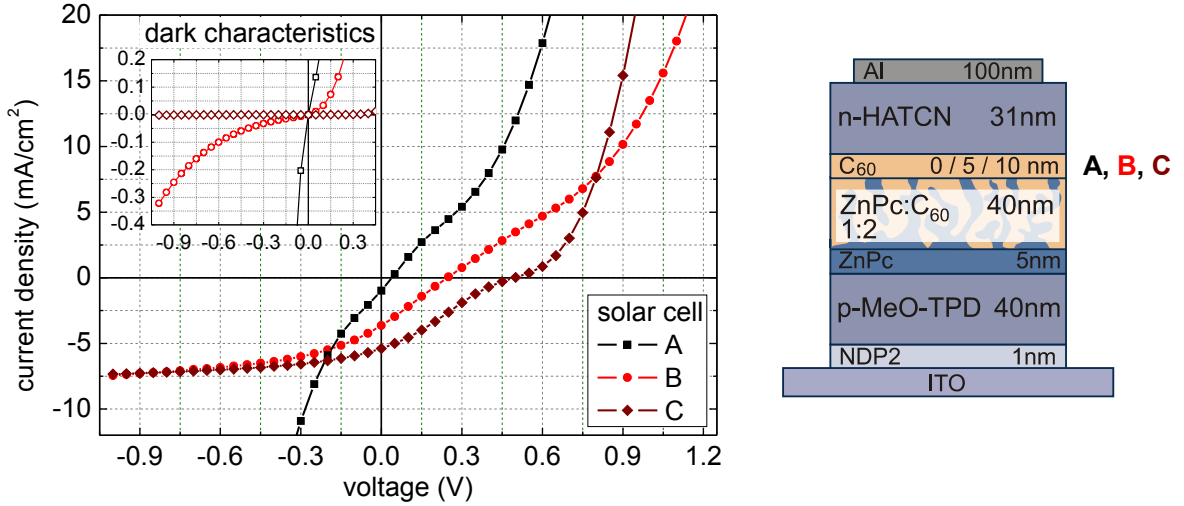


Figure 3.8: jV -curves and layer stacks of solar cells A, B and C comprising either 31nm n-HATCN (A, black squares), 5nm i-C₆₀/31nm n-HATCN (B, red circles) or 10nm i-C₆₀/31nm n-HATCN (C, brown diamonds) as electron extraction contact.

Device	ETM	V_{oc} (V)	j_{sc} (mA/cm ²)	FF (%)	Sat $j(-1V)/j_{sc}$	I_{eff} (mW/cm ²)	η (%)
A	31nm n-HATCN	0.04	1.0	< 1	94.03	94	< 0.1
B	5nm i-C ₆₀ /31nm n-HATCN	0.24	3.6	25	2.05	93	0.2
C	10nm i-C ₆₀ /31nm n-HATCN	0.50	5.3	25	1.36	94	0.7

Table 3.1: Characteristic parameters of solar cells A-C, displayed in Figure 3.8. I_{eff} denotes the mismatch corrected intensity which is used for calculating the power conversion efficiency η .

can be seen from Figure 3.8, the photovoltaic performance is improved and in both cases a photocurrent density of $j \simeq 7.4\text{mA/cm}^2$ is achieved at a negative bias of -1V . However, both jV -curves show a strong s-kink that depends on the i-C₆₀ thickness: The solar cell comprising the thicker i-C₆₀ layer has a higher j_{sc} of 5.3mA/cm^2 compared to $j_{sc}^B = 3.6\text{mA/cm}^2$ as well as an improved open circuit voltage of 0.50V compared to $V_{oc}^B = 0.24\text{V}$. There is no significant influence on the fill factor, which yields only 25% in both cases. Consequently, the power conversion efficiencies $\eta_B = 0.2\%$ and $\eta_C = 0.7\%$ are comparably low. Altogether, this result confirms the presence of an electron injection barrier as predicted in Figure 3.6b). The forward current is suppressed as charges can accumulate at the interface between i-C₆₀ and n-HATCN. Due to the low built-in field, the photocurrent in the region of V_{oc} is diffusion driven as the density of electrons at the D/A interface and especially at the ZnPc:C₆₀/C₆₀ interface is higher than at the C₆₀/n-HATCN interface. This leads to an increased recombination of photogenerated charge carriers mainly occurring at the ZnPc:C₆₀/C₆₀ interface and accordingly to a reduction of the current close to V_{oc} .

While the energy barrier can explain the origin of the s-shape, it does not account for the shift in V_{oc} and j_{sc} as the i-C₆₀ layer thickness is increased. Obviously, a layer as thin as 5nm C₆₀ cannot completely prevent a direct quenching of holes photogenerated in the blend and electrons present in n-HATCN. As the i-C₆₀ layer thickness is increased to 10nm in device C, the residual tunneling is decreased. This assumption is supported by the comparison of the dark jV -curves, which is done in the inset of Figure 3.8, revealing the poor rectifying behavior of solar cell B compared to solar cell C.

At first sight, these results render HATCN unsuitable as ETM. However, the next Section will show a way to deal with this problem and to finally remove the electron injection barrier.

3.2.2 Tailoring the Injection Barrier by Doping

As in inorganic semiconductors, doping can also be used to control the Fermi level position within the energy gap of organic semiconductors. Dependent on the p- or n-doping concentration, the Fermi level is fixed at a certain distance from the respective charge conduction level, leading to an increase of the

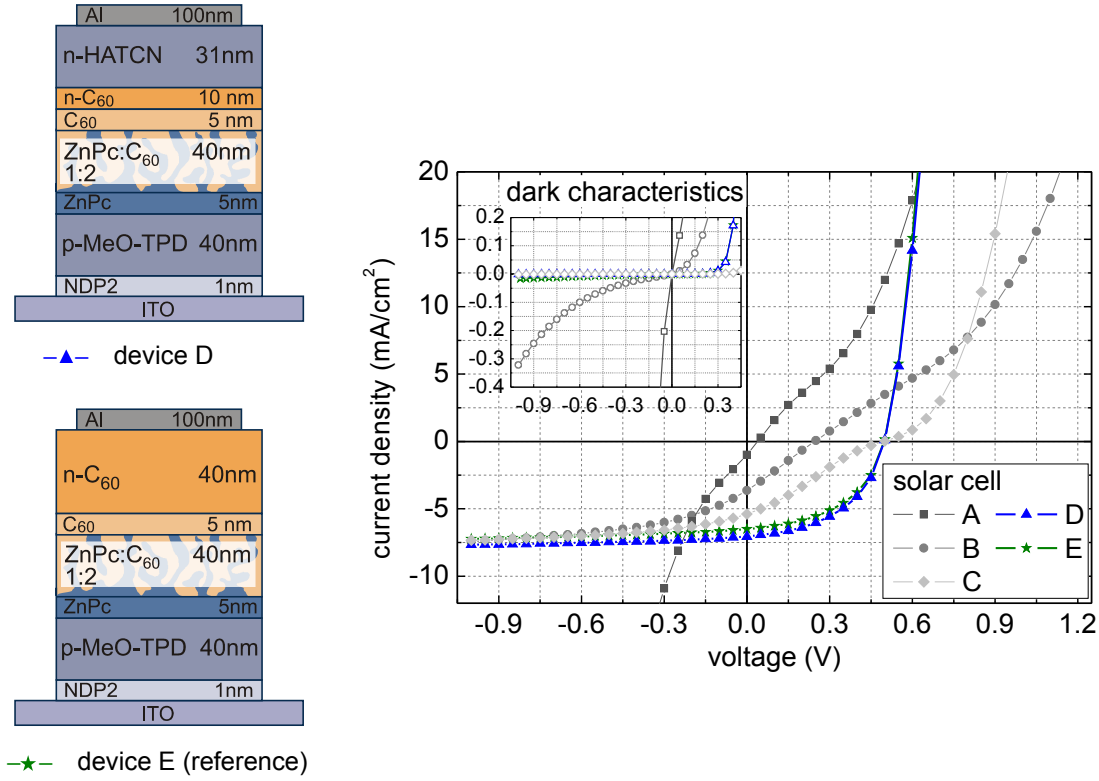


Figure 3.9: jV -curves and layer stacks of solar cells D and reference device E comprising either 5nm i - C_{60} /10nm n - C_{60} /31nm n -HATCN (D, blue triangles) or 5nm i - C_{60} /40nm n - C_{60} (E, green stars) as electron extraction contact.

free charge carrier density within the bulk. At efficient doping, the amount of charge carriers is large enough to achieve an alignment of the bulk Fermi levels when bringing the doped material in contact with a metal. The interface formation usually involves a charge transfer as well as the formation of a thin space charge layer (SCL) of a few nanometers thickness. Like at inorganic semiconductor/metal interfaces, this process is accompanied by band or rather energy level bending and additional interface dipoles^[35,37,188,194,195]. Neglecting these details that govern the interface formation in the vicinity of the contact, the bulk energy level alignment is relatively easy to predict if the hole or electron injection barrier, i.e. the fixed distance between E_F and EA or IP , is known. This general consideration also holds for the case of interfaces between two doped organic materials. Here, level bending might occur in both materials, however beyond the SCLs, the bulk Fermi level positions will prevail.

This effect can be exploited for removing the electron injection barrier observed in devices B and C by inserting a thin n -doped C_{60} layer between the intrinsic C_{60} of the photoactive region and n -HATCN. In both n -doped materials, the Fermi level is in a fixed position close to the respective electron transport level. When bringing the materials in contact, the Fermi levels will align and as consequence of the

Device	ETM	V_{oc} (V)	j_{sc} (mA/cm ²)	FF (%)	Sat $j(-1V)/j_{sc}$	I_{eff} (mW/cm ²)	η (%)
D	5nm i - C_{60} /10nm n - C_{60} /31nm n -HATCN	0.50	6.9	49	1.09	95	1.8
E	5nm i - C_{60} /40nm n - C_{60}	0.50	6.5	49	1.11	94	1.7

Table 3.2: Characteristic parameters of solar cells D and E, displayed in Figure 3.9. I_{eff} denotes the mismatch corrected intensity which is used for calculating the power conversion efficiency η .

different electron affinities, a simple vacuum level alignment cannot be assumed anymore. Instead, Fermi level pinning will lead to the formation of a large interface dipole and / or charge transfer accompanied by level bending at the contact. In the latter case, an SCL would form at the n-C₆₀/n-HATCN interface which, however, could be tunneled through by the electrons if it is thin enough. Such a situation results in the alignment of electron transport levels and barrier free transport. As already pointed out in the previous Section and as shown in Figure 3.7a), electron transport between n-C₆₀ and i-C₆₀ is also barrier free. Figure 3.7c) suggests an energy level diagram of the new situation in which potential level bending is omitted. Due to the alignment of electron transport levels, we expect solar cells with this type of n-contact to perform well.

For testing this hypothesis, a 10nm n-C₆₀ interlayer (3wt% NDN1) is inserted between the 5nm thin i-C₆₀ layer and the 31nm n-HATCN layer of device structure B. The resulting **layer stack D** is depicted in Figure 3.9 along with the corresponding jV -characteristics. As predicted, the introduction of an n-C₆₀ interlayer gives rise to a complete suppression of the s-shape in the jV -curve. For evaluating the degree of improvement, the performance of device D is compared to that of a **reference solar cell E** in which the combination of the two ETM is replaced by one, 40nm thick, n-C₆₀ layer. The jV -curves of both devices are nearly identical: having an equal V_{oc} of 0.50V and equal fill factors of 49%, the n-HATCN solar cell has only a slightly higher short circuit current density of $j_{sc}^D = 6.9\text{mA/cm}^2$ as compared to the reference device with $j_{sc}^E = 6.5\text{mA/cm}^2$. Overall, the mismatch corrected power conversion efficiency yields $\eta = 1.8\%$ for the n-HATCN device and $\eta = 1.7\%$ for the reference device. The increased photocurrent of the n-HATCN device is reproduced in similar stack structures and can be attributed to parasitic absorption by n-C₆₀ in device E which leads to a decreased photon flux within the photoactive region of the solar cell. The effect is expected to become more pronounced at higher window layer thickness^[196] (see Chapter 6).

All trends observed in solar cells A-D can be reproduced in solar cells with other n-HATCN layer thickness (8nm, 12nm, 16nm, and 23nm).

3.2.3 Impedance Spectra

Impedance spectroscopy (IS) can help to gain a deeper understanding of the microscopic effects causing the above described solar cell performances. For this, the samples response to a frequency variation of a small AC signal is measured. Furthermore, an additional DC bias voltage is applied which allows to set the solar cell to forward (positive bias at the p-side) or reverse (positive bias at the n-side) operating conditions. Within the given frequency range, only the states having a response time faster than the input AC signal are able to follow the modulation. This is usually the case for doped layers, in which many free charge carriers are present, while intrinsic layers or extended depletion regions produce a capacitive effect. Additionally, trap states can contribute to the capacitance when responding to the modulation signal by multiple trapping and release of charge carriers^[197,198].

Instead of solar cells A, B, C, and D, equivalent **samples A', B', C', and D'** having an n-HATCN thickness of 23nm are used for the impedance measurements*. The results are presented as capacitance-frequency ($C(f)$) and phase-frequency ($\varphi(f)$) plots in Figures 3.10 and 3.11. Spectra taken at zero bias are plotted as green stars while curves measured under negative (positive) bias are depicted in blue (red), respectively. Starting with reference device E comprising 40nm n-C₆₀ as standard ETM, the following paragraphs will give an interpretation of the results.

Reference device E

At zero and at negative bias, the $C(f)$ and $\varphi(f)$ spectra of reference device E show contributions from three different processes. At frequencies larger than 100kHz (region I, Figures 3.10a) and 3.11a)), the capacitance as well as the phase drop rapidly with increasing frequency. The device response is governed by its series resistance. In region II, between 1kHz and 100kHz, the capacitance remains nearly constant while the corresponding phase is only slightly lower than 90°. Both facts are clear indications for capacitive behavior. The plateau corresponds to the geometric capacitance C_{geo} of the intrinsic layers which are sandwiched between well conducting doped layers. Assuming a relative permittivity of $\epsilon = 5$ for layers composed of ZnPc and / or C₆₀ and applying equation (2.31)

$$d = \epsilon\epsilon_0 \frac{A}{C},$$

* Data evaluation assisted by Lorenzo Burtone, IAPP.

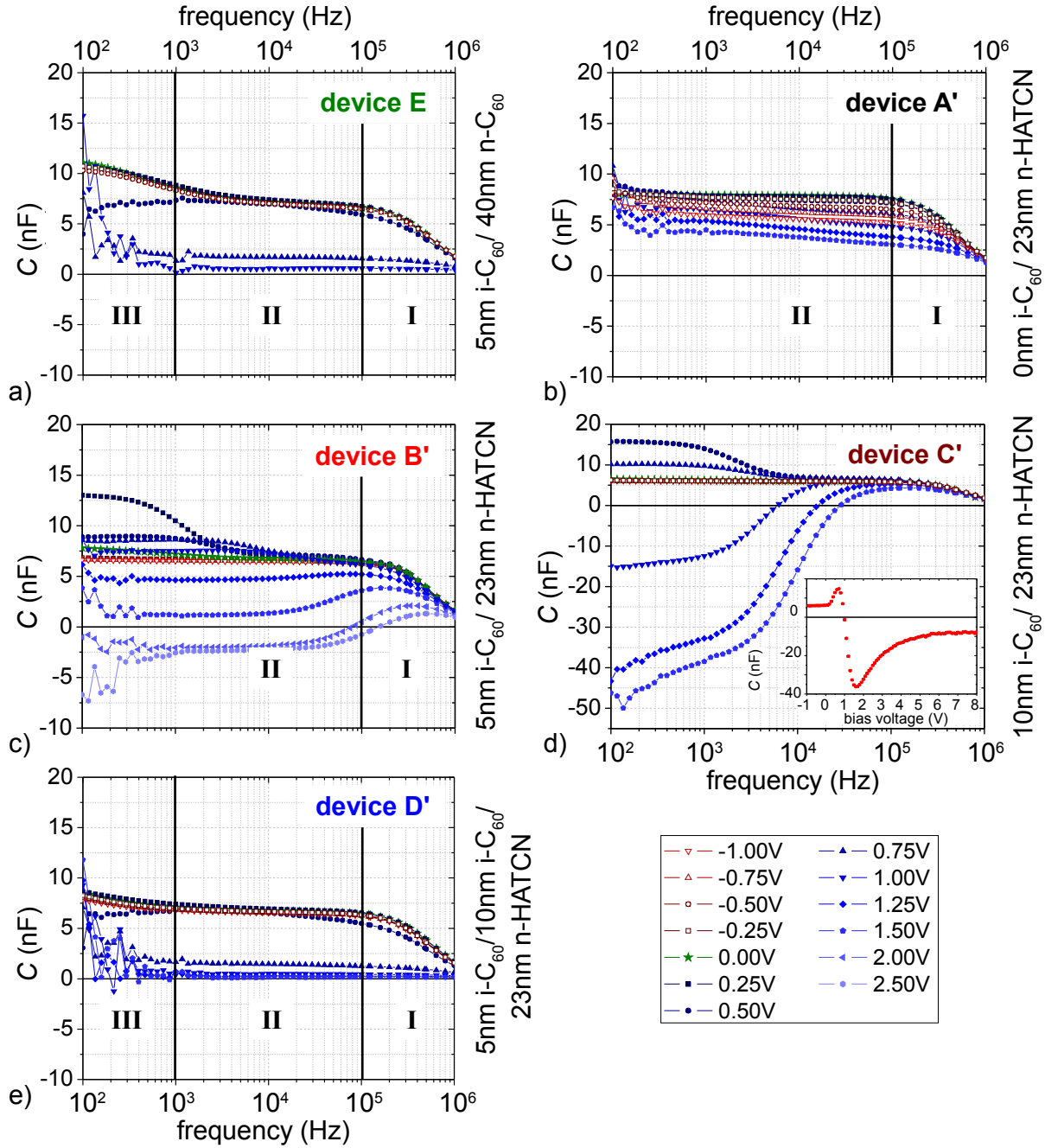


Figure 3.10: Results of the impedance measurements presented as capacitance-frequency plots evaluated at different positive (blue) and negative bias voltages (red). a) reference device E comprising 40nm $n\text{-C}_{60}$ as ETM, b) device A' comprising 23nm $n\text{-HATCN}$ without any interlayer, c) device B' comprising 5nm $i\text{-C}_{60}/23\text{nm } n\text{-HATCN}$, d) device C' comprising 10nm $i\text{-C}_{60}/23\text{nm } n\text{-HATCN}$, and e) device D' comprising 5nm $i\text{-C}_{60}/10\text{nm } i\text{-C}_{60}/23\text{nm } n\text{-HATCN}$. The inset in d) shows the $C(V)$ -curve of device C' recorded at 1kHz.

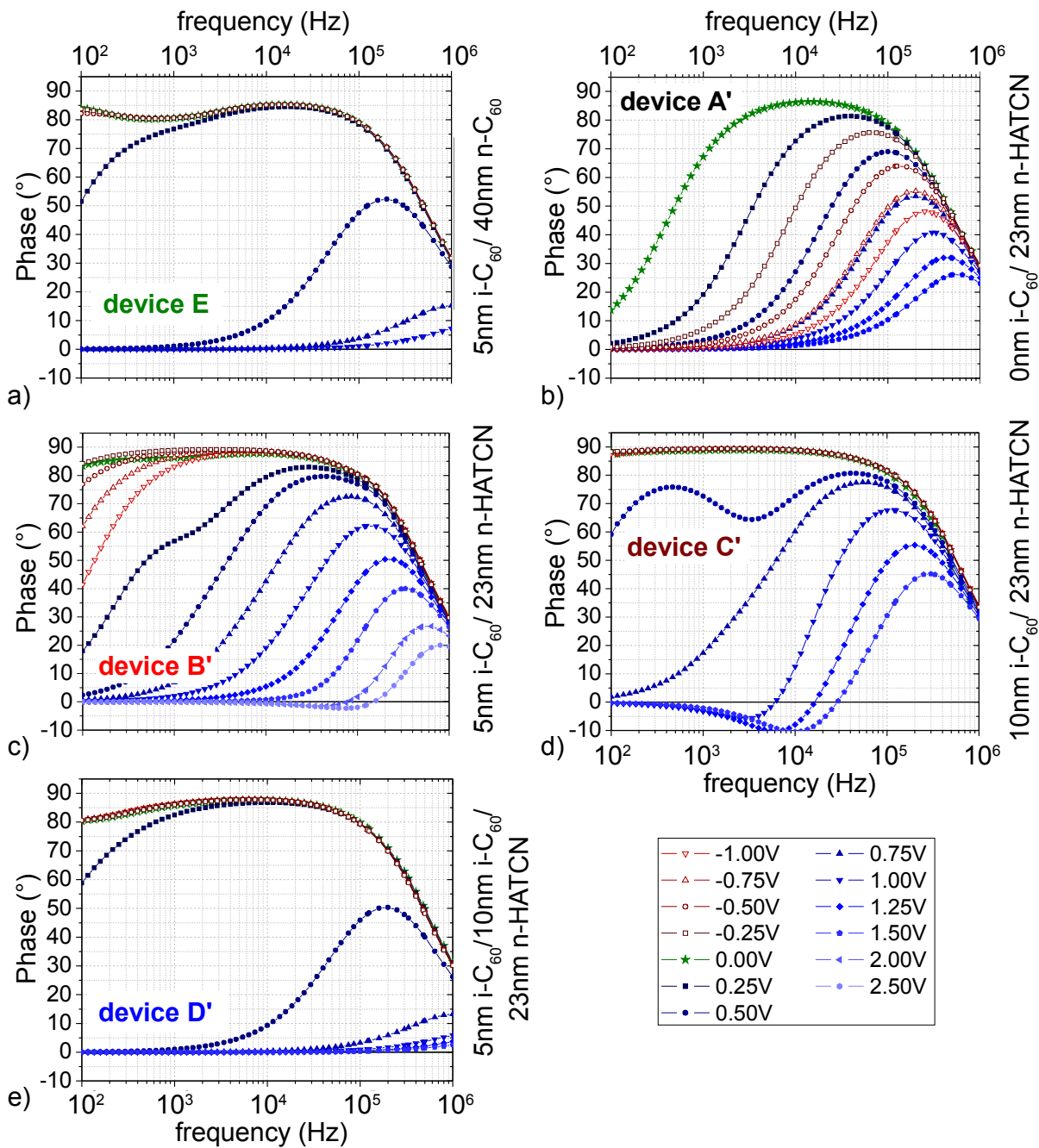


Figure 3.11: Results of the impedance measurements presented as phase-frequency plots evaluated at different positive (blue) and negative bias voltages (red). a) reference device E comprising 40nm $n-C_{60}$ as ETM, b) device A' comprising 23nm $n-HATCN$ without any interlayer, c) device B' comprising 5nm $i-C_{60}$ /23nm $n-HATCN$, d) device C' comprising 10nm $i-C_{60}$ /23nm $n-HATCN$, and e) device D' comprising 5nm $i-C_{60}$ /10nm $n-C_{60}$ /23nm $n-HATCN$.

the thickness d_{act} of the photoactive region is calculated as 41nm. This value is below the nominally deposited thickness of 50nm and only changes slightly to 42nm when applying a negative bias of -0.5V . Overall, the reverse bias barely affects shape and position of the $C(f)$ and $\varphi(f)$ spectra as it only leads to a further depletion of the nominally intrinsic region if residual free charge carriers are present. The slight bias voltage dependence of the geometric capacitance is an indication of a non-abrupt intrinsic/doped material interface. Finally, there is a third interesting region in the $C(f)$ plot: At frequencies lower than 1kHz, the formation of a second plateau having an even higher capacitance is indicated. As pointed out by Burtone et al., it can be assigned to trap states which are able to follow the modulated signal if it is slow enough^[198].

At *positive bias* (blue curves), we first find a very slight increase in capacitance and then, as the bias voltage exceeds V_{oc} , a rapid decrease until $C(f)$ reaches nearly 0nF at $V_{\text{bias}} = 1\text{V}$. At the same time, the phase signal is constantly decreasing and becomes clearly resistive at $V_{\text{bias}} > 0.5\text{V}$, i.e. the phase drops below 10° . This behavior is expected as under forward bias charges are driven through the whole device. There is no depletion capacitance anymore, and thus the equivalent circuit, which the calculation of $C(f)$ is based on, can no longer be applied. As will be explained below, an interpretation of the device response under forward bias can be achieved using the concept of chemical capacitance^[199,200].

Device A' - 0nm i-C₆₀

Knowing what the $C(f)$ and $\varphi(f)$ spectra of a standard solar cell look like, we start evaluating the response of the n-HATCN devices. Devices A and A', which are both lacking any kind of interlayer between the photoactive bulk and n-HATCN, show a symmetric jV -curve without any rectifying behavior rather than a solar cell performance. This time, the $C(f)$ plot depicted in Figure 3.10b) consists of only two regions: Region I at $> 100\text{kHz}$, which is characterized by the contribution of the devices series resistance, and region II, at frequencies $< 100\text{kHz}$, with a nearly constant capacitance of 7.8nF *at zero bias*. The corresponding layer thickness is 37nm which is again smaller than the nominal active layer thickness of 45nm. The absence of a second plateau at low frequencies indicates that there are no or only few trap states. The phase diagram reveals that the plateau is predominantly capacitive only between 3...75kHz where $\varphi > 80^\circ$. At higher and also at lower frequencies, the phase drops, i.e. unlike the $C(f)$ spectrum which has only two regions, the $\varphi(f)$ spectrum, shown in Figure 3.11b), can be divided into three regions. The drop at high frequencies (region I) has already been explained in the previous Section and is due to the contribution of the series resistance. The decrease at high frequencies is caused by the devices generally small parallel resistance R_p which is reflected by the bad rectification seen in the solar cell characteristics. Contrary to $\varphi(f)$, $C(f)$ does not show any change in the low frequency region as the value of R_p is not affecting the capacitance function used to calculate the curve. Applying a *positive or negative bias* voltage leads to both, a decrease in capacitance and a decrease in phase. This behavior is in accordance with the jV -curves which are symmetric and do not show any rectifying behavior. Independent of the electric field direction, charge carriers are injected and driven through the device. Thus, the resistive nature of the device response becomes more pronounced with increasing bias voltage, no matter if this voltage is positive or negative.

Device B' - 5nm i-C₆₀

The solar cell performance of devices B and B' is dominated by an electron injection barrier between the 5nm i-C₆₀ interlayer and n-HATCN, leading to an s-kink in the jV -characteristics and residual tunneling of charge carriers through this barrier. *At zero bias*, the corresponding $C(f)$ and $\varphi(f)$ spectra of device B' (Figures 3.10c) and 3.11c)) are similar to those of device A': The geometric capacitance results in a plateau at 6.7nF corresponding to a thickness of 43nm. The relative increase in thickness compared to device A' with $d_{\text{geom. cap.}} = 37\text{nm}$ is larger than can be attributed to the additional 5nm i-C₆₀. It is very likely that the geometric capacitance of device A' is decreased by a partial diffusion of charge carriers from the doped layers into the intrinsic since there is no built-in field opposing such a process. In device B' such a diffusion is hindered by the electron injection barrier. Next to the geometric capacitance, device B' shows a slight increase in $C(f)$ as the frequency falls below 8kHz (region III). The resulting additional contribution vanishes at negative bias voltages and becomes more pronounced under small forward bias ($V_{\text{bias}} \leq 1\text{V}$). At even higher *positive bias*, when charges are driven through the device, capacitance and phase drop in the whole frequency range. Above $V_{\text{bias}} = 2.0\text{V}$, the capacitance becomes negative. Such a behavior is at first unexpected as it corresponds to an inductance, i.e. to a process which hinders the increase in forward current. However, it has been observed before in various semiconductor

devices^[201–203]. As already stated above, at positive bias the model used for calculating $C(f)$ is not valid anymore, as it assumes a depletion capacitance which is no longer present in forward direction. A new model with a modified equivalent circuit needs to be introduced. Several attempts have been made to set up such a model and to explain the negative capacitance by either bipolar injection and recombination of minority charge carriers^[203], the accumulation of charge carriers upon space charge limited injection^[204], or by modulating the conductivity of a recombination diode^[205]. Basically, all three models involve the presence and accumulation of minority charge carriers. Recently, Burtone et al. developed a new comprehensive model that is able to explain and reproduce the observed changes in $C(f)$ under positive bias^[176]. The capacitance which replaces the depletion capacitance is the so-called chemical capacitance C_μ which is formally defined as

$$C_\mu = eL \frac{dn_{\text{acc}}}{dV_F}. \quad (3.5)$$

Here, L is the material thickness, n_{acc} the density of accumulated charge carriers, and V_F represents the potential that drops over the layer stack^[200,205]. With increasing forward bias more and more charge carriers are injected. Due to the injection barrier, electrons are piling up at the n-HATCN/i-C₆₀ interface. If the positive bias is small, the barrier cannot be overcome and the electrons cannot reach the D/A interface where a recombination with holes injected at the p-side would occur. As a consequence, also the holes are piling up (dn_{acc} positive) at the D/A interface and a chemical capacitance forms. As soon as the voltage is high enough for the electrons to overcome the barrier, the recombination current sets in. The amount of accumulated charge carriers decreases, i.e. $(dn_{\text{acc}}/dV_F) < 0$. This means that the chemical capacitance becomes negative and can overcome the geometric capacitance, causing the overall signal to be negative. The origin of this effect is in the unbalanced injection of electrons and holes as already discussed by Gommans et al.^[203] who base their observations on unbalanced mobilities. At very high forward voltages, the injection of electrons and holes is balanced which means that C_μ approaches zero. This effect is exemplarily shown for device C' in the inset of Figure 3.10d).

The phase signal associated with the chemical capacitance approaches zero as the forward voltage increases. The reason is again that R_p is getting smaller and $R_p \gg R_s$ holds not true anymore. In reverse, the phase slightly decreases with increasing negative voltage. This behavior is a clear indication of residual tunneling through the i-C₆₀ layer which prevents a complete depletion of the photoactive region.

Device C' - 10nm i-C₆₀

Devices C and C' differ from solar cells B and B' only by the thickness of the i-C₆₀ intermediate layer which is now 10nm instead of 5nm. Hence, the IS spectra of C' are very similar to those of device B'. Due to the additional intrinsic C₆₀ the tunneling of electrons from n-HATCN to ZnPc is nearly suppressed. *At zero and negative bias*, the plateau in $C(f)$ which is associated with the geometric capacitance is nearly perfectly flat until the lower end of the frequency range. The difference in the plateaus height as compared to C_{geo} of device B' accounts well for the difference in the i-C₆₀ thickness which is calculated to be 4nm (nominal thickness increase 5nm). The absence of residual tunneling is confirmed by the phase signal which remains constant at 88° in the low and medium frequency range. As a consequence more charge carriers can accumulate at the electron injection barrier *at positive bias* and the negative capacitance effect becomes more pronounced. For $V_{\text{bias}} = +0.50\text{V}$ the phase diagram even shows two maxima which means that geometrical capacitance and chemical capacitance are coexisting as the ZnPc:C₆₀ bulk is still depleted. In device B', this effect is much less pronounced. The negative phase signal at medium frequencies can be explained again by a negative derivative of the accumulated charges with respect to the change in voltage. For forward voltages larger than 1.5V, electron and hole injection are better balanced and the negative capacitance decreases, as shown in the $C(V)$ -curve depicted in the inset of Figure 3.10d).

Device D' - 5nm i-C₆₀ + 10nm n-C₆₀

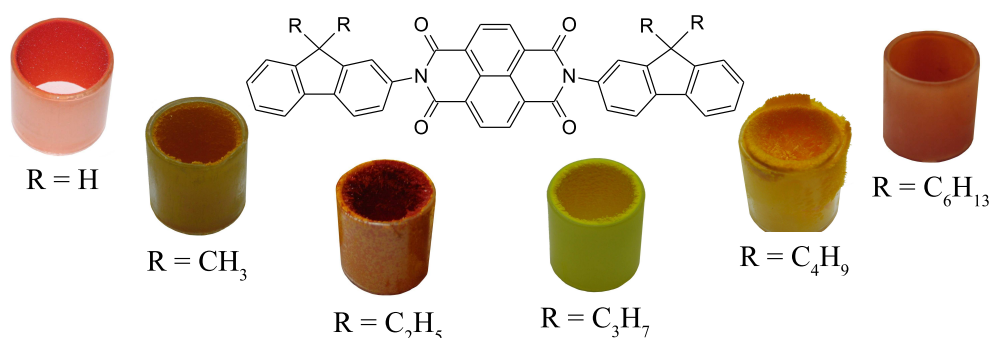
As pointed out in the previous section, the additional n-doped C₆₀, which is introduced into the layer stack of devices D and D', removes the injection barrier and therefore aligns the electron transport levels between n-HATCN and i-C₆₀. Any effects that had been caused by tunneling or charge accumulation should hence not be observable anymore. Indeed, when comparing Figure 3.10e) to Figure 3.10a), the differences are only marginal. Solely the trap contribution is reduced as it is probably related to the amount of n-C₆₀

in the solar cell. Altogether, this result verifies the conclusions drawn from the interpretation of the jV -curves in the preceding Sections 3.2.1 and 3.2.2.

3.3 Summary

- HATCN forms smooth and transparent thin films upon vacuum deposition onto glass substrates or organic underlayers. By co-evaporating HATCN with either AOB or NDN1, the lateral conductivity can be increased up to $2.2 \cdot 10^{-4} \text{S/cm}$ (7wt% NDN1). Both, electron affinity ($EA \simeq 4.8 \text{eV}$, estimated) as well as ionization potential ($IP = 9.6 \text{eV}$, UPS) are exceptionally high.
- When using n-HATCN as ETM in p-i-n type solar cells, the high electron affinity is detrimental for device performance:
 - Devices comprising a direct contact between the photoactive ZnPc:C₆₀ bulk and n-HATCN show short circuits. Due to the proximity of the electron transport level of n-HATCN and the hole transport level of ZnPc electrons and holes recombine at the interface between both materials.
 - In devices comprising an intrinsic C₆₀ interlayer between the photoactive bulk and n-HATCN, an electron injection barrier forms at the n-HATCN/i-C₆₀ interface due to the comparably low electron affinity of C₆₀ ($EA_{\text{C}_{60}} = 4.0 \text{eV}$ ^[49]). As a result, the jV -curves of corresponding solar cells display a pronounced s-kink.
- The introduction of an additional n-C₆₀ interlayer between i-C₆₀ and n-HATCN leads to a suppression of the s-kink and a solar cell performance which is comparable to that of a reference device containing only n-C₆₀ as ETM. n-doping pins the Fermi level close to the electron transport level in both, n-C₆₀ and n-HATCN. When bringing the materials in contact, Fermi level alignment will inevitably lead to an alignment of the bulk electron transport levels and hence to the elimination of the injection barrier. The formation of interface dipoles and / or a thin space charge layer at the n-C₆₀/n-HATCN interface does not impede charge transport.
- Impedance spectroscopy verifies the conclusions drawn from the interpretations of the jV -curves. The existence of an electron injection barrier is reflected by the occurrence of a negative capacitance when examining the devices under forward bias. The effect can be explained by means of the so-called chemical capacitance^[176].

4 Bis-Fl-NTCDI Derivatives - Influence of the Side Chain Length on Physical Properties and Solar Cell Performance



Variations in the molecular structure are known to have a considerable influence on the physical properties of an organic material. Understanding these structure-properties relationships is of fundamental importance and subject of ongoing research. In this Chapter, a series of Bis-Fl-NTCDI compounds with varying alkyl side chains is studied. We examine the dependence of absorption, thin film density, morphology, energy level positions, and *n*-doping efficiency on the side chain length. It is found that the achievable lateral conductivity upon doping with NDN1 decreases drastically with increasing alkyl chain length, although ionization potential and electron affinity remain virtually unaffected. Solely the compound without any side chains is capable of reaching a conductivity which is sufficient for an application as electron transport material. This fact is reflected by the performance of *p-i-n* devices comprising Bis-Fl-NTCDI derivatives as ETM which is discussed in the last Section.

4.1 Characterization

In total, six different Bis-Fl-NTCDI derivatives were synthesized by Dr. Markus Hummert at IAPP. Their molecular structures as well as photographs of the substances after purification are summarized in the Figure above. Either no side chain ($R = H$, Bis-HFl-NTCDI) or methyl ($R = CH_3$, Bis-MeFl-NTCDI), ethyl ($R = C_2H_5$, Bis-EtFl-NTCDI), propyl ($R = C_3H_7$, Bis-PrFl-NTCDI), butyl ($R = C_4H_9$, Bis-BuFl-NTCDI) or hexyl ($R = C_6H_{13}$, Bis-HexFl-NTCDI) chains are attached to the C9 position of the fluorene side groups. Table 4.1 gives the average sublimation temperatures T_s during the vacuum gradient purification process and evaporation temperatures T_{evap} of the purified materials. Concluding a trend is not recommended as these values are strongly system dependent, i.e. they might differ when using other evaporation sources or crucible materials.

The following Sections deal with the influence of the side chain length on the compounds thin film properties of the available compounds.

4.1.1 Optical and Electrical Properties

As described previously, the optical and electrical properties of organic solids are mainly determined by the molecular π electron system. Since alkyl side chains induce only very weak polar effects, their influence on the absorption spectrum or the energy level positions is expected to be low.

material	n	T_s ($^{\circ}\text{C}$)	T_{evap} ($^{\circ}\text{C}$)
Bis-HFI-NTCDI	0	380	250
Bis-MeFI-NTCDI	1	380	170
Bis-EtFI-NTCDI	2	340	170
Bis-PrFI-NTCDI	3	360	170
Bis-BuFI-NTCDI	4	320	200
Bis-HexFI-NTCDI	6	370	210

Table 4.1: Average sublimation temperatures T_s during the vacuum gradient purification process and evaporation temperatures T_{evap} of the purified materials in the UFO 1 system. n denotes the number of carbon atoms in the side chain.

Optical density

Figure 4.1a) shows the normalized optical densities of Bis-FI-NTCDI thin films deposited onto quartz glass substrates. OD_{norm} is calculated by dividing the measured absorbance by the layer thickness. Peak positions, spectral shape, and peak height are nearly independent of the side chain length. Merely the absorption bands of Bis-HFI-NTCDI, the compound without any side chains, are slightly broadened and shifted towards smaller wavelengths which can be a hint for increased crystallinity^[28,206]. The low energy absorption edge, which is used to determine the optical energy gap, is not affected by the spectral broadening. As displayed in Figure 4.1a), E_g^{opt} is found to be in the range of (3.0...3.1)eV. Variations in peak height are not systematic and might be due to errors in the thin film densities which were used for calculating the layer thickness (discussion in Section 4.1.2).

n & k values are only determined for Bis-HFI-NTCDI, the compound which turned out to be the most promising material for device fabrication. As can be seen from Figure 4.1b), the extinction coefficient k reflects the absorption properties. The refractive index is comparatively low: In the spectral range above 500nm n approaches 1.5, which is close to the refractive index of glass that is also depicted in the figure for reasons of comparison. I.e. in terms of optical properties, Bis-HFI-NTCDI is perfectly suited for the application as charge transport material and optical spacer for organic solar cells. Effects of the low refractive index on device performance will be discussed in Chapter 6, where the performance the most promising ETM identified in this thesis is compared in p-i-n type devices.

The finding that vacuum deposited thin films are transparent regardless of the side chain length is in contrast to the appearance of the purified substances which form yellow to orange colored crystallites. This effect is caused by the influence of π - π stacking in the crystal lattice on the color and is called crystallochromy. It has been studied extensively for perylene dyes by Graser, Hädicke and Klebe^[207,208] who explain it by a side group dependent displacement of neighboring molecules in the crystal lattice. Likewise, the conformation of Bis-FI-NTCDI single crystals, obtained during the sublimation process or from toluene solution, depends on the side chain length^[149] and gives rise to the different colors of the

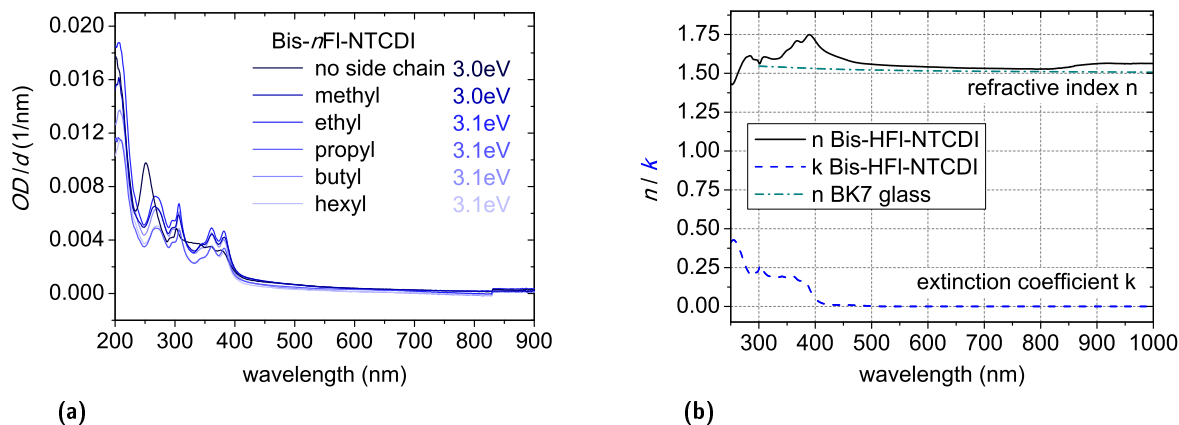


Figure 4.1: a) Normalized optical densities and optical energy gaps deduced from the onset of absorption for all Bis-FI-NTCDI compounds; and b) optical constants n & k of Bis-HFI-NTCDI in comparison to the optical properties of BK7 glass.

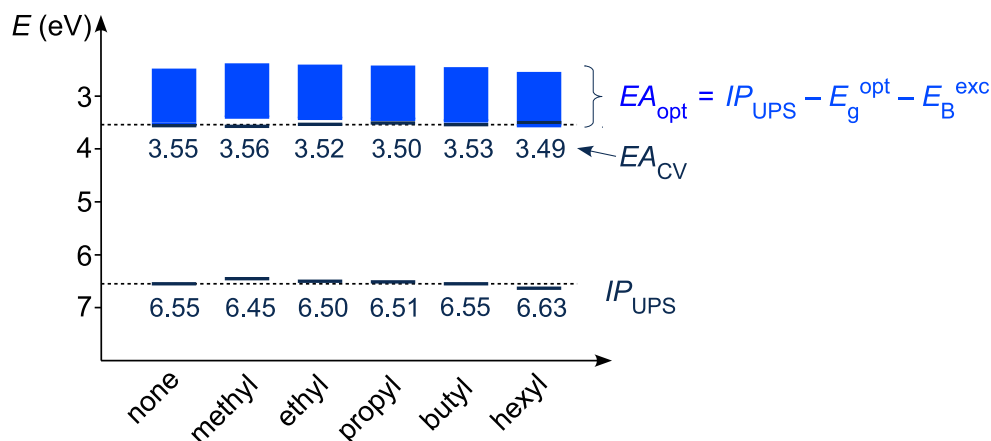


Figure 4.2: Summary of Bis-FI-NTCDI energy levels: Ionization potentials IP determined by UPS and electron affinities EA_{CV} (dark blue lines) extrapolated from CV reduction potentials E_{red} , or EA_{opt} deduced by subtracting the optical energy gap E_g^{opt} from the ionization potential (blue lines). The blue boxes indicate the uncertainty due to the unknown exciton binding energy E_B^{exc} . The latter is estimated to be 0.7eV by using an empirical relation published by Djurovich et al.^[19].

purified materials. However, the morphology of thin films usually significantly differs from the structure of corresponding single crystals. As will be described in the following, vacuum deposition of Bis-FI-NTCDI results in amorphous or only weakly crystalline films. Here, the molecular π electron system dominates the optical properties whereas the influence of π - π stacking is secondary.

Energy level positions

Ionization potentials of Bis-FI-NTCDI thin films, deposited either onto a clean gold or silver substrate, are measured by UPS*. The result, summarized in Figure 4.2, is given with two significant digits in order to visualize the development. The IP increases slightly from 6.45eV for methyl side chains to 6.63eV for hexyl side chains while Bis-HFI-NTCDI, the compound without side chains, has an IP of 6.55eV and accordingly does not follow the trend. For determining the electron affinity EA_{opt} , the optical energy gap is subtracted from the ionization potential. As the exciton binding energy is unknown, the resulting value, which is in the order of 3.5eV, corresponds to the lower limit of EA . According to Djurovich et al.^[19] E_B^{exc} is dependent on the energy gap and can be deduced by utilizing an empirical formula relating E_g^{opt} to the transport gap E_g^{tr} . In the given example of Bis-FI-NTCDI derivatives, it is in the order of 0.7eV. However, as the error of this method is as high as 0.9eV, this value can only be considered a very rough estimate. E_B^{exc} is represented by the blue boxes in Figure 4.2. Cyclic voltammetry is an alternative method for estimating EA . Here, the compounds are dissolved in the organic solvent DCM (dichloromethane) and reduced by an externally applied potential. As expected, the alkyl chain length has an almost negligible influence on the half wave reduction potential vs. Fc/Fc+ which is in the range of $-(1.02...1.08)V$. The corresponding electron affinities are calculated using equation (2.11) and are given in Figure 4.2. With an average of EA_{CV} of 3.5eV, the result is in good accordance with the above given estimation using the optical energy gap, thereby suggesting that the exciton binding energy is actually smaller than the estimated 0.7eV. However, both values EA_{opt} and EA_{CV} should be treated with caution as they include several approximations.

4.1.2 Thin Film Morphology

The importance of uniform layer growth for device fabrication has already been pointed out in Chapter 3. NTCDAs, which forms large crystalline islands independent of the substrate material, has been mentioned as an example to illustrate the drawbacks of materials which form non-uniform layers^[13]. According to Shirota^[146], there are several design rules for the synthesis of morphologically stable molecular glasses, i.e. materials which form amorphous thin films: These include: Increasing the number of conformers, a non-planarity of the molecular structure, an enlargement of the molecular size or the introduction of

* Measurements performed by Selina Olthof and Max Tietze, IAPP.

bulky and heavy substituents. We followed these guidelines by attaching fluorene side groups to the NTCDI core. The resulting Bis-Fl-NTCDI compounds are expected to have a higher glass transition temperature than NTCDI and thus to grow in an amorphous phase. In the following, the influence of additional alkyl side chains of varying length on the thin film morphology will be discussed.

Thin film density

The thin film density is either determined by XRR or by profilometer measurements*. Table 4.2 shows the results for all compounds except for Bis-HexFl-NTCDI which is not included in the study, due to the limited material amount. While the profilometer values scatter between 0.9 and 1.46g/cm³ in a non-systematic manner, the XRR densities show a systematic dependence: We find $\rho_{\text{XRR}} \approx (1.10 \pm 0.05)\text{g/cm}^3$ for all compounds with side chains and a slight increase to $\rho_{\text{XRR}} = 1.25\text{g/cm}^3$ for the material without side chains. XRR results are considered more reliable and are therefore used for determining film thicknesses throughout this work. According to the observed trend, a density of 1.10g/cm³ is assumed for Bis-HexFl-NTCDI.

	n	ρ_{XRR}	$\rho_{\text{profilometer}}$
		g/cm ³	
Bis-HFl-NTCDI	0	1.25	1.01
Bis-MeFl-NTCDI	1	1.12	1.31
Bis-EtFl-NTCDI	2	1.15	1.10
Bis-PrFl-NTCDI	3	1.05	1.46
Bis-BuFl-NTCDI	4	1.10	0.90

Table 4.2: Thin film densities of Bis-Fl-NTCDI derivatives determined by XRR or profilometer measurements. Data for Bis-HexFl-NTCDI are not available. n denotes the number of carbon atoms in the side chain.

Topography

The analysis of surface roughness and texture by AFM allows to draw first conclusions on the growth mode. All films are deposited onto clean glass substrates at room temperature. As in most cases the XRR densities were not yet known by the time the AFM measurement was performed, the layer thickness is different for all samples and varies between 40 and 62nm. Figure 4.3 shows an overview of AFM micrographs for all compounds on a scale of $(1 \times 1)\mu\text{m}^2$. All materials form closed layers being free of large pinholes, and accordingly, no problems are expected regarding device fabrication. However, the texture is not independent of the molecular structure: While all compounds with alkyl side chains exhibit a very smooth surface with a root mean square roughness below 1nm, Bis-HFl-NTCDI displays a granular structure and a larger rms roughness of $(2.5 \pm 0.5)\text{nm}$. This behavior might be an indication of crystalline or microcrystalline growth which is suppressed by the introduction of side chains. An influence of organic underlayers, like for instance C₆₀, is not observed (data not shown here).

Deposition on heated substrates increases the surface roughness at least by a factor of two. This is exemplarily shown in Figure 4.4 for Bis-HFl-NTCDI grown on glass which is kept at a temperature of 100°C during deposition. The rms roughness is increased from $(2.5 \pm 0.5)\text{nm}$ to $(9.0 \pm 0.5)\text{nm}$ along with the formation of larger grains due to a stronger aggregation of the molecules at elevated substrate temperature. The rms surface roughness of compounds with side chains is also slightly increased from $< 1\text{nm}$ to $(1.5 \pm 0.5)\text{nm}$ by substrate heating (results not shown here). A similar behavior is observed for various systems^[12,121,128]. In organic solar cells this effect is commonly used for optimizing the morphology of the photoactive bulk heterojunction^[106,209]. As in p-i-n and n-i-p geometry charge transport layers are deposited below the photoactive materials, their behavior upon substrate heating is an important factor. Regarding morphological issues, at least the use of Bis-Fl-NTCDI compounds with side chains is not a problem. The application of Bis-HFl-NTCDI on heated substrates might require special attention but cannot be excluded a priori.

* XRR measurements and data evaluation performed by Christoph Schünemann, IAPP. Profilometer measurements performed by Felix Holzmüller, IAPP.

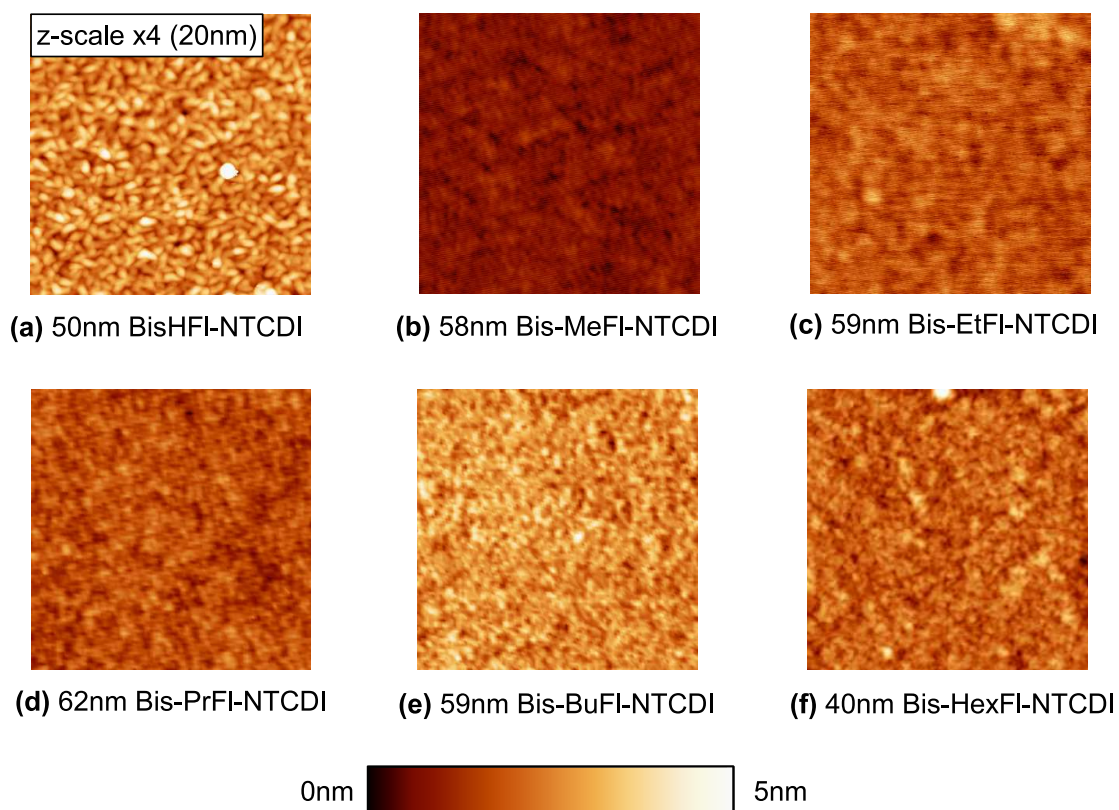


Figure 4.3: Overview of $(1 \times 1) \mu\text{m}^2$ AFM micrographs of Bis-FI-NTCDI derivatives on glass substrates. The z-scale in graph (a) is by a factor of 4 larger than the common z-scale of 5nm which is valid for all other graphs.

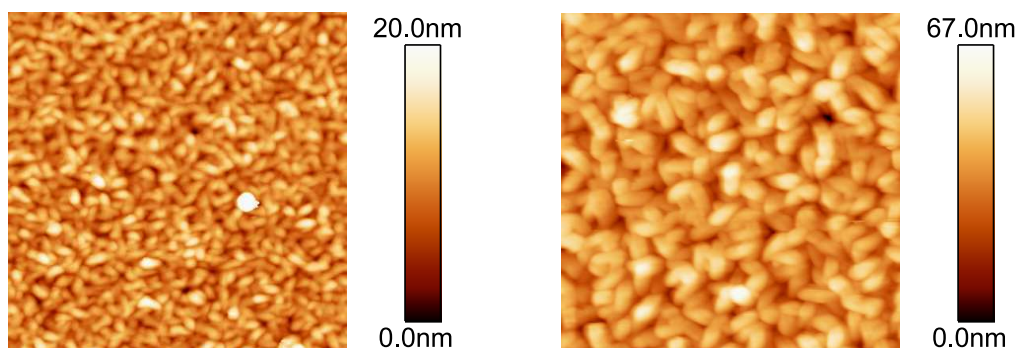


Figure 4.4: $(1 \times 1) \mu\text{m}^2$ AFM micrographs of (a) 50nm Bis-HFI-NTCDI deposited onto a glass substrate kept at room temperature and (b) 40nm Bis-HFI-NTCDI deposited onto a glass substrate heated to 100°C .

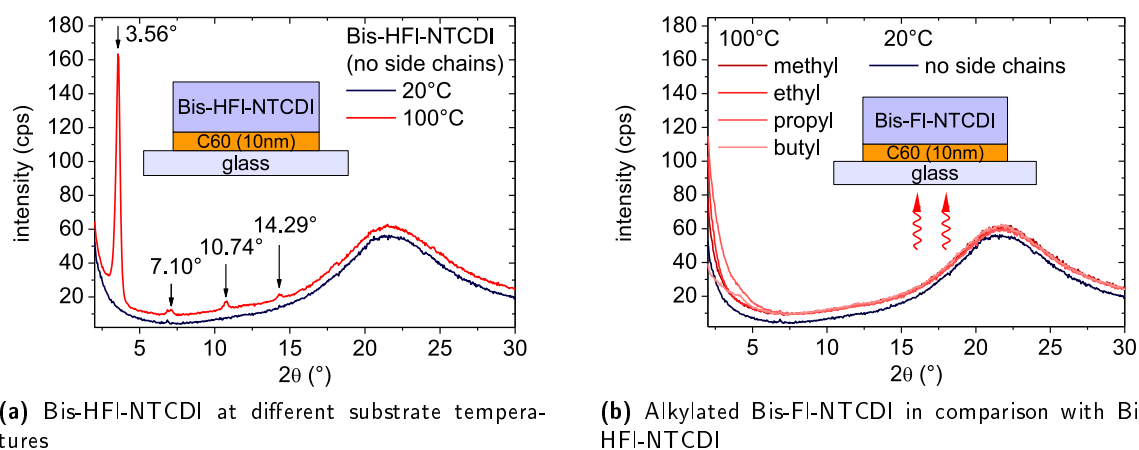


Figure 4.5: X-ray diffraction patterns of vacuum deposited Bis-FI-NTCDI thin films on glass substrates precovered with 10nm C₆₀: (a) 134nm Bis-HFI-NTCDI deposited at room temperature or at elevated substrate temperature and (b) XRD patterns of 117nm Bis-MeFI-NTCDI, 96nm Bis-EtFI-NTCDI, 139nm Bis-PrFI-NTCDI, and 118nm Bis-BuFI-NTCDI deposited at elevated substrate temperature in comparison with the room temperature XRD pattern of Bis-HFI-NTCDI.

X-ray diffraction

XRD. As AFM can only give a first hint on potential crystallinity, XRD is used to perform a more detailed analysis of this matter*. Bis-FI-NTCDI films, are deposited onto glass substrates precovered with 10nm C₆₀[†]. Again, the Bis-FI-NTCDI thickness differs from sample to sample as the correct thin film densities were not yet known when the samples were produced. However, these differences, indicated in the caption of Figure 4.5, are not expected to influence the measurement results. During the evaporation process, the substrate is either kept at room temperature or heated to 100°C in order to support potential crystallization. The samples are analyzed at IAPP using the URD-6 powder diffractometer described in Chapter 2. Figure 4.5a) compares the XRD patterns of Bis-HFI-NTCDI films deposited at different substrate temperatures. Both scans show a broad peak at large diffraction angles which can be assigned to the background signal of the amorphous glass substrate. Whereas there are no indications for crystallinity at room temperature, distinct Bragg reflections arise at $2\theta_{\text{Bragg}} = 3.56^\circ$, 7.10° , 10.74° , and 14.29° when depositing onto heated substrates. This result confirms the formation of crystalline films at elevated substrate temperature which had already been assumed by analyzing corresponding AFM samples. Moreover, the Bragg peaks are nearly equidistant, i.e. they represent higher orders of the same reflection, and hence, we conclude a preferential orientation of the molecules. By inserting a wavelength of $\lambda = 1.5406\text{\AA}$ for the incident x-rays into Bragg's law given in equation (2.5), we deduce a lattice plane distance of 2.47nm. Although the AFM results also suggest crystallinity at room temperature, this hypothesis could not be proven by XRD. It has to be noted that the URD-6 diffractometer is designed for the analysis of powders rather than thin films. Hence, nanocrystallinity at room temperature cannot be excluded at this point.

The effect of substrate heating on the alkylated compounds is studied in Figure 4.5b). It shows the diffraction patterns of compounds with side chains deposited at *elevated substrate temperature* in comparison with the just discussed *room temperature* sample of Bis-HFI-NTCDI. Again, the characteristic background signal of the glass substrate dominates the scan at high diffraction angles. No further Bragg peaks are observed and hence there are almost no differences between the curves. The introduction of side chains suppresses crystallization and leads to the formation of smooth films which are XRD-amorphous.

GIXRD. As by using the URD-6 powder diffractometer, microcrystallinity of Bis-HFI-NTCDI deposited onto room temperature substrates cannot be ruled out, a second measurement is performed with an Empyrean x-ray diffractometer that is designed for thin film analysis at PANalytical (Netherlands)[‡]. Two samples with either 50nm Bis-HFI-NTCDI or Bis-MeFI-NTCDI deposited onto 5nm i-C₆₀ are prepared at IAPP on room temperature glass substrates. They are packed in nitrogen atmosphere and

* Measurements and data evaluation performed / assisted by Christoph Schünemann, IAPP. † Due to a limited amount of material, Bis-HexFI-NTCDI had to be excluded from the study. ‡ Measurements and data evaluation performed by Dr. Alexandr Levin, IAPP.

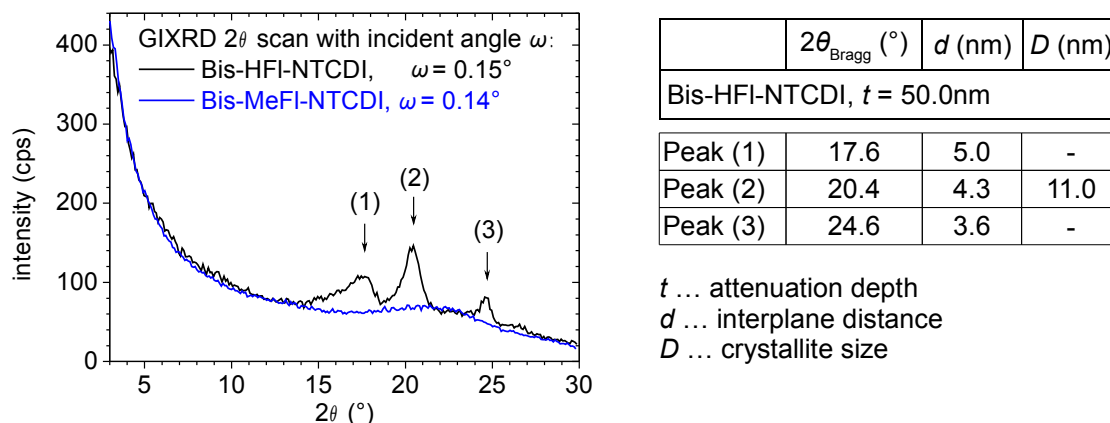


Figure 4.6: GIXRD patterns of 50nm Bis-HFI-NTCDI and Bis-MeFI-NTCDI thin films deposited onto 5nm C_{60} at room temperature. The incident angles ω are smaller than the glass substrates critical angle of refraction.

subsequently transported to PANalytical. By using small incident angles of $\omega < 1^{\circ}$ (GIXRD) the scan becomes more surface sensitive which results in a reduction of the strong background signal stemming from the glass substrate and an enhancement of the signal from the organic thin film. Figure 4.6 shows the $\omega - 2\theta$ -scans of the Bis-HFI-NTCDI sample taken at an incident angle ω of 0.15° in comparison with the signal of the Bis-MeFI-NTCDI film taken at an incident angle of 0.14° . Both angles are larger than the critical angle of total reflection of the glass substrate, which is at $\omega_{\text{cr},1} = 0.20^{\circ}$, and smaller than the critical angle of total reflection of the C_{60} film which is in the range of $\omega_{\text{cr},2} = (0.16..0.17)^{\circ}$. While for Bis-HFI-NTCDI three distinct Bragg reflections are visible at $2\theta_{\text{Bragg}} = 17.7^{\circ}$, 20.4° , and 24.6° , there is only one broad peak for Bis-MeFI-NTCDI at $2\theta_{\text{Bragg}} = 22.1^{\circ}$. As, however, the diffractogram of the crystalline sample is also slightly enhanced in the region of $2\theta = 22^{\circ}$, the peak can most likely be assigned to a background signal stemming from the evanescent wave in that penetrates into the glass substrate. The table included in Figure 4.6 gives the attenuation depth of the x-ray beam as well as the interplane distances belonging to the detected Bragg reflections, and the crystallite size estimated using the program SizeCr^[163]. The size of Bis-HFI-NTCDI crystals is approximately one fifth of the nominal layer thickness, i.e. the material is actually nanocrystalline. The fact that these crystallites cannot be detected using the URD-6 powder diffractometer can be explained by the small amount of crystals which is below the detection limit. With GIXRD a larger scattering volume is accessible and hence it is also possible to detect crystallites which are embedded in a mainly amorphous matrix.

In summary, XRD and GIXRD results confirm the formation of crystalline Bis-HFI-NTCDI thin films on heated and unheated glass/ C_{60} substrates. In contrast, there is no indication of crystallinity in thin films composed of alkylated Bis-FI-NTCDI compounds.

4.1.3 Conductivity

Doping with NDN1 - side chain dependent conductivity

The relative energy level positions of n-dopant and matrix are closely related to the efficiency of the doping process, or more precisely to the amount of charge transfer between the two species. For establishing an energetically favorable situation for this charge transfer, the ETMs electron affinity needs to be approximately equal to or larger than the IP of the dopant, i.e. NDN1 or $\text{Cr}_2(\text{hpp})_4$. In case of cationic dopants like AOB it is not the IP , but the dopants first excited state which is relevant for the charge transfer process (compare Section 1.1.3). Even if it is simplified to consider only the influence of energy level positions, it is obvious that n-doping becomes more difficult for smaller EA_{ETM} . In Section 4.1.1, the EA of Bis-FI-NTCDI is estimated to be in the range of 3.5eV which is relatively low in comparison with other ETM like C_{60} ($EA = 4.0\text{eV}^{[49]}$), NTCDA ($EA = 4.0\text{eV}^{[35]}$) or HATCN ($EA \simeq 4.8\text{eV}$). Therefore, initial conductivity tests are conducted using NDN1, the most effective of the three available n-dopants.

Figure 4.7 shows the lateral conductivity of Bis-FI-NTCDI thin films doped with either 7 or 7.5wt% NDN1. Surprisingly, the dopability strongly depends on the side chain length: While for Bis-HFI-NTCDI a good conductivity of $1.3 \cdot 10^{-4}\text{S/cm}$ is achieved, the conductivity of all alkylated compounds is smaller

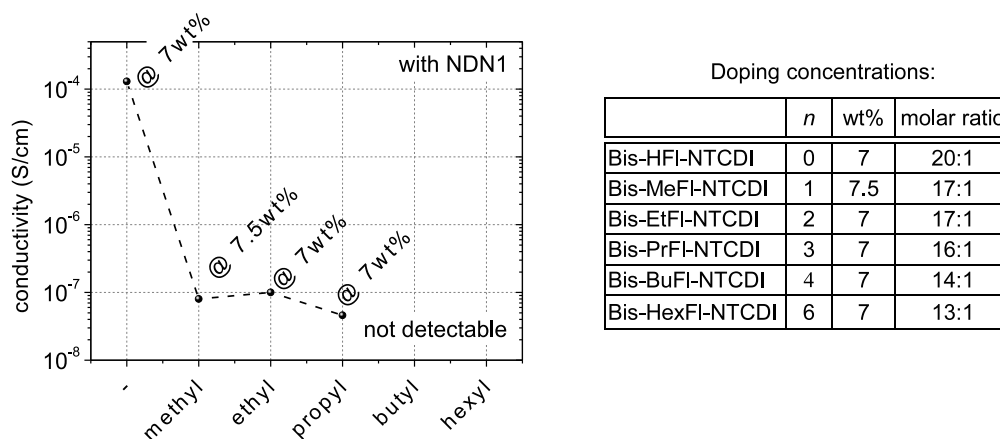


Figure 4.7: Dependence of the lateral conductivity of Bis-Fl-NTCDI derivatives on the alkyl chain length.

by at least three orders of magnitude. It has to be noted that with increasing molar mass, there are actually more dopant molecules per matrix molecule, i.e. though the weight ratio stays the same, the effective doping concentration is even enhanced. Still, we find a decrease in conductivity from $1 \cdot 10^{-7}$ S/cm for Bis-MeFl-NTCDI to $8.8 \cdot 10^{-8}$ S/cm for Bis-EtFl-NTCDI and $4.6 \cdot 10^{-8}$ S/cm for Bis-PrFl-NTCDI. The conductivities of derivatives with even longer side chains are not detectable anymore with our equipment. As according to equation (1.6), a materials conductivity is proportional to the product of electron density n and electron mobility μ_e , there are several possible explanations for this behavior: Alkylation could lead to (1) a decrease of the thin film electron affinity which affects the doping efficiency, (2) a strongly reduced charge transfer between dopant and matrix, or (3) a significantly reduced electron mobility. The first point – large changes in EA due effects not considered in the above made estimations – is unlikely as also both IP and the optical energy gap proved to be virtually independent of the alkyl chain length. However, the latter two effects can easily be caused by morphological issues like steric hindrance due to the long side chains affecting the π - π stacking. Indeed, the electron mobility of most compounds is too small to be detected by OFET measurements. The only compound which gives a reasonable result is again Bis-HFl-NTCDI with $\mu_e = (2..4) \cdot 10^{-6}$ cm²/Vs – a value which is already at the detection limit of the OFET technique. Although the microscopic mechanism responsible for the drop of the lateral conductivity with increasing side chain length cannot be identified by means of the available measurement techniques, the effect itself is an instructive example of the complicated interplay between molecular structure and physical properties. Concerning device application, only Bis-HFl-NTCDI is a promising candidate. All other materials will introduce a series resistance which is too high for allowing an efficient charge extraction.

Doping with Cr₂(hpp)₄ and AOB - concentration dependent conductivity

Due to its sufficiently high conductivity, only Bis-HFl-NTCDI is suited for performing further experiments on the doping effect involving also the less efficient dopants Cr₂(hpp)₄ and AOB. For activating the cationic dopant AOB, the vacuum chamber is additionally illuminated with a 12V halogen lamp during evaporation^[62]. The concentration dependent conductivity is determined in situ, i.e. during the co-evaporation of matrix and dopant onto one of the standard conductivity substrates described in Chapter 2. Figure 4.8 displays the lateral current flowing through a Bis-HFl-NTCDI layer doped with either Cr₂(hpp)₄ (left) or AOB (right) depending on the layer thickness and the doping concentration. As the conductivity only scales with the slope dI/dd_{ETM} of the curve, it is possible to evaluate the effect of different doping concentrations by increasing the weight ratio during deposition from 1.0 to 1.3, 2.0, 3.9, and 7.5wt%. These numbers are chosen since they correspond to well adjustable ratios of evaporation rates.

The experiment clearly reveals that the lateral conductivity increases at first strongly with increasing doping concentration and approaches saturation at higher concentrations. This type of behavior has been found before for p-doped^[28,38,81] as well as for n-doped systems^[40,58,62,64,65]. The superlinear increase at low doping concentrations is explained by Maennig et al.^[28] in the framework of a percolation model which assumes a Gaussian distribution of localized states instead of a single transport level. Charge

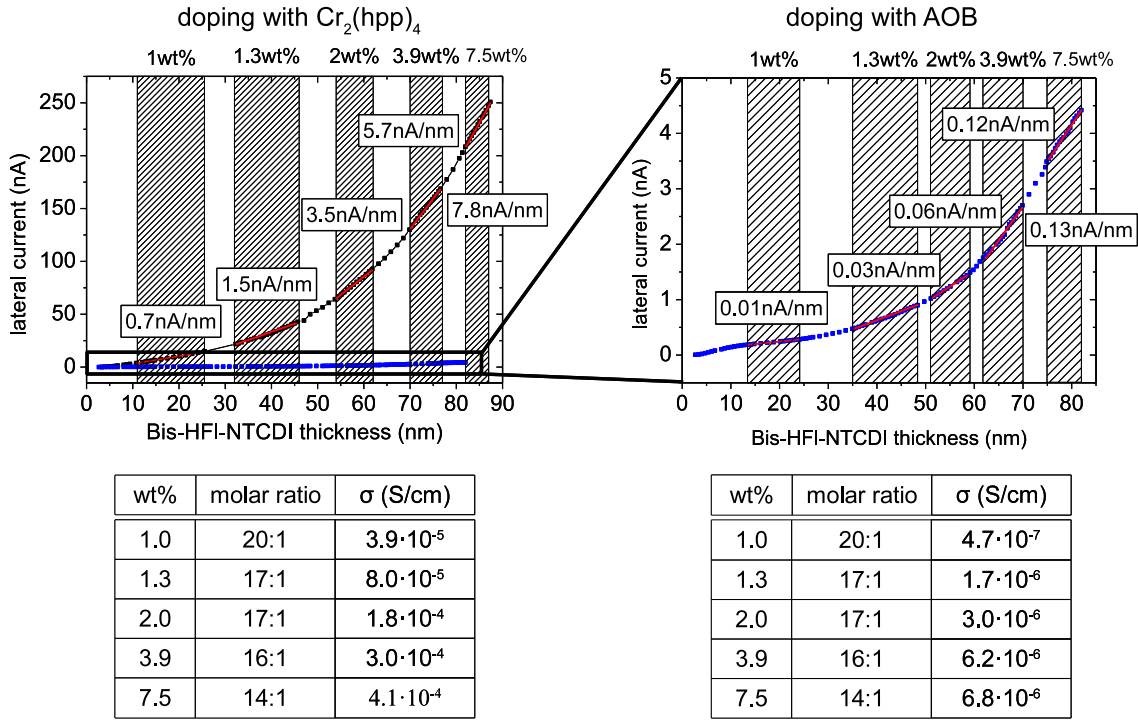


Figure 4.8: Increase of the lateral current flowing through a thin film of Bis-HFI-NTCDI doped with either $\text{Cr}_2(\text{hpp})_4$ (left) or AOB (right) depending on doping concentration given in weight percent (wt%) and layer thickness. The boxes highlight regions with the same doping concentration, red lines are linear fits of the $I(d)$ curve. Their slopes are given in nA/nm.

carriers induced by doping will at first fill up the deep trap states which is why trapping of additional free carriers becomes less likely. At the same time the Fermi level is shifted closer to the center of the DOS where more states are available for hopping. The saturation at very high doping concentrations is most likely due to the increased energetic disorder introduced by the dopant molecules^[182].

Considering doping efficiency, $\text{Cr}_2(\text{hpp})_4$ proves to be approximately as effective as NDN1. At a concentration of 7.5wt%, which corresponds to a molar ratio of 14:1, a conductivity of $3.0 \cdot 10^{-4} \text{S/cm}$ is achieved while using 7wt% NDN1, i.e. 1 dopant molecule per 20 matrix molecules, results in a conductivity of $1.3 \cdot 10^{-4} \text{S/cm}$. In comparison, the attainable lateral conductivities upon using the cationic dopant AOB are by two orders of magnitude lower. The highest value measured at 7.5wt% is only $6.8 \cdot 10^{-6} \text{S/cm}$ which is close to the limit defined usable for application.

Doping at elevated substrate temperatures

As already mentioned in the previous Section, heating the substrate during co-deposition of donor and acceptor can result in an advantageous morphology of the photoactive bulk heterojunction which is closer to the ideal interpenetrating network. When inserting a doped charge transport layer between the bottom electrode and the photoactive region, this layer will also be exposed to the elevated substrate temperature. This means that not only the organic materials need to withstand substrate heating, but also that the doping effect has to remain unaffected by temperatures in the range of approximately 100...120°C^[106,127,209]. Considering electron transport materials, this point is relevant when it comes to the fabrication of n-i-p type devices where the n-doped layer establishes the contact to the bottom electrode. For testing the suitability of doped Bis-HFI-NTCDI, the material is co-deposited with 7wt% $\text{Cr}_2(\text{hpp})_4$ onto a standard conductivity substrate which is held at a constant temperature of 100°C. Evaluating the lateral current results in a conductivity of $2.5 \cdot 10^{-3} \text{S/cm}$, a value which is by approximately one order of magnitude larger than the conductivity of an equivalent film deposited onto a room temperature substrate. The difference is due to a thermally activated behavior of the conductivity^[28,62,65]. Usually, both the mobility and the carrier density are temperature dependent, however, the contributions cannot be distinguished easily without performing further studies.

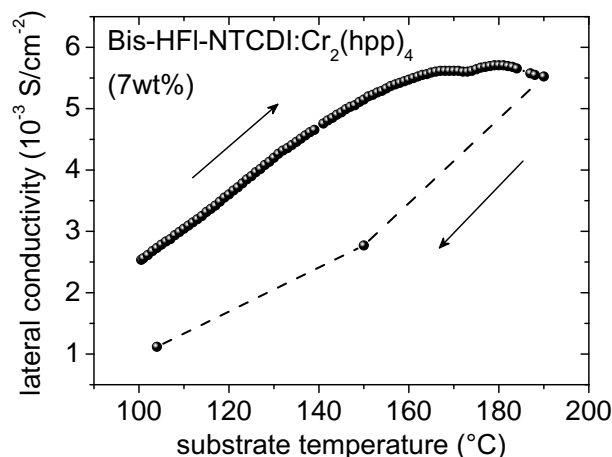


Figure 4.9: Development of the lateral conductivity of a Bis-HFI-NTCDI thin film co-deposited with 7wt% $\text{Cr}_2(\text{hpp})_4$ onto a 100°C hot substrate upon further increasing substrate temperature.

Figure 4.9 shows the evolution of the lateral conductivity when the substrate temperature is even further increased to 190°C after thin film deposition. Up to approximately 140°C the conductivity grows linearly with the substrate temperature. The slope can be related to the activation energy of the conductivity which is calculated to be 160meV . For higher temperatures the conductivity saturates at a value of $\approx 5.7 \cdot 10^{-3}\text{S/cm}$ until it eventually starts decreasing at $\approx 180^\circ\text{C}$. The values observed during the cooling process are smaller than those during heating, however, at room temperature $1.7 \cdot 10^{-4}\text{S/cm}$ are reached – a conductivity close to the one achieved when depositing onto room temperature substrates. Hence, the decrease at $> 180^\circ\text{C}$ can either be associated with a structural change which has only little impact on the doping effect or a starting decomposition which was stopped quick enough before causing permanent damage. The latter point is not unlikely as the evaporation temperature of $\text{Cr}_2(\text{hpp})_4$ is in the range of 180°C implying the possibility of a desorption process. Unfortunately, the substrate could not be heated further than 190°C as otherwise the Teflon sample holder would have been damaged. Nevertheless, the experiment can prove the excellent thermal stability of n-Bis-HFI-NTCDI layers and their suitability for an application in heated n-i-p type solar cells. Similar results are expected when using the n-dopant NDN1 which has an even higher evaporation temperature than $\text{Cr}_2(\text{hpp})_4$.

4.2 Solar Cells

Having evaluated the most important physical properties of the available Bis-FI-NTCDI compounds, the applicability in p-i-n type solar cells is tested. This Section shows only a proof-of-principle test for separating well performing and less suited materials. A comprehensive comparison of the best ETM identified in this thesis including a detailed discussion of device optimization in terms of thin film optics and the implementation of other device architectures is presented in Chapter 6.

Current-voltage characteristics

For testing the performance of n-doped Bis-FI-NTCDI derivatives, identical p-i-n type solar cells with the standard layer sequence ITO/NDP2 (1nm)/MeO-TPD:NDP2 (40nm, 2wt%)/ZnPc (5nm)/ZnPc:C₆₀ (30nm, 1:1)/C₆₀(5nm)/n-doped Bis-FI-NTCDI/Al (100nm) are fabricated in one Lesker Run. The electron transport layers are equally doped with a molar ratio of 20:1 for matrix to dopant molecules. NDN1 is used as standard n-dopant on the n-side while MeO-TPD is p-doped with NDP2. Since estimated thin film thicknesses had to be used for the deposition of all Bis-FI-NTCDI compounds, the ETM layer thickness is different in all devices and varies between 40nm for Bis-HFI-NTCDI and 69nm for Bis-PrFI-NTCDI. The corrected thickness values calculated using the XRR densities are given in Figure 4.10 along with the jV -curves of the solar cells. Table 4.3 lists the corresponding characteristic parameters.

The jV -curves show a clear dependence on the side chain length. Applying n-doped Bis-HFI-NTCDI results in a good solar cell with $V_{\text{oc}} = 0.51\text{V}$, $j_{\text{sc}} = 7.7\text{mA/cm}^2$, $FF = 52\%$ and a mismatch corrected power conversion efficiency of 2.1%. However, already when using the compound with only a short

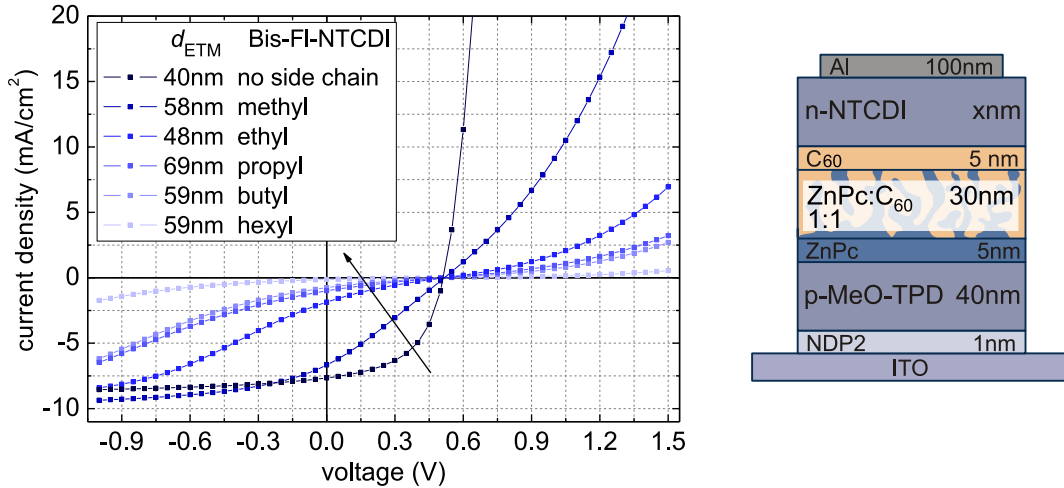


Figure 4.10: jV -curves and layer stacks of p - i - n type solar cells with different Bis-FI-NTCDI derivatives as ETM. For all compounds, the same molar ratio of 20:1 for matrix to NDN1 molecules is set. Due to the use of estimated thin film densities during deposition, the ETM thickness varies between 40 and 69nm.

	n	d_{ETM} (nm)	V_{oc} (V)	j_{sc} (mA/cm ²)	FF (%)	Sat $j(-1V)/j_{\text{sc}}$	I_{eff} (mW/cm ²)	η (%)
Bis-HFI-NTCDI	0	40	0.51	7.7	52	1.12	95	2.1
Bis-MeFI-NTCDI	1	58	0.52	6.7	27	1.40	97	1.0
Bis-EtFI-NTCDI	2	48	0.52	1.9	19	4.54	95	0.2
Bis-PrFI-NTCDI	3	69	0.52	1.0	20	6.48	98	0.1
Bis-BuFI-NTCDI	4	59	0.52	0.8	19	8.17	97	0.1
Bis-HexFI-NTCDI	6	59	0.52	0.1	18	12.77	97	0.0

Table 4.3: Characteristic parameters of p - i - n type solar cells with n -doped Bis-FI-NTCDI derivatives as ETM. The corresponding jV -curves and stacks are presented in Figure 4.10. I_{eff} denotes the mismatch corrected intensity which is used for calculating the power conversion efficiency η .

methyl group attached to the C9 position of the fluorene unit, the device performance is diminished by an s-kink. With increasing alkyl chain length, the s-kink becomes more pronounced until finally, for Bis-HexFI-NTCDI, it is completely dominating the device characteristic. While V_{oc} remains constant at 0.52V, photocurrent, fill factor and efficiency are significantly decreased. The behavior can be attributed to the large series resistance of layers of alkylated Bis-FI-NTCDI compounds which strongly reduces the current in forward direction. Furthermore, even at low negative voltages, the carrier extraction is markedly reduced as we find a strongly field dependent recombination of photogenerated charge carriers in reverse direction. This trend is in accordance with the drastic decrease in lateral conductivity observed for alkylated, NDN1 doped Bis-FI-NTCDI films outlined in Section 4.1.3. As the transport properties of the ETM dominate the solar cell performance, the variations in thin film optics due to different ETM thicknesses are secondary.

Altogether, this result confirms once more the importance of good charge transport properties for the fabrication of efficient devices. Obviously, a conductivity in the range of 10^{-7}S/cm or less is not sufficient for preventing recombination losses. Based on experience, the lower conductivity limit for the implementation of thick charge transport layers ($d_{\text{ETM}} \approx 100\text{nm}$) is 10^{-6} or rather 10^{-5}S/cm . Hence, only Bis-HFI-NTCDI is suited for application as ETM in efficient p - i - n type solar cells.

Impedance spectroscopy

IS is used for gaining a deeper understanding of the microscopic mechanisms causing the decline in device performance when using alkylated compounds*. The results are presented either as capacitance-frequency ($C(f)$) or Mott-Schottky ($C^{-2}(V)$) plots. As described in Chapter 2, the latter serves the

* Measurement and data evaluation performed / assisted by Lorenzo Burtone, IAPP.

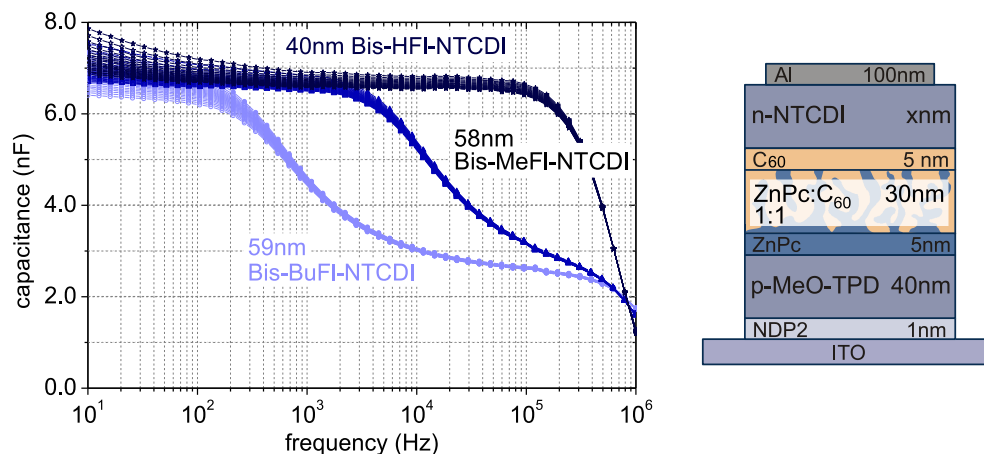


Figure 4.11: Capacitance-frequency spectra and layer stacks of *p-i-n* type devices with either 40nm Bis-HFl-NTCDI, 58nm Bis-MeFl-NTCDI or 59nm Bis-BuFl-NTCDI for bias voltages varying between 0V and -2V (arrays of curves). The corresponding solar cell characteristics and parameters are given in Figure 4.10 and Table 4.3.

evaluation of the density of ionized molecules N_{ion} within a layer. The analysis is focused on only three of the above presented devices: The solar cell with (1) Bis-HFl-NTCDI which gives the best performance, (2) Bis-MeFl-NTCDI with intermediate performance, and (3) Bis-BuFl-NTCDI which has a very poor performance.

Figure 4.11 plots the capacitance curves in the frequency range between 10 and 10^6 Hz, taken at bias voltages between 0 and -2V. Before discussing the bias voltage dependence which is similar for all devices, attention will be drawn to the **differences in curve shape**. *Bis-HFl-NTCDI* shows a behavior characteristic to a well performing solar cell. There is only one major plateau at medium frequencies corresponding to the geometric capacitance of the intrinsic ZnPc and C_{60} layers. Using $\epsilon = 5$, we calculate a thickness of 43nm which is close to the nominal thickness of 40nm. At high frequencies the device response is governed by the series resistance while at very low frequencies a small trap contribution becomes visible. These features are expected and have already been discussed in detail for the n-HATCN solar cells presented in Chapter 3. In case of *Bis-MeFl-NTCDI*, we also find the above described features. However, the plateau describing the geometric capacitance dominates a smaller frequency range and tails off at already 1kHz. As its capacitance is nearly unchanged compared to the Bis-HFl-NTCDI device, the signal can clearly be assigned to the intrinsic materials which are equal in both solar cells. At frequencies larger than 1kHz, a second plateau having a smaller capacitance and a voltage independent behavior is forming. It can be attributed to a second *RC*-circuit that has a smaller time constant. By fitting the data with a modified equivalent circuit, the additional capacitance C_2 is calculated to be 6.2nF which corresponds to a layer thickness of 46nm. Considering the moderate solar cell performance, it is reasonable to attribute C_2 to an insufficiently doped ETM even though it differs slightly from the expected geometric value of $C_{\text{ETM}} \approx 4.9$ nF. The deviation is mainly due to errors in the fit as the contribution at high frequencies is not behaving like an ideal capacitance (plateau is not horizontal). Further discrepancies might be due to a potentially incorrect density giving a too high thickness of n-Bis-MeFl-NTCDI or due to the ETM not being fully depleted. The latter case seems less likely since the high frequency capacitance plateau is not bias voltage dependent. For the last material, *Bis-BuFl-NTCDI*, the additional plateau is extended over a much broader frequency range while the frequency range in which only the photoactive layers are visible is limited to values below 200Hz. This is not surprising as the conductivity of n-doped Bis-BuFl-NTCDI is even smaller than that of n-doped Bis-MeFl-NTCDI. Hence, the characteristic time constant of the additional *RC*-element is increased. The capacitance C_2 has a value of 5.0nF which can be associated with a layer thickness of 57nm, i.e. it is in good agreement with the nominal ETM thickness of 59nm. This tells us that both the density of Bis-BuFl-NTCDI is correct and the layer is fully depleted. Overall, the results of the IS measurements are in accordance with the lateral conductivity measurements as they confirm once more that an insufficient conductivity is responsible for the poor performance of solar cells comprising alkylated Bis-Fl-NTCDI compounds.

Concerning the **bias voltage dependence** of the low frequency plateau, all investigated solar cells

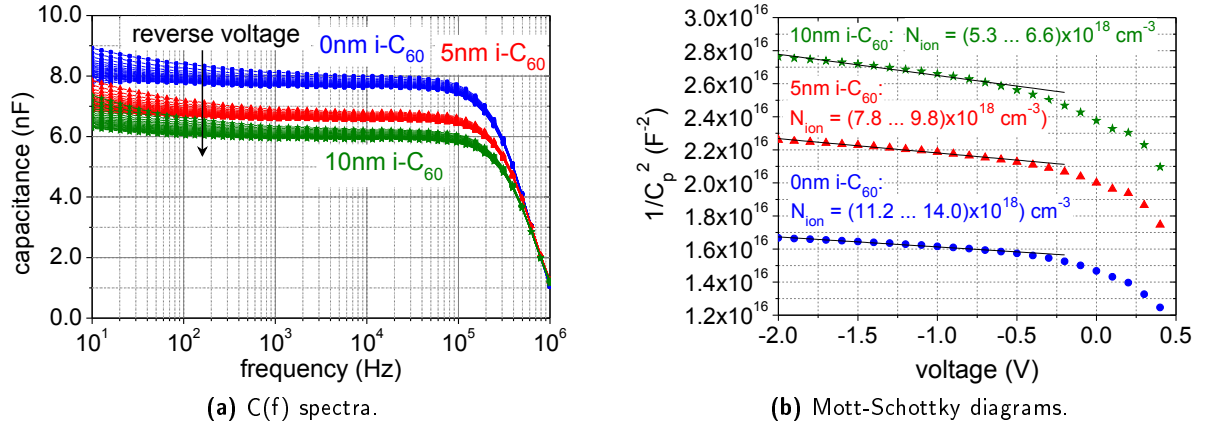


Figure 4.12: $C(f)$ spectra and Mott-Schottky plots of solar cells with n-Bis-HFI-NTCDI and a varying thickness of the intrinsic C_{60} interlayer for bias voltages between 0V and -2V.

respond in the same way. Therefore, it is sufficient to discuss the results only for one of the ETM. Figure 4.12a) displays the voltage dependent $C(f)$ plots of the above discussed n-Bis-HFI-NTCDI device along with the curves of two more devices which differ only by the thickness of the $i-C_{60}$ intermediate layer that separates the ZnPc: C_{60} bulk from the ETM. As the position of the capacitance plateau reflects the geometric capacitance of all intrinsic layers, C is highest for the device without any $i-C_{60}$ and decreases with increasing $i-C_{60}$ thickness. When evaluating the capacitance at $f = 1\text{kHz}$ and at a bias of -2V , at which the photoactive layer is completely depleted, the calculated layer thickness reflects the changes introduced by the intermediate layer: Using $\varepsilon = 5$ we find 48nm, 43nm, and 37nm when increasing the $i-C_{60}$ thickness from 0nm to 5nm and 10nm $i-C_{60}$, respectively. At bias voltages larger than -2V , we find a slightly larger capacitance, i.e. a smaller layer thickness. The bias voltage dependence is summarized in the Mott-Schottky plots displayed in Figure 4.12b). It is attributed to the penetration of dopants into the intrinsic layers during evaporation. As with increasing bias voltage residual free charge carriers are extracted from the device, the capacitance is decreasing, i.e. the depletion zone becomes larger. By evaluating the slope of the Mott-Schottky curves, it is possible to calculate the density of ionized dopants according to equation (2.32). We find that N_{ion} is increasing from $(5.3 \dots 6.6) \cdot 10^{18} \text{ cm}^{-3}$ for 10nm $i-C_{60}$ to $(7.8 \dots 9.8) \cdot 10^{18} \text{ cm}^{-3}$ for 5nm $i-C_{60}$ and finally to $(11.2 \dots 14.0) \cdot 10^{18} \text{ cm}^{-3}$ for 0nm $i-C_{60}$. This means that the blend and very thin C_{60} layers seem to allow for a better dopant penetration.

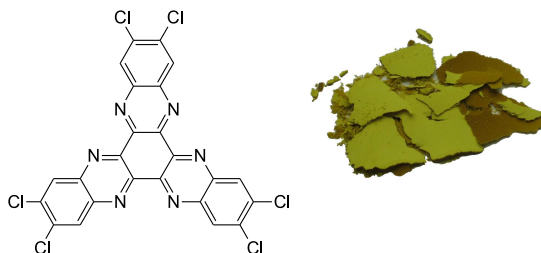
4.3 Summary

- Optical properties, thin film ionization potential, and the electron affinity determined by cyclic voltammetry in solution are nearly independent of the side chain length: We find $E_g^{opt} \approx 3.1\text{eV}$, an ionization potential (IP) in the range between 6.45eV and 6.63eV, and $EA \approx 3.5\text{eV}$ as estimated by means of the optical energy gap or from cyclic voltammetry.
- Alkylated Bis-FI-NTCDI compounds form smooth films with a surface roughness smaller than 1nm, as determined by AFM. Thin films of the side chain free compound display a granular structure and an increased rms roughness of $(2.5 \pm 0.5)\text{nm}$. Deposition on heated substrates leads to a higher surface roughness $((1.5 \pm 0.5)\text{nm}$ and $(9.0 \pm 0.5)\text{nm}$, respectively) and the formation of larger grains in case of Bis-HFI-NTCDI.
- XRD and GIXRD reveal that Bis-HFI-NTCDI forms nanocrystalline films on heated substrates and room temperature substrates while all alkylated compounds are amorphous for substrate temperatures $\leq 100^\circ\text{C}$. This means side chains alter the molecular packing and prevent crystallization.
- Doping:
 - The lateral conductivity of Bis-FI-NTCDI films n-doped with nearly equal concentrations of NDN1 is strongly dependent on the side chain length. While for the side chain free compound

a conductivity in the range of 10^{-4} S/cm is achieved, the attachment of alkyl chains causes a decrease of more than three orders of magnitude. The longer the side chain, the smaller the achievable conductivity.

- Using $\text{Cr}_2(\text{hpp})_4$ in Bis-HFI-NTCDI leads to similar conductivities as achieved with NDN1 while the values obtained with AOB are by two orders of magnitude smaller, e.g. $\sigma = 6.8 \cdot 10^{-6}$ S/cm for doping with 7.5wt% AOB.
- When depositing the doped layer onto a heated substrate, it is possible to achieve higher conductivities. For Bis-HFI-NTCDI: $\text{Cr}_2(\text{hpp})_4$ the conductivity shows a thermally activated behavior as it is increasing even further up to a temperature of $\approx 180^\circ\text{C}$. It can be concluded that the material is well suited for application in heated n-i-p type solar cells.
- Due to the poor conductivities of doped alkylated compounds, well performing solar cells can only be achieved using Bis-HFI-NTCDI. For all other derivatives, the jV -characteristics show pronounced s-kinks and a dramatic decrease of fill factor and photocurrent with increasing side chain length.
- Impedance spectroscopy confirms that a poor conductivity is responsible for the decline in power conversion efficiency. Furthermore, it reveals that a small amount of dopant molecules penetrates the intrinsic layers underneath the ETM during deposition.

5 HATNA-Cl₆ as Thick Window Layer in p-i-n Type Solar Cells



This Chapter will briefly present the material HATNA-Cl₆ as potential ETM for organic solar cells. The main focus will be on characterization with respect to the requirements of the p-i-n concept while details on the materials performance in solar cells will be presented in Chapters 6 and 7 in comparison to other ETM.

5.1 Characterization

Similar to HATCN, HATNA-Cl₆ is a star-shaped molecule containing six electron withdrawing nitrogen heteroatoms and six additional chlorine atoms at its periphery. The molecular structure and a picture of the purified material right after vacuum gradient sublimation are displayed in the Figure above. Pure HATNA-Cl₆ forms a fine yellow powder at a sublimation temperature of 360°C and evaporates at approximately 290°C from ceramic crucibles as used in the UFO and Lesker system.

Thin film density

For determining the thin film density, we perform profilometer measurements of HATNA-Cl₆ deposited onto a plain glass substrate and XRR measurements of thin films either deposited onto plain Si or Si precovered with 10nm C₆₀*. All samples yield similar results: In the order specified above, we find $\rho = 1.55\text{g/cm}^3$, 1.60g/cm^3 , and 1.65g/cm^3 . The layer thicknesses given in this thesis are referenced to the profilometer density.

Optical density

The thin film absorption properties of HATNA-Cl₆ are compared to those of the non-transparent reference material C₆₀. Figure 5.1 shows the normalized optical densities of both materials deposited onto clean quartz glass substrates. The absorption onset determines the optical energy gap which is 2.7eV for HATNA-Cl₆ and 1.7eV for C₆₀. This means that the HATNA-Cl₆ spectrum is blue shifted with respect to the C₆₀ spectrum, however, the material is still absorbing in the visible range of the sun spectrum which starts at about 380nm. As a result, it superimposes a part of the C₆₀ main absorption band. Hence, considering the application as ETM in solar cells with C₆₀ as photoactive acceptor, HATNA-Cl₆ displays partial parasitic absorption.

* Profilometer measurements performed by Felix Holzmüller, IAPP. XRR measurements and data evaluation performed by Christoph Schünemann, IAPP.

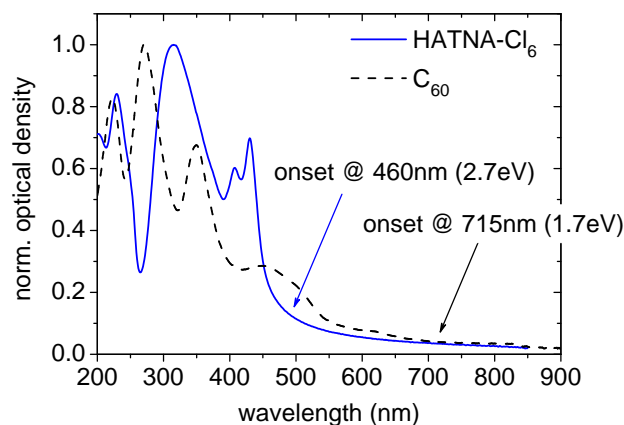


Figure 5.1: Normalized optical densities of HATNA-Cl₆ and C₆₀ thin films, both deposited onto a quartz glass substrate.

Morphology

The morphology of HATNA-Cl₆ thin films is studied by AFM and XRD measurements. For AFM, the material is deposited either onto a glass substrate kept at room temperature or a glass substrate which is heated to 80°C. Figure 5.2 shows a comparison of the resulting surface topographies on an area of (2.5x2.5)μm² using a common height scale of 15nm. Both scans are taken with a gold coated AFM tip as the standard silicon tips exhibit enhanced interaction with the sample surface that impedes the acquisition of clear images. This effect is most likely caused by the presence of the chlorine atoms at the molecules periphery as a similar behavior has been observed for other chlorinated materials. Nevertheless, images taken with a gold tip show a noise level higher than usual, accompanied by a faster wear of the tip. Regardless of these experimental issues, morphological differences introduced by substrate heating are evident: On *room temperature substrates*, HATNA-Cl₆ forms rather smooth films with an rms roughness in the order of 1nm and small grains having a size of approximately (50x50)nm². The roughness value is obtained by disregarding the few spikes that have a height > 15nm. At *elevated substrate temperature*, the roughness is doubled to (2.0 ± 0.5)nm and the grains are more than ten times larger. On closer inspection it can be seen that the material grows in a terrace-like fashion which is a clear indication of a higher degree of order or even crystallinity. A similar result has been obtained for Bis-HFI-NTCDI presented in Chapter 4.

For testing this hypothesis, XRD measurements are performed on 100nm thin HATNA-Cl₆ films deposited onto heated or unheated glass substrates which are precovered with 10nm C₆₀ to resemble the typical layer sequence in devices. When using the URD-6 powder diffractometer, both the room temperature sample and the sample deposited onto a substrate that is held at 100°C are XRD-amorphous*.

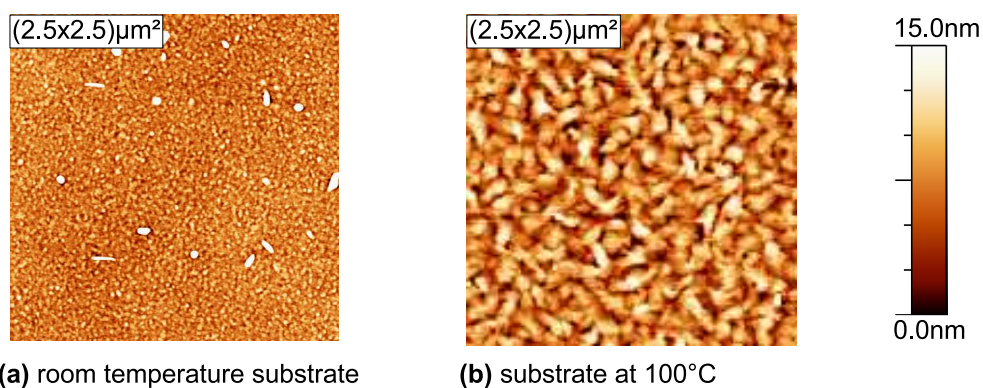


Figure 5.2: AFM micrographs of 30nm thin HATNA-Cl₆ films deposited onto glass substrates which are held at different temperatures.

* Measurement and data evaluation performed / assisted by Christoph Schünemann, IAPP.

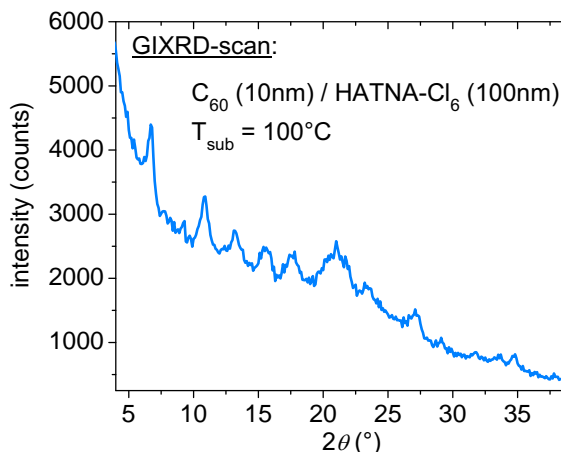


Figure 5.3: GIXRD scan of a 100nm thin HATNA-Cl₆ film deposited onto a heated glass substrate precovered with 10nm C₆₀.

To obtain a better resolution, a more detailed analysis is performed at Fraunhofer CNT (Dresden), utilizing a Bruker D8 Discover diffractometer in GIXRD scan mode*. Figure 5.3 shows the $\omega - 2\theta$ -scan of the sample that was produced at elevated substrate temperature, recorded using an incident angle of $\omega = 0.2^\circ$. In contrast to the previous measurement, we find a number of different Bragg peaks which can neither be assigned to a specific orientation of the crystals nor to a specific crystallographic phase. This means that HATNA-Cl₆ forms polycrystalline films on heated substrates.

Energy level positions

The ionization potential of HATNA-Cl₆ is determined by performing UPS on a 12nm thin film deposited onto a freshly sputtered gold foil[†]. With 7.3eV, the *IP* is close to the value determined by Barlow et al.^[150] who performed UPS and IPES studies of several HATNA derivatives on gold and found an *IP* of 7.5eV and an *EA* of 4.1eV. Both values are in accordance with the requirements of the p-i-n concept as (1) a barrier free extraction of electrons from C₆₀ to (n-)HATNA-Cl₆ is expected due to the alignment of electron affinities, and (2) the interface between both materials should be exciton blocking as a consequence of the offset in ionization potentials.

Furthermore, cyclic voltammetry of HATNA-Cl₆ dissolved in DCM is done for comparison[‡]. We find a reduction potential of (-1.35 ± 0.05) V with reference to the internal standard Fc/Fc⁺ which is converted to an estimated solid state electron affinity of 3.2eV using equation (2.11). This value is by 0.9eV smaller than the thin film *EA* determined directly by IPES, demonstrating that the extrapolation of thin film properties from solution data should always be treated with caution.

Electrical properties

The **mobility** of HATNA-Cl₆ is determined by an OFET measurement of a 30nm thin film deposited onto a standard Si substrate[§]. Evaluating the saturation regime of the source-drain characteristic yields an electron mobility of $2.2 \cdot 10^{-5} \text{cm}^2/\text{Vs}$. This value is by one order of magnitude larger than the OFET mobility of Bis-HFI-NTCDI – the most promising of the NTCDI derivatives presented in Chapter 4.

For testing the **dopability** of HATNA-Cl₆, the material is co-evaporated with either AOB, Cr₂(hpp)₄ or NDN1 using different doping concentrations. Figure 5.4a) shows the resulting conductivities over the molar doping ratio in a log-log plot. For activating the cationic dopant AOB, the vacuum chamber is additionally illuminated with a 12V halogen lamp during evaporation^[62]. As expected, using AOB results in a low conductivity. Only when the doping ratio exceeds $\text{MR} = 0.07$ (corresponding to 2.7wt% or dopant/matrix = 1:14), application-relevant values in the order of $1 \cdot 10^{-6} \text{S/cm}$ are achieved. However, at such high concentrations the doping effect saturates, i.e. there is hardly any increase in conductivity when further increasing the fraction of AOB molecules in the blend. This behavior, as well as the superlinear

* Measurement performed by Lutz Wilde, Fraunhofer CNT, data evaluation assisted by Christoph Schünemann, IAPP.

† Measurement performed by Selina Olthof, IAPP. ‡ Measurement performed by Dr. Markus Hummert, IAPP. § Measurement and data evaluation performed by Moritz Hein, IAPP.

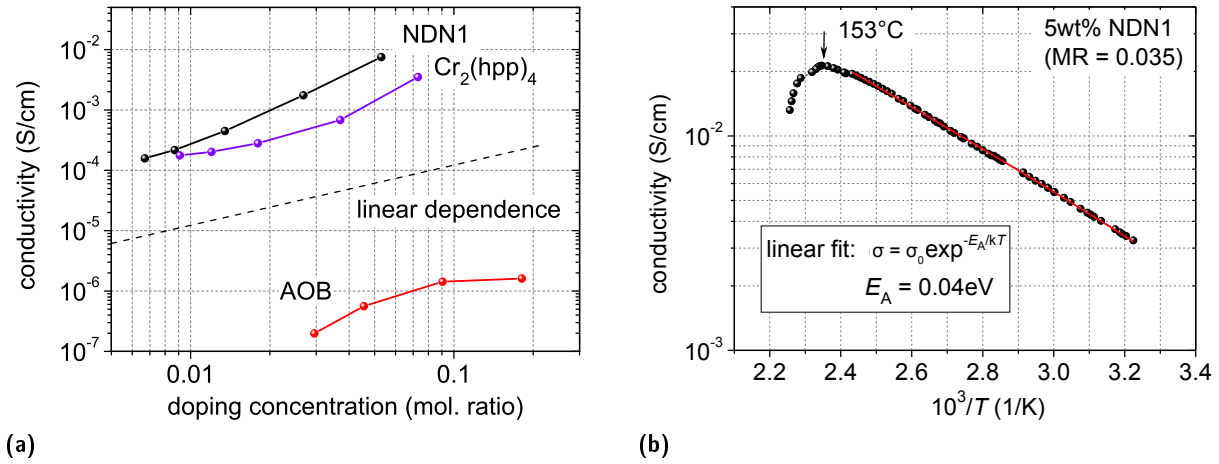


Figure 5.4: a) Concentration dependent lateral conductivity of HATNA-Cl₆ thin films doped with the molecular n-dopants NDN1, Cr₂(hpp)₄ or AOB. b) Development of the lateral conductivity of an NDN1 doped HATNA-Cl₆ layer upon substrate heating during the measurement.

increase in conductivity at lower doping concentrations, is common for doped organic semiconductors and has similarly been observed for the previously discussed Bis-Fl-NTCDI derivatives (see page 76).

Both Cr₂(hpp)₄ and NDN1 lead to conductivities above 10⁻⁴S/cm already for the lowest tested doping concentrations of MR_{Cr₂(hpp)₄}, min = 0.009 (1wt% or 1:110) and MR_{NDN1}, min = 0.0067 (1wt% or 1:150). Overall, NDN1 is slightly more effective than Cr₂(hpp)₄: For the highest tested doping concentration of MR = 0.053 (7.5wt% or 1:19), we achieve $\sigma = 7.5 \cdot 10^{-3}$ S/cm. As this value is more than sufficient for producing devices, higher doping concentrations have not been investigated and hence the saturation regime is not reached. For device application, we use 4wt% NDN1 which corresponds to a molar ratio of 0.028 (1:36).

The temperature stability of NDN1 doped HATNA-Cl₆ is evaluated by depositing a 30nm thin film, doped with a concentration of 5wt%, onto a standard conductivity substrate. In the next step, the substrate is slowly heated up to 170°C while monitoring the change of the lateral current. Up to a temperature of 153°C, the conductivity is steadily increasing from $3.3 \cdot 10^{-3}$ S/cm at room temperature to $2.1 \cdot 10^{-2}$ S/cm. As indicated in Figure 5.4b), the slope of the $\sigma(1/T)$ curve can be used to calculate the activation energy of the conductivity which yields 40meV. For temperatures higher than $\approx 150^\circ\text{C}$ the conductivity drops quickly, indicating either a structural change or a starting decomposition that is stopped quickly enough to prevent a complete destruction of the layer. After cooling back to room temperature the conductivity is only $7.4 \cdot 10^{-4}$ S/cm, i.e. it is by a factor of 4.5 smaller than the initial value. Nevertheless, an application of HATNA-Cl₆:NDN1 layers in heated n-i-p type solar cells is easily possible, since during processing the substrates are commonly heated up to a maximum of approximately 100...120°C.

5.2 Solar Cells - Proof of Principle

For proving the applicability of HATNA-Cl₆ in p-i-n type organic solar cells, this Section briefly presents the comparison of two exemplary n-HATNA-Cl₆ devices with corresponding n-C₆₀ reference devices. As a full evaluation of the materials potential primarily requires a comparison with other ETM candidates, a detailed discussion of device optimization in terms of thin film optics and the implementation of other device architectures like, for instance, n-i-p structures, will follow in the next Chapter.

The proof-of-principle test is performed using the standard p-i-n layer sequence ITO/NDP2 (1nm)/MeO-TPD:NDP2 (40nm, 2wt%)/ZnPc (5nm)/ZnPc:C₆₀ (30nm, 1:1)/C₆₀ (5nm)/n-doped ETM/Al with either 40 or 120nm n-HATNA-Cl₆ (4wt% NDN1) or n-C₆₀ (3wt% NDN1). While the smaller thickness is associated with the optimized geometry for n-C₆₀ devices, the benefits of the more transparent ETM will become significant at higher ETM thickness because any residual parasitic absorption is more prominent here. The *jV*-curves are displayed in Figure 5.5 and the characteristic parameters are given in Table 5.1. At $d_{\text{ETM}} = 40\text{nm}$ the device performance is nearly independent of the ETM: While the n-C₆₀ solar cell

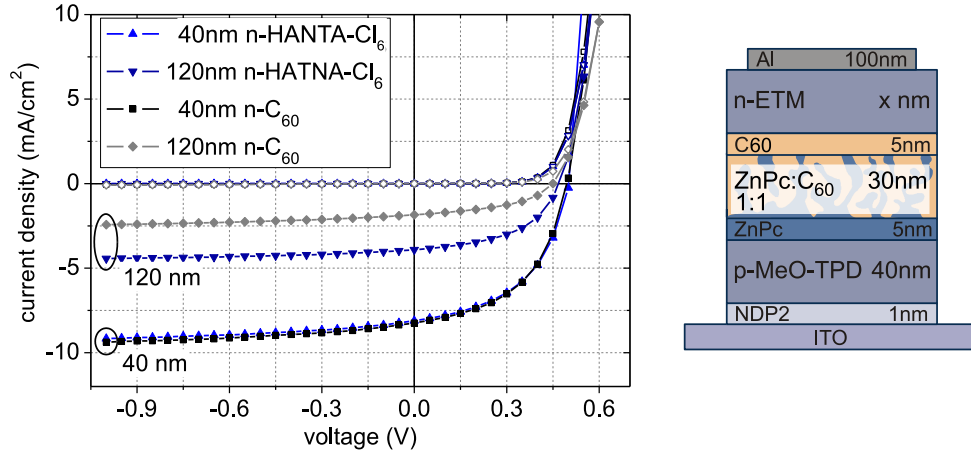


Figure 5.5: jV -curves and layer stacks of p - i - n type solar cells with either 40nm or 120nm HATNA-Cl₆ (triangles) or n-C₆₀ (squares). The corresponding characteristic parameters and effective, i.e. mismatch corrected intensities are given in Table 5.1.

d_{ETM} (nm)	ETM	V_{oc} (V)	j_{sc} (mA/cm ²)	FF (%)	Sat $j(-1V)/j_{\text{sc}}$	I_{eff} (mW/cm ²)	η (%)
40	n-HATNA-Cl ₆	0.50	8.1	50	1.13	97	2.1
40	n-C ₆₀	0.49	8.2	50	1.14	99	2.1
120	n-HATNA-Cl ₆	0.47	3.9	50	1.13	96	0.9
120	n-C ₆₀	0.45	1.8	46	1.32	97	0.4

Table 5.1: Characteristic parameters of n-HATNA-Cl₆ and n-C₆₀ solar cells displayed in Figure 5.5. I_{eff} denotes the mismatch corrected intensity which is used for calculating the power conversion efficiency η .

has a slightly higher short circuit current density of $j_{\text{sc}}^{\text{C}_{60}} = 8.2\text{mA/cm}^2 > j_{\text{sc}}^{\text{HATNA-Cl}_6} = 8.1\text{mA/cm}^2$, the open circuit voltage is marginally higher for the n-HATNA-Cl₆ device comprising $V_{\text{oc}}^{\text{HATNA-Cl}_6} = 0.50\text{V} > V_{\text{oc}}^{\text{C}_{60}} = 0.49\text{V}$. As the fill factor remains unchanged at 50%, both devices have an identical power conversion efficiency of $\eta = 2.1\%$. When increasing the ETM thickness to 120nm, the photocurrent is strongly decreased as the photoactive layers are shifted away from the optimum position with respect to thin film optics. As expected, at $d_{\text{ETM}} = 120\text{nm}$ the n-HATNA-Cl₆ solar cell is superior compared to the reference device: We find $j_{\text{sc}}^{\text{HATNA-Cl}_6} = 3.9\text{mA/cm}^2 > j_{\text{sc}}^{\text{C}_{60}} = 1.8\text{mA/cm}^2$, $V_{\text{oc}}^{\text{HATNA-Cl}_6} = 0.47\text{V} > V_{\text{oc}}^{\text{C}_{60}} = 0.45\text{V}$, and $FF^{\text{HATNA-Cl}_6} = 50\% > FF^{\text{C}_{60}} = 46\%$. Altogether this results in a higher power conversion efficiency $\eta_{\text{corr}}^{\text{HATNA-Cl}_6} = 0.9\% > \eta_{\text{corr}}^{\text{C}_{60}} = 0.4\%$. Although the ETM thickness is more than doubled, the fill factor is only slightly affected and decreases only four percentage points. This fact demonstrates that doping is a powerful tool for enhancing the transport properties of organic semiconductors.

However, even though at $d_{\text{ETM}} = 40\text{nm}$ the n-HATNA-Cl₆ solar cell proves to be comparable to the n-C₆₀ reference device, the advantage of the more transparent spacer layer is not as high as expected. For assessing this finding in a more general context, the examination of the window layer effect will be extended to other ETM, including n-Bis-HFI-NTCDI and NTCDA in the next Chapter.

5.3 Summary

- Having an optical energy gap of 2.7eV, HATNA-Cl₆ is not completely transparent in the visible range of the sun spectrum and overlaps the C₆₀ absorption spectrum at wavelengths smaller than 460nm.
- HATNA-Cl₆ forms smooth films with an rms roughness in the order of 1nm on unheated or 2nm on heated glass substrates, exhibiting polycrystallinity in the latter case.
- Both the ionization potential of 7.3eV and the electron affinity with 4.1eV^[150] fulfill the requirements of the p - i - n concept.

- The lateral conductivity of HATNA-Cl₆ is effectively enhanced by n-doping with either AOB, Cr₂(hpp)₄, or NDN1. At the highest doping concentrations tested, conductivities of $\sigma_{\text{AOB}} = 1.6 \cdot 10^{-6} \text{S/cm}$ (MR = 0.18), $\sigma_{\text{Cr}_2(\text{hpp})_4} = 3.5 \cdot 10^{-3} \text{S/cm}$ (MR = 0.07), and $\sigma_{\text{NDN1}} = 7.5 \cdot 10^{-3} \text{S/cm}$ (MR = 0.05) are achieved, respectively. Thin films doped with Cr₂(hpp)₄ are stable against post-annealing up to a temperature of $\approx 150^\circ\text{C}$.
- n-HATNA-Cl₆ is successfully implemented in p-i-n type solar cells which show either comparable ($d_{\text{ETM}} = 40\text{nm}$) or superior ($d_{\text{ETM}} = 120\text{nm}$) performance to n-C₆₀ reference devices.

6 Comparison of Transparent ETM in p-i-n and n-i-p Type Solar Cells

Having identified Bis-HfI-NTCDI and HATNA-Cl₆ as most promising ETM candidates in previous Chapters, a comprehensive comparison of the ETM performance with regard to the performance of the reference materials C₆₀ and NTCDA is needed. For quantifying the anticipated benefits, optical simulations of p-i-n and n-i-p type devices with varying ETM type and thickness are performed, showing that a decreased parasitic absorption in the visible range of the sun spectrum is expected to lead to an enhanced short circuit current density of respective solar cells. Subsequently, the reference ETM n-C₆₀ is investigated more closely by 1.) examining whether or not a fraction of the n-doped C₆₀ contributes to the photocurrent, and 2.) studying edge effects which affect the actual photoactive area of the solar cell. Based on these initial tests, the performance of devices comprising either n-Bis-HfI-NTCDI, n-HATNA-Cl₆, n-NTCDA or n-C₆₀ is compared. While for an ETM thickness < 50nm the anticipated photocurrent enhancement is only observed in solar cells with n-NTCDA, the potential of the other transparent materials develops at larger ETM thickness. Several possible origins for the deviation between the experimental results and the optical simulation are discussed, including parasitic absorption by dopant molecules and light scattering at the ETM/Al contact. As the unexpectedly small gain in short circuit current upon implementing transparent ETM is complemented by improved open circuit voltages and fill factors, the overall power conversion efficiencies are considerably improved compared to those of reference devices comprising the parasitically absorbing n-C₆₀. Finally, the performance of representative n-i-p devices is presented for proving the applicability of n-Bis-HfI-NTCDI and n-HATNA-Cl₆ in inverted device structures.

6.1 Optical Simulations

Optical simulations are performed for determining the optimum device architecture and the anticipated photocurrent gain by replacing the parasitically absorbing ETM n-C₆₀ by one of the new materials. For this, we model p-i-n and n-i-p type solar cells comprising either n-C₆₀, n-HATNA-Cl₆, n-Bis-HfI-NTCDI, or n-NTCDA using the program OSOLemio. HATCN is excluded from the study as its high EA limits its applicability to only few device geometries. As input for the simulation, the optical constants of all materials constituting the layer stack are needed. While the majority of the required data is available from the IAPP database, n & k values of Bis-HfI-NTCDI and HATNA-Cl₆ are determined by evaluating

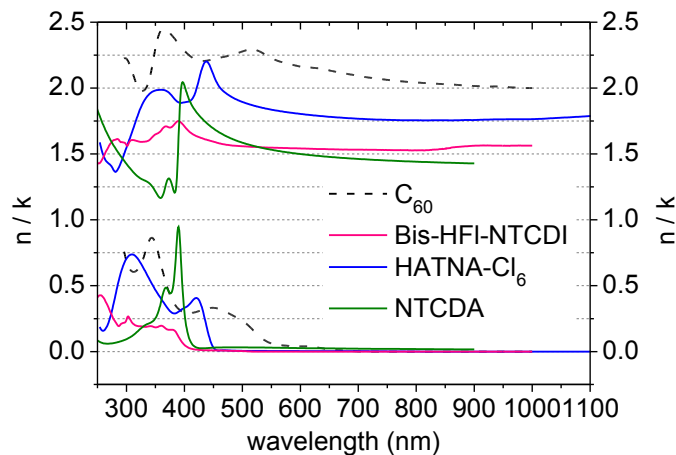


Figure 6.1: Refractive indices n and extinction coefficients k of the ETM tested in this thesis.

reflection and transmission data of several single layers of different thickness deposited onto quartz glass substrates. Figure 6.1 shows a comparison of the n and k values of C_{60} , Bis-HFI-NTCDI, HATNA- Cl_6 , and NTCDI. While the extinction coefficients reflect the absorption properties of the materials, the refractive index determines the propagation of light waves within the respective medium and is highest for C_{60} in the whole spectral range. At a wavelength of 630nm, which corresponds to the second absorption maximum of ZnPc, we find $n_{C_{60}} = 2.15$, $n_{HATNA-Cl_6} = 1.79$, $n_{Bis-HFI-NTCDI} = 1.54$, and $n_{NTCDI} = 1.49$. The latter two values resemble the refractive index of glass which is usually in the order of 1.5 (compare Figure 4.1b). Unfortunately, it is not easily possible to determine the n & k values of n-doped materials. As the standard dopant NDN1 is not air-stable and n-doping itself is sensitive to oxygen which is known to act as p-dopant^[66,68?,69], the setup for measuring the respective optical layer properties would have to be located in an inert atmosphere. Although p-doped layers are much easier to handle, n & k values of only few p-doped materials are currently known.

Based on the optical constants, OSOLemio calculates the optical field distribution within a layer stack using the transfer matrix algorithm^[174]. By this, the total spectral absorption as well as the absorption profile giving the number of photons absorbed per second and area at each position of the stack are determined. In a second step, this information is utilized to estimate the short circuit current density, assuming that all excitons generated in the photoactive intrinsic layers contribute to the photocurrent (IQE = 1). To be as close as possible to experimental results, the sun spectrum of our solar simulator, scaled to the intensity which is used for the measurement of actual solar cells, is used as input illumination source.

6.1.1 p-i-n Type Devices

The simulation is based on the p-i-n standard stack which has already been presented in previous Chapters. Since the optical constants of most doped layers and the dopants themselves are not known, the simulated structure is simplified and reduced to glass (1.1mm)/ITO (95nm)/MeO-TPD (40nm)/ZnPc (5nm)/ZnPc: C_{60} (30nm, 1:1)/ C_{60} (5nm)/ETM (0...210nm)/Al (100nm) (compare Figure 6.3). The influence of the ETM thickness on the absorption profile is exemplarily shown for n- C_{60} devices in Figure 6.2. It is a direct consequence of the optical interference pattern which forms upon the reflection of the incident light on the aluminum back contact. With increasing ETM thickness, the photoactive layers are shifted into the interference maximum until the optimum position is reached at $d_{C_{60}} = 40$ nm, while for even thicker n- C_{60} layers, the photon flux absorbed in the ZnPc: C_{60} bulk decreases again. Additionally, the absorption profiles give an illustration of the losses which occur in the aluminum electrode and the nominally n-doped ETM: A significant amount of photons is absorbed parasitically in parts of the device that do not contribute to the photocurrent. By using transparent ETM instead of n- C_{60} , it should be possible to avoid the loss mechanism arising from the charge transport layers.

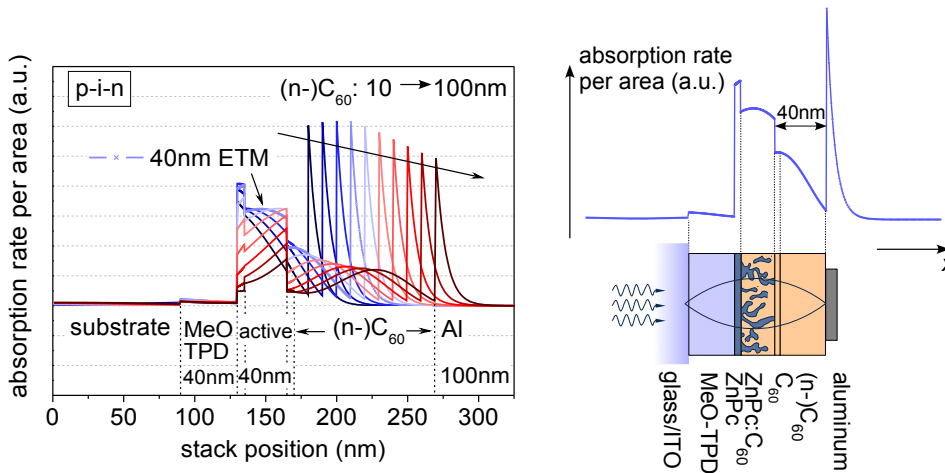


Figure 6.2: Absorption profiles of p-i-n type structures with varying n- C_{60} layer thickness obtained using the program OSOLemio. The calculation is based on the layer stack depicted in Figure 6.3. The right picture relates the absorption profile to a schematic representation of the optical field distribution which has its maximum in the active area when using the optimum n- C_{60} thickness of 40nm.

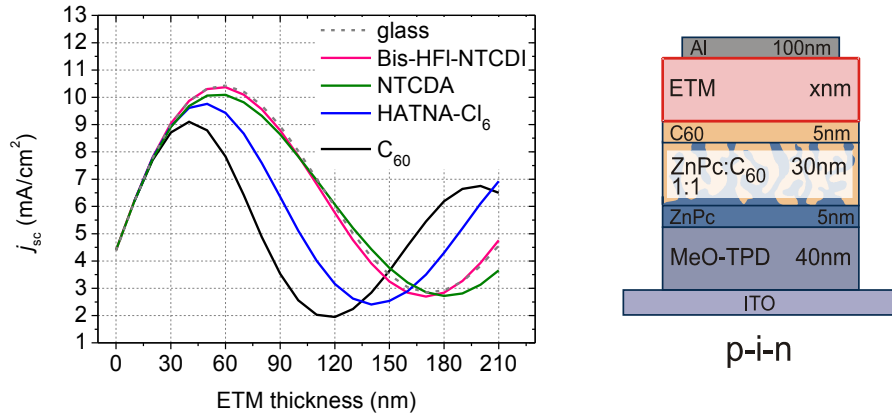


Figure 6.3: Calculated short circuit current densities when evaluating the absorption rate of the photoactive layers ZnPc (5nm)/ZnPc:C₆₀ (30nm, 1:1)/C₆₀ (5nm) that are embedded into the p-i-n type structure shown on the right. The ETM is either composed of C₆₀, HATNA-Cl₆, NTCDA, or Bis-HfI-NTCDI while its thickness varies between 0 and 210nm. The dashed grey curve shows the $j_{sc}(d_{ETM})$ -curve for an ETM which has the same optical properties as glass.

As described above, the absorption profiles are used for calculating a theoretical short circuit current density for each layer stack. Figure 6.3 depicts the resulting $j_{sc}(d_{ETM})$ curves in the range of $d_{ETM} = 0 \dots 210$ nm for devices comprising C₆₀ (black), HATNA-Cl₆ (blue), Bis-HfI-NTCDI (pink), and NTCDA (green) as spacer material between aluminum top contact and the photoactive area. The dashed grey curve represents the theoretical case of an organic material that has the same optical properties as glass. The modification of the ETM does not only cause a general increase in the achievable j_{sc} when more transparent compounds are used, but also a broadening of the curve accompanied by a shift of the j_{sc}^{max} position. The latter effect is due to the differences in refractive indices pointed out above. The lower the refractive index, the broader the curve: While the photocurrent maximum is expected at $d_{ETM} = 40$ nm for C₆₀ devices, it is moved to 50nm when inserting HATNA-Cl₆ and to 60nm for Bis-HfI-NTCDI and NTCDA. In the simulation, both Bis-HfI-NTCDI and NTCDA show nearly the same behavior as would be anticipated from glass. The relative increase in current density is expected to be in the order of 7% for HATNA-Cl₆, 11% for NTCDA, and even 15% for Bis-HfI-NTCDI. Hence, based on the simulation, we expect significant benefits by replacing n-C₆₀.

6.1.2 n-i-p Type Devices

Although the focus of this work will remain on p-i-n type devices, the simulation results for n-i-p structures are discussed for comparison. Here, the layer sequence glass (1.1mm)/ITO (95nm)/ETM (0...150nm)/C₆₀(5nm)/ ZnPc:C₆₀ (1:1, 30nm)/BF-DPB:NDP2 (65nm, 10wt%)/Al (100nm), as shown in Figure 6.5, is used as input for the simulation. While the ETM are again assumed intrinsic, the n & k values of the p-doped BF-DPB are known. Figure 6.4a) and 6.4b) compare the absorption profiles of devices with varying C₆₀ or Bis-HfI-NTCDI layer thickness. The distance of the photoactive layers to the reflecting back electrode stays constant, and thus also their position with respect to the antinode of the optical interference pattern is unchanged. At $d_{ETM} = 70$ nm, the use of transparent ETM is expected to result in a j_{sc} increase of 18% for HATNA-Cl₆, 24% for NTCDA, and 26% for Bis-HfI-NTCDI compared to the reference material C₆₀. In the latter case, the incident light has first to pass through a parasitically absorbing layer which causes a general decrease in intensity before the light even reaches the D/A heterojunction. Hence, the presence of n-C₆₀ reduces the absorption rate in the ZnPc:C₆₀ bulk. In contrast, when utilizing Bis-HfI-NTCDI as ETM, the absorption rate increases at first until a maximum is reached at $d_{ETM} = 70$ nm. It has to be noticed, that not only n-C₆₀ but also p-BF-DPB displays residual parasitic absorption which is disadvantageous for device performance.

Figure 6.5 depicts the resulting short circuit current densities for all ETM. As j_{sc} of n-C₆₀ devices is steadily decreasing with increasing ETM thickness, it can be concluded that m-i-p devices, in which the photoactive region is directly deposited onto the ITO ground contact, are expected to produce a higher photocurrent than n-i-p devices that comprise a parasitically absorbing ETM. For transparent ETM the $j_{sc}(d_{ETM})$ curve displays a broad maximum, whose height and position is – similar as for p-i-n devices –

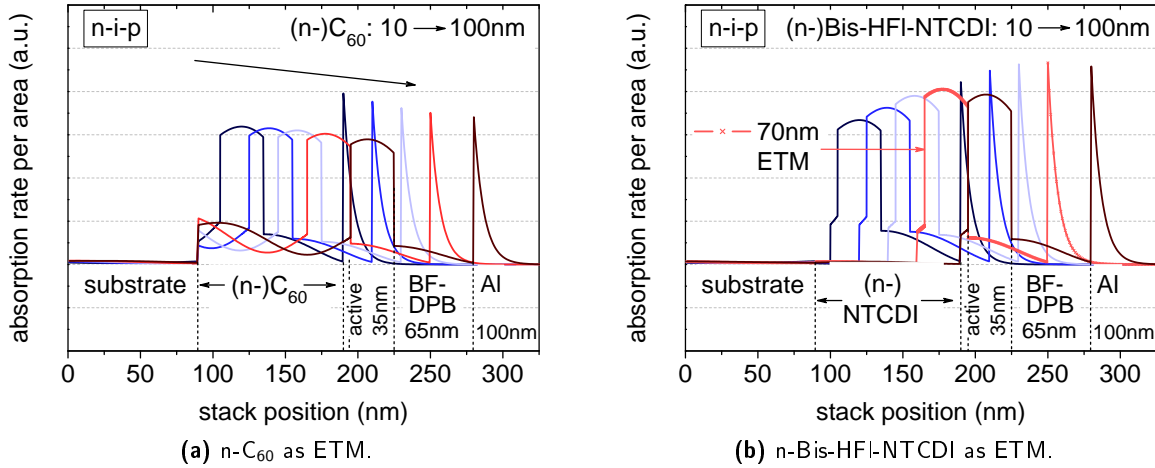


Figure 6.4: Absorption profiles of n-i-p type solar cells with varying ETM layer thickness obtained using the program OSOLemio. The calculation is based on the layer stack depicted in Figure 6.5.

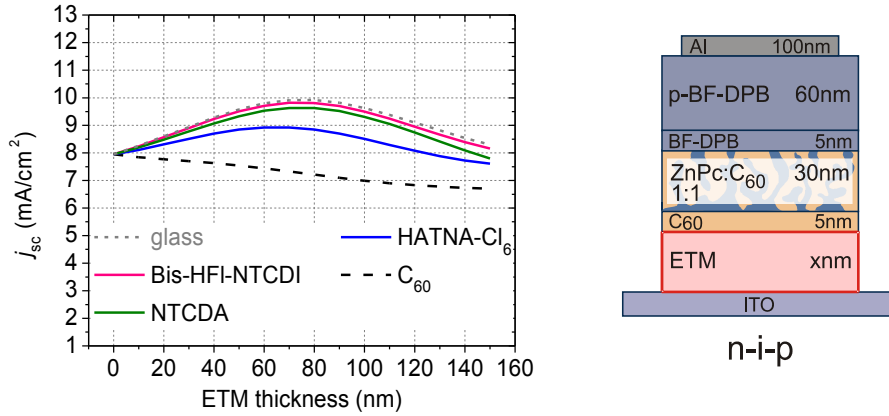


Figure 6.5: Calculated short circuit current densities when evaluating the absorption rate of the photoactive layers C₆₀ (5nm)/ZnPc:C₆₀ (30nm, 1:1) that are embedded in a n-i-p type structure as shown on the right. The ETM is either composed of C₆₀, HATNA-Cl₆, NTCDA, or Bis-HFI-NTCDI while its thickness varies between 0 and 150nm. The dashed grey curve shows the $j_{sc}(d_{ETM})$ -curve for an ETM which has the same optical properties as glass.

dependent on the degree of transparency and the materials refractive index.

6.2 Solar Cells

6.2.1 n-C₆₀ as Reference ETM

Exciton quenching in n-C₆₀

Up to now, non-transparent charge transport materials were generally referred to as *parasitic absorbers* assuming that they „steal“ photons from the photoactive layers. It is commonly expected that excitons generated in doped materials are readily quenched at the dopant molecules which are evenly distributed in the bulk, i.e. that they recombine non-radiatively before they are able to diffuse to the separating donor/acceptor heterojunction. Therefore, the optical simulation is based on the assumption that layers composed of n-doped C₆₀ do not contribute to the photocurrent. For confirming this hypothesis, the spectral response of six p-i-n type solar cells with a flat ZnPc/C₆₀ heterojunction and varying i-C₆₀/n-C₆₀ configurations is examined. In each device, having the general structure ITO/NDP2 (1nm)/MeO-TPD:NDP2 (40nm; 2wt%)/ZnPc (20nm)/C₆₀ (0 → 50nm)/C₆₀:NDN1 (50 ← 0nm; 3wt%)/Al (100nm), the layer thickness of intrinsic C₆₀ and n-doped C₆₀ adds up to 50nm, i.e. the absorption properties of

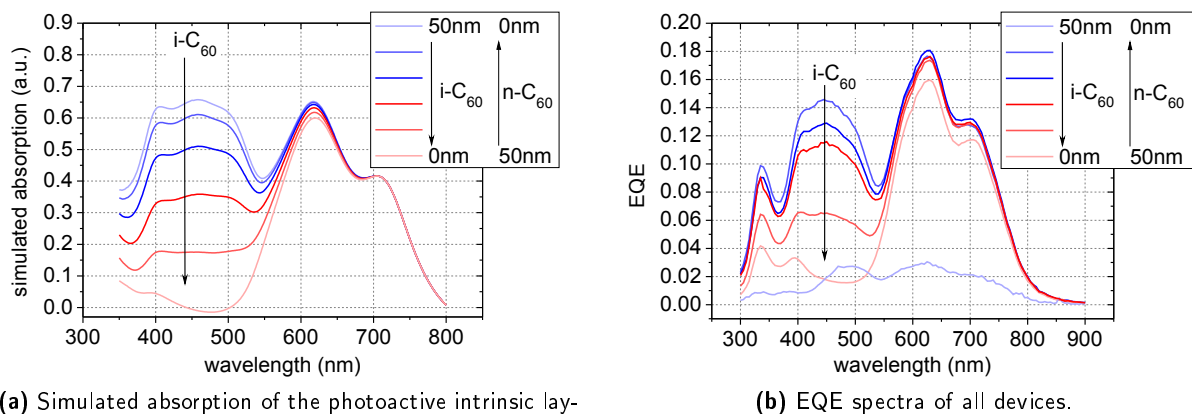


Figure 6.6: Photocurrent generation in solar cells with the structure ITO/NDP2 (1nm)/p-MeO-TPD (40nm, 2wt%)/ZnPc (20nm)/C₆₀ (0, 10, 20, 30, 40, 50nm)/C₆₀:NDN1 (50, 40, 30, 20, 10, 0nm; 3wt%)/Al (100nm). The total layer thickness of intrinsic and n-doped C₆₀ is 50nm in each case.

all six layer stacks are virtually equal, provided that the presence of n-dopants has a negligible influence. This presumption is validated by the absorption spectra of complete devices: There is only a slight decrease of the C₆₀ absorption in the region between 400 and 500nm as the fraction of dopant molecules increases with respect to the intrinsic material.

For visualizing the expected result, Figure 6.6a) displays the simulated absorption of the intrinsic photoactive materials ZnPc and C₆₀ as calculated by OSOLemio. While the ZnPc absorption is only slightly influenced by the variations of the acceptor/ETM combination, the C₆₀ absorption is steadily decreasing as the i-C₆₀ content is reduced to 0nm. This trend is indeed reproduced by the EQE spectra of the actual devices which are shown in Figure 6.6b). For determining the role of n-C₆₀ for the current generation, the performance of the solar cell comprising a direct ZnPc/n-C₆₀ interface is decisive. In the absence of intrinsic C₆₀, the EQE signal in the wavelength region between 400 and 500nm is completely suppressed, thus confirming that excitons which are created in n-C₆₀ cannot be converted into free charge carriers. Furthermore, the EQE spectrum is markedly reduced in the ZnPc absorption region which indicates that even a fraction of the ZnPc excitons is quenched at the interface to the ETM. In order to avoid this loss mechanism, all solar cells shown in this thesis comprise a 5nm thin i-C₆₀ layer in between the ZnPc:C₆₀ bulk and the n-doped ETM.

Apart from this finding, there is another noticeable result. The solar cell which is free of n-C₆₀ displays a significant deviation from the response expected from the optical simulation: We find a very low EQE in the whole spectral range as the device performance is dominated by a strong s-kink in the *jV*-curve (not shown here). This behavior has frequently been observed for devices with i-C₆₀/metal cathodes. It can be caused by several effects^[12]: On the one hand, metal/organic interfaces are expected to be exciton quenching, thereby inducing a reduction of the photocurrent, while on the other hand, the topmost C₆₀ layers are likely to be affected by chemical and / or morphological modifications caused by the Al deposition and by a potential penetration of Al into the organic material. Particularly, the latter two processes can change the interface energetics in a way that leads to the formation of an electron injection or extraction barrier manifesting in the observed s-kink. Clearly, for p-i-n type devices, the presence of a buffer material between the photoactive i-C₆₀ and the metal cathode is indispensable. Although also undoped materials like BPhen or BCP are suitable for this purpose^[12,119], the use of doped transport materials is beneficial as their thickness can be tuned freely without significantly affecting the devices series resistance^[196].

Area Dependent Photocurrent

For obtaining the current density, the measured current is usually divided by the area of the solar cell, here defined as the overlap of ITO bottom contact and metal top contact. The average pixel area of a standard Lesker substrate is determined by measuring the lateral dimensions of the respective electrodes with an optical microscope and yields 6.44mm². However, in this approach variations in the width of

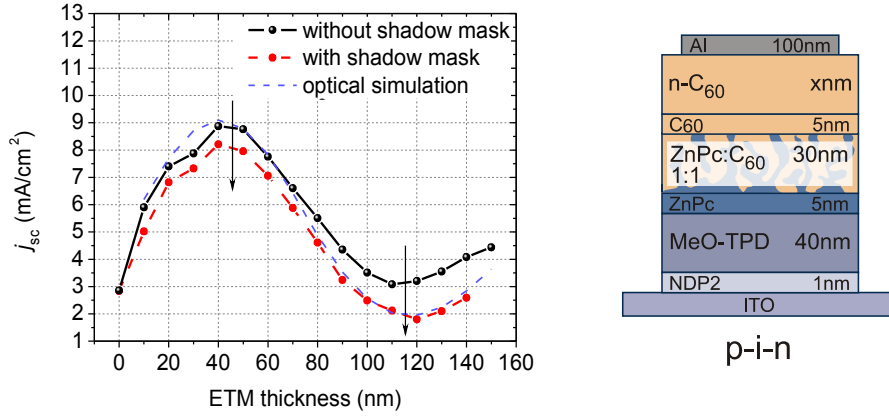


Figure 6.7: Short circuit current densities and layer stacks of p-i-n type solar cells with varying n-C₆₀ thickness measured with and without shadow mask in comparison with the values expected from the optical simulation.

the aluminum top electrode or possible edge effects are not taken into account. For instance, the actual active area might be underestimated if the metal evaporation does not produce a sharp edge.

To evaluate the actual photoactive area in n-C₆₀ solar cells, jV -characteristics of p-i-n type devices with varying ETM thickness are measured either without a shadow mask, assuming a photoactive area of 6.44mm², or using an aperture with a well-defined area of 5.10mm². The investigated layer stack is identical to the one that was used for the optical simulation. It is displayed along with the $j_{sc}(d_{ETM})$ curves in Figure 6.7. Generally, the short circuit current density follows the trend predicted by the simulation, showing a maximum at $d_{n-C_{60}} = 40$ nm and a minimum at $d_{n-C_{60}} = 120$ nm. However, j_{sc} is considerably reduced when measuring with aperture. The effect has a particularly large impact on devices with thick n-C₆₀ layers, for which the current is approximately 50% smaller, while the reduction in the current maximum is in the order of 10%. This behavior cannot simply be explained by a general overestimation of the actual photoactive area, as dividing the assumed area of 6.44mm² by a constant factor in order to adapt j_{sc} is not possible.

For identifying the nature of the observed effect, the area dependence of j_{sc} is examined more closely for two selected solar cells – *device nC₆₀-Max* with 40nm n-C₆₀ and *device nC₆₀-Min* with 120nm n-C₆₀. The illuminated area is varied by covering the glass substrate with black anodized metal plates having rectangular apertures of different sizes at the positions of the four pixels. Figure 6.8a) shows that for both devices the short circuit current increases linearly with the illuminated area. Extrapolating the straight line to the current that is measured in the absence of a mask yields the effective photoactive area of the unmasked device. For solar cell nC₆₀-Max, we find 6.8mm² while for solar cell nC₆₀-Min, the area needed for generating the measured current is as large as 10.2mm². This result emphasizes once more that the cause for the excess current cannot be a mere geometry issue. Since metal masks which cover exactly the overlap area of ITO bottom electrode and aluminum cathode are not available, homemade shadow masks are built. As depicted in Figure 6.8b) they consist of a piece of aluminum foil that is sandwiched between two stripes of insulating tape. This way the penetration of residual light is effectively blocked while at the same time back reflections of the incident light at the aluminum foil are prevented. Using these masks, either (1) the complete area surrounding the examined pixel, or (2) the area parallel to the ITO stripe, or (3) only the area parallel to the aluminum top contact is covered. Interestingly, options (1) and (2) result in the same short circuit current while for the third configuration, the measured I_{sc} is considerably enhanced. For solar cell nC₆₀-Min, we find $I_{sc}^{(1)} = 0.12$ mA, $I_{sc}^{(2)} = 0.12$ mA and $I_{sc}^{(3)} = 0.18$ mA, which is only slightly smaller than the current measured in the absence of an aperture that equals $I_{sc}^{(no\ mask)} = 0.20$ mA. Solar cell nC₆₀-Max responds in the same way. Here, we measure $I_{sc}^{(1)} = 0.46$ mA, $I_{sc}^{(2)} = 0.46$ mA, $I_{sc}^{(3)} = 0.54$ mA, and $I_{sc}^{(no\ mask)} = 0.56$ mA. Due to unavoidable inaccuracies when placing the masks onto the edges of the electric contacts, an error of at least $\Delta I_{sc} = 0.02$ mA has to be assumed. In both devices the difference between unmasked and fully masked device (3) is therefore approximately (0.10 ± 0.04) mA. The presence of this constant background current, which roughly corresponds to 50% of the I_{sc} of solar cell nC₆₀-Min, but to „only“ 18% of I_{sc} produced by solar cell nC₆₀-Max, explains the non-proportional scaling of j_{sc} for different ETM thickness. Interestingly, the excess current is only generated at the edges which are situated above the ITO ground

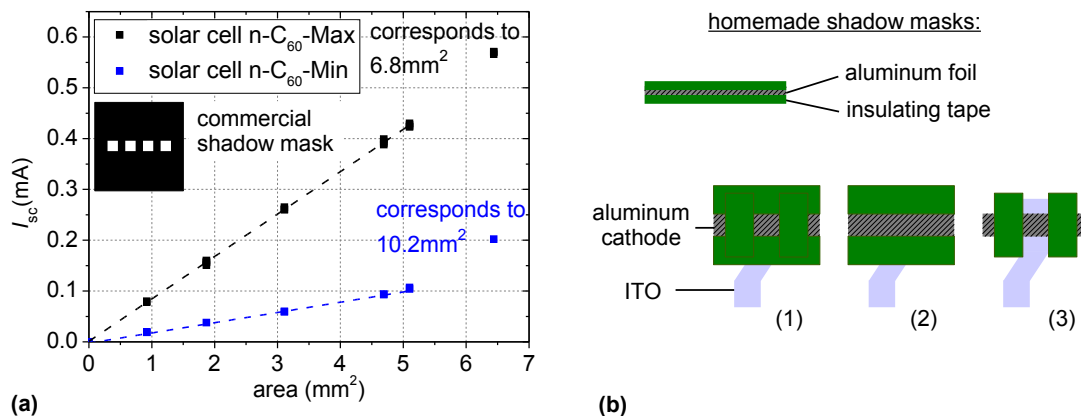


Figure 6.8: a) Dependence of the short circuit current of *p-i-n* type solar cells with 40nm *n-C*₆₀ (photoactive bulk heterojunction is in the interference maximum) or 120nm *n-C*₆₀ (photoactive bulk heterojunction is in the interference minimum) on the illuminated area. The area is defined by applying a rectangular aperture. b) Homemade shadow masks consisting of an aluminum foil sandwiched between 2 pieces of insulating tape and ways to apply the shadow masks for limiting the photoactive area.

contact, but not on the sides where plain glass is the underlying material and aluminum is on top. This implies that *n-C*₆₀ is expanding the effective area of the Al cathode to a certain extent, i.e. it acts as top electrode itself, thereby enlarging the area of the photoactive stack. Given the good conductivity of NDN1 doped *C*₆₀ which is in the order of 1S/cm and the fact that similar effects have been observed for extended PEDOT-PSS electrodes^[210], this is a reasonable hypothesis. Consequently, the unmasked pixel can be considered as parallel connection of three solar cells: one device sandwiched between ITO and aluminum electrode and two devices with presumably larger series resistance being sandwiched between ITO and *n-C*₆₀. As the latter two device areas do not comprise a reflecting metal electrode, the incident light travels through the layer stack without forming an interference pattern. Hence, it is not surprising that the excess current is nearly independent of the ETM layer thickness.

This finding shows that special care has to be taken when evaluating the performance of *n-C*₆₀ solar cells. For achieving comparable results, j_{sc} should always be determined using a shadow mask. However, the jV -characteristics and accordingly V_{oc} , FF , and saturation should be measured without aperture as otherwise the shaded region acts as large parallel resistance altering the shape of the jV -curve. This way, the characteristic parameters which are used for calculating the efficiency would be falsified. For displaying the jV -curve, the current density j is calculated using the effective device area, which is determined by measuring the exact short circuit current I_{sc} by means of a shadow mask and relating it to I_{sc} of the unmasked device. However, it has to be noted that a more accurate correction of *n-C*₆₀ devices would require measuring the performance of the additional device stacks at the edges. Here, especially an exact placement of respective shadow masks is crucial, but due to the small size of the pixels the implementation is difficult.

Considering commercialization which involves an up-scaling of the device area, the observed effect will lose significance. Here, the ratio between the additional contribution from the edges and the output of the actual solar cell which is sandwiched between anode and cathode will be comparatively small. For solar cells produced at lab scale, another possible side effect has to be taken into account: If, like on the IAPP standard substrates, several devices are situated next to each other, the use of a hole transport material which is as well conducting as *n-C*₆₀ or better might lead to a so-called *crosstalk effect*. This means that the charge transport materials could not only extend the area of one specific pixel, but they could even create a short circuit between the electrodes of all pixels, thereby creating a parallel connection of all devices. For most solar cells presented in this work MeO-TPD doped with 2wt% NDP2 is used as HTM. As upon using shadow mask configuration (2) no excess current is detected, the conductivity of *p*-MeO-TPD, which is in the range of $1 \cdot 10^{-4}$ S/cm*, is not sufficient for extending the area of the ITO anode.

The highest conductivity, achieved by one of the alternative ETM that are studied in this thesis, is measured for HATNA-Cl₆ doped with 7.5wt% NDN1 (molar ratio 1:19) and yields $7.5 \cdot 10^{-3}$ S/cm. Since this value is still by a factor of ~ 100 smaller than the conductivity of standard *n-C*₆₀, none of the new

* Measured by Selina Olthof, IAPP.

ETM is expected to generate a cathode extension effect. Indeed, re-measuring selected jV -curves of n-Bis-FI-NTCDI, n-HATNA-Cl₆, and n-NTCDA solar cells with aperture yields the same short circuit current density as a measurement which is performed without aperture.

6.2.2 Performance of p-i-n Type Solar Cells with Varying ETM

p-i-n type solar cells having the structure ITO/NDP2 (1nm)/MeO-TPD:NDP2 (40nm, 2wt%)/ZnPc (5nm)/ ZnPc:C₆₀ (30nm, 1:1)/C₆₀(5nm)/n-ETM (x nm)/Al (100nm) are produced for comparing the actual performance of n-Bis-FI-NTCDI, n-HATNA-Cl₆, n-NTCDA, and n-C₆₀ with the performance predicted by the optical simulation. The ETM thickness varies between 0 and 200nm for n-Bis-HFI-NTCDI solar cells and 0 and 150nm for n-HATNA-Cl₆, n-NTCDA, and n-C₆₀ devices. For determining correct j_{sc} values, apertures of 5.10mm² size are applied to the n-C₆₀ solar cells, while for all other materials this procedure proved not to be necessary as j_{sc} determined with an aperture equals j_{sc} calculated when assuming an active area of 6.44mm². Unfortunately, the solar cell comprising 150nm n-C₆₀ was destroyed during the measurement with the shadow mask and hence, j_{sc} and η could not be calculated.

Due to the large amount of data, only the characteristic device parameters will be discussed, while plotting the jV -characteristics is omitted. The focus will be on j_{sc} , as it is subject to the strongest variations and as, here, a comparison with the expectations from the optical simulation is possible. Figure 6.9 shows the development of j_{sc} , V_{oc} , FF , saturation, and mismatch corrected η in dependence of ETM type and thickness. The corresponding values are listed in a table in Appendix A along with the effective illumination intensities I_{eff} which are used for measuring the jV -curves.

Short circuit current density: Figure 6.9a) shows the response of j_{sc} to the variations introduced at the n-side of the solar cell. For better comparability, Figure 6.9b) depicts the theoretical values deduced from the optical simulation for relevant ETM thicknesses. Altogether, the simulated $j_{sc}(d_{ETM})$ -curves reproduce the development of the measurement values, however, there are some discrepancies that need to be discussed. Concerning *curve shape*, and particularly the positions of current maxima and minima, the $j_{sc}(d_{ETM})$ -curve of n-Bis-HFI-NTCDI solar cells appears to be stretched compared to the prediction whereas the opposite applies for n-NTCDA devices. In contrast, the $j_{sc}(d_{ETM})$ curve shapes of n-C₆₀ and n-HATNA-Cl₆ devices coincide well with the prediction. The differences are either due to the use of incorrect thin film densities during solar cell fabrication or due to errors in the input n & k values. For adapting the experimental values to the simulation, thin film densities in the order of 1.40g/cm³ and 1.55g/cm³ have to be chosen for Bis-HFI-NTCDI and NTCDA, respectively, while for processing, densities of 1.25g/cm³ (determined with XRR) and 1.78g/cm³ (extracted from literature^[156]) were used.

All *absolute measurement values* of j_{sc} are smaller than the predicted values, as internal losses during charge generation and charge extraction are neglected in the simulation. Nevertheless, the trend of increasing photocurrent with decreasing parasitic absorption is reproduced for $d_{ETM} > 70$ nm. However, for smaller ETM thickness, the differences are smaller than expected. We find maximum short circuit current densities of $j_{sc}^{n-C_{60}} = 8.2$ mA/cm² at $d_{ETM} = 40$ nm, $j_{sc}^{n-HATNA-Cl_6} = 8.4$ mA/cm² at $d_{ETM} = 50$ nm, $j_{sc}^{n-Bis-HFI-NTCDI} = 8.5$ mA/cm² at $d_{ETM} = 60$ nm, and $j_{sc}^{n-NTCDA} = 9.4$ mA/cm² at $d_{ETM} = 50$ nm. Compared to the device comprising the reference ETM n-C₆₀, these numbers correspond to a relative increase of 2.4% for n-HATNA-Cl₆, 3.7% for n-Bis-HFI-NTCDI, and 14.6% for n-NTCDA. Particularly the difference between the performance of n-Bis-HFI-NTCDI and n-NTCDA devices, which are expected to have very similar optical properties, is noteworthy. As the calculation of j_{sc} is based on a simulation which is purely optical and involves a number of assumptions, discrepancies are to be expected. In the following, several factors which contribute to those discrepancies are presented.

1. For calculating j_{sc} , a constant *IQE of unity* is assumed for all ETM and in the whole wavelength range under consideration. In contrast, the IQE of actual solar cells is expected to be in the order of 0.75 to 0.80^[211-213] and might, furthermore, be wavelength dependent^[211]. The latter effect is caused by imbalanced exciton harvesting in donor and acceptor. Exchanging the ETM is expected to induce only minor changes in the overall IQE, as exciton diffusion efficiency η_{ED} and charge transfer efficiency η_{CT} are primarily dependent on the photoactive blend. However, a reduced η_{ED} is possible if the acceptor/ETM interface introduces exciton quenching sites or if it allows for exciton diffusion into the n-doped region. Especially for the i-C₆₀/n-C₆₀ interface the latter effect might be relevant, as there is no step in ionization energies between the two materials and, hence, exciton blocking is not expected. Finally, an effect on the charge collection efficiency η_{CC} , i.e. the introduction of losses during charge transport and extraction, is unlikely as it would have an effect on the jV -curve.

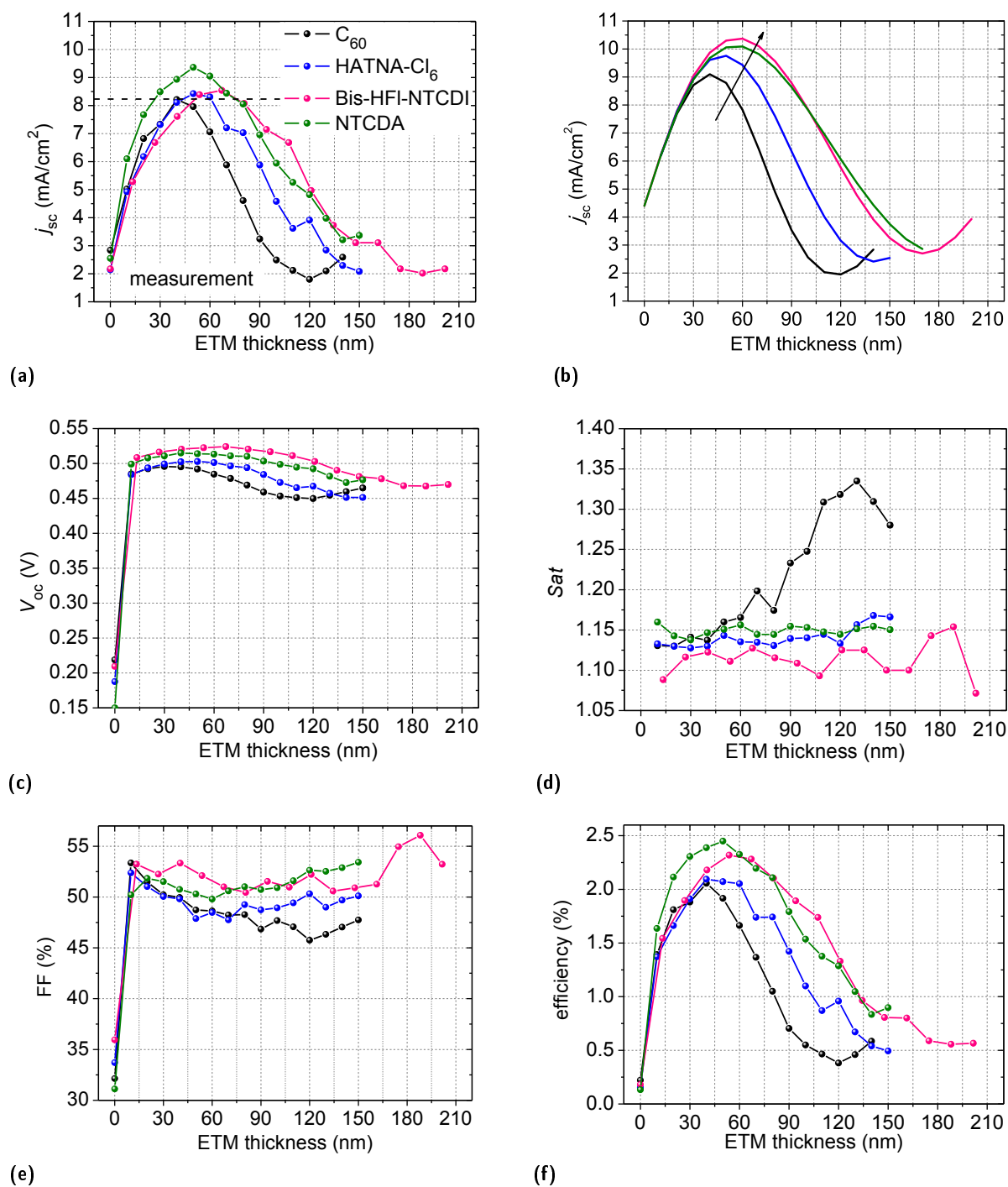


Figure 6.9: Overview over characteristic parameters of $p-i-n$ type solar cells with varying ETM type and thickness: a) measured short circuit current densities j_{sc} , the dotted line marks the maximum current achievable with $n-C_{60}$, b) simulated j_{sc} for comparison (extracted from Figure 6.3), c) measured open circuit voltages V_{oc} , d) saturation factors, e) fill factors, and f) efficiencies η . The current density of $n-C_{60}$ devices is determined with an aperture of 5.1mm^2 size.

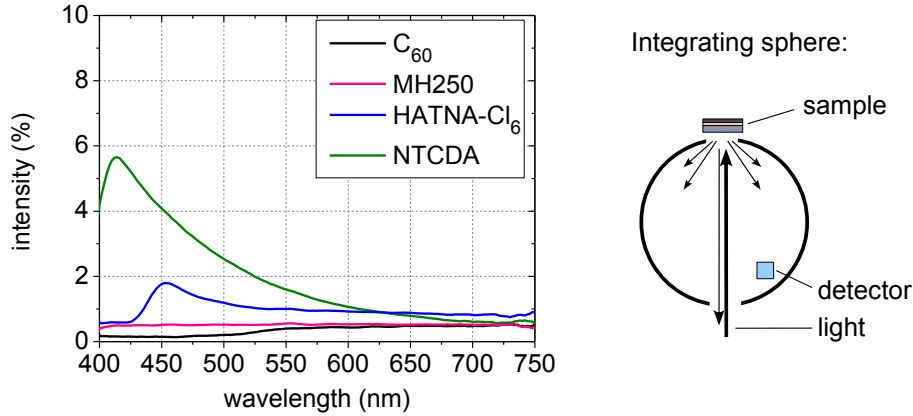


Figure 6.10: Amount of light which is diffusely reflected at the ETM (50nm)/Al (100nm) contact and setup used for the detection thereof.

Unfortunately, calculating a conclusive IQE spectrum for the investigated p-i-n type solar cells is not easily possible: When simply dividing the EQE by the measured total absorption, the parasitic absorption which occurs in the electrodes and in the transport layer is neglected. Hence, it is reasonable to define an active IQE which is calculated by dividing the EQE by the absorption of only the photoactive layers. However, the latter can not be measured directly and has to be deduced from the optical simulation which proves to be unsuitable when considering the partly huge deviations between simulated and measured absorption. The reasons for these differences will be discussed in the following.

2. *Inaccuracies in the input n & k values* cannot be excluded. Depending on the method which is used for extracting the optical constants from reflection and transmission data of single layers of varying thickness, slight differences are expected in the $n(\lambda)$ and $k(\lambda)$ spectra. Here, also the layer thickness which depends on the use of a correct thin film density is used as a fit parameter. Incorrect n & k values will introduce a random error to the optical simulation.
3. As the optical constants of many materials are only available in a *limited spectral range*, the simulation is only performed between 350 and 800nm. Hence, any residual ZnPc absorption taking place at higher wavelengths is not included in the simulation and cannot add to the calculated j_{sc} .
4. The *n & k values of doped layers are unknown*, which means that the absorption of the dopants cannot be taken into account. This means that there is an additional parasitic absorption at unknown wavelengths while, due to the admixture of dopant molecules, the total amount of matrix material for electron or hole transport is less than assumed in the simulation. Furthermore, it is possible that the absorption signal of the matrix materials is altered by the doping process which ionizes a fraction of the molecules. For instance, when comparing the total absorption of layer stacks that are lacking the ETM with the simulated absorption signal (data not shown here), it can be assumed that p-doping introduces some parasitic absorption between 400 and 550nm. On the other hand, there are indications that n-doping reduces the absorption of C_{60} in the visible range*. Overall, the uncertainty introduced to the simulation when omitting the dopants is one of the main obstacles for calculating IQE spectra.
5. Furthermore, the optical simulation assumes *smooth interfaces*, i.e. it ignores potential light scattering at rough surfaces. However, especially considering the ETM/aluminum top contact, this assumption is not necessarily true. The amount of light scattered at the cathode is estimated by measuring the reflection signal of the ETM (50nm)/Al (100nm) stack, deposited onto a glass substrate by means of an integrating sphere. Figure 6.10 shows the setup together with the measurement result. As the substrate is perpendicular to the incident light, only the diffusely reflected fraction is detected while the directly reflected light leaves the sphere again through the entrance slit. The scattering signal, which mainly emerges from the organic/metal contact, is below 0.5%

* n- C_{60} absorption measured under ambient conditions by André Merten, IAPP.

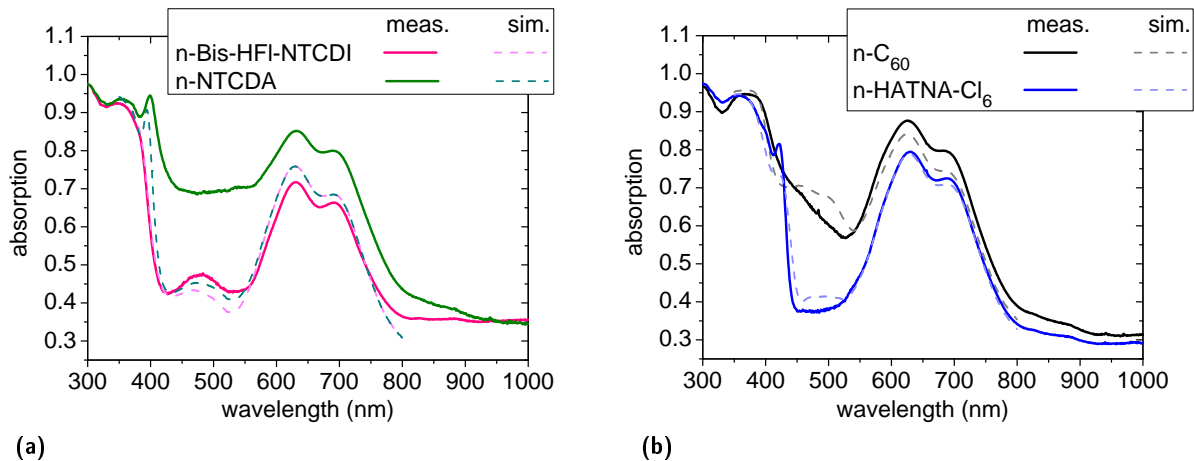


Figure 6.11: Simulated and measured absorption of *p-i-n* type solar cells comprising 40nm a) *n*-Bis-HFI-NTCDI or *n*-NTCDA and b) *n*-C₆₀ or *n*-HATNA-Cl₆ and as ETM. The corresponding layer stack is shown in Figure 6.3.

for the C₆₀/Al and the Bis-HFI-NTCDI/Al contact, whereas HATNA-Cl₆/Al exhibits a maximum of 1.8% diffuse reflection at $\lambda = 452\text{nm}$ which decreases to $R_{\text{diff}} = 1\%$ for $\lambda > 500\text{nm}$. Finally, the NTCDA/Al interface displays the strongest scattering. R_{diff} continuously increases from 0.6% at 750nm to 5.7% at 414nm. This behavior is linked to the island-like growth of NTCDA which results in a surface roughness that is by approximately a factor of 10 larger than the rms roughness of the other ETM^[15].

The observed behavior has direct consequences for the optical properties of the devices under investigation. As shown in Figure 6.11a), the measured absorption spectrum of a solar cell comprising 40nm *n*-NTCDA is not only broadened compared to the simulated spectrum, but also much higher. This result is caused by the considerable amount of light which is scattered at the *n*-NTCDA/Al contact. As a large fraction of the diffusely reflected light does not reach the detector, the missing signal is misinterpreted as additional absorption. In contrast, the absorption of a comparable device with *n*-Bis-HFI-NTCDI as ETM is slightly smaller than predicted. In Figure 6.11b), an equivalent comparison is done for *n*-C₆₀ and *n*-HATNA-Cl₆ devices: Apart from the already discussed general deviations between 400 and 550nm, the absorption properties of the HATNA-Cl₆ solar cell are modeled well by the simulation program. In contrast, at $\lambda > 550\text{nm}$, the absorption of the *n*-C₆₀ solar cell exceeds the simulated absorption spectrum and is also slightly broadened. According to measurements with the integrating sphere, this behavior is probably not caused by light scattering and must therefore be an actual excess absorption. It matches the fact that the photocurrent of *n*-C₆₀ devices is generally larger than expected. The origin of this behavior is still under debate and might be related to a weakening of the C₆₀ absorption as a result of the charge transfer between matrix and dopant.

In general, a diffusely reflecting cathode can have different implications for the solar cell performance: i) Scattering disturbs the thin film interference effect and, hence, the interference maximum will be less pronounced. This would reduce the absorption in the photoactive area. ii) Scattering might induce a so-called light trapping effect^[214] which actually increases the absorption in the photoactive area. It is based on the fact that the ZnPc:C₆₀ layer is sandwiched between two materials having a lower refractive index than the blend itself. Hence, light which is entering the absorber layer under an angle which is larger than the critical angle of total reflection will be reflected several times at the interface to the charge transport layers and consequently repeatedly pass the blend. It is not clear which of the processes is dominating in *n*-NTCDA devices, but it is obvious that the scattering interface does not diminish the device performance.

Overall, it is shown that the optical simulation predicts trends concerning the development of the solar cell performance upon exchanging the ETM or modifying the ETM layer thickness. However, several assumptions need to be made for the simulation which prevent more accurate predictions – especially issues 4.) and 5.) play an important role, here. It should be noted that at optimized device geometries,

the expected advantage of the transparent ETM is less pronounced than anticipated. The unexpectedly high short circuit current density in n-C₆₀ devices is probably due to an enhanced ZnPc absorption of undisclosed origin. Due to the strong light scattering at the ETM/Al interface which considerably influences the interference pattern, n-NTCDA devices have a special status.

Open circuit voltage: The dependence of open circuit voltage on ETM type and layer thickness is plotted in Figure 6.9c). The d_{ETM} dependent variation follows the variation in j_{sc} and is the same for all ETM. It is due to the fact that the open circuit voltage increases with the number of photogenerated charge carriers which increase the Fermi level splitting. Concerning absolute values, V_{oc} is smallest for n-C₆₀ devices with $V_{\text{oc}}^{\text{max}} = 0.50\text{V}$, followed by n-HATNA-Cl₆ devices with $V_{\text{oc}}^{\text{max}}$ slightly larger than 0.50V, n-NTCDA devices with $V_{\text{oc}}^{\text{max}} = 0.51\text{V}$, and finally n-BisHfI-NTCDI devices with $V_{\text{oc}}^{\text{max}} = 0.52\text{V}$. The behavior is caused by a superposition of two effects: (i) The increased charge carrier generation in devices with more transparent ETM and (ii) changes in the built-in field caused by the differences in electron affinity.

Saturation factor: Figure 6.9d) shows the development of the saturation factor which is a measure for the field dependence of the photocurrent collection at negative bias voltage under illumination and is defined as $j(-1\text{V})/j_{\text{sc}}$. Low saturation factors are beneficial for a good device performance. Similar as observed for V_{oc} , the transparent ETM prove to be advantageous: The lowest *Sat* is exhibited by n-Bis-HfI-NTCDI devices, followed by n-HATNA-Cl₆ devices, n-NTCDA devices, and finally n-C₆₀ devices. For the latter, *Sat* is even increasing significantly with increasing ETM thickness. As has been pointed out in Section 6.2.1, devices with n-C₆₀ can be described by a parallel connection of the solar cell, which is sandwiched between ITO and aluminum, and two additional device areas sandwiched between ITO and n-C₆₀ acting as extended cathode. The additional areas clearly add to the parallel resistance of the device and cause the increased saturation. Furthermore, the existence of a so-called *photoshunt effect* is suspected for devices comprising n-C₆₀. It causes a constant parallel resistance which prevents a saturation of the reverse current and occurs only upon illumination. The effect is assumed to be due to the photogeneration of free excess charge carriers in the organic material(s)*.

Fill factor: The fill factors of all devices are compared in Figure 6.9e). Only for solar cells with $d_{\text{ETM}} = (10\dots 20)\text{nm}$, it is equally good for all ETM, i.e. it is in the range of (51...53)%. While for n-Bis-HfI-NTCDI and n-NTCDA devices it stays > 50% also for higher ETM thickness, it is generally lower for n-HATNA-Cl₆ devices ($FF = 48\dots 50\%$) and n-C₆₀ solar cells ($FF = 46\dots 50\%$). For the latter, the development of the FF coincides with the changes in the saturation behavior which means that it decreases constantly with increasing ETM thickness. However, concerning the other ETM, the differences in FF are not correlated to variations in the series resistance and only weakly related to changes in the saturation. Yet, the $FF(d_{\text{ETM}})$ -curve has a characteristic shape: First the FF decreases with increasing d_{ETM} until it reaches a minimum at about 60 to 80nm, while for higher ETM thickness, it tends to increase again. There are two effects contributing to this behavior: (1) For devices with optimized geometry, the charge carrier density within the photoactive bulk and thus the probability of non-geminate recombination is generally increased. Consequently, the fill factor is decreased and shows exactly the opposite behavior than the short circuit current density and the open circuit voltage. (2) If the mobilities of electrons and holes in the bulk D/A heterojunction are unbalanced, the fill factor exhibits a dependence on the optical field distribution^[215]. In the given example of a 1:1 blend of ZnPc and C₆₀, the hole mobility in ZnPc has been determined to be $1.5 \cdot 10^{-4}\text{cm}^2/\text{Vs}$ whereas the electron mobility in C₆₀ is by two orders of magnitude larger and reaches $1.4 \cdot 10^{-2}\text{cm}^2/\text{Vs}$ [†]. As a result, a space charge might arise at low bias and limit the charge extraction which in turn decreases the fill factor. The effect of imbalanced mobilities is diminished when the maximum of the optical field distribution is closer to the p-side of the device because in this situation, the are generated in the vicinity of the HTM and extraction is facilitated. As illustrated in Figure 6.2, this is the case for low ETM thickness. On the other hand, the imbalance is aggravated at high ETM thickness, when the maximum of the optical interference pattern is shifted towards the n-side of the device. Here, the majority of the holes is generated further away from the HTM and the recombination probability is enhanced. Overall, effect (1), i.e. the general decrease of the charge carrier density counteracts the mobility effect (2) and leads to an increase in FF .

Efficiency: Finally, Figure 6.9f) presents the dependence of the power conversion efficiency on type and thickness of the ETM. The development basically follows the trend observed for j_{sc} , i.e. there is a maximum at moderate ETM thickness when the photoactive layer is positioned in the maximum of the optical interference pattern and accordingly a minimum at large ETM thickness when the layer stack is not optimized in terms of thin film optics. We find maximum efficiencies of $\eta_{\text{n-C}_{60}}(d_{\text{ETM}} =$

* Private communication with Wolfgang Tress, IAPP. † Field effect mobilities, measured by Moritz Hein, IAPP.

40nm) = 2.1%, $\eta_{\text{n-HATNA-Cl}_6}(d_{\text{ETM}} = 40\text{nm}) = 2.1\%$, $\eta_{\text{n-Bis-HFl-NTCDI}}(d_{\text{ETM}} = 54\text{nm}) = 2.3\%$, and $\eta_{\text{n-NTCDA}}(d_{\text{ETM}} = 50\text{nm}) = 2.4\%$. All devices comprising transparent ETM show a performance either comparable to the performance of the respective n-C₆₀ reference device or better. Up to $d_{\text{ETM}} = 30\text{nm}$, n-C₆₀, n-Bis-HFl-NTCDI, and n-HATNA-Cl₆ devices exhibit similar efficiencies and solely the use of n-NTCDA results in an improvement, whereas at larger ETM thickness, also the other transparent ETM display significant advantages compared to n-C₆₀.

In summary, the best performance of p-i-n type solar cells is achieved using n-NTCDA. However, this result should be treated with care. Although the light scattering, which is induced by the large surface roughness of the ETM, seems to be advantageous in terms of thin film optics, it constitutes a huge problem when changing the design of the layer stack. The implementation of NTCDA in n-i-p or tandem structures inevitably results in short-circuited devices as the pronounced island growth disturbs the arrangement of all following layers^[13]. Hence, the use of n-Bis-HFl-NTCDI should be preferred. It leads to similarly high efficiencies as n-NTCDA and, as will be shown in the following, can easily be applied in n-i-p type structures as well.

6.2.3 n-i-p Type Solar Cells – Proof of Principle

In n-i-p structures, the ETM needs to establish an ohmic contact with the ITO bottom contact. Furthermore, as mentioned above, it is required to form a smooth layer which allows an undisturbed growth of the photoactive layers that are deposited on top of the ETM. Last but not least, it has to withstand substrate heating during the evaporation of the photoactive materials up to temperatures in the order of 120°C which might be necessary for optimizing the morphology of the bulk heterojunction. In the following, two examples will be shown which prove the applicability of Bis-HFl-NTCDI and HATNA-Cl₆ in n-i-p type solar cells.

Bis-HFl-NTCDI

The performance of n-Bis-HFl-NTCDI is compared to the performance of the reference material n-C₆₀ using devices with the layer sequence ITO/n-ETM (60nm)/C₆₀ (5nm)/ZnPc:C₆₀ (30nm, 1:1)/BF-DPB (5nm)/BF-DPB:NDP9 (50nm, 10wt%)/NDP9 (1nm)/Al (100nm). Either Bis-HFl-NTCDI:NDN1 (7wt%) or C₆₀:NDN1 (3wt%) are applied as ETM. In order to establish an ohmic contact to the Al electrode, NDP9 doped BF-DPB replaces MeO-TPD:NDP2 as HTM. The stack is close to the optimized geometry and is displayed in Figure 6.12 along with the resulting jV -curves and the characteristic parameters. Again, the effective device area, which is used for calculating the current density, is determined by measuring the precise short circuit current $I_{\text{sc}}^{\text{mask}}$ by means of a well defined aperture and relating it to I_{sc} of the unmasked device. Apart from $j_{\text{sc, corr}}$, all other parameters are derived from the measurement without mask.

The jV -curve of the n-C₆₀ device reveals the expected disadvantage of a parasitically absorbing ETM. We find $j_{\text{sc, corr}}^{\text{C}_{60}} = 7.1\text{mA/cm}^2 < j_{\text{sc, corr}}^{\text{Bis-HFl-NTCDI}} = 8.5\text{mA/cm}^2$, $V_{\text{oc}}^{\text{C}_{60}} = 0.54\text{V} < V_{\text{oc}}^{\text{Bis-HFl-NTCDI}} =$

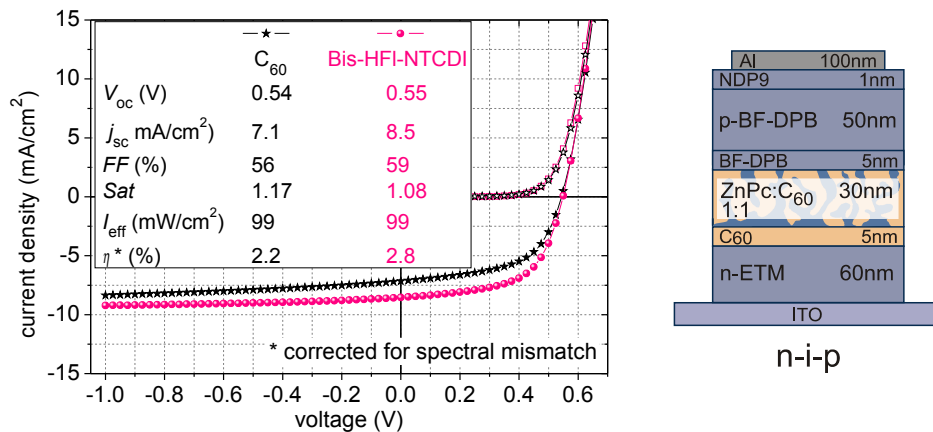


Figure 6.12: jV -curves, characteristic parameters and layer stacks of n-i-p type solar cells with n-Bis-HFl-NTCDI or n-C₆₀ as ETM.

0.55V, $FF^{C_{60}} = 56\% < FF^{Bis-HF1-NTCDI} = 59\%$, and $Sat^{C_{60}} = 1.17 > Sat^{Bis-HF1-NTCDI} = 1.08$. Consequently, the power conversion efficiency is increased from $\eta^{C_{60}} = 2.2\%$ to $\eta^{Bis-HF1-NTCDI} = 2.8\%$ when exchanging n- C_{60} by n-Bis-HF1-NTCDI. The large difference in saturation factors is most likely caused by the edge effects in the n- C_{60} device which considerably add to the parallel resistance of the stack.

Overall, the difference between optically optimized n-i-p devices with either parasitically absorbing or transparent ETM is more pronounced than the difference observed in optimized p-i-n stacks. Considering the influence of the ETM on the device optics and hence, on the photocurrent generation which is reflected in Figures 6.3 (p-i-n) and 6.5 (n-i-p), this result is to be expected. In p-i-n devices, the ETM is decisive for the formation of the optical interference pattern, i.e. even the use of a parasitically absorbing material of a certain thickness can improve the device performance compared to a device which is lacking an optical spacer between photoactive region and aluminum cathode. However, in n-i-p type devices, a non-transparent material is detrimental in any case as it instantly decreases the intensity of the incident light before it reaches the photoactive region.

HATNA-Cl₆

To test the applicability of n-HATNA-Cl₆ as ETM in n-i-p structures, devices with the layer sequence ITO/n-ETM (30nm)/ C_{60} (5nm)/DCV6T: C_{60} (30nm, 2:1)/BPAPF (5nm)/BPAPF:NDP9 (30nm, 10wt%)/NDP9 (1nm)/Al (100nm) are built. The ETM consists either of HATNA-Cl₆:NDN1 (4wt%) or C_{60} :NDN1 (4wt%). As the donor material DCV6T has a larger ionization potential than the formerly used ZnPc, also the HTM needs to be replaced by a material with large IP . Here, the compound BPAPF in combination with the p-dopant NDP9 is chosen. For supporting the phase separation of DCV6T and C_{60} and thus optimizing the morphology of the interpenetrating network of the two materials, the substrate is heated to 85°C during the deposition of the blend. Consequently, the ETM is exposed to an annealing process. An additional optimization of the thin film optics is omitted.

Figure 6.13 presents the corresponding jV -curves and characteristic parameters. The current density is calculated using the actual photoactive area which is determined by means of an aperture while the characterization itself is performed without aperture. While both devices have the same V_{oc} of 0.88V and the same FF of 52%, the use of n-HATNA-Cl₆ results in a higher j_{sc} of 7.1mA/cm² compared to 6.5mA/cm² in the reference device comprising n- C_{60} . Consequently, there is an increase in power conversion efficiency from $\eta^{C_{60}} = 2.9\%$ to $\eta^{HATNA-Cl_6} = 3.2\%$. As anticipated, n-HATNA-Cl₆ withstands the annealing to 85°C. Furthermore, due to its reduced parasitic absorption compared to n- C_{60} , it causes an increased absorption in the photoactive layers, thus an increase in photocurrent. The high open circuit voltage compared to ZnPc: C_{60} solar cells results from the higher IP of DCV6T which leads to a larger effective energy gap at the heterointerface to C_{60} . V_{oc} scales with this energy gap^[95,184–187] and can – at least to a certain extent – be tuned by carefully selecting suitable donor and acceptor materials.

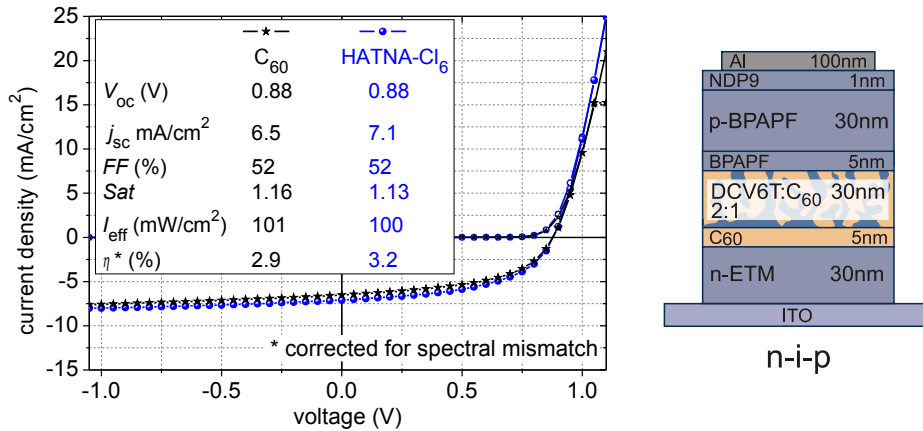


Figure 6.13: jV -curves, characteristic parameters and layer stacks of n-i-p type solar cells with n-HATNA-Cl₆ or n- C_{60} as ETM.

6.3 Summary

- By performing optical simulations it is possible to estimate the photocurrent gain which is anticipated when exchanging the parasitically absorbing material n-C₆₀ by transparent materials like n-HATNA-Cl₆, n-Bis-HfI-NTCDI, or n-NTCDA in p-i-n and n-i-p type solar cells:
 - In *p-i-n type devices*, the ETM thickness determines the position of the photoactive layers with respect to the maximum of the optical interference pattern. Hence, it is an important factor considering device optimization in terms of thin film optics. The magnitude of the ETMs refractive index determines the optimum ETM thickness. We find $d_{\text{ETM}}^{\text{opt}} = 40, 50, 60,$ and 60nm for n-C₆₀, n-HATNA-Cl₆, n-Bis-HfI-NTCDI, and n-NTCDA, respectively. A decrease in parasitic absorption is expected to result in an increased j_{sc} .
 - In *n-i-p type devices*, the variation of ETM type and thickness has a comparably small effect on the position of the interference maximum. Nevertheless, the implementation of transparent ETM is expected to result in a slight increase of the photocurrent, whereas the use of a parasitically absorbing ETM generally decreases the photocurrent density compared to a device in which the ETM is completely omitted.
- Excitons generated in n-doped C₆₀ are quenched at the dopant molecules and do not contribute to the photocurrent.
- The effective solar cell area of p-i-n type devices comprising n-C₆₀ is larger than the geometric overlap between ITO bottom and metal top contact. Due to its good lateral conductivity n-C₆₀ extends the area of the cathode. Consequently, this type of solar cell can be considered as parallel connection of the actual stack sandwiched between ITO anode and Al cathode and two additional stacks which are sandwiched between ITO anode and n-C₆₀ cathode. This effect is not observed for the other ETM.
- The performance of p-i-n type devices with varying ETM type and thickness is in accordance with the trends predicted by the optical simulation. However, at optimized device geometries, the photocurrent gain upon using transparent ETM is less pronounced than expected. This result is mainly due to the fact that the optical simulation is based on a number of assumptions as it, for instance, neglects the influence of doping on the optical properties of charge transport materials or the existence of diffusely reflecting interfaces. Nevertheless, the device efficiency is improved from $\eta_{\text{max}}^{\text{C}_{60}, \text{HATNA-Cl}_6} = 2.1\%$ for n-C₆₀ and n-HATNA-Cl₆ solar cells to $\eta_{\text{max}}^{\text{Bis-HfI-NTCDI}} = 2.3\%$ for n-Bis-HfI-NTCDI solar cells and $\eta_{\text{max}}^{\text{NTCDA}} = 2.4\%$ for n-NTCDA solar cells. This development is supported by generally higher V_{oc} and FF in solar cells with transparent ETM.
- The implementation of n-Bis-HfI-NTCDI and n-HATNA-Cl₆ in n-i-p type solar cells is successfully shown.

7 Stability Issues

Device stability is one of the crucial issues concerning the commercialization of organic solar cells. A material with ideal physical properties is useless if it leads to rapid device degradation. This Chapter deals with the effect of accelerated ageing on the performance of p-i-n type solar cells with varying ETM. By comparing the development of the characteristic device parameters and capacitance-frequency spectra, the durability of the most promising ETM presented in this thesis is evaluated.

7.1 Lifetime of p-i-n Type Solar Cells with Different ETM

Simple test stacks having the layer sequence ITO/NDP2 (1nm)/BF-DPB:NDP2 (30nm, 10wt%)/ZnPc:C₆₀ (30nm, 1:1)/C₆₀ (30nm)/n-ETM (30nm)/Al (100nm) are produced for examining device stability. Either n-C₆₀ (3wt%), n-HATNA-Cl₆ (5wt%), n-Bis-HfI-NTCDI (7wt%), or n-NTCDA (6wt%) is used as ETM. HATCN is excluded from the study as its high *EA* limits its applicability to only few device geometries. Hence, it is rather suited as model system than as commercial ETM. As described in Chapter 2, the devices are aged at a constant temperature of $(50 \pm 5)^\circ\text{C}$ while being illuminated with an LED which emits white light of a broad spectral range*. The results shown in the following represent the behavior of the pixels that are exposed to an intensity of approximately 2 suns, i.e. $\approx 200\text{mW}/\text{cm}^2$. At $t_0 = 0\text{h}$, the performance of all solar cells is nearly identical. We find initial parameters of $V_{\text{oc}} = (0.50 \pm 0.01)\text{V}$, $I_{\text{sc}} = (1.0 \pm 0.1)\text{mA}/\text{cm}^2$, and $FF = (58 \pm 1)\%$.

Figure 7.1 presents the evolution of I_{sc} , FF , V_{oc} , and power conversion efficiency η , normalized to the respective values of the unaged device. Here, η is defined as $(V_{\text{oc}} \cdot I_{\text{sc}} \cdot FF) / [V_{\text{oc}}(t_0) \cdot I_{\text{sc}}(t_0) \cdot FF(t_0)]$. To illustrate the effects of degradation, some exemplary *IV*-curves that are taken after 5, 100, 200, 500, 1000, 1500, 2000, 2500, and 3000 hours (HATNA-Cl₆) or 5, 100, 200, 500, 1500, and 1850 hours (all other ETM) are shown in Figure 7.2. Solar cells comprising **n-Bis-HfI-NTCDI** or **n-C₆₀** show a very good stability: After 1850h of accelerated ageing, the *IV*-characteristics are nearly unchanged. In this case, applying an exponential decay function to the $\eta(t)$ -curves does not lead to useful results and hence, the average lifetime is determined by fitting the data linearly and subsequently extrapolating the time at which the efficiency is expected to equal 80% of its initial value. Assuming that doubling the intensity of the incident light accelerates the degradation by a factor of two, the calculated time t_{80} has to be doubled for extracting the device lifetime. By this, we find a lifetime of 14 000h for n-Bis-HfI-NTCDI devices and 36 500h for n-C₆₀ solar cells. According to the information system of the Joint Research Center (JRC) of the European Commission, a yearly radiation of 986kWh/m² is illuminated in Dresden on a horizontal plane, i.e. on average, there are 986h of full sunshine per year^[216]. Consequently, the device lifetimes correspond to approximately 14 and 37 years, respectively.

In terms of total device lifetime, **n-NTCDA** is the next best material. The decay in efficiency is mainly caused by the changes in I_{sc} which steadily decreases from 0.9mA after 5h to 0.8mA after 1850h. As NTCDA is known for its tendency to form very rough thin films that grow in an island like fashion^[14,15], a morphological effect like (re-)crystallization is likely to be responsible for the observed behavior. Crystal formation can result in a partial demixing of matrix material and dopant, thereby dividing the ETM in well conductive and less conductive regions which impede charge transport and lead to an increased probability for recombination. By fitting the $\eta(t)$ -curve with a stretched exponential decay function, a device lifetime of 4500h is extracted.

Concerning the last material, **n-HATNA-Cl₆**, we find a rapid degradation of all characteristic parameters except for V_{oc} : While I_{sc} is constantly decreasing from 1.0mA after 2h to 0.6mA after 3200h, the FF quickly drops below 35% after only 400h. The average lifetime of n-HATNA-Cl₆ devices as derived from the decay in power conversion efficiency yields approximately 445h. As can be seen from the *IV*-curves in Figure 7.2, this development is due to an increase in series resistance which limits the current in forward direction and leads to the formation of an s-kink. This behavior indicates either (1)

* Measurement performed by Martin Hermenau.

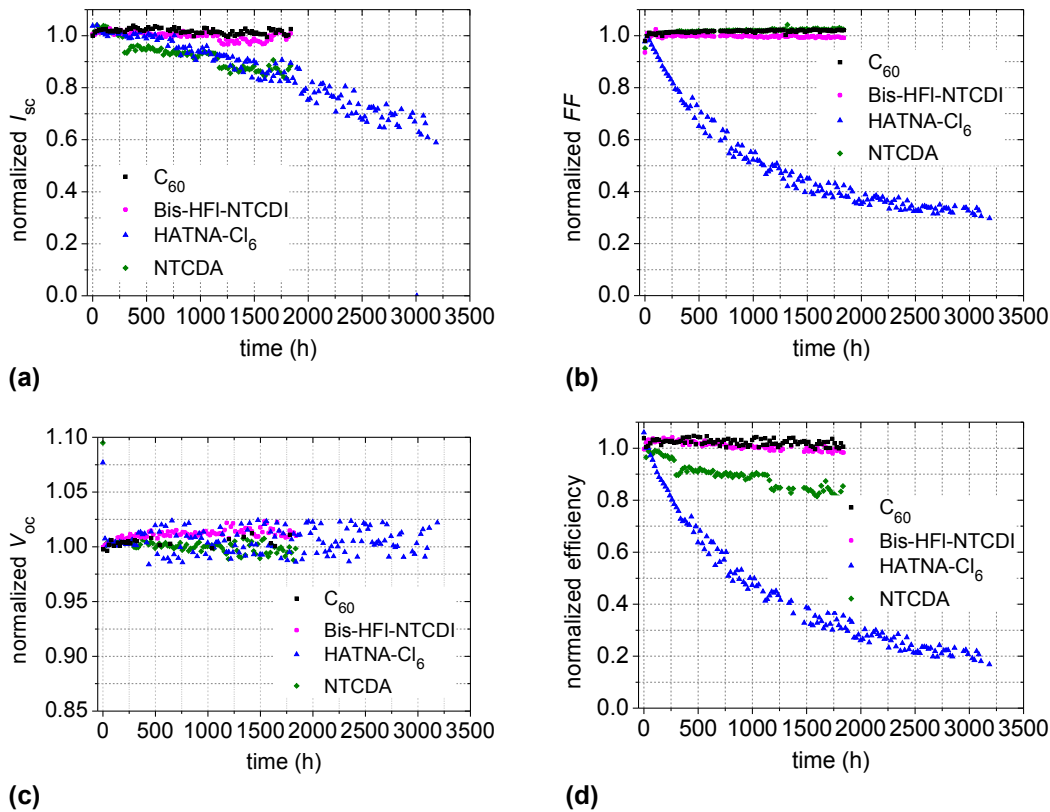


Figure 7.1: Relative changes in a) short circuit current, b) fill factor, c) open circuit voltage, and d) power conversion efficiency of *p-i-n* type solar cells with different ETM when being aged with an illumination intensity of approximately 2 suns. The corresponding layer stack is shown in Figure 7.2.

the formation of energy barriers for charge carrier injection or extraction^[113], or (2) imbalanced charge transport properties between *p*- and *n*-side^[217]. As will be outlined in the following, the two effects do not have to occur independently, but can be linked to each other. However, the microscopic processes responsible for the observed degradation are not easily distinguishable. On the one hand, the elevated temperature and / or the continuous illumination might cause a decomposition of HATNA-Cl₆, mostly followed by a chemical reaction. The resulting reaction product will probably have different physical properties and different energy levels than the educt. Accordingly, an alignment of electron transport levels between the acceptor and the modified ETM is no longer given. Furthermore, the doping efficiency will be affected by a change in energy level positions. This means that the formation of an energy barrier (1) is, in the worst case, accompanied by a decline in the ETMs conductivity leading to an imbalance considering electron and hole extraction (2). Alternative to the decomposition of HATNA-Cl₆, morphological changes in the ETM could promote dopant diffusion throughout the layer. The resulting de-doping of the ETM would also lead to a strongly increased series resistance providing an explanation for the changes in the jV -curves. Here, the energy levels of the matrix material remain unaffected and the situation is comparable to the one observed in *p-i-n* type solar cells comprising insufficiently doped Bis-FI-NTCDI compounds (see Chapter 4.2).

It has to be noted that it is currently unknown whether the encapsulation glue is affected by the elevated temperature, i.e. if a small amount of oxygen and water is able to penetrate into the organic layers. While water was found to have a considerable influence on the stability of the photoactive ZnPc:C₆₀ layers as well as on the aluminum cathode^[218], oxygen is known to act as *p*-dopant^[66,68,69]. Both H₂O and O₂ might accelerate the degradation.

Finally, it must be emphasized that the lifetimes which are extrapolated from accelerated ageing are to be considered as estimates. For instance, it is not self-evident that t_{80} scales linearly with light intensity. Furthermore, the differences between the illumination spectra of an LED and the AM1.5G spectrum need to be taken into account as some degradation processes are wavelength dependent. Independent of these arguments, the results show important trends about material quality and device stability.

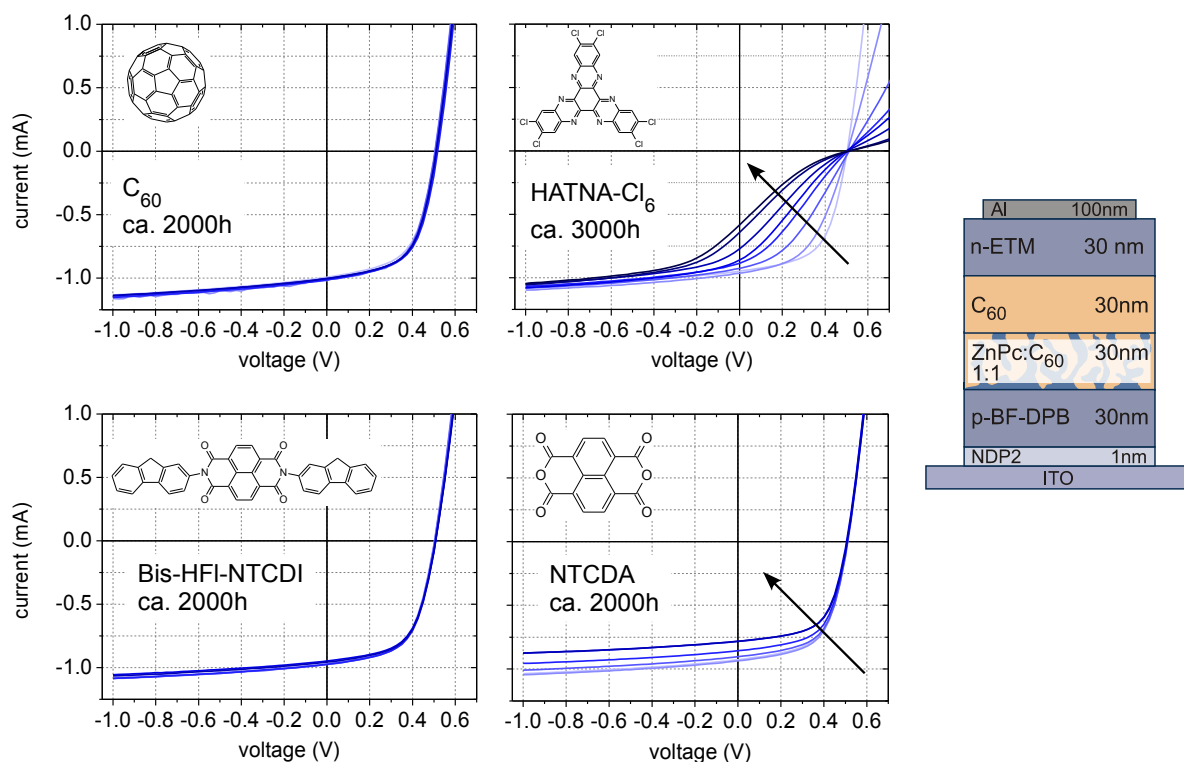


Figure 7.2: Development of IV-curves of *p-i-n* type solar cells which are aged at 50°C and under an illumination of approximately 2 suns ($200\text{mW}/\text{cm}^2$). The arrows illustrate the development over time, i.e. after approximately 5, 100, 200, 500, 1000, 1500, 2000, 2500, and 3000h (HATNA-Cl₆) or 5, 100, 200, 500, 1500, and 1850h (all other ETM).

7.2 Impedance Spectroscopy Measurements

To investigate the degradation mechanisms more closely, all devices discussed above are investigated by means of impedance spectroscopy before and after the accelerated ageing*. The results are plotted as capacitance-frequency functions in Figure 7.3 which also shows the equivalent circuit associated with the layer stack. It contains the *RC*-circuit representing the intrinsic layers of the solar cell, a series resistance and a transmission line, i.e. a connection of many *RC*-elements describing the trap distribution within the devices.^[176]

The spectra of the **unaged devices** (filled symbols) mostly consist of three major regions. At very high frequencies of $> 10^5\text{Hz}$, the series resistance dominates the device response and we find a strongly decreasing capacitance. In contrast, there is a constant plateau at medium frequencies between 10^3 and 10^5Hz which can be assigned to the geometric capacitance of the intrinsic materials. As the photoactive region is the same in all solar cells, the value of C_{geo} is nearly independent of the ETM. Assuming a dielectric constant of $\varepsilon = 5$ for layers composed of ZnPc and / or C₆₀, the geometric capacitance is expected in the range of 4.8nF. However, the experimental value of $\approx 5.6\text{nF}$ is slightly larger corresponding to an intrinsic layer thickness smaller than the nominal value. As already mentioned in Chapter 4 this observation can be explained by the penetration of n-dopants into the intrinsic materials. In the low frequency region, the formation of an additional plateau of higher capacitance is indicated. As outlined in previous Chapters, such a behavior is assigned to the presence of filled trap states which respond to the modulation of the applied AC signal. The states are assumed to be located in the intrinsic materials or at the organic/metal interfaces and are activated in the presence of free charge carriers^[197]. While in bulk heterojunction solar cells that are lacking doped transport layers, they are only observed under illumination, they are already visible in the dark spectra of devices comprising doped transport layers, thereby implying that here free charges are already present in the absence of light. Two possible hypotheses for explaining the latter finding are currently under discussion: (1) As already mentioned, we find a penetration of dopants into the intrinsic materials which is either connected to the evaporation

* Measurement and data evaluation performed / assisted by Lorenzo Burtone.

process or to rough interfaces. The release of electrons or holes from the dopants can explain the presence of excess charge carriers. (2) There is a strong concentration gradient of free charge carriers at the interface between intrinsic and doped materials which causes a diffusion of holes into the donor or electrons into the acceptor. As a consequence, a filling of the trap states is expected in the vicinity of such an interface. From Figure 7.3 it becomes clear that the trap signal is considerably influenced by the matrix material which is chosen for electron transport: In n- C_{60} devices, the trap contribution is most pronounced and we find even two new plateaus with $C > C_{geo}$. The origin of this peculiarity is still under debate and expected to be related to the fact that acceptor and ETM consist of the same material. With $C_{trap} = 13.4\text{nF}$, the trap capacitance at $f = 100\text{Hz}$ is highest for n-HATNA- Cl_6 devices followed by n- C_{60} devices with $C_{trap} = 13.6\text{nF}$, n-Bis-HFI-NTCDI devices with $C_{trap} = 13.2\text{nF}$, and finally n-NTCDA devices with $C_{trap} = 10.9\text{nF}$. The decrease can roughly be linked to the dopant concentration in the respective matrix

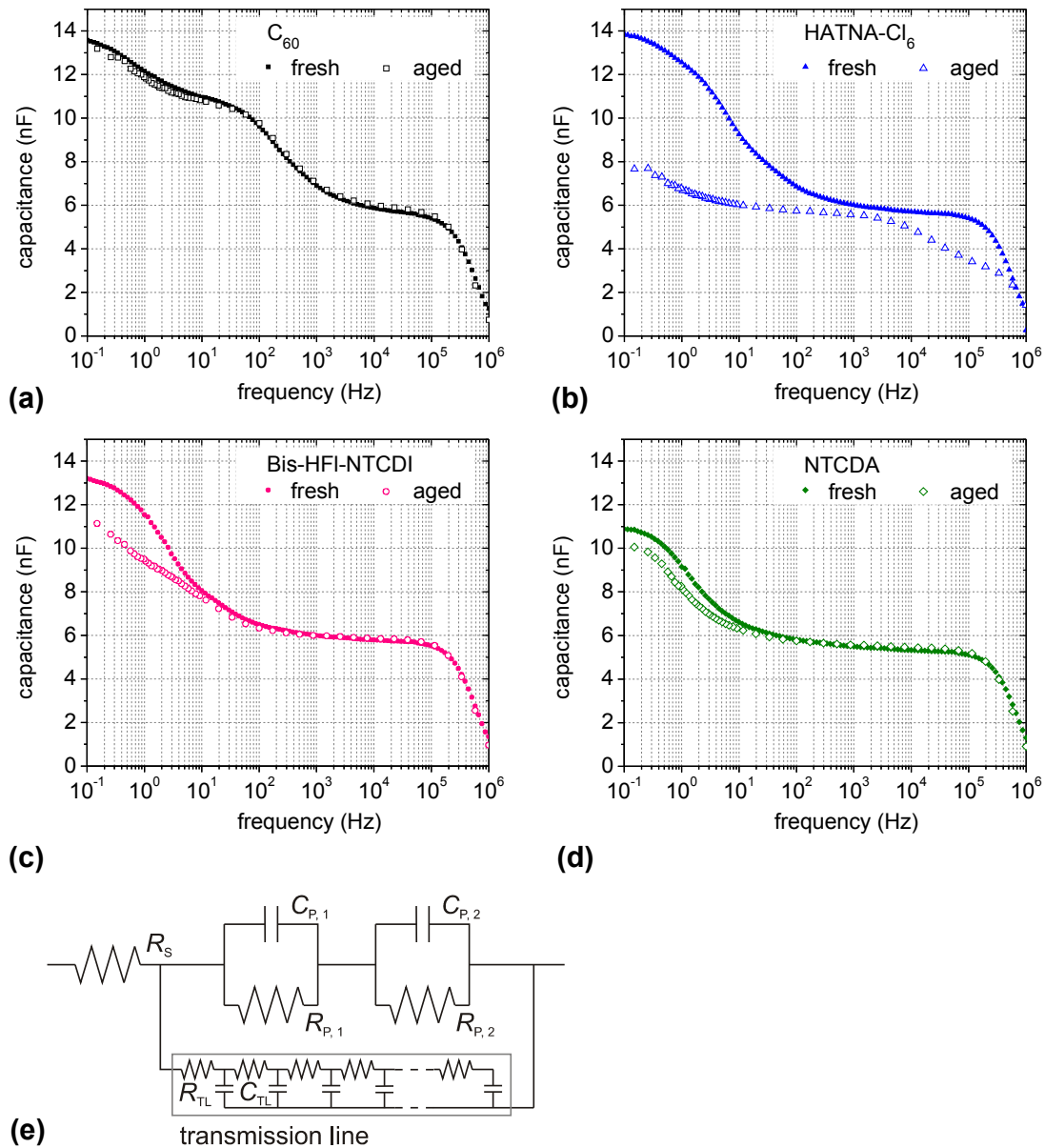


Figure 7.3: Capacitance-frequency plots of the *p-i-n* type devices presented above, measured at a bias voltage of 0V. The last graph shows the equivalent circuit which is used for fitting the results.

material: The molar ratio between the ETM and NDN1 is lowest for n-NTCDA (65:1) and comparably high in n- C_{60} (42:1), n-HATNA- Cl_6 (30:1) and n-Bis-HFI-NTCDI (29:1). This finding proves the strong impact of n-doped layers on the trap response and shows that at least a part of the states preferably

traps electrons. The contribution of p-doped layers and the specific origin of the traps are unknown and are currently under investigation.

After the ageing procedure, the trap contribution is decreased in all devices except for the n-C₆₀ solar cell for which the $C(f)$ -curve is nearly unchanged. This fact reflects the exceptionally good device stability that has already been pointed out in the previous Section. In the devices comprising transparent ETM a larger fraction of the traps seems to be depopulated. Provided that the encapsulation becomes porous during heating, one possible explanation for the observed behavior is the above discussed penetration of oxygen into the organic materials. Oxygen can act as p-dopant which compensates the trap filling near the i-C₆₀/n-ETM interface. However, this hypothesis is in conflict with the comparatively small changes in the $C(f)$ spectrum of n-C₆₀ devices. Furthermore, the role of potential modifications at the p-side cannot be resolved without performing further experiments. Hence, the observed decrease of the trap contribution can currently not provide a satisfactory explanation of the degradation mechanisms.

The strongly degraded n-HATNA-Cl₆ device not only shows the most pronounced decline in trap response, but also a general decrease of the capacitance at medium frequencies between 10² and 10⁴Hz, accompanied by the formation of a second plateau with a smaller capacitance at frequencies larger than 10⁴Hz. This behavior is very similar to the response of p-i-n type devices comprising alkylated n-Bis-FI-NTCDI compounds presented in Chapter 4. Here, the additional plateau was attributed to the insufficient charge transport properties of the ETM which could not be enhanced by n-doping and caused the formation of a pronounced s-kink in the jV -characteristics. Therefore, it is reasonable to assign the new signal to a decline in the conductivity of n-HATNA-Cl₆ as already suspected above. The related „de-doping“ can either be due to a decomposition of the matrix material or due to dopant diffusion. Consequently, the capacitance plateau at medium frequencies can be assigned to a combination of an RC -circuit describing the photoactive layers and a new RC -circuit associated with the quasi-intrinsic ETM. When fitting the curve with an equivalent circuit containing two RC -elements, we find a capacitance of 3.1nF for the new high-frequency plateau. Using $\varepsilon = 5$, this value is converted to a thickness of 91nm which is in very good agreement with the sum of the nominal thicknesses of all intrinsic layers (60nm) and the ETM (30nm).

7.3 Summary

- The performance of p-i-n type devices comprising n-C₆₀ or n-Bis-HFI-NTCDI as ETM is barely affected by accelerated aging at 50°C. Device lifetimes t_{80} of 36500 and 14000h are achieved. In contrast, n-NTCDA devices suffer from a constant decrease of the photocurrent. A device lifetime of 4500h is extrapolated. n-HATNA-Cl₆ devices show a rapid degradation, accompanied by the formation of an s-kink in the IV -characteristics. The average device lifetime is only 445h.
- Impedance spectroscopy reveals that the contribution of trap signals is coupled to the variations of the ETM. Hence, at least a part of the traps, which are assumed to be located in the intrinsic materials, are electron traps. They are activated by electrons diffusing from the ETM into the acceptor.
- In all devices, except for the n-C₆₀ solar cell, ageing is accompanied by a decrease of the trap response. However, determining the underlying mechanism is not easily possible.
- n-HATNA-Cl₆ devices show additional changes in the $C(f)$ spectra. The presence of an additional plateau at high frequencies indicates the formation of a quasi-intrinsic ETM which is either due to de-doping by dopant diffusion or a complete decomposition of HATNA-Cl₆.

8 Summary and Outlook

8.1 Summary

The aim of this thesis is to identify organic materials which are suited for an application as electron transport materials (ETM) in vacuum deposited organic solar cells. The ETM establishes an ohmic contact between the cathode and the acceptor in the photoactive layer. According to the p-i-n concept^[11], which provides design rules for the construction of efficient devices, the ETM needs to fulfill a number of criteria including: (1) Transparency in the visible range of the sun spectrum which is needed for avoiding parasitic absorption. (2) Suitable energy level positions with respect to the adjacent acceptor material for an alignment of electron transport levels causing a barrier-free electron transport. Furthermore, a step in ionization potentials for blocking holes and hindering the diffusion of excitons towards the electrodes is favorable. In state-of-the-art organic solar cells, C₆₀, having an electron affinity (*EA*) of 4.0eV^[49] and an ionization potential (*IP*) of 6.4eV*, is used as acceptor. (3) High conductivity which is preferably larger than 10⁻⁵S/cm and is usually achievable by n-doping. (4) The formation of smooth layers which are morphologically stable; and finally (5) thermal stability not only during production but also during operation at potentially elevated temperatures.

Presently, many solar cells contain only a thin buffer layer composed of either BCP (bathocuproine) or BPhen (bathophenanthroline) between acceptor and metal cathode protecting the organic layers from the energy input during metal evaporation. As a consequence of their insufficient electron transport properties and often misaligned energy level positions, such buffer layers are usually limited to a thickness of < 15nm. At the beginning of this thesis, the choice of dopable ETM was limited to C₆₀ and NTCDA (naphthalenetetracarboxylic dianhydride). As the first material is commonly used as acceptor in the photoactive layer, it shows a considerable parasitic absorption in the spectral range between 400 and 550nm. The latter compound exhibits an unfavorable morphology due to its presumably low glass transition temperature and therefore its applicability is limited to few device geometries^[14,15]. Based on this situation, the suitability of several materials is evaluated with regard to the above presented requirements for efficient ETM. For testing the performance in p-i-n type devices, a standard layer stack composed of ITO/p-MeO-TPD (40nm)/ZnPc (5nm)/ZnPc:C₆₀ (30nm, 1:1)/C₆₀ (5nm)/n-ETM/Al (100nm) is used.

First, the compound **HATCN** (hexaazatriphenylene hexacarbonitrile) is investigated. The material forms smooth thin films having an optical energy gap of 3.3eV, thus being transparent in the visible range of the sun spectrum. It is dopable with both the commercial n-dopant AOB (acridine orange base) and the proprietary material NDN1 leading to conductivities of 7.6·10⁻⁶S/cm and 2.2·10⁻⁴S/cm at 5wt% and 7wt%, respectively. Owing to its strongly electron withdrawing character, electron affinity and ionization potential are exceptionally high. While *EA* is estimated to be in the order of 4.8eV by several different methods, the *IP* is determined by ultraviolet photoelectron spectroscopy (UPS) and yields 9.6eV. When applying n-doped HATCN in organic p-i-n type solar cells, the high *EA* is detrimental for the device performance: Solar cells with a direct ZnPc:C₆₀/n-HATCN interface result in short circuits as due to the close proximity of the hole transport level in ZnPc and the electron transport level in n-HATCN electrons and holes can recombine at the interface. By inserting an interlayer composed of intrinsic C₆₀, the recombination can be avoided and the photovoltaic performance is improved. However, there is still an offset in electron affinities at the C₆₀/n-HATCN interface which creates an electron injection barrier and a pronounced s-kink in the *jV*-characteristics. It is found that this injection barrier and thus the s-kink can be removed by exploiting the benefits of molecular doping. In n-doped compounds, the Fermi level is pinned close to the electron transport level. When introducing an additional n-C₆₀ layer between i-C₆₀ and n-HATCN, Fermi level alignment takes place and is consequently accompanied by an alignment of the bulk electron transport levels between the two n-doped compounds and i-C₆₀. The formation of interface dipoles and narrow space charge layers at the respective interfaces does not impede charge

* Measured at IAPP by Selina Olthof.

transport. Overall, a layer stack improved in this way shows a slightly larger power conversion efficiency of $\eta_{n\text{-HATCN}} = 1.8\%$ compared to $\eta_{n\text{-C}_{60}} = 1.7\%$ of a reference device with only n-C₆₀. Impedance spectroscopy is used to verify the conclusions drawn from the development of the jV -curves. Here, the electron injection barrier manifests as a negative capacitance under forward bias.

Next, a series of six **Bis-Fl-NTCDI** (N,N-bis(flourene-2-yl)-naphthalenetetracarboxylic diimide) derivatives is studied. The molecules only differ by the length of the alkyl side chains attached to the C9 position of the fluorene functional groups, i.e. starting with a compound having no side chains, the number of carbon atoms increases from one (methyl) to two (ethyl), three (propyl), four (butyl), and six (hexyl). As expected, the optical properties as well as the energy levels are nearly independent of the structural modifications: With an average optical energy gap of $\approx 3.1\text{eV}$, all compounds are transparent. The IP measured by UPS increases only slightly from 6.45eV for methyl side chains to 6.63eV for hexyl side chains, while the value of the bare material Bis-HFl-NTCDI is 6.55eV and, therefore, does not follow the trend. Due to a lack of measurement methods for directly determining thin film EA , the values are estimated by cyclic voltammetry (CV). In the organic solvent DCM, the reduction potentials versus the internal standard ferrocene/ferrocinium yield $-(1.05 \pm 0.02)\text{V}$ for all compounds, i.e. an EA in the range of 3.5eV is deduced. Concerning thin film morphology, the addition of alkyl chains results in the formation of smooth films with an rms surface roughness smaller than 1nm whereas the surface of films composed of Bis-HFl-NTCDI, the side chain free compound, displays a granular structure with an increased rms roughness of $(2.5 \pm 0.5)\text{nm}$. Substrate heating further increases the roughness to $(1.5 \pm 0.5)\text{nm}$ (derivatives with side chains) and $(9 \pm 0.5)\text{nm}$ (Bis-HFl-NTCDI), respectively. X-ray diffraction (XRD) and grazing incident x-ray diffraction (GIXRD) confirm that the addition of side chains supports the formation of amorphous films on heated and unheated substrates while Bis-HFl-NTCDI thin films are nanocrystalline already at room temperature. It is found that the electrical properties are also affected by the side chain length. An effective n-doping is only achieved in the unsubstituted compound whose conductivity is increased to $1.3 \cdot 10^{-4}\text{S/cm}$ by adding 7wt% NDN1. In contrast, when applying the same or larger doping concentrations in any of the alkylated materials, the conductivity is at least 3 orders of magnitude smaller. This behavior is either due to a morphologically induced reduction of the charge transfer efficiency between dopant and matrix, or due to a significantly reduced electron mobility upon alkylation. The fact that the electron mobilities of the alkylated compounds are below the detection limit of our standard organic field effect transistor (OFET) setup, i.e. $< 10^{-6}\text{cm}^2/\text{Vs}$, provides evidence for the second effect. As a consequence, alternative n-dopants are tested only in Bis-HFl-NTCDI, resulting in $\sigma = 6.8 \cdot 10^{-6}\text{S/cm}$ with 7.5wt% of the less effective cationic dopant AOB and $\sigma = 3.0 \cdot 10^{-4}\text{S/cm}$ for 7.5wt% Cr₂(hpp)₄ which shows a similar performance to NDN1. Post-annealing of the substrate up to a temperature of $\approx 180^\circ\text{C}$ can further increase the conductivity by approximately one order of magnitude. Beyond this temperature, either a structural change or a starting decomposition of the material causes the conductivity to decrease. Finally, the performance of all compounds as ETM in p-i-n type organic solar cells is compared. Here, the differences in electron transport properties turned out to be decisive: While using n-Bis-HFl-NTCDI results in a good solar cell with a fill factor of 52% and a power conversion efficiency of 2.1%, the low conductivities of all other compounds cause the formation of a pronounced s-kink in the jV -characteristics leading to a dramatic decrease in fill factor (FF) and efficiency to minimum values of $FF = 18\%$ and $\eta < 0.1\%$ for n-Bis-HexFl-NTCDI (hexyl side chains). Impedance spectroscopy is able to confirm that insufficient charge transport properties are responsible for the decline in power conversion efficiency. Furthermore, it reveals that a fraction of n-dopants penetrates into the intrinsic materials either during deposition or due to the surface roughness of the underlying materials.

HATNA-Cl₆ (2,3,8,9,14,15-hexachloro-5,6,11,12,17,18-hexaazatrinaphthylene) is the last material investigated in the framework of this thesis. Having an optical energy gap of 2.7eV it is not completely transparent in the visible range of the sun spectrum. Below a wavelength of 460nm, its absorption spectrum overlaps the main absorption band of C₆₀ which is commonly used as photoactive acceptor. Despite this drawback, the favorable energy level positions of $EA = 4.1\text{eV}$, which is known from literature^[150], and $IP = 7.3\text{eV}$, determined by UPS, make HATNA-Cl₆ a promising ETM for solar cells comprising i-C₆₀. Depositing HATNA-Cl₆ onto glass substrates which are kept at room temperature results in the formation of smooth films with an rms roughness in the range of 1nm. On substrates heated to 100°C, the rms roughness is doubled and polycrystallinity is proven by GIXRD. Concerning dopability, an enhancement of the lateral conductivity is achieved with all available n-dopants. For the highest tested doping concentration of 7.5wt%, we find $\sigma_{\text{AOB}} = 1.6 \cdot 10^{-6}\text{S/cm}$, $\sigma_{\text{Cr}_2(\text{hpp})_4} = 3.5 \cdot 10^{-3}\text{S/cm}$, and $\sigma_{\text{NDN1}} = 7.5 \cdot 10^{-3}\text{S/cm}$, respectively. The stability of doped layers upon post-annealing is exemplarily tested for films doped with Cr₂(hpp)₄ which are able to withstand a substrate heating up to 150°C. Finally,

n-HATNA-Cl₆ is successfully implemented into p-i-n type solar cells. While choosing an ETM thickness of 40nm results in identical power conversion efficiencies of $\eta = 2.1\%$, the benefits of the more transparent ETM are more pronounced at $d_{\text{ETM}} = 120\text{nm}$ where we find $\eta_{\text{n-HATNA-Cl}_6} = 1.1\% > \eta_{\text{n-C}_{60}} = 0.4\%$.

To quantify the benefits of transparent charge transport materials and to evaluate the potential of the most promising ETM identified in this thesis, the performance of **p-i-n type solar cells with varying ETM type and thickness** is investigated. Optical simulations are used to calculate the absorption properties of the associated layer stacks and to deduce the photocurrent gain expected when replacing n-C₆₀ by n-Bis-HfI-NTCDI, n-HATNA-Cl₆, or the previously studied n-NTCDA^[13-15]. In p-i-n type devices, the ETM thickness determines the position of the photoactive layers with respect to the maximum of the optical interference pattern which forms upon the reflection of the incident light at the aluminum cathode. Consequently, it is an important parameter considering device optimization in terms of thin film optics. Due to the differences in refractive indices, an optimum layer thickness of $d_{\text{ETM}}^{\text{opt}} = 40, 50, 60,$ and 60nm is anticipated for n-C₆₀, n-HATNA-Cl₆, n-Bis-HfI-NTCDI, and n-NTCDA when being used as ETM in the standard test stack. Furthermore, the decrease in parasitic absorption is expected to result in $j_{\text{sc}}^{\text{n-C}_{60}} < j_{\text{sc}}^{\text{n-HATNA-Cl}_6} < j_{\text{sc}}^{\text{n-NTCDA}} \leq j_{\text{sc}}^{\text{n-Bis-HfI-NTCDI}}$. A similar result is anticipated for n-i-p type devices. However, here the thickness dependence is less pronounced as the influence of the ETM on the thin film interference pattern is much smaller. Before focusing on the actual performance of the new ETM, the performance of the reference material n-C₆₀ is examined more closely. Analyzing the spectral response of flat heterojunction solar cells comprising a direct interface between the donor ZnPc and the ETM n-C₆₀, confirms that excitons created in n-doped layers do not contribute to the photocurrent. Thus, non-transparent charge transport layers are rightly called „parasitic absorber materials“. It is found that n-C₆₀ devices exhibit a peculiarity considering the effective solar cell area. Because of its good lateral conductivity in the order of 1S/cm, n-doped C₆₀ extends the area of the cathode, thus expanding the effective device area to values larger than the geometric overlap between ITO bottom and metal top contact. The current generated in the edge area is mainly dependent on the thickness of the photoactive layers as due to the absence of a reflecting metal film the light passes the layer stack only once and thin film interference does not occur. Overall, this effect leads to a considerable overestimation of the device performance and hence a shadow mask has to be used for determining correct j_{sc} values. Similar edge effects are not observed for the other ETM investigated in this thesis. Based on this knowledge, the performance of p-i-n type devices comprising either n-C₆₀, n-Bis-HfI-NTCDI, n-HATNA-Cl₆, or n-NTCDA layers of varying thickness is examined. Although the experimental results are generally in good agreement with the trends predicted by the optical simulation, the gain in photocurrent upon using transparent ETM is less than expected at optimized device geometries. This finding can be explained by deficiencies in the optical simulation which is partly based on simplified assumptions. For instance it neglects the influence of doping on the absorption of charge transport layers or the possibility of diffusely reflecting interfaces. Nevertheless, at larger ETM thickness, i.e. $d_{\text{ETM}} > 50\text{nm}$, the benefits of transparent ETM compared to the parasitically absorbing n-C₆₀ are more pronounced. Overall, also V_{oc} and FF are improved by implementing transparent ETM and the resulting maximum device efficiencies are $\eta_{\text{max}}^{\text{C}_{60}, \text{HATNA-Cl}_6} = 2.1\%$ for n-C₆₀ and n-HATNA-Cl₆ solar cells, $\eta_{\text{max}}^{\text{Bis-HfI-NTCDI}} = 2.3\%$ for n-Bis-HfI-NTCDI solar cells, and $\eta_{\text{max}}^{\text{NTCDA}} = 2.4\%$ for n-NTCDA solar cells.

Furthermore, the applicability of n-Bis-HfI-NTCDI and n-HATNA-Cl₆ is tested in inverted **n-i-p device geometries**. The replacement of n-C₆₀ by n-Bis-HfI-NTCDI in a n-i-p type solar cell comprising a bulk heterojunction composed of ZnPc:C₆₀ as photoactive system improves photocurrent, V_{oc} , and FF resulting in $\eta_{\text{n-Bis-HfI-NTCDI}} = 2.8\% > \eta_{\text{n-C}_{60}} = 2.2\%$. For testing the performance of n-HATNA-Cl₆, devices with the alternative absorber system DCV6T:C₆₀ are used. In order to achieve an optimized morphology of the bulk heterojunction, the substrate is heated to 85°C during deposition, i.e. the respective ETM is exposed to a post-annealing process. While there is no difference in V_{oc} and FF upon replacing n-C₆₀, the photocurrent and thus the efficiency is improved from $\eta_{\text{n-C}_{60}} = 2.9\%$ to $\eta_{\text{n-HATNA-Cl}_6} = 3.2\%$ by using the more transparent material.

Finally p-i-n type solar cells with varying ETM are investigated with regard to **device stability**. It is found that the performance of solar cells comprising n-C₆₀ or n-Bis-HfI-NTCDI remains nearly unaffected by an accelerated ageing at a temperature of 50°C and an illumination intensity of approximately two suns. In contrast, n-NTCDA devices suffer from a constant decrease of the photocurrent which is presumably due to a morphological effect like (re-)crystallization. n-HATNA-Cl₆ devices show a rapid degradation of I_{sc} and FF which can either be associated with a decomposition of the material or a complete de-doping of the ETM. Overall, device lifetimes t_{80} of 36 500h, 14 000h, 4 500h, and 445h are extracted by applying a stretched exponential decay function to the $\eta(t)$ -curves of n-C₆₀, n-Bis-HfI-NTCDI, n-NTCDA, and

n-HATNA-Cl₆ devices, respectively. Impedance spectroscopy reveals that the density of occupied trap states within the intrinsic layers varies with the composition of the ETM and is related to the amount of n-doping. Thus, at least a part of the traps are electron traps. Furthermore, it is shown that, except for the n-C₆₀ device which is most stable, the density of filled trap states is decreased upon ageing.

8.2 Outlook

This work demonstrates the benefits of transparent charge transport materials for achieving improved device efficiencies. Bis-HFI-NTCDI is identified as the first transparent and durable electron transport material which can replace n-C₆₀ in both p-i-n and n-i-p type organic solar cells. It should serve as starting point for further research on device optimization, thereby utilizing the potential of the p-i-n concept to its full extent.

Up to now, only few device geometries mainly comprising the standard material system ZnPc:C₆₀ together with p-doped MeO-TPD have been investigated. For accomplishing better power conversion efficiencies, it is useful to combine the ETM with photoactive material systems that are capable of achieving higher V_{oc} and higher photocurrents. As demonstrated in the example shown in Chapter 6.2.3, it is usually sufficient to exchange only the donor and the HTM – here DCV6T instead of ZnPc and BPAPF instead of MeO-TPD – while leaving the acceptor C₆₀ unvaried. By this, also the ETM which is designed for matching the electron transport level of C₆₀ remains unaffected. Currently, diindenoperylene derivatives^[129,219] and dicyanovinyl (DCV)-substituted oligothiophenes^[213,220] are considered the most promising alternatives for ZnPc. Establishing the use of n-Bis-HFI-NTCDI or similar transparent compounds together with those materials as a standard routine is a promising path towards improving the device performance.

The majority of the solar cells based on new absorber systems are either m-i-p type devices with a direct ITO/acceptor contact^[220] or n-i-p type devices with only a 5nm thin ETM composed of n-doped C₆₀ that establishes the electrical contact between ITO and acceptor. The reason for this is easily comprehensible when considering the results presented in Chapter 6: On the one hand, a transparent spacer layer between photoactive area and the reflecting metal electrode is needed for optimizing the stack in terms of thin film optics. Due to a lack of suitable ETM, the n-i-p geometry has to be chosen and transparent HTM are implemented as optical spacer. On the other hand, optical modeling shows that utilizing a parasitically absorbing material like n-C₆₀ is always detrimental for efficiency of n-i-p type devices which is why the n-C₆₀ layer is either as thin as possible or even omitted. By using the new opportunities of transparent ETM in n-i-p geometry, it is not only possible to avoid these disadvantages but to also achieve an additional improvement of the absorption in the photoactive layers. Similar to the systematic study of p-i-n devices presented in this work, a further investigation of n-i-p devices is necessary to quantify the expected benefits and to systematically compare the influence of the specific device architecture.

The same arguments apply for tandem device structures. Here, a transparent ETM can replace the n-C₆₀ layers that are, for instance, needed for establishing an efficient recombination contact between the two subcells^[127,221]. Furthermore it can be employed as optical spacer layer, thus replacing the currently used transparent HTM which is responsible for ensuring a controlled current matching in the tandem stack^[118].

Regarding the fact that an ETM is always designed for matching the energy levels of the photoactive acceptor material, the synthesis of further compounds might become necessary as soon as C₆₀ is replaced by alternative acceptors with other physical properties. First studies identified C₇₀^[130] or K12^[131] as interesting candidates. Apart from the application in small molecule solar cells, it is also possible to insert a vacuum deposited ETM as optical spacer layer below the reflecting metal cathode of polymer solar cells. Here, all layers up to the acceptor are spin cast. Typical polymeric acceptor materials are based on fullerenes^[222] like for instance the most common representative PC₆₀BM that is based on C₆₀. However, the relevance of this approach, which introduces further processing steps into device fabrication, remains questionable. In any case, it is useful to extend the selection of transparent ETM that are available for device fabrication.

Last but not least, as demonstrated by the Bis-FI-NTCDI series, but also by the comparison of HATCN with the similar but larger HATNA-Cl₆ molecule, electron transport materials are an interesting class for studying the relationship between molecular structure and macroscopic physical properties. Here, the large variability of organic compounds opens up numerous possibilities, as even small variations of the molecule can have a strong impact on its performance. In terms of application, the influence of functional

groups or side chains on energy level positions, absorption spectrum, thin film morphology, charge carrier mobility, dopability and thermal as well as morphological stability is of particular relevance. Gaining an understanding of these structure-properties relationships is of fundamental importance when aiming for the design of materials for a specific application. Concerning ETM, the most important properties are energy level positions and charge transport properties which should be tuneable by doping. However, it has to be noted that the doping mechanism itself is not well understood. As illustrated by the results on Bis-FI-NTCDI derivatives presented in Chapter 4, well suited energy level positions are not necessarily sufficient for achieving an adequate enhancement of a materials conductivity upon doping. Unfortunately, the influence of the electron mobility on the observed effect could not be determined since an appropriate experimental method for measuring mobilities $< 10^{-6}\text{cm}^2/\text{Vs}$ had not been available. Here, either impedance spectroscopy or space charge limited current measurements on single carrier devices might be capable of complementing the OFET results. Combining the mobility data with IPES measurements for determining more reliable values for the thin film electron affinity would constitute a first step towards a better understanding of the doping effect. Further experiments involving a larger variety of matrix and dopant molecules need to follow. Hence, not only the synthesis of further Bis-FI-NTCDI derivatives constitutes a promising approach. Alternatively, the HATNA series can be used as a starting point for a study of this type as recently the two fluorinated derivatives HATNA-F₆ and HATNA-F₁₂ have been identified as suitable ETM in the framework of a diploma thesis at the IAPP^[223].

Appendix A - Characteristic Parameters of Devices Presented in Chapter 6

The following table lists the characteristic parameters presented in Figure 6.9. I_{eff} denotes the mismatch corrected intensity which is used for calculating the power conversion efficiency η . While j_{sc} of the n-C₆₀ devices is determined using an aperture of 5.1mm² size, this procedure proved to be unnecessary for devices comprising n-HATNA-Cl₆, n-NTCDA, or n-Bis-HfI-NTCDI. V_{oc} , FF and Sat are deduced from the jV -curves measured without aperture. Unfortunately, the solar cell comprising 150nm n-C₆₀ was destroyed during the measurement with the shadow mask. Hence, j_{sc} and η could not be calculated.

d_{ETM} (nm)	V_{oc} (V)	j_{sc} (mA/cm ²)	FF (%)	Sat ($j(-1V)/j_{\text{sc}}$)	I_{eff} mW/cm ²	η (%)
n-C ₆₀						
0	0.22	2.8	32	2.06	90	0.2
10	0.48	5.1	53	1.13	93	1.4
20	0.49	6.8	52	1.13	96	1.8
30	0.49	7.3	50	1.14	97	1.9
40	0.49	8.2	50	1.14	99	2.1
50	0.49	8.0	49	1.16	100	1.9
60	0.48	7.1	49	1.17	100	1.7
70	0.48	5.9	48	1.20	99	1.4
80	0.47	4.6	48	1.17	99	1.0
90	0.46	3.2	47	1.23	99	0.7
100	0.45	2.5	48	1.25	98	0.5
110	0.45	2.1	47	1.31	97	0.5
120	0.45	1.8	46	1.32	97	0.4
130	0.45	2.1	46	1.34	96	0.5
140	0.46	2.6	47	1.31	96	0.6
150	0.46	-	48	1.28	95	-
n-Bis-HfI-NTCDI						
0	0.21	2.2	36	5.43	91	0.2
13	0.51	5.3	53	1.09	93	1.5
27	0.52	6.7	52	1.12	95	1.9
40	0.52	7.6	53	1.12	97	2.2
54	0.52	8.4	52	1.11	99	2.3
67	0.52	8.5	51	1.13	100	2.3
81	0.52	8.1	50	1.12	101	2.1
94	0.52	7.1	52	1.11	101	1.9
108	0.51	6.7	51	1.09	100	1.7
121	0.50	5.0	52	1.13	98	1.3
134	0.49	3.8	51	1.13	96	1.0
148	0.48	3.1	51	1.10	94	0.8
161	0.48	3.1	51	1.10	95	0.8
175	0.47	2.2	55	1.14	95	0.6
188	0.47	2.0	56	1.15	95	0.6
202	0.47	2.2	53	1.07	96	0.6

d_{ETM} (nm)	V_{oc} (V)	j_{sc} (mA/cm ²)	FF (%)	Sat ($j(-1V)/j_{\text{sc}}$)	I_{eff} mW/cm ²	η (%)
n-HATNA-Cl ₆						
0	0.19	2.1	34	4.46	89	0.2
10	0.48	4.9	52	1.13	90	1.4
20	0.49	6.2	51	1.13	94	1.7
30	0.50	7.3	50	1.13	96	1.9
40	0.50	8.1	50	1.13	97	2.1
50	0.50	8.4	48	1.14	98	2.1
60	0.50	8.3	49	1.14	98	2.1
70	0.50	7.2	49	1.14	98	1.7
80	0.49	7.0	49	1.13	98	1.7
90	0.48	5.9	49	1.14	98	1.4
100	0.47	4.6	49	1.14	96	1.1
110	0.47	3.6	49	1.15	96	0.9
120	0.47	3.9	50	1.13	96	0.9
130	0.46	2.8	49	1.16	95	0.7
140	0.45	2.3	50	1.17	95	0.5
150	0.45	2.1	50	1.17	95	0.5
n-NTCDA						
0	0.15	2.5	31	4.80	90	0.1
10	0.50	6.1	50	1.16	93	1.6
20	0.51	7.7	52	1.14	96	2.1
30	0.51	8.5	52	1.14	97	2.3
40	0.51	8.9	51	1.15	98	2.4
50	0.51	9.4	50	1.15	99	2.4
60	0.51	9.0	50	1.16	99	2.3
70	0.51	8.4	51	1.14	99	2.2
80	0.51	8.1	51	1.14	99	2.1
90	0.50	7.0	51	1.16	99	1.8
100	0.50	5.9	51	1.15	98	1.5
110	0.49	5.3	52	1.15	98	1.4
120	0.49	4.8	53	1.15	97	1.3
130	0.48	4.0	53	1.16	96	1.0
140	0.47	3.2	53	1.16	96	0.8
150	0.48	3.4	53	1.15	96	0.9

Appendix B - Database Numbers of Solar Cells Shown in this Thesis

Chapter 3 – HATCN solar cells		
device	database name	production tool
flat hj device	CF74 (no database number)	UFO
device A	OSOL-198 Sample 25	Lesker B
device B	OSOL-198 Sample 15	
device C	OSOL-198 Sample 05	
device D	OSOL-198 Sample 45	
device E	OSOL-198 Sample 40	
device A'	OSOL-198 Sample 24	
device B'	OSOL-198 Sample 14	
device C'	OSOL-198 Sample 04	
device D'	OSOL-198 Sample 44	
Chapter 4 – Bis-Fl-NTCDI solar cells		
Bis-HFl-NTCDI, 5nm i-C ₆₀	OSOL-494 Sample 25	Lesker B
Bis-MeFl-NTCDI, 5nm i-C ₆₀	OSOL-494 Sample 24	
Bis-EtFl-NTCDI, 5nm i-C ₆₀	OSOL-494 Sample 23	
Bis-PrFl-NTCDI, 5nm i-C ₆₀	OSOL-494 Sample 22	
Bis-BuFl-NTCDI, 5nm i-C ₆₀	OSOL-494 Sample 21	
Bis-HexFl-NTCDI, 5nm i-C ₆₀	OSOL-494 Sample 20	
Bis-HFl-NTCDI, 0nm i-C ₆₀	OSOL-494 Sample 15	
Bis-HFl-NTCDI, 10nm i-C ₆₀	OSOL-494 Sample 45	
Chapter 5 – HATNA-Cl ₆		
40nm n-HATNA-Cl ₆	OSOL-472 Sample 24	Lesker A
40nm n-C ₆₀	OSOL-436 Sample 24	
120nm n-HATNA-Cl ₆	OSOL-472 Sample 44	
120nm n-C ₆₀	OSOL-436 Sample 44	
Chapter 6 – comparison of different ETM		
flat ZnPc/C ₆₀ (0nm)/n-C ₆₀ (50nm)	OSOL-568 Sample 25	Lesker A
flat ZnPc/C ₆₀ (10nm)/n-C ₆₀ (40nm)	OSOL-568 Sample 24	
flat ZnPc/C ₆₀ (20nm)/n-C ₆₀ (30nm)	OSOL-568 Sample 33	
flat ZnPc/C ₆₀ (30nm)/n-C ₆₀ (20nm)	OSOL-568 Sample 22	
flat ZnPc/C ₆₀ (40nm)/n-C ₆₀ (10nm)	OSOL-568 Sample 21	
flat ZnPc/C ₆₀ (50nm)/n-C ₆₀ (0nm)	OSOL-568 Sample 30	
p-i-n variation: n-C ₆₀	OSOL-436, all samples	
p-i-n variation: n-Bis-HFl-NTCDI	OSOL-548, all samples	
p-i-n variation: n-HATNA-Cl ₆	OSOL-472, all samples	Lesker B
p-i-n variation: n-NTCDA	OSOL-618, all samples	
n-i-p: n-Bis-HFl-NTCDI	OSOL-597 Sample 24	
n-i-p: n-C ₆₀ (reference for Bis-HFl-NTCDI)	OSOL-597 Sample 20	
n-i-p: n-HATNA-Cl ₆	PV-091 Sample 23	
n-i-p: n-C ₆₀ (reference for HATNA-Cl ₆)	PV-091 Sample 24	
Chapter 7 – Stability Issues		
n-C ₆₀ device	OSOL-367 Sample 14	Lesker B
n-Bis-HFl-NTCDI device	OSOL-367 Sample 11	
n-HATNA-Cl ₆ device	OSOL-367 Sample 13	
n-NTCDA device	OSOL-367 Sample 10	

Appendix C - Abbreviations

A	acceptor
AFM	atomic force microscopy
CGL	charge generation layer
CIGS	copper indium gallium selenide, $\text{CuIn}_{1-x}\text{Ga}_x\text{Se}_2$
CS state	charge separated state
CT state	charge transfer state
CV	cyclic voltammetry
D	donor
D/A	donor/acceptor
DMSO	dimethyl sulfoxid (solvent)
DOS	density of states
DSC	differential scanning calometry
EIB	electron injection barrier
EQE	external quantum efficiency
ETM	electron transport material
ESI-MS	electrospray ionization mass spectrometry
FTIR	Fourier transform infrared spectroscopy
GIXRD	grazing incidence x-ray diffraction
HBEC	high binding energy cutoff
HIB	hole injection barrier
HOMO	highest occupied molecular orbital
HTM	hole transport material
IPES	inverse photoelectron spectroscopy
IQE	internal quantum efficiency
ITO	indium tin oxide
IS	impedance spectroscopy
ISC	intersystem crossing
LED	light emitting diode
LUMO	lowest unoccupied molecular orbital
OFET	organic field effect transistor

OLED	organic light emitting diode
OPV	organic photovoltaic device
OSC	organic solar cell
PES	photoelectron spectroscopy
SCL	space charge layer
SRC	standard reporting conditions
STC	standard testing conditions
TBAB	tetrabutyl ammoniumbromide (phase transfer catalyst)
TGA	thermogravimetric analysis
UPS	ultraviolet photoelectron spectroscopy
UV	ultraviolet
XPS	x-ray photoelectron spectroscopy
XRD	x-ray diffraction
XRR	x-ray reflectometry

Appendix D - Materials

Alq ₃	tris (8-hydroxy-quinolinato)-aluminium
AOB	acridine orange base
BCP	2,9-dimethyl-4,7 diphenyl-1,10-phenanthroline
BEDT-TTF	bis(ethylenedithio)-tetrathiafulvalene
Bis-Fl-NTCDI	N,N-Bis(fluorene-2-yl)-naphthalenetetracarboxylic diimide
BPAPF	9,9-bis[4-(N,N-bis-biphenyl-4-yl-amino)phenyl]-9H-fluorene
BPhen	4,7-diphenyl-1,10-phenanthroline
BTQBT	bis(1,2,5-thiadiazolo)-p-quinobis(1,3-dithiole)
(BuFl) ₂ -B ₁₀ C ₂ H ₁₀	1,2-bis(9,9-dibutyl-fluorene-2-yl)carborane
Bu-Fl-DAB	N,N-Bis(9,9-dibutylfluorene-2-yl)-1,4-diaza-2,3-dimethyl-1,3-butadiene
Bu-Fl-DOB	2-(difluoro-1,3,2-H-dioxaborinyl)-1,1'-(9,9-dibutyl-9H-fluorene)
Bu-Fl-ZnCl-ACN	Bis[(9,9-dibutylfluorene-2-yl)imino]acenaphthene zinc dichloride
C ₆₀	buckminster fullerene
CoCp ₂	cobaltocene
Cr(bpy) ₃	tris(2,2'-bipyridine)chromium(III)
Cr ₂ (hpp) ₄	tetrakis(1,3,4,6,7,8-hexahydro-2H-pyrimido[1,2-a]pyrimidinato)dichromium (II)
Cr(TMB) ₃	tris(4,4',5,5'-tetramethyl-2,2'-bipyridine)chromium(III)
CuPc	copper phthalocyanine
DCM	decamethylcobaltocene (n-dopant) or dichloromethane (solvent)
DCV5T	α, α'-bis-(2,2-dicyanovinylene)-quinquethiophene
DCV6T	α,ω-bis-(dicyanovinylene)-sexithiophene
DDQ	dichlorodicyanoquinone
DIP	diindenoperylene
F ₂ -HCNQ	3,6-difluoro-2,5,7,7,8,8-hexacyanoquinodimethane
F ₄ -TCNQ	2,3,5,6-tetrafluoro-7,7,8,8-tetracyanoquinodimethane
F ₄ -ZnPc	tetrafluoro-zinc phthalocyanine
F ₆ -TNAP	1,3,4,5,7,8-hexafluorotetracyanonaphthoquinodimethane
Fc/Fc+	ferrocene/ferrocinium
Fl-DOB	2-(difluoro-1,3,2-H-dioxaborinyl)-1,1'-(9H-fluorene)
HATCN	hexaazatriphenylene hexacarbonitrile

HATNA	hexaazatrinaphthylene
HATNA-Cl ₆	2,3,8,9,14,15-hexachloro-5,6,11,12,17,18-hexaazatrinaphthylene
HATNA-F ₆	2,3,8,9,14,15-hexafluoro-5,6,11,12,17,18-hexaazatrinaphthylene
HATNA-F ₁₂	1,2,3,4,7,8,9,10,13,14,15,16-dodecafluoro-5,6,11,12,17,18-hexaazatrinaphthylene
K12	2-[[7-(9,9-di- <i>n</i> -propyl-9 <i>H</i> -fluoren-2-yl)benzo[<i>c</i>][1,2,5]thiadiazol-4-yl]methylene]malononitrile
LCV	leuco crystal violet
MeO-TPD	N,N,N',N'-tetrakis(4-methoxyphenyl)-benzidine
NDN1	Novaled n-dopant 1
NDP2	Novaled p-dopant 2
NDP9	Novaled p-dopant 9
NPB	4,4'-bis(N-phenyl-1-naphthylamino)biphenyl
NTCDA	1,4,5,8-naphthalenetetracarboxylic dianhydride
NTCDI	naphthalenetetracarboxylic diimide
PC ₆₀ BM	phenyl-C61-butyrac acid methyl ester
PyB	pyronine B
Ru(terpy) ₂	bis(terpyridine)ruthenium(II)
TBAB	tetrabutyl ammoniumbromide
TCNQ	tetracyanoquinodimethane
TTN	tetrathianaphthacene
ZnPc	zinc phthalocyanine

Appendix E - Symbols

a	average lattice distance
A	area
a_0	lattice constant
a_{th}	thermalization radius of a hot exciton
b	width of the metal free channel on a conductivity substrate
c	speed of light / calibration factor of the solar simulator
C	capacitance
C_{geo}	geometric capacitance
C_P	parallel capacitance
C_{μ}	chemical capacitance
d	film thickness / interplane distance in crystalline samples
D	diffusion coefficient
$d_{\text{D,M}}$	correct thickness of dopant / matrix layers
$d_{\text{D,M}}^*$	thickness of dopant / matrix layers displayed by the quartz monitor
d_{ETM}	ETM thickness
e	elementary charge
E	energy
$E_{1/2}^0$	half cell potential
$E_{\text{AM1.5/sim}}$	spectral irradiance of an AM1.5G light source / of our sun simulator
E_{B}	binding energy
$E_{\text{B}}^{\text{exc}}$	exciton binding energy
$E_{\text{C,V}}$	conduction / valence band energy
E_{F}	Fermi energy
$E_{\text{F,C/V}}$	quasi-Fermi level positions for electrons / holes
$E_{\text{F,n/p}}$	Fermi level positions for electrons / holes in doped semiconductors
E_{g}	energy gap
E_{HBEC}	energy of the high binding energy cutoff
E_{HIB}	energy of the hole injection barrier
E_{HOMO}	energy of the HOMO cutoff

E_{kin}	kinetic energy
E_t	energy of trap state
E_{vac}	vacuum energy
EA	electron affinity
f	frequency of the AC input voltage for IS
F	electric field
F_C	Coulomb force
FF	fill factor
$G(E)$	Gaussian distribution of states (diagonal disorder)
h	Planck's constant
I	current
I_{corr}	nominal illumination intensity measured by the reference diode when the solar simulator is adjusted to the spectral mismatch
I_{eff}	effective mismatch corrected illumination intensity used for calculating the mismatch corrected power conversion efficiency η
I_{light}	light intensity
I_{SD}	source-drain current of an OFET
I_{sc}	short circuit current
IP	ionization potential
j	current density
j_{MPP}	current density at the maximum power point of a solar cell
j_{photo}	photocurrent density
j_s	saturation current density
j_{sc}	short circuit current density
$j_{\text{TC}}^{\text{AM1.5/sim}}$	short circuit current density of the test solar cell when illuminated with an AM1.5G spectrum or a solar simulator
$j_{\text{ref}}^{\text{AM1.5/sim}}$	short circuit current density of the Si reference diode when illuminated with an AM1.5G spectrum or a solar simulator
k	extinction coefficient
k_B	Boltzmann constant
$k_{\text{CT/CS}}$	rate constant for the generation of a CT or CS state
$k_{\text{gem/bimol}}$	rate constant for geminate or bimolecular recombination
k_T	rate constant for triplet back transfer from CT state
l	length of the metal free channel on a conductivity substrate
L	channel length of an OFET
l_0	mean free path
L_D	exciton diffusion length

M	mismatch factor
$m_{D,M}$	mass of dopant / matrix material
n	charge carrier density / refractive index
n_i	charge carrier density in thermodynamic equilibrium
n_n/p_p	density of majority charge carriers (electrons / holes)
$N_{A,D}$	density of donors / acceptors
$N_{C,V}$	effective density of electrons / holes in the conduction / valence band
N_{ion}	density of ionized molecules
OD	optical density
P	polarization energy
$P(E)$	escape probability of an exciton
p_p/n_n	density of majority charge carriers (holes / electrons)
$P_{e,h}$	polarization energy for electrons / holes
q	charge
r	distance / radius
\hat{R}	ohmic resistance
r_C	Coulomb capture radius
R_{diff}	diffuse reflection
R_p	parallel resistance
R_s	series resistance
$\Delta R_{i,j}$	distance between hopping sites i and j
S_0	molecular ground state
S_1	first excited singlet state
Sat	saturation factor of a solar cell
SR	spectral response
t	time / attenuation depth of an x-ray beam
t_{80}	lifetime of an organic solar cell
T	temperature / transmission
T_1	first excited triplet state
t_t	trapping time
r	radius / distance
V	voltage
V_{bi}	built-in potential
V_{bias}	DC bias voltage
V_G	gate voltage

V_{MPP}	voltage at the maximum power point of a solar cell
V_{oc}	open circuit voltage
\mathbf{v}_D	drift velocity (vector)
V_s	input AC signal for IS experiments
V_{SD}	source-drain voltage of an OFET
V_{th}	threshold voltage
W	channel width of an OFET
Wf	work function
\hat{X}	reactance
Z	complex impedance
β	field amplification factor
γ	inverse Bohr radius
Δ	interface dipole
ε	dielectric constant
ε_0	vacuum permittivity
$\varepsilon_{i,j}$	site energies of hopping sites i and j
η	electrochemical potential or power conversion efficiency
η_A	probability for exciton generation upon absorption
η_{CC}	charge collection efficiency
η_{CT}	probability for charge transfer and dissociation
η_{ED}	probability for the exciton to reach the D/A interface
θ	1/2 scattering angle in XRD and GIXRD measurements
λ	wavelength
μ_0	mobility of disorder free semiconductor
$\hat{\mu}_{e,h}/\mu_{e,h}$	electron / hole mobility (tensor / scalar)
ν	frequency
ν_0	prefactor in Bässler equation for hopping rate
ν_{ij}	hopping rate between states i and j
$\xi_{n,p}$	chemical potential of electrons / holes
ρ	thin film density
$\hat{\sigma}/\sigma$	conductivity (tensor / scalar)
$\sigma_{n,p}$	electron / hole conductivity
$\tilde{\sigma}$	width of a Gaussian distribution (diagonal disorder)
Σ	width of a Gaussian distribution (off-diagonal disorder)
τ_0	lifetime of an exciton

τ_h	localization time or hopping time
τ_l	lattice relaxation time
τ_v	vibronic relaxation time
φ	electric potential
$\phi(p)$	atomic p orbital
$\phi(s)$	atomic s orbital
ω	incident angle for GIXRD measurements

Bibliography

- [1] S. Teske, A. Zervos, O. Schäfer, energy [r]evolution - a sustainable world energy outlook, European Renewable Energy Council (EREC) and Greenpeace International (2007).
- [2] www.sharp.de, product data sheets (October 2011).
- [3] product data sheets, <http://www.sanyo-solar.eu> (October 2011).
- [4] www.sunpowercorp.de (2011).
- [5] M. A. Green, K. Emery, Y. Hishikawa, W. Warta, E. D. Dunlop, Solar cell efficiency tables (version 38), *Progr. Photovoltaics* 19 (1) (2011) 565.
- [6] www.basf.com (October 2011).
- [7] press release, <http://investor.firstsolar.com> (July 2011).
- [8] annual report, <http://www.showa-shell.co.jp/english/ir/annual/index.html> (2010).
- [9] press release, <http://www.miasole.com/> (December 2010).
- [10] C. Tang, Two-layer organic photovoltaic cell, *Appl. Phys. Lett.* 48 (2) (1986) 183.
- [11] B. Männig, J. Drechsel, D. Gebeyehu, P. Simon, F. Kozlowski, A. Werner, F. Li, S. Grundmann, S. Sonntag, M. Koch, K. Leo, M. Pfeiffer, H. Hoppe, D. Meissner, N. Sariciftci, I. Riedel, V. Dyakonov, J. Parisi, Organic p-i-n solar cells, *Appl. Phys. A-Mater.* 79 (1) (2004) 1.
- [12] P. Peumans, A. Yakimov, S. Forrest, Small molecular weight organic thin-film photodetectors and solar cells, *J. Appl. Phys.* 93 (7) (2003) 3693.
- [13] C. Falkenberg, Untersuchung der Eigenschaften von transparenten Elektronentransportmaterialien und deren Anwendung in p-i-n-Solarzellen (Diplomarbeit, 2007).
- [14] C. Falkenberg, C. Uhrich, S. Olthof, B. Maennig, M. K. Riede, K. Leo, Efficient p-i-n type organic solar cells incorporating 1,4,5,8-naphthalenetetracarboxylic dianhydride as transparent electron transport material, *J. Appl. Phys.* 104 (3) (2008) 034506.
- [15] C. Falkenberg, C. Uhrich, B. Maennig, M. K. Riede, K. Leo, 1,4,5,8-naphthalenetetracarboxylic dianhydride as transparent electron transport material in organic p-i-n solar cells, *P. Soc. Photo-Opt. Ins.* 6999 (2008) S9990.
- [16] N. Karl, Organic semiconductors, *Festkörperprobleme* 14 (1974) 261.
- [17] O. D. Gordan, M. Friedrich, D. R. T. Zahn, The anisotropic dielectric function for copper phthalocyanine thin films, *Org. Electronics* 5 (6) (2004) 291.
- [18] E. A. Silinsh, *Organic Molecular Crystals - Their Electronic States*, Springer Verlag, Berlin, 1980.
- [19] P. I. Djurovich, E. I. Mayo, S. R. Forrest, M. E. Thompson, Measurement of the lowest unoccupied molecular orbital energies of molecular organic semiconductors, *Org. Electron.* 10 (3) (2009) 515.
- [20] S. Krause, M. B. Casu, A. Schoell, E. Umbach, Determination of transport levels of organic semiconductors by UPS and IPS, *New J. Phys.* 10 (2008) 085001.
- [21] D. L. Dexter, A theory of sensitized luminescence in solids, *J. Chem. Phys.* 21 (5) (1953) 836.

- [22] T. Förster, Zwischenmolekulare Energiewanderung und Fluoreszenz, *Ann. Phys. – Berlin* 2 (1-2) (1948) 55.
- [23] L. Stryer, Fluorescence energy-transfer as a spectroscopic ruler, *Annu. Rev. Biochem.* 47 (1978) 819.
- [24] N. Karl, Charge carrier transport in organic semiconductors, *Synthetic Met.* 133 (Sp. Iss. SI) (2003) 649.
- [25] Y. C. Cheng, R. J. Silbey, D. A. da Silva, J. P. Calbert, J. Cornil, J. L. Bredas, Three-dimensional band structure and bandlike mobility in oligoacene single crystals: A theoretical investigation, *J. Chem. Phys.* 118 (8) (2003) 3764.
- [26] A. Miller, B. Abrahams, Impurity conduction at low concentrations, *Phys. Rev.* 120 (1960) 745.
- [27] M. C. J. M. Vissenberg, M. Matters, Theory of the field-effect mobility in amorphous organic transistors, *Phys. Rev. B* 57 (20) (1998) 12964.
- [28] B. Männig, M. Pfeiffer, A. Nollau, X. Zhou, K. Leo, P. Simon, Controlled p-type doping of polycrystalline and amorphous organic layers: Self-consistent description of conductivity and field-effect mobility by a microscopic percolation model, *Phys. Rev. B* 64 (19) (2001) 195208.
- [29] H. Baessler, Charge transport in disordered organic photoconductors, *Phys. Status Solidi B* 175 (15) (1993) 15.
- [30] M. Schwoerer, H. C. Wolf, *Organic Molecular Solids*, WILEY-VCH Verlag GmbH Weinheim, 2007.
- [31] J. Frenkel, On pre-breakdown phenomena in insulators and electronic semiconductors, *Phys. Rev.* 54 (8) (1938) 647.
- [32] W. D. Gill, Drift mobilities in amorphous charge-transfer complexes of trinitrofluorenone and poly-n-vinylcarbazole, *J. Appl. Phys.* 43 (12) (1972) 5033.
- [33] O. Madelung, *Semiconductors - Basic Data*, Springer Verlag, Berlin, 1996.
- [34] S. M. Sze, K. K. Ng, *Physics of Semiconductor Devices*, John Wiley & Sons Inc., New York, 2006.
- [35] C. K. Chan, E. G. Kim, J. L. Bredas, A. Kahn, Molecular n-type doping of 1,4,5,8-naphthalene tetracarboxylic dianhydride by pyronin B studied using direct and inverse photoelectron spectroscopies, *Adv. Funct. Mater.* 16 (6) (2006) 831.
- [36] C. K. Chan, W. Zhao, S. Barlow, S. Marder, A. Kahn, Decamethylcobaltocene as an efficient n-dopant in organic electronic materials and devices, *Org. Electron.* 9 (5) (2008) 575.
- [37] J. Blochwitz, T. Fritz, M. Pfeiffer, K. Leo, D. M. Alloway, P. A. Lee, N. R. Armstrong, Interface electronic structures of controlled doped organic semiconductors, *Org. Electron.* 2 (2) (2001) 97.
- [38] S. Olthof, W. Tress, R. Meerheim, B. Lüssem, K. Leo, Photoelectron spectroscopy study of systematically varied doping concentrations in an organic semiconductor layer using a molecular p-dopant, *J. Appl. Phys.* 106 (10) (2009) 103711.
- [39] L. Yan, N. J. Watkins, S. Zorba, Y. L. Gao, C. W. Tang, Direct observation of Fermi-level pinning in Cs-doped CuPc film, *Appl. Phys. Lett.* 79 (25) (2001) 4148.
- [40] K. Iwasaki, K. Umishita, M. Sakata, S. Hino, Electrical conductivity and electronic structure of potassium doped PTCDA, *Synthetic Met.* 121 (1-3) (2001) 1395.
- [41] H. Ding, Y. Gao, Electronic structure of doping in organic semiconductor, *Proc. of SPIE* 7015 (2008) 705111.
- [42] J. Kido, T. Matsumoto, Bright organic electroluminescent devices having a metal-doped electron-injecting layer, *Appl. Phys. Lett.* 73 (20) (1998) 2866.

- [43] Q. T. Le, L. Yan, Y. G. Gao, M. G. Mason, D. J. Giesen, C. W. Tang, Photoemission study of aluminum/tris-(8-hydroxyquinoline) aluminum and aluminum/LiF/tris-(8-hydroxyquinoline) aluminum interfaces, *J. Appl. Phys.* 87 (1) (2000) 375.
- [44] M. G. Mason, C. W. Tang, L. S. Hung, P. Raychaudhuri, J. Madathil, D. J. Giesen, L. Yan, Q. T. Le, Y. Gao, S. T. Lee, L. S. Liao, L. F. Cheng, W. R. Salaneck, D. A. dos Santos, J. L. Bredas, Interfacial chemistry of Alq(3) and LiF with reactive metals, *J. Appl. Phys.* 89 (5) (2001) 2756.
- [45] J. Wusten, S. Berger, K. Heimer, S. Lach, C. Ziegler, Interaction of alkali metals with perylene-3,4,9,10-tetracarboxylic-dianhydride thin films, *J. Appl. Phys.* 98 (1) (2005) 013705.
- [46] M. Y. Chan, C. S. Lee, S. L. Lai, M. K. Fung, F. L. Wong, H. Y. Sun, K. M. Lau, S. T. Lee, Efficient organic photovoltaic devices using a combination of exciton blocking layer and anodic buffer layer, *J. Appl. Phys.* 100 (9) (2006) 094506.
- [47] X. Zhou, M. Pfeiffer, J. S. Huang, J. Blochwitz-Nimoth, D. S. Qin, A. Werner, J. Drechsel, B. Maennig, K. Leo, Low-voltage inverted transparent vacuum deposited organic light-emitting diodes using electrical doping, *Appl. Phys. Lett.* 81 (5) (2002) 922.
- [48] G. Parthasarathy, C. Shen, A. Kahn, S. R. Forrest, Lithium doping of semiconducting organic charge transport materials, *J. Appl. Phys.* 89 (9) (2001) 4986.
- [49] W. Zhao, A. Kahn, Charge transfer at n-doped organic-organic heterojunctions, *J. Appl. Phys.* 105 (12) (2009) 123711.
- [50] D. T. Sawyer, M. J. Gibian, M. M. Morrison, E. T. Seo, Chemical reactivity of superoxide ion, *J. Am. Chem. Soc.* 100 (2) (1978) 627.
- [51] J. Wilshire, D. T. Sawyer, Redox chemistry of dioxygen species, *Accounts Chem. Res.* 12 (3) (1979) 105.
- [52] F. A. Cotton, N. E. Gruhn, J. D. Gu, P. Huang, D. L. Lichtenberger, C. A. Murillo, L. O. Van Dorn, C. C. Wilkinson, Closed-shell molecules that ionize more readily than cesium, *Science* 298 (5600) (2002) 1971.
- [53] C. J. Bloom, C. M. Elliott, P. G. Schroeder, C. B. France, B. A. Parkinson, Low work function reduced metal complexes as cathodes in organic electroluminescent devices, *J. Phys. Chem. B* 107 (13) (2003) 2933.
- [54] K. Harada, A. Werner, M. Pfeiffer, C. Bloom, C. Elliott, K. Leo, Organic homojunction diodes with a high built-in potential: Interpretation of the current-voltage characteristics by a generalized Einstein relation, *Phys. Rev. Lett.* 94 (3) (2005) 036601.
- [55] A. Nollau, M. Pfeiffer, T. Fritz, K. Leo, Controlled n-type doping of a molecular organic semiconductor: naphthalenetetracarboxylic dianhydride (NTCDA) doped with bis(ethylenedithio)-tetrathiafulvalene (BEDT-TTF), *J. Appl. Phys.* 87 (9) (2000) 4340.
- [56] N. Sato, K. Seki, H. Inokuchi, Polarization energies of organic-solids determined by ultraviolet photoelectron-spectroscopy, *J. Chem. Soc. Farad. T.* 2 77 (1981) 1621.
- [57] S. Tanaka, E. Kawabe, K. Kanai, T. Iwahashi, T. Nishi, Y. Ouchi, K. Seki, n-type doping effect on the electronic structure of organic semiconductor: doping of tetrathianaphthacene (TTN) into hexadecafluorophthalocyaninatozinc (F16ZnPc) by co-evaporation, *J. Electron. Spectrosc.* 144 (Sp. Iss. SI) (2005) 533, 14th International Conference on Vacuum Ultraviolet Radiation Physics, Cairns, Australia, Jul 19-23, 2004.
- [58] J. G. Xue, S. R. Forrest, Bipolar doping between a molecular organic donor-acceptor couple, *Phys. Rev. B* 69 (24) (2004) 245322.
- [59] C. K. Chan, F. Amy, Q. Zhang, S. Barlow, S. Marder, A. Kahn, N-type doping of an electron-transport material by controlled gas-phase incorporation of cobaltocene, *Chem. Phys. Lett.* 431 (1-3) (2006) 67.

- [60] C. K. Chan, A. Kahn, Q. Zhang, S. Barlow, S. R. Marder, Incorporation of cobaltocene as an n-dopant in organic molecular films, *J. Appl. Phys.* 102 (1) (2007) 014906.
- [61] A. Werner, N-type doping of organic thin films using a novel class of dopants, Ph.D. thesis, TU-Dresden (2003).
- [62] F. H. Li, M. Pfeiffer, A. Werner, K. Harada, K. Leo, N. Hayashi, K. Seki, X. J. Liu, X. D. Dang, Acridine orange base as a dopant for n doping of C60 thin films, *J. Appl. Phys.* 100 (2) (2006) 023716.
- [63] A. Werner, F. Li, K. Harada, M. Pfeiffer, T. Fritz, K. Leo, Pyronin B as a donor for n-type doping of organic thin films, *Appl. Phys. Lett.* 82 (25) (2003) 4495.
- [64] A. Werner, F. H. Li, K. Harada, M. Pfeiffer, L. Fritz, K. Leo, S. Machill, n-type doping of organic thin films using cationic dyes, *Adv. Funct. Mater.* 14 (3) (2004) 255.
- [65] F. Li, A. Werner, M. Pfeiffer, K. Leo, X. Liu, Leuco crystal violet as a dopant for n-doping of organic thin films of fullerene C60, *J. Phys. Chem. B* 108 (44) (2004) 17076.
- [66] A. Twarowski, Oxygen doping of zinc phthalocyanine thin films, *J. Chem. Phys.* 77 (11) (1982) 5840.
- [67] A. K. Hassan, R. D. Gould, Asymmetric electrical-conductivity in oxygen-doped thin-films of copper phthalocyanine, using gold and aluminum electrodes, *Int. J. Electron.* 69 (1) (1990) 11.
- [68] T. D. Anthopoulos, T. S. Shafai, Influence of oxygen doping on the electrical and photovoltaic properties of Schottky type solar cells based on alpha-nickel phthalocyanine, *Thin Solid Films* 441 (1-2) (2003) 207.
- [69] T. Nishi, K. Kanai, Y. Ouchi, M. R. Willis, K. Seki, Oxygen effects on the interfacial electronic structure of titanyl phthalocyanine film: p-type doping, band bending and Fermi level alignment, *Chem. Phys.* 325 (1) (2006) 121.
- [70] J. Curry, E. P. Cassidy, Effect of halogens on resistance of single crystals of copper phthalocyanine, *J. Chem. Phys.* 37 (9) (1962) 2154.
- [71] W. A. Orr, S. C. Dahlberg, Effect of iodine incorporation on the electrical-conductivity of films of nickel phthalocyanine, *J. Am. Chem. Soc.* 101 (11) (1979) 2875.
- [72] D. R. Kearns, G. Tollin, M. Calvin, Electrical properties of organic solids II. effects of added electron acceptor on metal-free phthalocyanine, *J. Chem. Phys.* 32 (4) (1960) 1020.
- [73] M. Maitrot, G. Guillaud, B. Boudjema, J. André, J. Simon, Molecular material based junctions: Formation of a Schottky contact with metallophthalocyanine thin films doped by the cosublimation method, *J. Appl. Phys.* 60 (7) (1986) 2396.
- [74] M. Pfeiffer, A. Beyer, T. Fritz, K. Leo, Controlled doping of phthalocyanine layers by cosublimation with acceptor molecules: A systematic Seebeck and conductivity study, *Appl. Phys. Lett.* 73 (22) (1998) 3202.
- [75] W. Y. Gao, A. Kahn, Controlled p-doping of zinc phthalocyanine by coevaporation with tetrafluorotetracyanoquinodimethane: A direct and inverse photoemission study, *Appl. Phys. Lett.* 79 (24) (2001) 4040.
- [76] R. Meerheim, S. Olthof, M. Hermenau, S. Scholz, B. Lüssem, M. Riede, K. Leo, Investigation of C60F36 as non-volatile p-dopant for hole transport layers in small-molecule organic optoelectronic devices, *J. Appl. Phys.* (2011) submitted.
- [77] Z. Q. Gao, B. X. Mi, G. Z. Xu, Y. Q. Wan, M. L. Gong, K. W. Cheah, C. H. Chen, An organic p-type dopant with high thermal stability for an organic semiconductor, *Chem. Commun.* (1) (2008) 117.

- [78] P. K. Koech, A. B. Padmaperuma, L. Wang, J. S. Swensen, E. Polikarpov, J. T. Darsell, J. E. Rainbolt, D. J. Gaspar, Synthesis and application of 1,3,4,5,7,8-hexafluorotetracyanonaphthoquinodimethane (F6-TNAP): A conductivity dopant for organic light-emitting devices, *Chem. Mater.* 22 (13) (2010) 3926.
- [79] C. C. Chang, M. T. Hsieh, J. F. Chen, S. W. Hwang, C. H. Chen, Highly power efficient organic light-emitting diodes with a p-doping layer, *Appl. Phys. Lett.* 89 (25) (2006) 253504.
- [80] T. Matsushima, C. Adachi, Enhanced hole injection and transport in molybdenum-dioxide-doped organic hole-transporting layers, *J. Appl. Phys.* 103 (3) (2008) 034501.
- [81] J. H. Lee, D. S. Leem, H. J. Kim, J. J. Kim, Effectiveness of p-dopants in an organic hole transporting material, *Appl. Phys. Lett.* 94 (12) (2009) 123306.
- [82] M. Kroger, S. Hamwi, J. Meyer, T. Riedl, W. Kowalsky, A. Kahn, P-type doping of organic wide band gap materials by transition metal oxides: A case-study on molybdenum trioxide, *Org. Electron.* 10 (5) (2009) 932.
- [83] M. Kroger, S. Hamwi, J. Meyer, T. Riedl, W. Kowalsky, A. Kahn, Role of the deep-lying electronic states of MoO₃ in the enhancement of hole-injection in organic thin films, *Appl. Phys. Lett.* 95 (12) (2009) 123301.
- [84] J. H. Lee, D. S. Leem, J. J. Kim, High performance top-emitting organic light-emitting diodes with copper iodide-doped hole injection layer, *Org. Electron.* 9 (5) (2008) 805.
- [85] J. Endo, T. Matsumoto, J. Kido, Organic electroluminescent devices with a vacuum-deposited lewis-acid-doped hole-injecting layer, *Jpn. J. Appl. Phys.* 2 41 (3B) (2002) L358.
- [86] P. Würfel, *Physik der Solarzellen*, Spektrum, Akademischer Verlag, Heidelberg, Berlin, 2000.
- [87] K. Emery, *Handbook of Photovoltaic Science and Engineering*, Ch. 16, Wiley, Chichester, UK, 2003.
- [88] <http://www.ise.fraunhofer.de/servicebereiche/callab/internationale-standards-1> (March 2011).
- [89] V. D. Mihailetschi, L. J. A. Koster, J. C. Hummelen, P. W. M. Blom, Photocurrent generation in polymer-fullerene bulk heterojunctions, *Phys. Rev. Lett.* 93 (21) (2004) 216601.
- [90] M. Pope, C. E. Swenberg, *Electronic Processes in Organic Crystals and Polymers*, 2nd Edition, Oxford University Press, Inc., New York, 1999.
- [91] L. Onsager, Deviation from Ohm's Law in Weak Electrolytes, *J. Chem. Phys.* 2 (1934) 599.
- [92] L. Onsager, Initial recombination of ions, *Phys. Rev.* 54 (8) (1938) 554.
- [93] C. L. Braun, Electric-field assisted dissociation of charge-transfer states as a mechanism of photo-carrier production, *J. Chem. Phys.* 80 (9) (1984) 4157.
- [94] T. M. Clarke, J. R. Durrant, Charge photogeneration in organic solar cells, *Chem. Rev.* 110 (11) (2010) 6736.
- [95] M. C. Scharber, D. Wuhlbacher, M. Koppe, P. Denk, C. Waldauf, A. J. Heeger, C. L. Brabec, Design rules for donors in bulk-heterojunction solar cells - towards 10% energy-conversion efficiency, *Adv. Mater.* 18 (6) (2006) 789.
- [96] H. Ishii, K. Seki, Energy level alignment at organic/metal interfaces studied by uv photoemission: Breakdown of traditional assumption of a common vacuum level at the interface, *IEEE T. Electron. Dev.* 44 (8) (1997) 1295.
- [97] A. Kahn, N. Koch, W. Y. Gao, Electronic structure and electrical properties of interfaces between metals and pi-conjugated molecular films, *J. Polym. Sci. Pol. Phys.* 41 (21) (2003) 2529.

- [98] S. Scholz, Q. Huang, M. Thomschke, S. Olthof, P. Sebastian, K. Walzer, K. Leo, S. Oswald, C. Corten, D. Kuckling, Self-doping and partial oxidation of metal-on-organic interfaces for organic semiconductor devices studied by chemical analysis techniques, *J. Appl. Phys.* 104 (10) (2008) 104502.
- [99] S. Olthof, Photoelectron spectroscopy on doped organic semiconductors and related interfaces, Dissertation, TU Dresden (Mar. 2010).
- [100] M. Hiramoto, H. Fujiwara, M. Yokoyama, 3-layered organic solar-cell with a photoactive interlayer of codeposited pigments, *Appl. Phys. Lett.* 58 (10) (1991) 1062.
- [101] G. Yu, J. Gao, J. Hummelen, F. Wudl, A. Heeger, Polymer photovoltaic cell: Enhanced efficiency via a network of internal donor-acceptor heterojunctions, *Science* 270 (5243) (1995) 1789.
- [102] J. J. M. Halls, C. A. Walsh, N. C. Greenham, E. A. Marseglia, R. H. Friend, S. C. Moratti, A. B. Holmes, Efficient photodiodes from interpenetrating polymer networks, *Nature* 376 (6540) (1995) 498.
- [103] J. Peet, M. L. Senatore, A. J. Heeger, G. C. Bazan, The role of processing in the fabrication and optimization of plastic solar cells, *Adv. Mater.* 21 (14-15) (2009) 1521.
- [104] C. Deibel, V. Dyakonov, Polymer-fullerene bulk heterojunction solar cells, *Rep. Prog. Phys.* 73 (9) (2010) 096401.
- [105] S. Pfuetzner, A. Petrich, J. Meiss, M. Riede, K. Leo, Thick C60:ZnPc bulk heterojunction solar cells with improved performance by film deposition on heated substrates, *Appl. Phys. Lett.* 94 (2009) 253303.
- [106] D. Wynands, M. Levichkova, M. Riede, M. Pfeiffer, P. Baeuerle, R. Rentenberger, P. Denner, K. Leo, Correlation between morphology and performance of low bandgap oligothiophene: C60 mixed heterojunctions in organic solar cells, *J. Appl. Phys.* 107 (1) (2010) 014517.
- [107] F. Yang, M. Shtein, S. R. Forrest, Controlled growth of a molecular bulk heterojunction photovoltaic cell, *Nat. Mater.* 4 (1) (2005) 37.
- [108] W. Tress, K. Leo, M. Riede, Effect of concentration gradients in ZnPc:C60 bulk heterojunction organic solar cells, *Sol. Energ. Mat. Sol. C.* 95 (2011) 2981.
- [109] M. Hiramoto, T. Yamaga, M. Danno, K. Suemori, Y. Matsumura, M. Yokoyama, Design of nanostructures for photoelectric conversion using an organic vertical superlattice, *Appl. Phys. Lett.* 88 (21) (2006) 213105.
- [110] Z. R. Hong, Z. H. Huang, X. T. Zeng, Investigation into effects of electron transporting materials on organic solar cells with copper phthalocyanine/C60 heterojunctions, *Chem. Phys. Lett.* 425 (1-3) (2006) 62.
- [111] N. Wang, J. Yu, Y. Zang, J. Huang, Y. Jiang, Effect of buffer layers on the performance of organic photovoltaic cells based on copperphthalocyanine and C60, *Sol. Energ. Mat. Sol. C.* 94 (2010) 263.
- [112] C. Uhrich, D. Wynands, S. Olthof, M. K. Riede, K. Leo, S. Sonntag, B. Maennig, M. Pfeiffer, Origin of open circuit voltage in planar and bulk heterojunction organic thin-film photovoltaics depending on doped transport layers, *J. Appl. Phys.* 104 (4) (2008) 043107.
- [113] W. Tress, K. Leo, M. Riede, Influence of hole-transport layers and donor materials on open-circuit voltage and shape of I-V curves of organic solar cells, *Adv. Funct. Mater.* 21 (2011) 2140.
- [114] C. Falkenberg, S. Olthof, R. Rieger, M. Baumgarten, K. Muellen, K. Leo, M. Riede, The role of energy level matching in organic solar cells—Hexaazatriphenylene hexacarbonitrile as transparent electron transport material, *Sol. Energ. Mat. Sol. C.* 95 (3) (2011) 927.
- [115] N. Koch, Organic electronic devices and their functional interfaces, *Chemphyschem* 8 (10) (2007) 1438.

- [116] S. Duhm, I. Salzmann, B. Broker, H. Glowatzki, R. L. Johnson, N. Koch, Interdiffusion of molecular acceptors through organic layers to metal substrates mimics doping-related energy level shifts, *Appl. Phys. Lett.* 95 (9) (2009) 093305.
- [117] K. Schulze, C. Uhrich, R. Schuppel, K. Leo, M. Pfeiffer, E. Brier, E. Reinold, P. Baeuerle, Efficient vacuum-deposited organic solar cells based on a new low-bandgap oligothiophene and fullerene C60, *Adv. Mater.* 18 (21) (2006) 2872.
- [118] R. Schueppel, R. Timmreck, N. Allinger, T. Mueller, M. Furno, C. Uhrich, K. Leo, M. Riede, Controlled current matching in small molecule organic tandem solar cells using doped spacer layers, *J. Appl. Phys.* 107 (4) (2010) 044503.
- [119] C. K. Chan, W. Zhao, A. Kahn, I. G. Hill, Influence of chemical doping on the performance of organic photovoltaic cells, *Appl. Phys. Lett.* 94 (20) (2009) 203306.
- [120] S. Reineke, F. Lindner, G. Schwartz, N. Seidler, K. Walzer, B. Lüssem, K. Leo, White organic light-emitting diodes with fluorescent tube efficiency, *Nature* 459 (7244) (2009) 234.
- [121] C. Schünemann, C. Elschner, L. A. A., M. Levichkova, K. Leo, M. Riede, Zinc phthalocyanine - influence of substrate temperature, film thickness, and kind of substrate on the morphology, *Thin Solid Films* 519 (2011) 3939.
- [122] H. R. Kerp, H. Donker, R. B. M. Koehorst, T. J. Schaafsma, E. E. van Faassen, Exciton transport in organic dye layers for photovoltaic applications, *Chem. Phys. Lett.* 298 (4-6) (1998) 302.
- [123] S. Pfuetzner, C. Mickel, J. Jankowski, M. Hein, J. Meiss, C. Schuenemann, C. Elschner, A. A. Levin, B. Rellinghaus, K. Leo, M. Riede, The influence of substrate heating on morphology and layer growth in C60:ZnPc bulk heterojunction solar cells, *Org. Electronics* 12 (3) (2011) 435.
- [124] D. Wynands, Untersuchung der photovoltaischen Eigenschaften neuartiger Oligothiophene (Diplomarbeit, TU-Dresden, 2006).
- [125] D. Wynands, Strategies for optimizing organic solar cells: Correlation between morphology and performance in DCV6T-C60 heterojunctions, Ph.D. thesis, TU-Dresden (2010).
- [126] C. Elschner, A. A. Levin, L. Wilde, J. Grenzer, C. Schroer, K. Leo, M. Riede, Determining the C60 molecular arrangement in thin films by means of X-ray diffraction, *J. Appl. Crystallogr.* 44 (2011) 983.
- [127] M. Riede, C. Uhrich, J. Widmer, R. Timmreck, D. Wynands, G. Schwartz, W. M. Gnehr, D. Hildebrandt, A. Weiss, J. Hwang, S. Sudharaka, P. Erk, M. Pfeiffer, K. Leo, Efficient organic tandem solar cells based on small molecules, *Adv. Funct. Mater.* 21 (2010) 3019.
- [128] J. Wagner, M. Gruber, A. Hinderhofer, A. Wilke, B. Broker, J. Frisch, P. Amsalem, A. Vollmer, A. Opitz, N. Koch, F. Schreiber, W. Brutting, High fill factor and open circuit voltage in organic photovoltaic cells with diindenoperylene as donor material, *Adv. Funct. Mater.* 20 (24) (2010) 4295.
- [129] J. Meiss, M. Hummert, A. Petrich, S. Pfuetzner, K. Leo, M. Riede, Tetrabutyl-tetraphenyl-diindenoperylene derivatives as alternative green donor in bulk heterojunction organic solar cells, *Sol. Energ. Mat. Sol. C.* 95 (2) (2011) 630.
- [130] S. Pfuetzner, J. Meiss, A. Petrich, M. Riede, K. Leo, Improved bulk heterojunction organic solar cells employing C70 fullerenes, *Appl. Phys. Lett.* 94 (22) (2009) 223307.
- [131] P. E. Schwenn, K. Gui, A. M. Nardes, K. B. Krueger, K. H. Lee, K. Mutkins, H. Rubinstein-Dunlop, P. E. Shaw, N. Kopidakis, P. L. Burn, P. Meredith, A small molecule non-fullerene electron acceptor for organic solar cells, *Adv. Energy Mater.* 1 (1) (2011) 73.
- [132] S. E. Jang, J. Y. Lee, Organic interlayer for high power efficiency in organic light-emitting diodes, *Synthetic Met.* 161 (1-2) (2011) 40.
- [133] K. S. Yook, S. O. Jeon, J. Y. Lee, Efficient hole injection by doping of hexaazatriphenylene hexacarbonitrile in hole transport layer, *Thin Solid Films* 517 (21) (2009) 6109.

- [134] L. S. Liao, W. K. Slusarek, T. K. Hatwar, M. L. Ricks, D. L. Comfort, Tandem organic light-emitting mode using hexaazatriphenylene hexacarbonitrile in the intermediate connector, *Adv. Mater.* 20 (2) (2008) 324.
- [135] T. Chiba, Y. J. Pu, R. Miyazaki, K. Nakayama, H. Sasabe, J. Kido, Ultra-high efficiency by multiple emission from stacked organic light-emitting devices, *Org. Electronics* 12 (4) (2011) 710.
- [136] Y. K. Kim, J. W. Kim, Y. Park, Energy level alignment at a charge generation interface between 4,4'-bis(N-phenyl-1-naphthylamino)biphenyl and 1,4,5,8,9,11-hexaazatriphenylene-hexacarbonitrile, *Appl. Phys. Lett.* 94 (6) (2009) 063305.
- [137] H. Glowatzki, B. Broker, R. P. Blum, O. T. Hofmann, A. Vollmer, R. Rieger, K. Mullen, E. Zojer, J. P. Rabe, N. Koch, "soft" metallic contact to isolated C60 molecules, *Nano Lett.* 8 (11) (2008) 3825.
- [138] B. Broeker, R. P. Blum, J. Frisch, A. Vollmer, O. T. Hofmann, R. Rieger, K. Muellen, J. P. Rabe, E. Zojer, N. Koch, Gold work function reduction by 2.2 eV with an air-stable molecular donor layer, *Appl. Phys. Lett.* 93 (24) (2008) 243303.
- [139] S. H. Park, J. G. Jeong, H. J. Kim, S. H. Park, M. H. Cho, S. W. Cho, Y. Yi, M. Y. Heo, H. Sohn, The electronic structure of C60/ZnPc interface for organic photovoltaic device with blended layer architecture, *Appl. Phys. Lett.* 96 (1) (2010) 013302.
- [140] L. S. Liao, K. P. Klubek, Power efficiency improvement in a tandem organic light-emitting diode, *Appl. Phys. Lett.* 92 (22) (2008) 223311.
- [141] K. S. Yook, S. O. Jeon, C. W. Joo, J. Y. Lee, Hole injection improvement by doping of organic material in copper phthalocyanine, *J. Ind. Eng. Chem.* 15 (6) (2009) 907.
- [142] J. G. Laquindanum, H. E. Katz, A. Dodabalapur, A. J. Lovinger, n-channel organic transistor materials based on naphthalene frameworks, *J. Am. Chem. Soc.* 118 (45) (1996) 11331.
- [143] H. E. Katz, J. Johnson, A. J. Lovinger, W. J. Li, Naphthalenetetracarboxylic diimide-based n-channel transistor semiconductors: Structural variation and thiol-enhanced gold contacts, *J. Am. Chem. Soc.* 122 (32) (2000) 7787.
- [144] C. R. Newman, C. D. Frisbie, D. A. da Silva, J. L. Bredas, P. C. Ewbank, K. R. Mann, Introduction to organic thin film transistors and design of n-channel organic semiconductors, *Chem. Mater.* 16 (23) (2004) 4436.
- [145] P. Strohriegl, J. V. Grazulevicius, Charge-transporting molecular glasses, *Adv. Mater.* 14 (20) (2002) 1439.
- [146] Y. Shirota, Organic materials for electronic and optoelectronic devices, *J. Mater. Chem.* 10 (1) (2000) 1.
- [147] S. Lee, T. Tsutsu, Molecular design of fluorene-based polymers and oligomers for organic light-emitting diodes, *Thin Solid Films* 363 (1-2) (2000) 76.
- [148] J. U. Wallace, S. H. Chen, Fluorene-based conjugated oligomers for organic photonics and electronics, *Adv. Polym. Sci.* 212 (2008) 145.
- [149] C. Falkenberg, M. Hummert, Naphthalenetetracarboxylic diimide derivatives as electron transport materials in organic solar cells: Correlation between side groups, physical properties, and solar cell performance, (2012) in preparation.
- [150] S. Barlow, Q. Zhang, B. R. Kaafarani, C. Risko, F. Amy, C. K. Chan, B. Domercq, Z. A. Starikova, M. Y. Antipin, T. V. Timofeeva, B. Kippelen, J. L. Bredas, A. Kahn, S. R. Marder, Synthesis, ionisation potentials and electron affinities of hexaazatriphenylene derivatives, *Chem.-Eur. J.* 13 (12) (2007) 3537.

- [151] B. R. Kaafarani, T. Kondo, J. S. Yu, Q. Zhang, D. Dattilo, C. Risko, S. C. Jones, S. Barlow, B. Domercq, F. Amy, A. Kahn, J. L. Bredas, B. Kippelen, S. R. Marder, High charge-carrier mobility in an amorphous hexaazatrinaphthylene derivative, *J. Am. Chem. Soc.* 127 (47) (2005) 16358.
- [152] S. D. Ha, B. R. Kaafarani, S. Barlow, S. R. Marder, A. Kahn, Multiphase growth and electronic structure of ultrathin hexaazatrinaphthylene on Au(111), *J. Phys. Chem. C* 111 (28) (2007) 10493.
- [153] B. Gao, Y. Liu, Y. Geng, Y. Cheng, L. Wang, X. Jing, F. Wang, Starburst substituted hexaazatrinaphthylene compounds: synthesis, photophysical and electrochemical properties, *Tetrahedron Lett.* 50 (14) (2009) 1649.
- [154] H. Bock, A. Babeau, I. Seguy, P. Jolinat, P. Destruel, Electron-deficient columnar plastic crystals, *Chemphyschem* 3 (6) (2002) 532.
- [155] M. Lehmann, G. Kestemont, R. G. Aspe, C. Buess-Herman, M. H. J. Koch, M. G. Debije, J. Piris, M. P. de Haas, J. M. Warman, M. D. Watson, V. Lemaure, J. Cornil, Y. H. Geerts, R. Gearba, D. A. Ivanov, High charge-carrier mobility in pi-deficient discotic mesogens: Design and structure-property relationship, *Chem.-Eur. J.* 11 (11) (2005) 3349.
- [156] L. Born, G. Heywang, Crystal-structure of 1,4,5,8-naphthalene-tetracarboxylic-dianhydride (NTDA), *Z. Krist.* 190 (1-2) (1990) 147.
- [157] Y. L. Tung, S. W. Lee, Y. Chi, Y. T. Tao, C. H. Chien, Y. M. Cheng, P. T. Chou, S. M. Peng, C. S. Liu, Organic light-emitting diodes based on charge-neutral Os(II) emitters: generation of saturated red emission with very high external quantum efficiency, *J. Mater. Chem.* 15 (4) (2005) 460.
- [158] R. Nitsche, Optical properties of organic semiconductors: From (sub-)monolayers to crystalline films, Dissertation, TU Dresden (2005).
- [159] T. Fritz, J. Hahn, H. Bottcher, Determination of the optical-constants of evaporated dye layers, *Thin Solid Films* 170 (2) (1989) 249.
- [160] L. G. Parratt, Surface studies of solids by total reflection of x-rays, *Phys. Rev.* 95 (2) (1954) 359.
- [161] S. K. Sinha, E. B. Sirota, S. Garoff, H. B. Stanley, X-ray and neutron-scattering from rough surfaces, *Phys. Rev. B* 38 (4) (1988) 2297.
- [162] I. Horcas, R. Fernandez, G.-R. J. M., C. J., G.-H. J., B. A. M., WSXM: A software for scanning probe microscopy and a tool for nanotechnology, *Rev. Sci. Instrum.* 78 (2007) 013705.
- [163] A. A. Levin, M. Levichkova, D. Hildebrandt, M. Klisch, D. Weiss, A. Wynands, C. Elschner, M. Pfeiffer, K. Leo, M. Riede, Effect of film thickness, type of buffer layer, and substrate temperature on the morphology of dicyanovinyl-substituted sexithiophene films by X-ray methods, *Thin Solid Films* in press.
- [164] B. L. Henke, E. M. Gullikson, J. C. Davis, X-ray interactions - photoabsorption, scattering, transmission, and reflection at E=50-30,000 eV, Z=1-92, *Atom. Data Nucl. Data* 54 (2) (1993) 181.
- [165] S. Huefner, *Photoelectron Spectroscopy*, Springer Verlag, Berlin, 2003.
- [166] N. Koch, A. Kahn, J. Ghijssen, J. J. Pireaux, J. Schwartz, R. L. Johnson, A. Elschner, Conjugated organic molecules on metal versus polymer electrodes: Demonstration of a key energy level alignment mechanism, *Appl. Phys. Lett.* 82 (1) (2003) 70.
- [167] W. Zhao, E. Salomon, Q. Zhang, S. Barlow, S. R. Marder, A. Kahn, Substrate-dependent electronic structure of an organic heterojunction, *Phys. Rev. B* 77 (16) (2008) 165336.
- [168] N. G. Connelly, W. E. Geiger, Chemical redox agents for organometallic chemistry, *Chem. Rev.* 96 (2) (1996) 877.
- [169] B. W. D'Andrade, S. Datta, S. R. Forrest, P. Djurovich, E. Polikarpov, M. E. Thompson, Relationship between the ionization and oxidation potentials of molecular organic semiconductors, *Org. Electron.* 6 (1) (2005) 11.

- [170] H. Seifert, Externe Quanteneffizienz von organischen Solarzellen (Diplomarbeit, TU-Dresden, 2008).
- [171] V. Shrotriya, G. Li, Y. Yao, T. Moriarty, K. Emery, Y. Yang, Accurate measurement and characterization of organic solar cells, *Adv. Funct. Mater.* 16 (15) (2006) 2016.
- [172] G. Dennler, The value of values, *Mater. Today* 10 (11) (2007) 56.
- [173] M. Furno, program OSOLemio, unpublished.
- [174] E. Centurioni, Generalized matrix method for calculation of internal light energy flux in mixed coherent and incoherent multilayers, *Appl. Optics* 44 (35) (2005) 7532.
- [175] J. Meiss, M. Furno, S. Pfuetzner, K. Leo, M. Riede, Selective absorption enhancement in organic solar cells using light incoupling layers, *J. Appl. Phys.* 107 (5) (2010) 053117.
- [176] L. Burtone, K. Leo, M. Riede, Negative capacitance in ZnPc p/n homjunction diodes, (2011) in preparation.
- [177] M. O. Reese, S. A. Gevorgyan, M. Jorgensen, E. Bundgaard, S. R. Kurtz, D. S. Ginley, D. C. Olson, M. T. Lloyd, P. Morvillo, E. A. Katz, A. Elschner, O. Haillant, T. R. Currier, V. Shrotriya, M. Hermenau, M. Riede, K. R. Kirov, G. Trimmel, T. Rath, O. Inganäs, F. Zhang, M. Andersson, K. Tvingstedt, M. Lira-Cantu, D. Laird, C. McGuinness, S. J. Gowrisanker, M. Pannone, M. Xiao, J. Hauch, R. Steim, D. M. DeLongchamp, R. Rösch, H. Hoppe, N. Espinosa, A. Urbina, G. Yaman-Uzunoglu, J.-B. Bonekamp, A. J. van Breemen, C. Girotto, E. Voroshazi, F. C. Krebs, Consensus stability testing protocols for organic photovoltaic materials and devices, *Sol. Energ. Mat. Sol. C.* 95 (5) (2011) 1253, special Issue : 3rd International Summit on OPV Stability.
- [178] B. Servet, G. Horowitz, S. Ries, O. Lagorsse, P. Alnot, A. Yassar, F. Deloffre, P. Srivastava, R. Hajlaoui, P. Lang, F. Garnier, Polymorphism and charge-transport in vacuum-evaporated sexithiophene films, *Chem. Mater.* 6 (10) (1994) 1809.
- [179] K. Narushima, T. Kontani, R. F. Egerton, R. Urao, M. Takeuchi, Influence of crystal structure on carrier transport in titanylphthalocyanine thin films, *Appl. Surf. Sci.* 113 (1997) 326.
- [180] S. Tatemichi, M. Ichikawa, T. Koyama, Y. Taniguchi, High mobility n-type thin-film transistors based on N,N'-ditridecyl perylene diimide with thermal treatments, *Appl. Phys. Lett.* 89 (11) (2006) 112108.
- [181] K. Harada, F. Li, B. Männig, M. Pfeiffer, K. Leo, Ionized impurity scattering in n-doped C60 thin films, *Appl. Phys. Lett.* 91 (9) (2007) 092118.
- [182] V. I. Arkhipov, P. Heremans, E. V. Emelianova, H. Bassler, Effect of doping on the density-of-states distribution and carrier hopping in disordered organic semiconductors, *Physical Review B* 71 (4) (2005) 045214.
- [183] P. Amsalem, J. Frisch, A. Wilke, A. Vollmer, R. Rieger, K. Muellen, J.-P. Rabe, N. Koch, Poster, DPG Frühjahrstagung (SKM), Regensburg, 2010.
- [184] C. Brabec, A. Cravino, D. Meissner, N. Sariciftci, M. Rispens, L. Sanchez, J. Hummelen, T. Fromherz, The influence of materials work function on the open circuit voltage of plastic solar cells, *Thin Solid Films* 403 (2002) 368–372.
- [185] A. Gadisa, M. Svensson, M. R. Andersson, O. Inganäs, Correlation between oxidation potential and open-circuit voltage of composite solar cells based on blends of polythiophenes/fullerene derivative, *Applied Physics Letters* 84 (9) (2004) 1609–1611.
- [186] R. Schueppel, K. Schmidt, C. Urich, K. Schulze, D. Wynands, J. L. Bredas, E. Brier, E. Reinold, H. B. Bu, P. Baeuerle, B. Maennig, M. Pfeiffer, K. Leo, Optimizing organic photovoltaics using tailored heterojunctions: A photoinduced absorption study of oligothiophenes with low band gaps, *Phys. Rev. B* 77 (8) (2008) 085311.
- [187] D. Cheyns, J. Poortmans, P. Heremans, C. Deibel, S. Verlaak, B. P. Rand, J. Genoe, Analytical model for the open-circuit voltage and its associated resistance in organic planar heterojunction solar cells, *Phys. Rev. B* 77 (16) (2008) 165332.

- [188] W. Gao, A. Kahn, Controlled p-doping of the hole-transport molecular material alpha-NPD mit tetrafluortetracyanoquinodimethane, *J. Appl. Phys.* **94** (1) (2003) 359.
- [189] C. K. Chan, A. Kahn, N-doping of pentacene by decamethylcobaltocene, *Appl. Phys. A-mater.* **95** (1) (2009) 7.
- [190] A. Kahn, W. Zhao, W. Y. Gao, H. Vazquez, F. Flores, Doping-induced realignment of molecular levels at organic-organic heterojunctions, *Chem. Phys.* **325** (1) (2006) 129.
- [191] R. Schlaf, B. A. Parkinson, P. A. Lee, K. W. Nebesny, N. R. Armstrong, Determination of frontier orbital alignment and band bending at an organic semiconductor heterointerface by combined x-ray and ultraviolet photoemission measurements, *Appl. Phys. Lett.* **73** (8) (1998) 1026.
- [192] R. Schlaf, B. A. Parkinson, P. A. Lee, K. W. Nebesny, N. R. Armstrong, HOMO/LUMO alignment at PTCDA/ZnPc and PTCDA/ClInPc heterointerfaces determined by combined UPS and XPS measurements, *J. Phys. Chem. B* **103** (15) (1999) 2984.
- [193] C. Hein, E. Mankel, T. Mayer, W. Jaegermann, Engineering the electronic structure of the CuPc/BPE-PTCDI interface by WO₃ doping of CuPc, *Phys. Status Solidi A* **206** (12) (2009) 2757.
- [194] S. Olthof, R. Meerheim, M. Schober, K. Leo, Energy level alignment at the interfaces in a multilayer organic light-emitting diode structure, *Phys. Rev. B* **79** (24) (2009) 245308.
- [195] S. Olthof, H. Kleemann, B. L'ussem, K. Leo, Built-in potential of a pentacene pin homojunction studied by ultraviolet photoemission spectroscopy, *Mater. Res. Soc. Symp. Proc.* **1270** (2010) 1270-II09-49.
- [196] C. Falkenberg, K. Leo, M. Riede, Improved photocurrent by using n-doped 2,3,8,9,14,15-hexachloro-5,6,11,12,17,18-hexaazatrinaphthylene (hatna-cl6), *J. Appl. Phys.*, in press 110.
- [197] D. Ray, L. Burtone, K. Leo, M. Riede, Detection of trap charge in small molecular organic bulk heterojunction solar cells, *Phys. Rev. B* **82** (12) (2010) 125204.
- [198] L. Burtone, D. Ray, K. Leo, M. Riede, Impedance model of trap states for organic semiconductor devices characterization, *Org. Electron.*, submitted.
- [199] C. T. Sah, *Fundamentals of solid-state electronics*, World Scientific Publishing Co Pte Ltd, 1991.
- [200] J. Bisquert, Chemical capacitance of nanostructured semiconductors: Its origin and significance for nanocomposite solar cells, *Phys. Chem. Chem. Phys.* **5** (24) (2003) 5360.
- [201] B. K. Jones, J. Santana, M. McPherson, Negative capacitance effects in semiconductor diodes, *Solid State Commun.* **107** (2) (1998) 47.
- [202] M. Ershov, H. C. Liu, L. Li, M. Buchanan, Z. R. Wasilewski, A. K. Jonscher, Negative capacitance effect in semiconductor devices, *IEEE T. Electron. Dev.* **45** (10) (1998) 2196.
- [203] H. H. P. Gommans, M. Kemerink, R. A. J. Janssen, Negative capacitances in low-mobility solids, *Phys. Rev. B* **72** (23) (2005) 235204.
- [204] N. D. Nguyen, M. Schmeits, H. P. Loeb, Determination of charge-carrier transport in organic devices by admittance spectroscopy: Application to hole mobility in alpha-NPD, *Phys. Rev. B* **75** (7) (2007) 075307.
- [205] J. Bisquert, A variable series resistance mechanism to explain the negative capacitance observed in impedance spectroscopy measurements of nanostructured solar cells, *Phys. Chem. Chem. Phys.* **13** (10) (2011) 4679.
- [206] Y. Maruyama, N. Iwasaki, Absorption spectra of amorphous organic films, *Chem. Phys. Lett.* **24** (1974) 26.
- [207] F. Graser, E. Hadicke, Crystal-structure and color of perylene-3,4,9,10-bis(dicarboximide) pigments 2, *Liebigs Ann. Chem.* (3) (1984) 483.

- [208] G. Klebe, F. Graser, E. Hadicke, J. Berndt, Crystallochromy as a solid-state effect - correlation of molecular-conformation, crystal packing and color in perylene-3,4-9,10-bis(dicarboximide) pigments, *Acta Crystallogr. B* 45 (1989) 69.
- [209] A. Opitz, J. Wagner, W. Brutting, I. Salzmann, N. Koch, J. Manara, J. Pflaum, A. Hinderhofer, F. Schreiber, Charge separation at molecular donor-acceptor interfaces: Correlation between morphology and solar cell performance, *IEEE J. Sel. Top. Quant.* 16 (6) (2010) 1707.
- [210] A. Cravino, P. Schilinsky, C. J. Brabec, Characterization of organic solar cells: the importance of device layout, *Adv. Funct. Mater.* 17 (18) (2007) 3906.
- [211] G. F. Burkhard, E. T. Hoke, M. D. McGehee, Accounting for interference, scattering, and electrode absorption to make accurate internal quantum efficiency measurements in organic and other thin solar cells, *Adv. Mater.* 22 (30) (2010) 3293.
- [212] L. H. Slooff, S. C. Veenstra, J. M. Kroon, D. J. D. Moet, J. Sweelssen, M. M. Koetse, Determining the internal quantum efficiency of highly efficient polymer solar cells through optical modeling, *Appl. Phys. Lett.* 90 (14) (2007) 143506.
- [213] D. Wynands, M. Levichkova, K. Leo, C. Uhrich, G. Schwartz, D. Hildebrandt, M. Pfeiffer, M. Riede, Increase in internal quantum efficiency in small molecular oligothiophene: C(60) mixed heterojunction solar cells by substrate heating, *Appl. Phys. Lett.* 97 (7) (2010) 073503.
- [214] A. V. Shah, H. Schade, M. Vanecek, J. Meier, E. Vallat-Sauvain, N. Wyrsh, U. Kroll, C. Droz, J. Bailat, Thin-film silicon solar cell technology, *Prog. Photovoltaics* 12 (2-3) (2004) 113.
- [215] W. Tress, Device physics of organic solar cells (2011).
- [216] Photovoltaic Geographical Information System (PVGIS), <http://re.jrc.ec.europa.eu/pvgis/index.htm> (October 2011).
- [217] W. Tress, A. Petrich, M. Hummert, M. Hein, K. Leo, M. Riede, Imbalanced mobilities causing S-shaped IV curves in planar heterojunction organic solar cells, *Appl. Phys. Lett.* 98 (2011) 063301.
- [218] M. Hermenau, M. Riede, K. Leo, S. A. Gevorgyan, F. C. Krebs, K. Norrman, Water and oxygen induced degradation of small molecule organic solar cells, *Sol. Energ. Mat. Sol. C.* 95 (5) (2011) 1268.
- [219] J. Meiss, M. Hermenau, W. Tress, C. Schuenemann, F. Selzer, M. Hummert, J. Alex, G. Lackner, K. Leo, M. Riede, Tetrapropyl-tetraphenyl-diindenoperylene derivative as a green absorber for high-voltage stable organic solar cells, *Phys. Rev. B* 83 (2011) 165305.
- [220] R. Fitzner, E. Reinold, A. Mishra, E. Mena-Osteritz, H. Ziehlke, C. Korner, K. Leo, M. Riede, M. Weil, O. Tsaryova, A. Weiss, C. Uhrich, M. Pfeiffer, P. Bauerle, Dicyanovinyl-substituted oligothiophenes: Structure-property relationships and application in vacuum-processed small-molecule organic solar cells, *Adv. Funct. Mater.* 21 (5) (2011) 897.
- [221] R. Timmreck, S. Olthof, K. Leo, M. K. Riede, Highly doped layers as efficient electron-hole recombination contacts for tandem organic solar cells, *J. Appl. Phys.* 108 (2010) 033108.
- [222] P. A. Troshin, H. Hoppe, A. S. Peregudov, M. Egginger, S. Shokhovets, G. Gobsch, N. S. Sariciftci, V. F. Razumov, [70]fullerene-based materials for organic solar cells, *ChemSusChem* 4 (1) (2011) 119.
- [223] F. Selzer, Untersuchung transparenter Elektronentransportmaterialien für die Anwendung in organischen p-i-n Solarzellen (Diplomarbeit, TU-Dresden, 2011).

Acknowledgements / Danksagung

Betrachtet man die Zeit, die ich in den letzten Jahren am IAPP verbracht habe, kann man es schon fast als zweites zu Hause bezeichnen. Dank des freundschaftlichen Arbeitsklimas ist es ein Ort, an dem man sich gern aufhält um zu forschen, zu lernen und kreative Ideen auszutauschen. Bei Professor Karl Leo möchte ich mich daher nicht nur für die Möglichkeit bedanken, mir ein so facettenreiches und interessantes Thema zur Verfügung gestellt zu haben, sondern auch dafür, das IAPP und die Dresdner Forschungslandschaft auf so unverwechselbare Weise geprägt zu haben. Professor Klaus Müllen gilt mein Dank für die Erstellung des Zweitgutachtens sowie für die konstruktive Kooperation bezüglich einiger interessanter Moleküle. In dieser Reihe sei noch mein Arbeitsgruppenleiter und „Inno Profile Team Captain“ Dr. Moritz Riede genannt, der immer ein offenes Ohr für Fragen hatte, obwohl seine Arbeit (und die Anliegen der vielen anderen Arbeitsgruppenmitglieder) ihn meist von früh bis spät in Beschlag nahmen. Das Entziffern seiner, nebenbei gesagt sehr hilfreichen Korrekturen, führte im Büro BEY 95 oft zu hitzigen Diskussionen.

Wie man schon am Methodenkapitel sehen kann, haben zahlreiche Leute zum Gelingen dieser Arbeit beigetragen indem sie mich tatkräftig bei Herstellung, Messung und Auswertung der Proben unterstützt haben. Ihnen allen kann ich gar nicht genug danken, insbesondere dafür, dass das gemeinsame Arbeiten oft viel Spaß gemacht hat. Dr. Markus Hummert danke ich für die *Synthese* zahlreicher Materialien, für die das Erlangen des Prädikats „ETM“ meist nicht einfach war; weiterhin für die Beantwortung vieler Fragen über organische Chemie, das Durchführen der Zyklovoltammetriemessungen und die erfolgreiche Zusammenarbeit am Patent. Für die Synthese von HATCN danke ich insbesondere Ralph Rieger aus der Arbeitsgruppe von Prof. Martin Baumgarten und Prof. Klaus Müllen. HATNA-Cl₆ wurde freundlicherweise von der Novaled AG zur Verfügung gestellt. Ich danke weiterhin vielen Menschen für die Unterstützung bei der umfassenden *Charakterisierung* der vielen ETM Kandidaten: Dr. Selina Olthof hat mir nicht nur bei UPS Messungen und Auswertung zur Seite gestanden, sondern mit ihrer Gesellschaft auch oft das Arbeiten in unserem Lieblingslabor UFO 1 verschönert. Auch abseits des beruhigenden Brummens der Vakuumpumpen war sie stets für ein gutes Gespräch oder eine Unternehmung zu haben. Nach ihrem Abschied hat Max Tietze die Betreuung der UPS Anlage und damit das Durchführen der Messungen übernommen und mich ebenso erfolgreich beim Ringen mit der Anlage „Pho(i)bos“ unterstützt. Ich möchte mich bei Christoph Schünemann für seinen Röntgenblick bedanken, mit dem er nicht nur meine Proben im XRD und XRR durchleuchtet hat, sondern mir auch in anderen Wissens- und Lebensbereichen auf die Sprünge geholfen hat. Fazit: Es lohnt sich viele Fragen zu stellen und in objektiv komplizierten Situationen zu unkonventionellen Lösungen zu greifen. Das Bild über die Morphologie meiner Proben vervollständigte sich durch die Unterstützung von Dr. Alexandr Levin, und Dr. Lutz Wilde, die freundlicherweise die GIXRD Messungen für mich durchführten. Moritz Hein und Jens Jankowski danke ich für die Vermessung von OFET Proben und die damit verknüpfte Bestimmung der Elektronenbeweglichkeiten. Ein großer Dank gilt auch Felix Holzmüller und Peter Schmidt, die im Rahmen ihrer Tätigkeit als studentische Hilfskräfte viele Proben hergestellt und charakterisiert haben. Einige theoretische Erkenntnisse über Energieniveaus verdanke ich den DFT Berechnungen von Roland Gresser. Allen Materialien, die die ersten Eignungstests bestanden hatten, wurde anschließend die Ehre zuteil in *Solarzellen* eingesetzt zu werden. Ein großer Dank gilt hier Dr. Mauro Furno für die Programmierung des Simulationsprogrammes OSOLEmio, das ein sehr nützliches Werkzeug bei der Planung und Optimierung von Solarzellenstrukturen darstellt. Aufgrund der großen Menge an Proben wäre die Charakterisierung ohne LIV und EQE Roboter schwer denkbar gewesen. Das Betreiben dieser beiden Geräte ist wiederum ohne die Hilfe von Dr. André Merten und Johannes Widmer unvorstellbar, die geduldig alle Fragen beantwortet und Fehler repariert haben – manchmal durch bloßes Handauflegen. Auch wenn es die Tandembaulemente nicht mehr in die Arbeit geschafft haben, danke ich Ronny Timmreck für die Kooperation bei Planung und Vermessung. Das nächste Mal bauen wir bessere Zellen! Von Lorenzo Burtone habe ich viel über Impedanzspektroskopie und die Interpretation der zugehörigen Spektren gelernt. Vielen Dank für die große Unterstützung bei Messung und Auswertung der Proben.

Die Methode ist wirklich sehr lohnend und hat die vorliegende Arbeit an vielen Stellen vorangebracht. Schließlich danke ich Martin Hermenau für die gezielte Zerstörung, sprich beschleunigte Alterung, meiner Solarzellen, die einen Test der Anwendungstauglichkeit der neuen Materialien erlaubte.

Neben den bereits genannten Personen gibt es in der Kategorie *Rat und Tat* viele Menschen, die stets ein offenes Ohr für mich hatten, mögliche Antworten auf schwierige Fragen mit mir gesucht und manchmal auch gefunden haben, oder falls letzteres nicht klappte, mich einfach ein bisschen von der Arbeit abgelenkt haben. Allen voran stehen hier alle derzeitigen und ehemaligen Mitbewohner des Büros BEY 95, welches ganz subjektiv betrachtet das schönste Büro im IAPP ist. Mein ganz besonderer Dank gilt dabei Dr. David Wynands, dem Erstkorrektor dieser Arbeit, mit dem ich nicht nur über Solarzellen philosophiert, sondern auch Abenteuer in fernen Ländern bestanden habe. Dabei sind gute Reisegefährten bekanntlich sehr wichtig. Weiterhin danke ich Wolfgang Tress, dem Ruhepol unseres Büros und ebenfalls Teil der Reisegruppe nach Down Under, für das Teilen seines umfangreichen Hintergrundwissens über *jV*-Kennlinien und S-Knicke. Johannes Widmer, der als Vierte Person mit uns das Land der Kängurus bereiste, bin ich für kreative Vorschläge zur Lösung diverser messtechnischer Probleme und insbesondere für den Gedankenaustausch zur Streuung am Metall/Organik Kontakt dankbar. Zusätzlich möchte ich sein unermüdliches Engagement für die Arbeitsgruppe und die Begeisterung beim Vermitteln von Grundlagenwissen über organische Elektronik an ahnungslose Mitbürger lobend erwähnen. Auch wenn Toni Müller die BEY 95 schon vor einer ganzen Weile verlassen hat, bin ich ihm dennoch für zahlreiche Meinungen und Ideen, für den Run-Button und für viele kurzweilige Spieleabende dankbar. Sarah Röttinger danke ich für spannende Geschichten rund ums AFM sowie so manche Inspiration und Lebensweisheit. Dr. Patricia Freitag danke ich für die vielen schönen Stunden, in denen wir uns umgeben von vielen duftenden Pfefferkuchen, anderen Backwaren oder den Einzelteilen einer Papierfrauenkirche nicht nur, aber doch gelegentlich, über unsere Arbeit unterhalten haben. Christian Körner gilt mein großer Dank dafür, dass er sich unserem Lieblingslabor UFO 1 trotz (oder wegen?) dessen Kapriolen so fürsorglich angenommen hat, nachdem ich dafür weniger Zeit aufbringen konnte. Außerdem danke ich Franz Selzer für Hilfe bei der Betreuung der Farb 2 und die Gesellschaft an der ETM Front. Auch von außerhalb der BEY 95 gab es moralische Unterstützung. Ich danke dem Teufelchen, alias Dr. Jan Meiß, für viele interessante Gespräche und das „Approven“ einiger Lesker Runs; Dr. Lars Müller-Meskamp für das Organisieren einiger Ausflüge aufs (Glatt-)Eis; sowie Torben Menke für seine erfrischend direkte Art mir das Fliegen beizubringen bzw. mich dazu zu überreden eine halsbrecherische Sportart zu erlernen.

Zu den *Menschen, ohne die am IAPP gar nichts läuft* gehören ohne Frage unsere Techniker. Besonders hat sich hier unser UFO Pilot Carsten Wolf hervorgetan, der für die Wartung des „Unbekannten FluchObjekts“ verantwortlich war, aber auch sonst alles repariert hat, was seine Kollegen beim Forschen kaputt gemacht haben. Es war eine große Freude ihm ab und zu beim Schrauben und Schimpfen zu helfen. Vielen Dank auch an René Michel und Sven Kunze für das gewissenhafte Reinigen der UFO Substrate. Ohne das Lesker Team keine Lesker Proben – und von denen hatte ich wirklich einige. Ein großer Dank gebührt allen Lesker Technikern um Sandro Egert (früher) und Tobias Günther (heute), ohne deren Einsatz die Uhren hier anders ticken würden. Annette Petrich möchte ich für das Aufreinigen der vielen neuen Materialien danken, von denen die meisten zu unserer Freude im Ergebnis der Sublimation schöne, bunt schillernde Pülverchen oder Kristallite ergeben haben. Ein weiterer ganz wichtiger, aber leider besonders nervenaufreibender Punkt ist die Instandhaltung und Verwaltung unserer virtuellen Infrastruktur, die das Beheben zahlreicher Hardwareprobleme einschließt. Ich möchte mich an dieser Stelle für die hervorragende Arbeit unserer „IT Crowd“ bedanken, die die meiste Zeit über aus Kai Schmidt und Peter Leumer bestand und sich als Beherrscher des Chaos bewährt hat. Schließlich gibt es noch die guten Seelen, die für uns das bürokratische Chaos verwalten und so manche Fäden im Hintergrund ziehen: Ein herzliches Dankeschön an Dr. Angelika Wolf und Dr. Christian Zschalig, die unserer stark gewachsenen OSOL Gruppe und insbesondere der kleinen Innoprofile Untergruppe eine große Hilfe sind; weiterhin an Eva Schmidt und Jutta Hunger, ohne die das IAPP schwer vorstellbar ist und die jederzeit geduldig auf Fragen antworten, die sie bestimmt schon tausendmal gehört haben; und schließlich an Dr. Annette Polte, die mit viel Elan die Organisation vieler kleiner und großer Dinge übernimmt. Zum Schluss möchte ich noch Dr. Hartmut Fröb erwähnen, der in keine der Kategorien passt und dennoch für vieles an diesem Institut steht. Es ist nicht zuletzt sein Einsatz für Tradition und Fortschritt, der das IAPP zu etwas Besonderem macht.

Vielen Dank auch an alle *Freunde*, die indirekt zum Gelingen dieser Arbeit beigetragen haben, indem sie mich stets unterstützt haben beziehungsweise meine wechselhafte Laune während des Verfassens dieser Arbeit abgefedert haben. In ganz hohem Maße gilt das für meine ehemaligen und derzeitigen Mitbewohner / Nachbarn, die immer ganz nah am Geschehen waren.

Da den zuerst und zuletzt genannten Personen meistens eine besondere Bedeutung zukommt, möchte ich abschließend meiner Familie danken, die stets hinter mir stand und steht und mich bei allen meinen Vorhaben vorbehaltlos unterstützt hat. Ohne Euch wäre ich nicht wo ich heute bin.

Erklärung

Diese Dissertation wurde am Institut für Angewandte Physik/Photophysik der Fakultät Mathematik und Naturwissenschaften an der Technischen Universität Dresden unter wissenschaftlicher Betreuung von Prof. Dr. Karl Leo angefertigt.

Hiermit versichere ich, dass ich die vorliegende Arbeit ohne unzulässige Hilfe Dritter und ohne Benutzung anderer als der angegebenen Hilfsmittel angefertigt habe; die aus fremden Quellen direkt oder indirekt übernommenen Gedanken sind als solche kenntlich gemacht. Die Arbeit wurde bisher weder im Inland noch im Ausland in gleicher oder ähnlicher Form einer anderen Prüfungsbehörde vorgelegt. Ich versichere weiterhin, dass bislang keine Promotionsverfahren stattgefunden haben.

Ich erkenne die Promotionsordnung der Fakultät Mathematik und Naturwissenschaften an der Technischen Universität Dresden vom 20.03.2000, in der Fassung der vom Fakultätsrat am 19.06.2002 und 12.07.2002 beschlossenen und mit Erlass des Sächsischen Staatsministeriums für Wissenschaft und Kunst vom 18.03.2003 genehmigten Änderungen gemäß Satzung vom 16.04.2003 sowie gemäß der Änderungsatzung vom 17.07.2008 an.

Christiane Falkenberg

Dresden, den 02.12.2011